LINE THERMALS AND BUOYANT JETS IN CROSS-FLOW

by Mohammad Reza Dehghani January 1996



Civil Engineering and Applied Mechanics

McGill University

Montreal, Canada

A THESIS SUBMITTED TO THE FACULTY OF GRADUATE STUDIES AND RESEARCH IN PARTIAL FULFILMENT OF THE REQUIREMENTS FOR THE DEGREE OF DOCTOR OF PHILOSOPHY

© Copyright 1996 by Mohammad Reza Dehghani



Acquisitions and Bibliographic Services Branch

395 Wellington Street Ottawa, Ontario K1A 0N4 Bibliothèque nationale du Canada

Direction des acquisitions et des services bibliographiques

395, rue Wellington Ottawa (Ontario) K1A 0N4

Your file Votre référence

Our file Notre référence

The author has granted an irrevocable non-exclusive licence allowing the National Library of Canada to reproduce, loan, distribute or sell copies of his/her thesis by any means and in any form or format, making this thesis available to interested persons.

L'auteur a accordé une licence irrévocable et non exclusive la Bibliothèque permettant à nationale du Canada reproduire, prêter, distribuer ou vendre des copies de sa thèse de quelque manière et sous quelque forme que ce soit pour mettre des exemplaires de cette à la disposition personnes intéressées.

The author retains ownership of the copyright in his/her thesis. Neither the thesis nor substantial extracts from it may be printed or otherwise reproduced without his/her permission. L'auteur conserve la propriété du droit d'auteur qui protège sa thèse. Ni la thèse ni des extraits substantiels de celle-ci ne doivent être imprimés ou autrement reproduits sans son autorisation.

ISBN 0-612-12351-0



Abstract

The thesis has two related parts. The first part is concerned with an experimental investigation of a line thermal conducted in a large tank. The tracer concentration distribution in the line thermal was determined by a video imaging method. Contrary to the results of previous investigations, the spreading rate of the thermal before bifurcation was constant for all tests, and was quite independent of the initial momentum and buoyancy at the source. Bifurcation was observed as the thermal passed the mid-depth due to the interaction of the thermal with the tank bottom. The bifurcation caused the thermal to increase its spreading rate significantly, which may explain the large variation in rate obtained by previous studies.

An integral analysis of the thermal motion was conducted. The results of the analysis show that the added-mass effect due to the motion around the thermal must be included for consistent formulation of the problem. The thermal characteristics predicted by the analysis are in agreement with the experimental data.

The second part of the thesis is concerned with the development of a general integral model for buoyant jets in cross flow. Two modes of spreading in the tangential and normal directions simulated the entrainment processes. The experimental data of buoyant jets with a wide range of discharge conditions were reproduced by the model simulation using the same set of model coefficients. The model includes the initial development of the buoyant jet in the potential core region, which was not attempted in any of the previous investigations.

Résumé

Cette thèse comporte deux parties reliées entre elles. La première partie a trait à une étude expérimentale portant sur un thermique cylindrique réalisée dans un bassin de grandes dimensions. La répartition de la concentration de marqueurs dans le thermique cylindrique a été déterminée à l'aide d'une technique d'imagerie vidéo. Contrairement aux résultats desétudes antérieures, le taux de diffusion du thermique avant la bifurcation s'est révélé constant dans tous les essais et tout à fait indépendant de toute quantité de mouvement initial et de toute force ascendante à la source. Une bifurcation a été observée au moment où le thermique franchissait la ligne de mi-profondeur; ce phénomne est dû à l'interaction entre le thermique et le fond du réservoir. La bifurcation a pour effet d'accroître considérablement le taux de diffusion du thermique, ce qui pourrait expliquer les fortes variations de taux précédemment observées.

On a procédé à une analyse intégrale du mouvement thermique. Les résultats de cette analyse montrent qu'il faut prendre en compte l'effet de masse supplémentaire résultant du mouvement autour du thermique pour formuler le problème de façn cohérente. Les caractéristiques du thermique prédites par l'analyse concordent avec les données expérimentales.

La seconde partie de la thèse a trait à la formulation d'un modèle intégral général de flux ascendant dans un coulement transversal. Deux modes de diffusion dans l'axe tangentiel et dans l'axe normal reproduisent l'écoulement pour une vaste fourchette de conditions d'écoulement. Dans ces conditions d'écoulement, le modèle de flux ascendant est étalonné en fonction des données expérimentales. Le modèle tient compte de la formation initiale du flux ascendant dans la région centrale potentielle, ce dont aucune étude anterieure n'a tenté de rendre compte.

Acknowledgments

I would like to express my gratitude to my supervisor, Professor Vincent H. Chu, for his guidance and especially for his constant encouragement throughout the course of this study.

The effort and technical assistance given by Mr. Claudio Navas, for building the experimental apparatus, are greatly appreciated.

I would like to thank my fellow students and the staff in the Department of Civil Engineering and Applied Mechanics at McGill University for providing a pleasant and stimulating atmosphere for my graduate studies.

The financial assistance provided by the Ministry of Reconstruction of the Islamic Republic of Iran is gratefully acknowledged. In addition, I wish to thank Professor R. Hosseini, representative of the ministry of higher education of Iran, for his assistance during my stay in Canada.

Finally. I would like to thank my parents for their moral support during my studies. I would like also to express my appreciation to my wife Azar who encouraged me during the course of this study and to my sons, Mohsen and Milad, for their patience.

Table of Contents

	Abs	stract	
	Rés	umé	i
	Ack	nowledgments	ii
	List	of Figures	v
	List	of Tables	x
	List	of Symbols	xi
1	Intr	roduction	1
_	1.1]
	1.2	Literature Review	6
	1.2	1.2.1 Four asymptotic regimes	6
		1.2.2 Dilution Ratio	10
		1.2.3 Line thermals	12
		1.2.4 Integral formulation	18
	1.3	Objectives	19
	1.4	Scope of the Present Investigation	21
	т•	(D)	22
2		e Thermal Experiments	22
	2.1	Introduction	
	2.2	Experiment	23
		2.2.1 Visualization and Data Collection	25
		2.2.2 Mass Centres and Skewness	26
		2.2.3 Size and Path of the Turbulent Cores	27
		2.2.4 Overturning	28
		2.2.5 Dilution	29
	2.3	Two Stages of Development	30
		2.3.1 Free Thermal $(\zeta_c < 0.55H)$	31
		2.3.2 Velocity Along the Floor $(\zeta_c > 0.70H)$	32
		2.3.3 Front and Back	32
	2.4	Integral Analysis	35
	2.5	Concluding Remarks	38
3	Inte	egral Analysis	63
	3.1	Dominant Eddy Hypothesis	63
		3.1.1 Buoyancy and Momentum Equation	64
	3.2	Zone of Established Flow	65
	3.3	Potential Core	68
	3.4	Source Condition and Model Coefficients	72

Table of Contents

4	Model Verification for Non-buoyant Jets	74
	4.1 Jet Normal to the Cross-flow	74
	4.2 Oblique Jets in Cross-flows	76
5	Model Verification for Buoyant Jets	92
	5.1 Buoyant Jets in Stagnant Environment	92
	5.2 Buoyant Jets Normal to the Cross-flow	94
	5.3 Negative Buoyant Jets	95
	5.4 Buoyant Jets With Three Dimensional Trajectories	96
	5.5 Buoyant Jets in Fluids With Stratification	97
	5.6 Summary	98
6	Conclusions	123
	6.1 Summary and Conclusions	123
	6.2 Recommendations for Future Research	
	6.3 Statement of Originality	125
	References	131
A	Line Thermal Images	141
В	3 Concentration Contours 14	
_		
U	C Cross Sections defined by the 20% Contours	
D	Experimental Data 16	
\mathbf{E}	Computer Program 17	

List of Figures

1.1	Bifurcation of chimney plumes in a smooth wind. Photograph reproduced from Scorer (1958)	2
1.2	Aerial view of the thermal discharge (21 m ³ /s) from a coastal power plant made visible with a scanning infrared radiometer. Vertical discharge is 5 m below the surface and the peak temperature difference is 11.1°C. There is a coastal current of 0.27 knot (0.14 m/s) and grid spacing is 30.5 m. Photograph reproduced from Fischer et al (1979).	3
1.3	Plume bifurcation in a confined cross-flow.	4
1.4	Plume bifurcation in a confined cross-flow. Photograph reproduced from Abdelwahed and Chu (1978)	5
1.5	Three-dimensional turbulent buoyant jets in a non-uniform cross-flow. The control volume, AB, is defined by the movement of the dominant eddies produced at the source over a period of one time unit	20
1.6	The development of the mixing layer in the potential core region near the source	20
2.1	Definition sketch. The location and the dimensions of the thermal are defined by a set of key coordinates, 1 through 8, as shown in the figure.	40
2.2	Experiment apparatus: (a) 2.4 m wide, 1.2 m high and 0.06 m thick; (b) and (c) two arrangements for the release of source fluid from a 5.2 cm × 6.4 cm enclosure; the initial impulse is produced by arranging the source fluid at a level 2.6 cm above the water level in the tank as	
2.3	shown in (c)	41
2.4	respectively	42
2.5	dots. See Appendix C	43
	2.4	11

2.6	Locus of the turbulent core. The geometrical center, (z_c, y_c) , is denoted by the + symbol, and the mass center, (z_m, y_m) , by \odot . The dotted lines	
	delineate the initial spreading rate of $dy_c/dz_c \simeq dy_m/dz_m \simeq 0.18$. Upon impingment of the thermal on the bottom of the tank, the cores move	
	in opposite directions along the floor.	45
2.7	Skewness center and mass center; the symbol \odot denotes the position of the mass center, (z_m, y_m) , and the symbol + the skewness center,	
2.8	$(z_m + \gamma_z, y_m + \gamma_y)$	46
2.9	point to overturning events	47
2.10	reduced	48
	is maximum	49
	The mechansim of overturning; the images are those from test no.6.	50
2.12	Variation of R and σ with distance, ζ_c or ζ_m , from the source; the initial spreading rates, $dR/d\zeta = 0.29$ and $d\sigma/d\zeta = 0.10$ are denoted by the solid lines and the short deshed lines, respectively; the long deshed lines denote the rate, $dR/d\zeta = 0.34$, of the later development. R and σ are the radii of the equivalent circles that have the same areas as the elliptical cross section of the turbulent cores	51
2.13	Dye concentration maximum, C_m , and dye concentration averaged over the thermal cross section, C_a . The data are normalized by the total dye mass per unit length of the thermal, γ_o , initially released from the source	52
2.14	The maximum-to-average concentration ratio; $C_m/C_a = 1.61.$	53
2.15	The visual radius to standard deviation ratio, $R/\sigma=3$	54 55
2.17	Two stages of development for (a) front and (b) back of the thermals;	00
2.18	the data, ζ_f and ζ_b , are plotted versus time, $B_o^{\frac{1}{2}}t$	56
2.19	is significant to the velocity along the floor	57
	dilution for these two tests.	58

List of Figures viii

2.20	Fitting the width-to-height ratios, R_h^*/R_v and σ_h/σ_v , by emprirical formulae	59
2.21	Width of the thermal compared with the experimental data of Tsang (1971); the data of Tsang are denoted by the solid symbols; data of test no.3 and no.4 are denoted by the symbols + and ×	60
2.22	The data of $Z^{\frac{3}{2}}$ versus $B_{\sigma}^{\frac{1}{2}}t$ compared with the data of Tsang (1971); data of test no.3 and no.4 are denoted by the symbols $+$ and \times	61
2.23	Path of the thermal obtained from integral model and the comparison of the path with the experimental data; the short deshed lines are the predictions by the model that include the added-mass effect; the short dotted lines are the model prediction obtained by setting $k=0.\ldots$	62
3.1	Buoyant jets in a non-uniform cross-flow. The control volume, AB, is	
3.2	defined by the movement of the dominant eddies and is produced at the source over a period of one time unit	66
•	the source.	66
4.1	A schematic diagram of buoyant jets normal to cross flow	76
4.2	The development of the jet in the near field region; (a) $W_o/U_{a\infty}=2.37$, (b) $W_o/U_{a\infty}=3.95$, (c) $W_o/U_{a\infty}=6.35$. The contours of constant velocity in (a), (b) and (c) are reproduced from Chassaing <i>et al.</i> (1974). The dots indicates the locations where the velocity are measured by	
	hot-wire anemometry.	78
4.3	Length of the potential core in cross flow; data are obtained by Pratte and Baines (1967)	81
4.4	The development of the jet in the far field region; (a) $W_o/U_{a\infty}=5$, (b) $W_o/U_{a\infty}=15$ and (c) $W_o/U_{a\infty}=35$. The pair of curves in each figure denote the upper and lower boundaries of the turbulent jet. The experimental data of Pratte and Baines (1967) were obtained by flow	
	visualization of smoke jets in a wind tunnel	82
4.5	Thickness, $\Delta \zeta$, of jets in cross flow; $\Delta \zeta / \tilde{b} = 0.90$	83
4.6	Width, $\Delta \eta$, of jets in cross flow; $\Delta \eta / \hat{b} = 1.11$ comparison of observed and model predictions for the half-widths and	83
4.7	the center-line dilution ratios of non-buoyant jets in cross flow	84
4.8	Jet dilution as a function of vertical elevation; the momentum length scale is $\ell_m = (M_o/U_a^2)^{\frac{1}{2}}$. S_c is the minimum dilution ratio obtained from the concentration profile on the plane of symmetry. The model prediction is the average value multiplied by a factor of 0.85, i.e., $S_c = 0.85\overline{S}$	86
4.9	Comparison between the model prediction (solid line) and experimental	00
	data (denoted by symbol o) in the oblique jets in cross flow	87
5.1	Trajectories of buoyant jets discharged into stagnant and homogeneous ambient fluid. Data due to Fan (1967).	99

List of Figures ix

5.3	comparison of observed and model predictions for the half-widths and	
	the center-line dilution ratios of buoyant jets in cross flow; $\delta_{\nu}/\tilde{b}=.62$,	
	$S_c/\overline{S}=0.85.$	104
5.4	Dilution ratio as a function of the vertical elevation for buoyant jets	
	discharged into homogeneous cross-flow. Experimental data are due	
	to Fan (1967). The model prediction is $S_c = 0.85\overline{S}$. • Field data in	
	Gasport, Bridport and Hasting outfall in the U.K. (Reproduced from	
	Lee and Neville Jones, 1987)	106
5.5	Dilution ratio of buoyant jets in homogeneous cross flow. Experimental	
	data were obtained on the plane of symmetry. Model predictions are	
	$S_c = 0.85\overline{S}$	107
5.6	Normalized path of buoyant jets discharged into homogeneous cross	
	flow. Experimental data are due to Fan (1967)	108
5.7	Trend of buoyant jet thickness in a homogeneous cross flow; $\delta_v/\tilde{b}=.62$,	
	ℓ_s =13	109
5.8	Negative buoyant jets. Model results in a stagnant fluid are compared	
	with Zeitoun's data.	110
5.9	Negative buoyant jets. Model results in a stagnant fluid are compared	
	with Baines's data.	111
5.10	Buoyant jets with three-dimensional trajectories. The jets are initially	
	in a horizontal direction perpendicular to the cross flow. The experi-	
	mental data are obtained from the experiments by Chu (1975)	112
5.11	Buoyant jets with three-dimensional trajectories. Experimental data	
	of Ayoub(1971) are compared with the model prediction	115
5.12	(a) Smoke plume generated by large oil tank fire in a stable density	
	stratified environment; Photo courtesy of Los Angeles Times. (b)	
	Schematic diagram of the plume in a linearly stratified fluid	118
5.13	Model predictions compared with data of Fan (1967) for inclined and	
	horizontal buoyant jets in stagnant stratified fluid; S_p is the model	
	prediction of the averaged dilution at the peak of the buoyant jet	119
5.14	Model predictions compared with experimental data by Wright (1977)	
	for vertical buoyant jets in a stratified cross-flow: S_p is the averaged	
	dilution ratio obtained by the model for the buoyant jet at the peak.	121
5.15	Maximum rise of the buoyant plume in a stratified stagnant and strat-	
	ified fluid. Model results are compared with Briggs's data (1969)	122
0.1		
6.1	Plumes in non-uniform cross flows; $Fr = 0.1$; (a) $\theta/d_o = 0.5$, (b) $\theta/d_o = 0.5$	
	1.0, (c) $\theta/d_o = 2.0$, (d) $\theta/d_o = 0.5$; $\ell_s = [M_o^2/F_oU_a]^{\frac{1}{3}}$	128
6.2	Jets in non-uniform cross flows; $Fr = 10$; (a) $\theta/d_o = 0.5$, (b) $\theta/d_o =$	
	1.0, (c) $\theta/d_o = 2.0$, (d) $\theta/d_o = 0.5$	129
6.3	Height of the buoyant jet, z_6/ℓ_s , obtained at a downwind location where	
	$x = 6\ell_s$	130
6.4	Length of the potential core, ℓ_p/d_o , obtained for three densimetric	
	Froude numbers, $Fr = 0.1$, 1.0 and 10.0	130

List of Figures

A.1	Images of test no. 1 at 4 second intervals	142
A.2	Images of test no. 2 at 4 second intervals	143
A.3	Images of test no. 3 at 4 second intervals	144
A.4	Images of test no. 4 at 4 second intervals	148
A.5	Images of test no. 5 at 4 second intervals	146
A.6	Images of test no. 6 at 4 second intervals	14'
B.1	Concentration contours of the images in test no.1 at 4 sec intervals	149
B.2	Concentration contours of the images in test no.2 at 4 sec intervals	150
B.3	Concentration contours of the images in test no.3 at 4 sec intervals	15
B.4	Concentration contours of the images in test no.4 at 4 sec intervals	152
B.5	Concentration contours of the images in test no.5 at 4 sec intervals	153
B.6	Concentration contours of the images in test no.6 at 4 sec intervals	154
C.1	Images of test no.1 defined by the 20% contour; the key coordinates are marked	156
C.2	Images of test no.2 defined by the 20% contour; the key coordinates are marked	157
C.3	Images of test no.3 defined by the 20% contour; the key coordinates	10
0.0	are marked	158
C.4	Images of test no.4 defined by the 20% contour; the key coordinates are marked	159
C.5	Images of test no.5 defined by the 20% contour; the key coordinates are marked	160
C.6	Images of test no.1 defined by the 20% contour; the key coordinates	100
J. •	are marked	161
D.1	Definition for the location of the key coordinates $(x_i, y_i; i = 1, 8)$	162

List of Tables xi

List of Tables

1.1	Formulae for the four regimes of buoyant jets in cross flows: mdnf,	
	bdnf, mdff, and bdff	8
1.2	Asymptotic solutions for the four regimes of buoyant jets in cross flows:	
	mdnf, bdnf, mdff, and bdff	ç
1.3	Buoyant jet experiments: the width, W , height, H , and length of the	
	tank, L , in meters, are given in the last column of the table	13
1.4	Line thermal experiments: the width, W , height, H , and depth, D of	
	the tank are given in metres; cross section area of the source is given	
	in cm ²	17
2.1	Summary of test conditions	24
3.1	Summary of Equations in the Zone of Established Flow	69
3.2	Summary of Equations in the Potential Core Region	70
0.2	building of Equations in the Potential Cole Region.	•
4.1	Summary of available experiments and flow conditions for non-buoyant	
	jets in cross flow	75
5.1	Summary of available experiments and flow conditions for buoyant jets.	93
D.1	Source coordinates (x_o, y_o) and key coordinates $(x_i, y_i, i = 1, 8)$	163
D.2	Average concentration, C_a , and maximum concentration at the cores	
		169

List of Symbols xii

List of Symbols

Latin Symbols

\boldsymbol{A}	cross sectional area
A_i	cross sectional area of the i^{th} cell
$ ilde{b}$	radius of the jet
В	Buoyancy
C_m	maximum concentrations
C_a	average concentration
d_o	jet diameter at the source
f	buoyancy flux per unit length
F	buoyancy flux
F_o	buoyancy flux at the source
Fr	densimetric Froude number
g	gravitational constant
g'	reduced gravity (buoyancy force per unit mass of fluid)
h	spacing between walls
H	water depth
K_f,K_c,K_b	path coefficients of the line thermal
k_s	added-mass coefficient in the tangential direction
k_n	added-mass coefficient in the normal direction
ℓ_b	buoyant length scale
ℓ_m	momentum length scale
ℓ_p	length of the potential core
ℓ_s	a length scale associated with the line impulse
L	channel length

List of Symbols xiii

m	momentum flux per unit length
m_s	relative momentum in the s-direction
m_n	relative momentum in the n-direction
M	momentum flux
M_o	source momentum flux
N	Brunt-Väisälä frequency
q	volume flux per unit length
Q	volume flux
R	radius of the equivalent circle= $\sqrt{\pi R_h R_v}$
R_e	Reynolds number
R_h, R_h^*	Radius of thermal cross section in y-direction
R_v	Radius of thermal cross section in z-direction
S	dilution ratio
\overline{S}	average dilution ratio
S_m	minimum dilution ratio
S_c	minimum dilution ratio on the centre plane of symmetry
t	time
t_s	time scale
u_s	relative velocity in s-direction
u_n	relative velocity in n-direction
U_a	ambient velocity
$ ilde{U}_c$	average velocity in mixing layer
U_s	velocity in s-direction
V	volume
V_f	velocity along the floor
V_o	source volume
W	rising velocity
W_o	velocity at the source
$W_o/U_{a\infty}$	exit-to-cross flow velocity ratio

List of Symbols xiv

x, y, z	cartesian coordinates
z_e	equilibrium height of rise in a stably stratified environment
z_m	maximum hight of rise in a stably stratified fluid
y_c, z_c	geometric centre of the line thermal cross section
y_m, z_m	mass centre of the line thermal cross section

Greek Symbols

$oldsymbol{eta}$	spreading coefficient
eta_h	spreading coefficient in the horizontal direction
β_n	spreading coefficient in the normal direction
eta_s	spreading coefficient in the tangential direction
eta_v	spreading coefficient in the vertical direction
δ	boundary-layer thickness
δ_v	half width on the plane of symmetry
$(\Delta ho)_o$	density difference of the source fluid
γ	mass per unit width
Γ	total mass
ϕ_o	initial angle of discharge on the $x-y$ plane
ρ	fluid density
$ ho_a$	ambient density
σ	standard deviation
σ_h	standard deviation in the horizontal direction
σ_v	standard deviation in the vertical direction
θ	momentum thickness
θ_o	initial angle of discharge on a plane passed through the z-axis
ζ	path of the thermal

List of Symbols xv

Subscripts and Superscripts

Ь	denotes the back of the thermal
c	denotes the centre of the thermal
f	denotes the front of the thermal
m	denotes the maximum or the mass centre
)	denotes the conditions at the source

Chapter 1

Introduction

1.1 Buoyant Jets in Cross Flows

Studies of buoyant jets in cross flows have been motivated by a variety of engineering applications. Examples are the design of V/STOL aircraft (Jordinson, 1956; Crowe and Riesebieter, 1967; Margason, 1968), the mixing of fuel in industrial furnaces (Perchanok et al., 1989), the dispersion of toxic fumes in the atmosphere (Hoult et al. 1969; Scorer, 1968), and the disposal of waste water in lakes and oceans (Muellenhoff et al., 1985; Lee and Neville-Jones, 1987).

The nature of the flow is best illustrated by chimney plumes in cross winds (see Figure 1.1). The rise of plumes in wind is due to both buoyancy and momentum fluxes. The flow behaves like a jet (a source of momentum flux) in the initial rise but becomes a plume (a source of buoyancy flux) in the far field region. Scorer (1958) analyzed the flow using a reference frame moving with the cross wind, and treated the buoyant element in the far field as a line thermal (a line of buoyancy) in a stagnant environment. He noted that chimney plumes have the tendency to bifurcate into a pair of counter-rotating line elements, and that bifurcation of chimney plumes is always observed in smooth winds.

Figure 1.2 is another example of a buoyant jet in a cross flow. In this case, the buoyant jet is produced by cooling water discharge from a coastal power plant. The cooling water is lighter than the surrounding sea water. It rises through the depth of the ocean as a plume in a cross flow as shown in Figures 1.3 and Figure 1.4. Upon impingement of the line element on the sea surface, the plume becomes bifurcated. The initial momentum flux is negligible in this case. The nature of the bifurcation

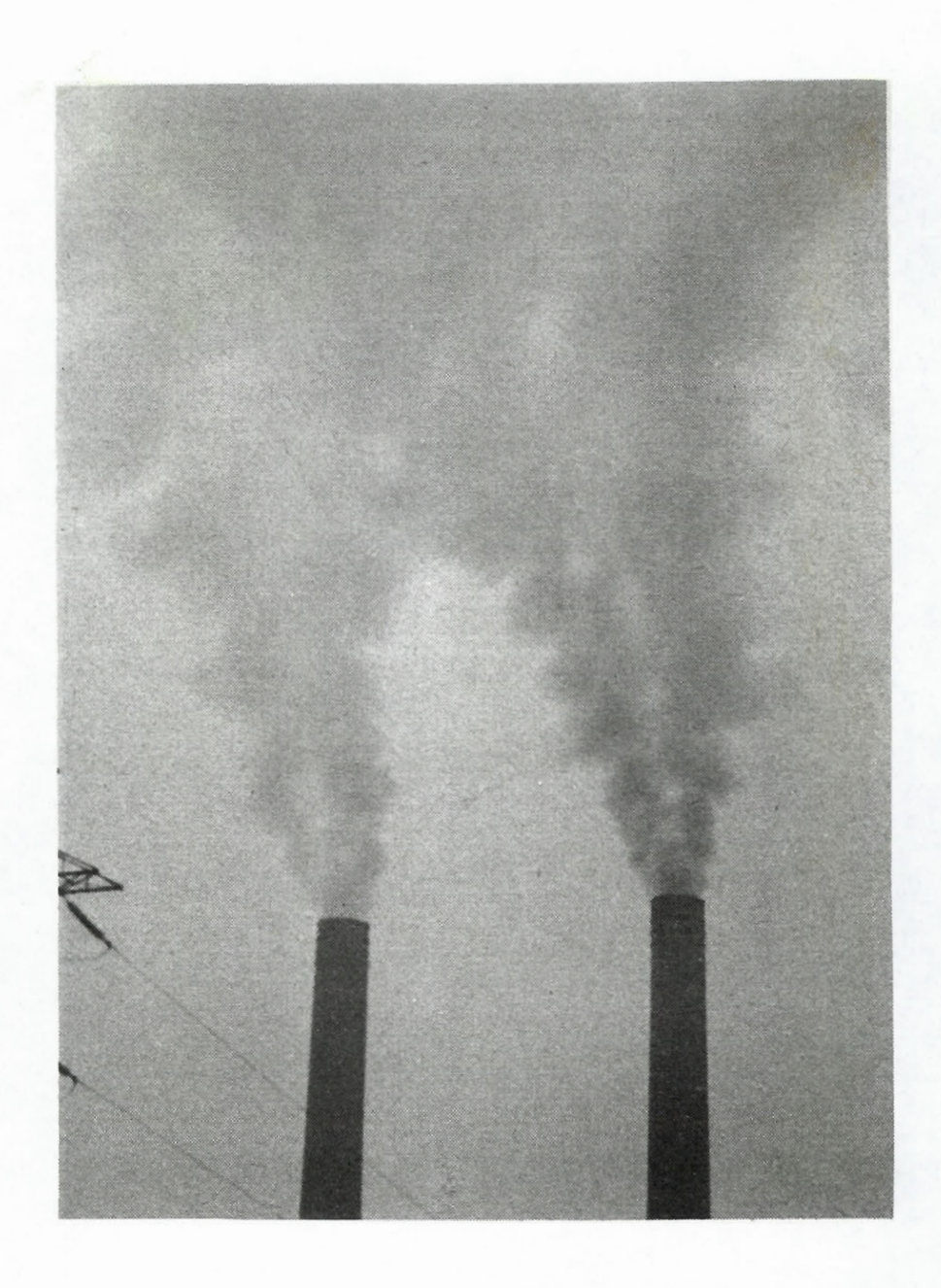


Figure 1.1: Bifurcation of chimney plumes in a smooth wind. Photograph reproduced from Scorer (1958).

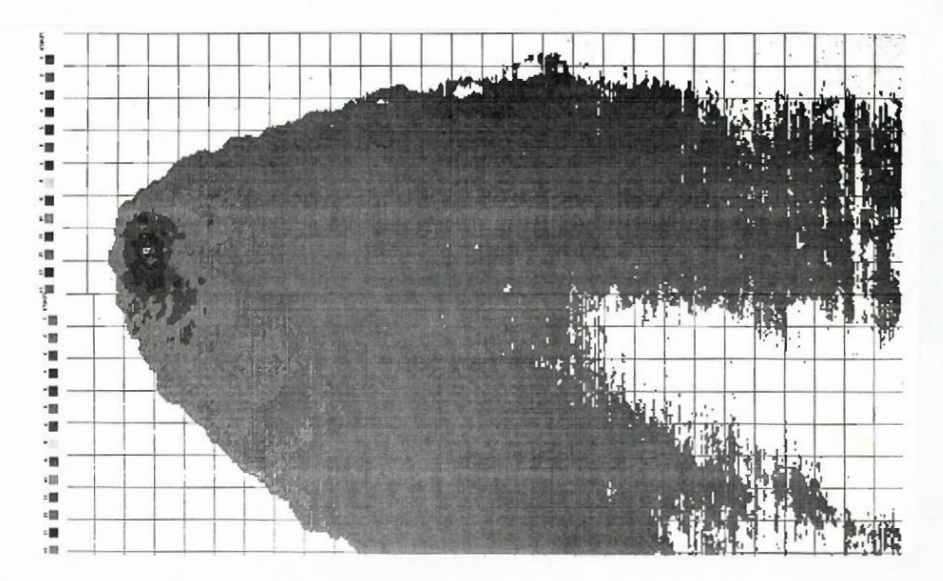


Figure 1.2: Aerial view of the thermal discharge (21 m³/s) from a coastal power plant made visible with a scanning infrared radiometer. Vertical discharge is 5 m below the surface and the peak temperature difference is 11.1°C. There is a coastal current of 0.27 knot (0.14 m/s) and grid spacing is 30.5 m. Photograph reproduced from Fischer et al (1979).

process is not well understood but knowledge of the process is important in assessing the impact of cooling water discharge on coastal environments.

Most of the laboratory investigations of buoyant jets in cross flows were based on flow visualization. A few measurements of the velocity field were made of the flow in the near field region. The measurement of the concentration field has been conducted primarily in the far field and on the centre plane of symmetry. Analyses of the data in many instances were based on dimensional reasoning. Several integral formulations of the problem were attempted. The flow was generally treated in these integral formulations as a point source of momentum and buoyancy flux in uniform cross flow. In reality, the velocity of the cross flow is not uniform and the size of the source is not often small compared with the depth of flow. The problems in practice are further complicated by the finite depth of the cross flow and the possible interaction of the buoyant jets with the boundaries of the cross flow. A review of previous research is given in the subsequent sections of this chapter.

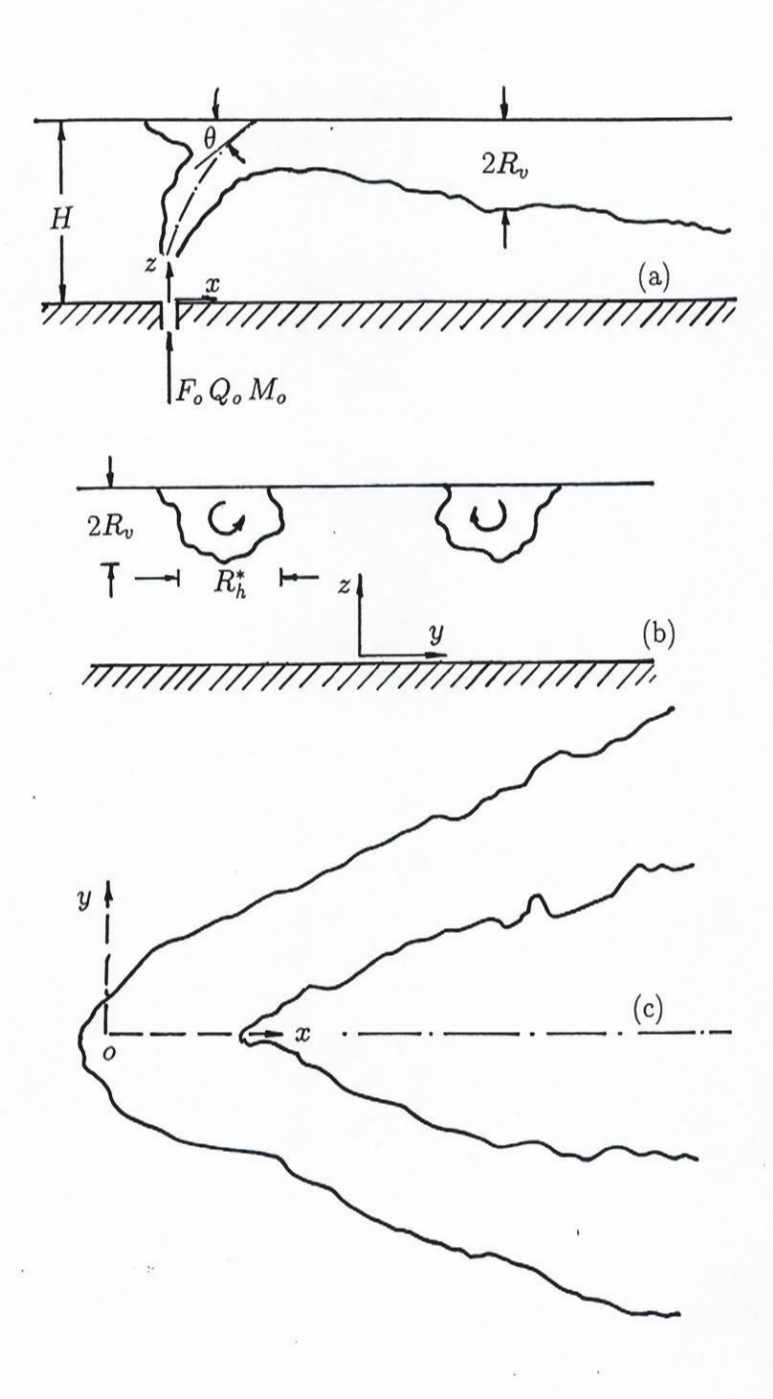


Figure 1.3: Plume bifurcation in a confined cross-flow.

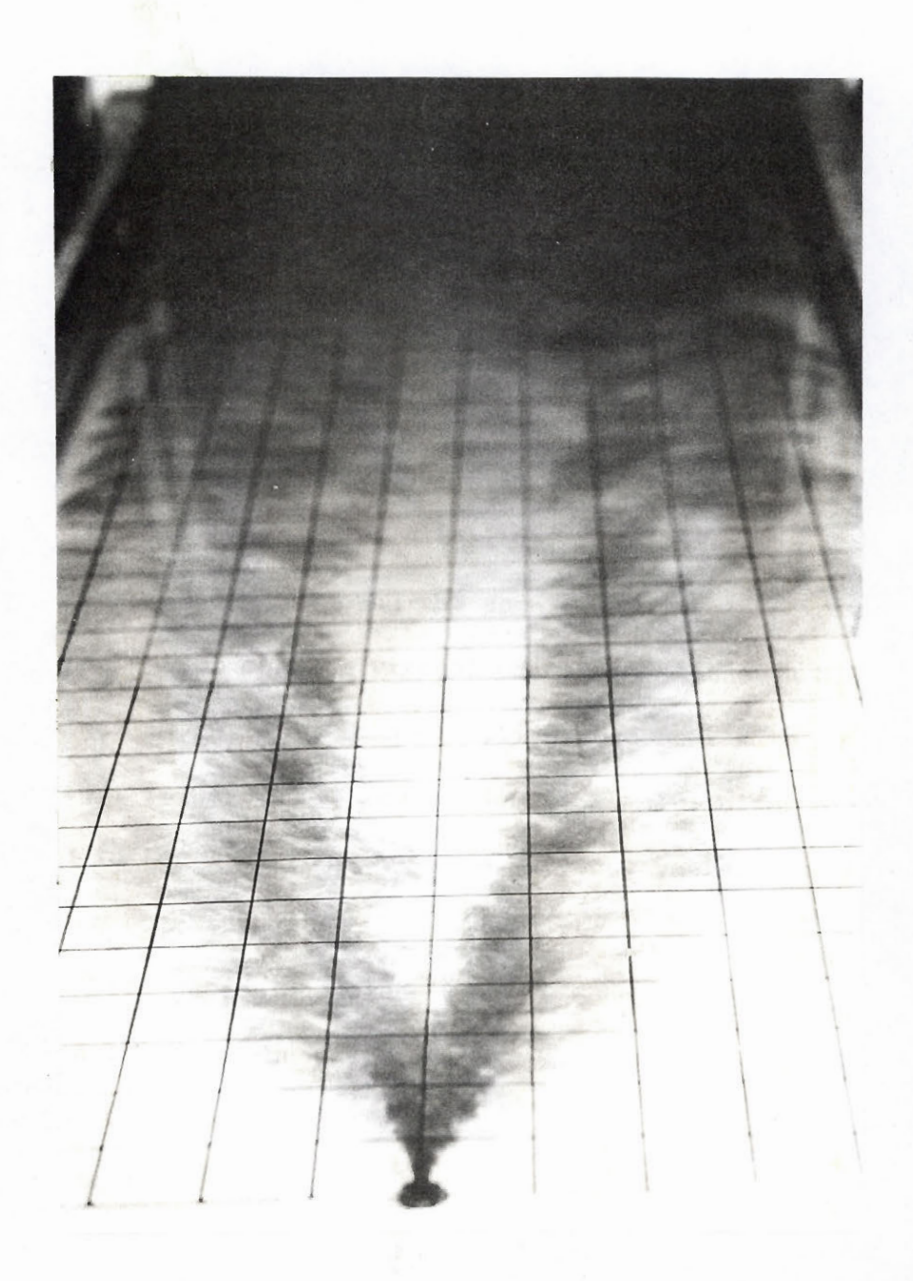


Figure 1.4: Plume bifurcation in a confined cross-flow. Photograph reproduced from Abdelwahed and Chu (1978).

The present study of buoyant jets in cross flows is both an experimental and an analytical investigation of the problem. Experiments were conducted to measure the concentration distribution over the cross section of a buoyant jet using the simulation of the flow as a line thermal in a large tank. A general integral formulation of buoyant jets with three-dimensional trajectories in a non-uniform cross flow was conducted. The numerical solution of the problem was carried out for a variety of discharge configurations, including initial discharge from large sources. The calculations compared well with a comprehensive set of experimental data from both the present and many previous experimental investigations.

1.2 Literature Review

Most of the previous studies of buoyant jets in cross flows were concerned with jet discharge in a direction perpendicular to the cross flow. The analyses of the experimental data were generally based on dimensional reasoning. Wright (1977), for example, classified the flow according to the effects of source momentum and buoyancy, and the effect of the cross flow. Four regimes have been proposed for buoyant jet discharges that are perpendicular to the cross flow: momentum dominated near field (mdnf), buoyancy dominated near field (bdnf), momentum dominated far field (mdff) and buoyancy dominated far field (bdff). This literature survey begins with asymptotic analysis of flow in the four regimes.

1.2.1 Four asymptotic regimes

In the mdnf, the buoyancy effect is negligible. The jet may be assumed to move with the cross flow passively, and the mixing process is not affected by the cross flow. Under this assumption, the volume flux of the jet, Q, is a unique function of the source momentum flux, M_o , the fluid density, ρ , and the distance from the source, z: $Q = \text{fn}(M_o, \rho, z)$. Since $[Q] = L^3/T$, $[M_o/\rho] = L^4/T^2$ and [z] = L, the only dimensionless parameter of the problem is $Q/(z\sqrt{M_o/\rho})$ which must be constant.

This dimensional reasoning leads to the following dilution relation:

$$S = \frac{Q}{Q_o} = c_3 \frac{z}{Q_o} \sqrt{\frac{M_o}{\rho}} \tag{1.1}$$

where c_3 is a constant. The functional relation for the path of the jet is $z = \text{fn}(M_o, \rho, t)$. The dimensionless parameter is $z^4/(t^2M_o/\rho)$. Hence, the relation for the path of the jet in the mdnf becomes

$$z = c_1 \left(\frac{M_o}{\rho}\right)^{\frac{1}{4}} \left(\frac{x}{U}\right)^{\frac{1}{2}} \tag{1.2}$$

where x = Ut and U is the velocity of the cross flow. Equations 1.1 and 1.2 are rewritten into the dimensionless forms given in Table 1.1, using the momentum length scale,

$$\ell_m = \sqrt{M_o/U^2},\tag{1.3}$$

for normalization. The constants c_1 and c_3^c (a coefficient for the minimum dilution on the centre plane of the symmetry) were determined from experiments. The values of these constants obtained by different investigations are also summarized in Table 1.1.

In the bdnf, the momentum effect is negligible. The volume flux of the jet, Q, is a unique function of the source buoyancy flux, F_o , the fluid density, ρ , and the distance from the source, z: $Q = \text{fn}(F_o, \rho, z)$. Since $[Q] = L^3/T$, $[F_o/\rho] = L^4/T^3$ and [z] = L, the only dimensionless parameter of the problem is $Q/z^{\frac{5}{3}}(F_o/\rho)^{\frac{1}{3}}$ which must be constant. This dimensional reasoning leads to the following dilution relation

$$S = \frac{Q}{Q_o} = c_5 \frac{z^{\frac{5}{3}}}{Q_o} (\frac{F_o}{\rho})^{\frac{1}{3}}.$$
 (1.4)

Following a similar argument, the path of the jet is $z = \text{fn}(F_o, \rho, t)$. The dimensionless parameter is $z^4/(t^3F_o/\rho)$. Hence, the relation for the path of the jet in the bdnf becomes

$$z = c_7 (\frac{F_o}{\rho})^{\frac{1}{4}} (\frac{x}{U})^{\frac{3}{4}}. \tag{1.5}$$

Neville Jones, 1991)

Regime	Path	Dilution Ratio	Theory	Wright (1977	7) Other
mdnf	$\frac{z}{\ell_m} = c_1 \left[\frac{x}{\ell_m}\right]^{\frac{1}{2}}$	$\frac{SQ_o}{U\ell_m^2} = c_3 \frac{z}{\ell_m}$	$c_1 = 2.5$ $\overline{c}_3 = 0.27$	$c_1 = 2.5$ $c_3^c = 0.42$	
mdff	$\frac{z}{\ell_m} = c_2 \left[\frac{x}{\ell_m}\right]^{\frac{1}{3}}$	$\frac{SQ_o}{U\ell_m^2} = c_4 \left(\frac{z}{\ell_m}\right)^2$	$c_2 = 1.6$ $\overline{c}_4 = 0.36$	$c_2 = 1.5$ $c_4^c = 0.38$	$c_4^c = 0.46 (\text{Wong}, 1991)$ $c_4^c = 0.68 (\text{Chu}, 1979)$
bdnf	$\frac{z}{\ell_b} = c_5 \left[\frac{x}{\ell_b}\right]^{\frac{3}{4}}$	$\frac{SQ_o}{U\ell_b^2} = c_7 \left(\frac{z}{\ell_b}\right)^{\frac{5}{3}}$	$c_5 = 1.8$ $\overline{c}_7 = 0.17$	$c_5 = 2.3$ $c_7^c = 0.42$	
					$c_8^c = 0.53 (\text{Wong}, 1991)$

Table 1.1: Formulae for the four regimes of buoyant jets in cross flows: mdnf, bdnf, mdff, and bdff.

bdff $\frac{z}{\ell_b} = c_6 \left[\frac{x}{\ell_b}\right]^{\frac{2}{3}}$ $\frac{SQ_o}{U\ell_b^2} = c_8 \left(\frac{z}{\ell_b}\right)^2$ $c_6 = 1.3$ $c_6 = 1.0$ $c_8^c = 0.68 \, \text{(Chu, 1979)}$ $\overline{c}_8 = 0.36$ $c_8^c = 0.41$ $c_8^c = 0.51 \, \text{(Lee and } 0.51)$

Regime	Path	Average Dilution Ratio
mdnf	$z = \sqrt{\frac{2}{\beta_s}} \left[\frac{M_o}{\pi \rho (1 + k_s)} \right]^{\frac{1}{4}} \left[\frac{x}{U} \right]^{\frac{1}{4}}$	$S = \beta_s \left[\frac{\pi M_o}{\rho (1+k_s)}\right]^{\frac{1}{2}} \frac{z}{Q_o}$
mdff	$z = \left[\frac{3M_o}{\pi \beta_n^2 \rho (1 + k_n) U}\right]^{\frac{1}{3}} \left(\frac{x}{U}\right)^{\frac{1}{3}}$	$S = \frac{\pi \beta_n^2 z^2 U}{Q_o}$
bdnf	$z = \sqrt{rac{4}{3eta_s}} [rac{F_o}{\pi ho(1+k_s)}]^{rac{1}{4}} [rac{x}{U}]^{rac{3}{4}}$	$S = \pi \beta_s \left[\frac{3\beta_s F_o}{4\pi \rho (1 + k_s)} \right]^{\frac{1}{3}} \frac{z^{\frac{5}{3}}}{Q_o}$
bdff	$z = \left[\frac{3F_o}{2\pi\beta_n^2\rho(1+k_n)U}\right]^{\frac{1}{3}} \left(\frac{x}{U}\right)^{\frac{2}{3}}$	$S = \frac{\pi \beta_n^2 z^2 U}{Q_o}$

Table 1.2: Asymptotic solutions for the four regimes of buoyant jets in cross flows: mdnf, bdnf, mdff, and bdff.

The dimensionless forms of these asymptotic relations for the flow in the bdnf are given in Table 1.1. The length scale for normalization in this case is the buoyant length scale,

$$\ell_b = \frac{F_o}{\rho U^3}.\tag{1.6}$$

The values of the constants c_5 and c_7 are given in Table 1.1.

The solutions for the flow in mdff and bdff are based on the line puff and line thermal assumptions of Scorer (1958). Expressing the significant parameters of the line puff as the momentum per unit length, $M_o/\rho U$, the time, x/U, and the path of the jet is $z = \text{fn}(M_o/\rho U, x/U)$. Since $[M_o/\rho U] = L^3/T$, and [x/U] = T, the dimensionless parameter is $z^3/(M_o/\rho)/(x/U)$, and hence, the one-third power law,

$$z = c_2 \left(\frac{M_o}{\rho U}\right)^{\frac{1}{3}} \left(\frac{x}{U}\right)^{\frac{1}{3}} \tag{1.7}$$

is the path of the jet in the mdff. The volume flux per unit length of the line puff, Q/U, has a dimension of L^2 . Therefore, the dilution of the line puff is proportional to the elevation square, z^2 , as follows:

$$S = \frac{Q}{Q_o} = c_4 \frac{Uz^2}{Q_o}. (1.8)$$

A similar dimensional reasoning for bdff leads to a two-third power law for the path

$$z = c_6 \left(\frac{F_o}{\rho U}\right)^{\frac{1}{3}} \left(\frac{x}{U}\right)^{\frac{2}{3}},\tag{1.9}$$

and the same quadratic relation for the dilution ratio

$$S = \frac{Q}{Q_o} = c_8 \frac{Uz^2}{Q_o}. (1.10)$$

The solutions for the flows in the four asymptotic regimes can be obtained analytically as asymptotic solutions of the general problem. The formulations of the general problem are given in Chapter 3. The analytical solutions are summarized in Table 1.2. The constants c_1 through c_8 , are determined from the analytical solutions using the coefficients $\beta_s = 0.17$, $\beta_n = 0.34$, $k_s = 0.18$ and $k_n = 1$.

1.2.2 Dilution Ratio

The path coefficients that were obtained in the various studies are generally in agreement with each other (see Table 1.1). This is not so with the coefficients for the dilution ratios. The difficulty is partially related to the different definitions for the dilution ratio adopted by the different researchers.

The fluid in the jet becomes diluted due to entrainment of the surrounding fluid. The volume flux through a cross section of the jet, Q, is greater than the volume flux at the source, Q_o . The dilution ratio, $S = Q/Q_o$, is greater than unity. For the transport of conservative substance along the jet axis, the mass flux is constant, i.e., $\Gamma = \Gamma_o$, or $Q\overline{C} = Q_oC_o$. Therefore, the dilution ratio,

$$\overline{S} = \frac{Q}{Q_o} = \frac{C_o}{\overline{C}},\tag{1.11}$$

is inversely proportional to concentration; the overbar denotes the average over the jet cross section, and the subscript 'o' denotes the condition at the source. This formal

definition of the dilution ratio is related to the average of the concentration over the cross section. The integral formulation in Chapter 3 is concerned with the averages. Therefore, the values of the constants, $\overline{c_3}$, $\overline{c_4}$, $\overline{c_7}$, and $\overline{c_8}$, under the Theory column in the table, are also averages.

In most of the experiments, the concentration measurements were made on the centre plane of symmetry. The dilution ratio based on the maximum concentration on this centre plane, C_c , is

$$S_c = \frac{C_o}{C_c}. ag{1.12}$$

In the bifurcated region between the vortex pair, the concentration is nearly zero, and the dilution is nearly infinity. The measurement of the concentration on the centre plane is therefore very sensitive to the bifurcation and meandering of the plume in the cross flow.

Chu (1979) analyzed Fan's data on buoyant jets in cross flow. According to his analysis, the coefficient for the minimum dilution on the centre plane of the symmetry, indicated by the superscript 'c' is $c_4^c \simeq c_8^c \simeq 0.68$. This value is higher than the values of $c_4^c = 0.38$ and $c_8^c = 0.41$ proposed by Wright (1977). However, it is comparable to the value of $c_8^c = 0.51$ defined by Lee and Cheung (1991) and the values of $c_4^c = 0.46$ and $c_8^c = 0.53$ proposed by Wong (1991). See Table 1.1.

More meaningful measurement of the plume dilution should be based on the maximum concentration, C_m . The corresponding minimum dilution

$$S_m = \frac{C_o}{C_m},\tag{1.13}$$

should be obtained from the cores of the vortex pair. This minimum value, S_m , is also sensitive to turbulence in the cross flow. The measurement for minimum dilution at the core is quite rare. The location of the core cannot be determined unless the measurements are made over the entire cross section of the plume. Fan (1967) nevertheless obtained concentration contours for two cross sections of the buoyant jets. Chu (1979) analyzed Fan's data and proposed the constant $c_4^m \simeq c_8^m \simeq 0.41$ for the minimum dilution at the core. Some of the field data analyzed by Lee and

Neville-Jones (1987) was close to the minimum dilution, S_m , at the core because the data obtained from the dye test were selected samples of the maximum concentration over the sea outfall. The constant proposed by Lee and Neville-Jones (1987) for the minimum dilution at the core was $c_8^m = 0.32$. More extensive measurements of the concentration field over the plume cross sections have been made recently by Cheung (1991) and Wong (1991). The full results of their experiments have yet to be reported.

Considerable scatter in the values of the constants was obtained by the different researchers for the concentration field. It is not clear how the difference in the results may be attributed to difference in experimental conditions. Some of the experiments were conducted by towing the jet in stationery ambient fluid. Other experiments were conducted in wind tunnels or turbulent channel flows. The widths of the cross flow (varying from 0.45 m to 0.76 m in the water flumes and from 1.22 m to 2.4 m in wind tunnels were often comparable to the lateral dimensions of the turbulent jet (see Table 1.3).

One of the objectives of the present investigation is to provide more reliable data for the concentration distribution over the plume cross section. To this end, a series of line thermal experiments were conducted in a large tank. The line thermals is a simulation of the line vortex pair of the buoyant jets in cross flow. The concentration distributions over the thermal cross sections were determined by video imaging technique. The details of the experimental investigation are given in Chapter 2. A review of literature related to the line thermal experiments is given below.

1.2.3 Line thermals

Closely related to the study of buoyant jets in cross flow are the studies of line puffs and line thermals. The motion of the buoyant jets in coordinates moving with the cross flow is similar to that of line puffs and line thermals rising in stationary ambient fluid. Experimental study of line puffs was difficult (see Richards, 1965). Hence, most of the experimental work was on line thermals. Dimensional analysis shows that the radius of the cross section of a line thermal increases with the distance from the

Table 1.3: Buoyant jet and non-buoyant jet experiments: the width, W. height. H. and length of the tank, L, in meters, are given in the last column of the table.

Experiments	Nature of the discharge	Method of observations	Channel dimensions $W \times H \times L$	
Pratte and Baines (1967)	Jet normal to uniform cross flow	Oil aerosol Flow visualisation Trajectory, Thickness, Width and Potential core length	$1.2 \times 2.4 \times 6.0$ Wind Tunnel	
Hoult and Weil (1972)	Plumes in a uniform cross flow	Fe Cl ₃ Towed tank Trajectory Entrainment coef.	1.0 × .30 × 1.5 Water flume	
Hoult, Fay and Forney (1969)	Chimney in a uniform cross wind	Flow visualisation Trajectory	Atmosphere	
Fan (1967)	Buoyant jet normal to a uniform cross flow	Salinity method Concentration distribution Towed tank Minimum dilution Trajectory	.61 × 1.07 × 2.26 Water flume	
Chassaing et al. (1982)	Jet normal to a uniform cross flow	Hot-wire anemometry Velocity profile Trajectory	-	
Andreopoulos and Rodi (1967)	Jet normal to a uniform cross flow	Hot-wire anemometry Velocity field	$1.5 \times 1.5 \times 6.0$ Wind Tunnel	

Table 1.3, contd.

Experiments	Nature of the discharge	Method of observations	Channel dimension $W \times H \times L$	
Lee and Neville Jones (1987)	Horizontal jet in uniform cross flow	Analysis of field data Dilution ratio Trajectory	- Sea Outfall	
Schatzmann (1978, 1979)	Buoyant jet in a uniform cross flow	Integral analysis Concentration Velocity Trajectory	-	
Chu	Buoyant jet and oblique jet in a uniform cross flow	Trajectory	.45 × .30 × 9.0	
(1974, 1985)		Flow visualisation	Water flume	
Wright	Jet normal to	Light probe Flow visualisation Dye concentration on the center plane of symmetry	.61 × .61 × 8.7	
(1977)	cross flow		Water flume	
Abdelwahed	Jet normal to	Flow visualisation Jet bifurcation	.60 × .15 × 8.0	
and Chu (1978)	uniform cross flow		Open channel	

Table 1.3, contd.

Experiments	Nature of the discharge	Method of observations	Channel dimension $W \times H \times L$	
Wood et al. (1967)	Horizontal jet in uniform cross flow	Trajectory Dilution ratio	-	
Keffer and Baines (1967)	Jet normal to uniform cross flow	Hot-wire anemometry Trajectory Velocity	2.4 × 1.2 × 10.8 Wind Tunnel	
Ooms (1972)	Plume in a uniform cross flow	Trajectory	Wind Tunnel	
Roberts and. Toms (1987)	Inclined dense jet in uniform cross flow	Flow visualisation Maximum hight of rise Dilution at impact	1.22 × 2.44 × - Wind Tunnel	
Lee and Cheung (1986)	Advected thermal in uniform cross flow	Salinity method Maximum hight of rise	$.76 \times .33 \times 3.0$	
Platten and Keffer (1971)	Inclined Jet in Uniform Cross Flow	Oil Aerosol Hot wire anemometery Trajectory	1.22 × 2.44 × - Wind Tunnel	

source, following a linear spreading relation,

$$R = \beta z. \tag{1.14}$$

The distance of the advancing front increases with time following a two-third power relation,

$$Z = K_f B_o^{\frac{1}{3}} t^{\frac{2}{3}}. (1.15)$$

where B_o is the buoyancy per unit length of the thermal.

The primarily preoccupation of the previous experimental studies of line thermals was to evaluate the spreading coefficient, β , in Equation 1.14 and the path constant, K_f , in Equation 1.15. Little attention was given to the possible interaction of the thermal with the tank walls, although the experiments were conducted in small tanks comparable to the size of the thermal under observation. Table 1.4, summarizes the range of β and K_f values, the sizes of the tanks, and the shape and size of the source, used by the different laboratory investigations for line thermals.

Richards (1963) found the spreading coefficient, β , to vary over a wide range of values from 0.18 to 0.39, and the path coefficient. K_f , to vary from 1.03 to 2.22. The width of the tank in Richards' experiment was 87 cm. The diameter of the thermal in his experiment was as large as 30 cm in some tests. The advance of a 30 cm thermal in an 87 cm wide tank must be affected by the side walls of the tank, which may explain the large variability in the value of the spreading coefficients obtained in his experiment.

The experiments by Tsang (1971) were conducted in a tank of 1.2 m wide. The spreading and the path coefficients obtained from Tsang's experiment have a narrower range: $.27 < \beta < .32$ and $1.42 < K_f < 1.74$. This is a significant improvement over the Richards' results. The diameter of the thermals in Tsang's experiment was nevertheless quite large, compared with the tank width. For example some of the thermals in the experiment were 60 cm thick in a tank 120 cm wide.

Noh, Fernando and Ching (1992) studied the impingement of line thermals on a density interface. They were primarily interested in the interaction of the thermal Chapter 1 Introduction ______

17

Table 1.4: Line thermal experiments: the width, W, height, H, and depth, D of the tank are given in metres; cross section area of the source is given in cm^2 .

Experiments	Spreading and path coefficient	Source density $(\Delta \rho)_o/ ho$	Tank dimensions $W \times H \times D$ (m)	Source shape	Source area cm ²
Gee Tsang (1971)	$.27 < \beta < .32$ $1.42 < K_f < 1.74$.010039	1.50 × 1.20 × 0.90	0	45.6
Richards (1963)	$.18 < \beta < .39$ $1.03 < K_f < 2.22$	_	0.87 × 1.50 × 1.50	ЦЦ	
Noh et al. (1992)	$eta \simeq 0.33 \pm 10\% \ K_f \simeq 2.03 \pm 10\%$	-	$2.40 \times 0.60 \times 0.30$	\Box	9.8
Present Exp.	$eta \simeq 0.29 \pm 10\%$ $1.39 < K_f < 1.65$.047173	2.40 × 1.20 × 0.06		32.2

with the interface. The spreading coefficients and path coefficients of the line thermal before impingement were found to be $\beta = 0.33 \pm 10\%$ and $K_f = 2.03 \pm 10\%$. The width, height and depth of tank in their experiment were $2.4 \text{m} \times 0.6 \text{m} \times 0.3 \text{m}$. The height of the upper homogeneous layer was only 0.4 m.

The present experiments were conducted in a large tank. The width of the tank used in the present setup was three times wider than the tank used by Richards (1963) and twice as wide as the tank used by Tsang (1971). The height of the tank is about the same as the height of the tanks of Tsang and Richards but is two-and-a-half times higher than the depth of the upper layer in experiment Noh et al. (1992). In analysing the experimental data, special care was taken to isolate the effects of the side walls and the bottom of the tank. During the experiment, dye was released with the source fluid. The concentration of the dye in the thermal was measured by a video imaging method. The measurement of the concentration field provided a precise description of the process by turbulence that was not attempted in any of the previous experimental studies of line thermals.

1.2.4 Integral formulation

The asymptotic solutions of buoyant jets in cross flows reviewed in the previous sections were based on the assumptions of uniform velocity and fluid density in the cross flow, and the assumption that the buoyant jet is dependent only on the momentum flux and the buoyancy flux from the source. In reality, both the density and velocity of the cross flow may vary with distance from the source. The direction of the buoyancy flux and the momentum flux is not necessarily in the same direction and also not necessarily perpendicular to the cross flow. The path of the buoyant jet in the cross flow generally follows a three dimensional trajectory. The solutions for these more complex discharge and cross flow configurations cannot be determined by dimensional analysis and must be handled by computational models as explained in chapter 3.

Models of different degrees of sophistication have been developed. Malin and

Younis (1990), Gosman et al. (1994), and Lee and Rodi (1994) have calculated buoyant jets normal to the cross flow for the development of a turbulence model. Integral models have been developed by Fan (1967), Hirst (1972), Ooms (1972). Chu (1977, 1979), Schatzmann (1979), and Lee and Cheung (1990). With various degrees of complexity, some were able to handle density stratification, while others were for jets with three dimensional trajectories. However, none of the existing formulations are able to account correctly for the non-uniform velocity of the cross flow. Many calculations have ignored the initial development of the flow at the potential core. These models therefore are not suitable for situations when the source sizes are large compared with the boundary layer thickness of the cross flow.

Besides the difficulty in formulation, the development of most of the models was hampered by the inability to provide acceptable entrainment functions. The entrainment coefficients were often not a constant, but changed greatly from one flow to the other. The entrainment model by Schatzmann (1979), for example, has five empirical constants. Despite the large number of tuning parameters, none of the existing models were applicable to the case of non-uniform cross flow.

1.3 Objectives

The objective of the present investigation is to develop an integral model for the buoyant jets in cross flows of non-uniform velocity and density stratification. Figures 1.5 and 1.6 show the general problem. An effort is made to re-examine the entrainment relation in order to reduce the degree of empiricism associated with the current models. The model is calibrated against a wide range of available experimental conditions. Calculations were conducted for the buoyant jets with a three-dimensional trajectory and for jets and plumes with finite source sizes. The spreading coefficients and the added mass coefficients were evaluated based on these calculations.

To complement the integral model development, a series of line-thermal experiments were conducted. The experimental observation provides the physical insights needed both for model development and for calibration of the model coefficients.

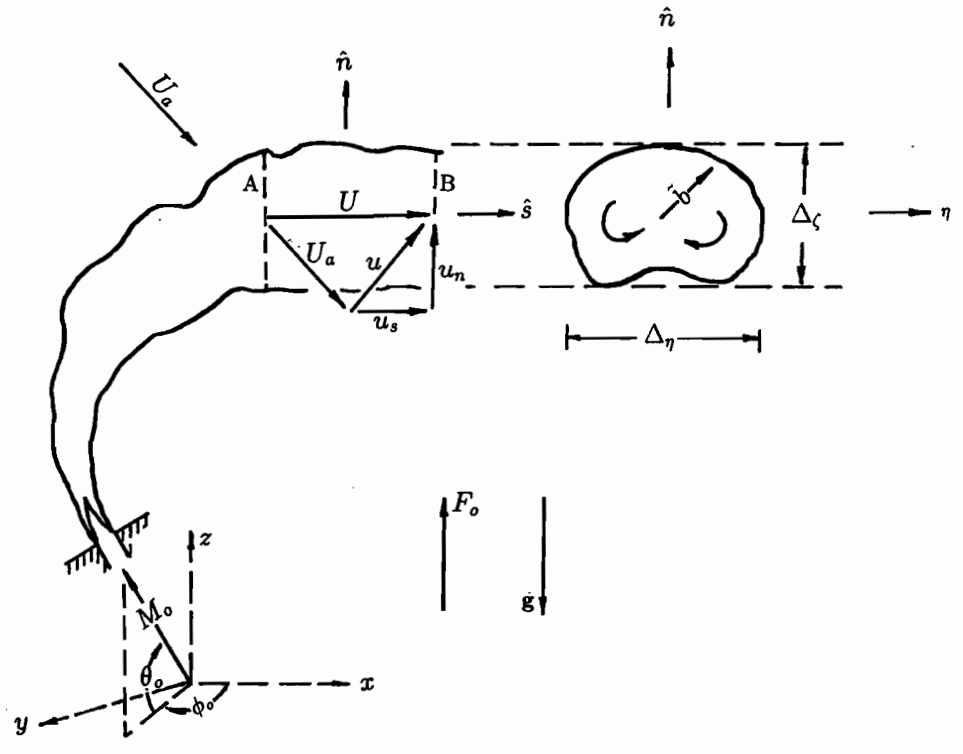


Figure 1.5: Three-dimensional turbulent buoyant jets in a non-uniform cross-flow. The control volume, AB, is defined by the movement of the dominant eddies produced at the source over a period of one time unit.

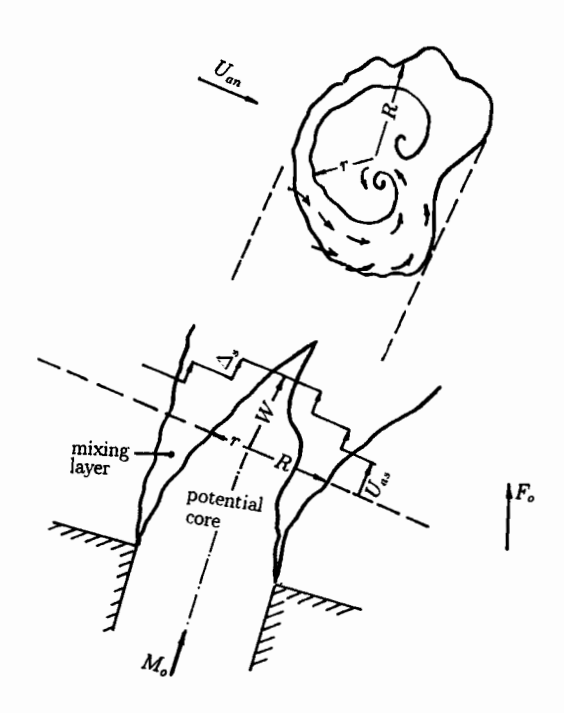


Figure 1.6: The development of the mixing layer in the potential core region near the source.

1.4 Scope of the Present Investigation

The thesis has six chapters. The Introduction Chapter provides a general description of the problem, a review of previous work, a summary of the objectives, and the scope of the investigation. The results of the experimental study of the line thermals are presented in Chapter 2. The concentration distributions in cross sections of the line thermals are determined using a video imaging technique. These results are used as the basis for the subsequent considerations of buoyant jets in cross flows. A general integral formulation is given in Chapter 3. The calibration of the integral model and the evaluation of the model coefficients are described in Chapter 4 and Chapter 5. Chapter 4 examines non-buoyant jets in cross flow, including detailed analyses of (a) the development of the potential core at the source, (b) the effect of non-uniform velocity of the cross flow, and (c) the oblique discharges to the cross flow. Chapter 5 is concerned with the buoyancy effect. The analyses in this chapter include (a) three-dimensional cases of buoyant discharges that are not in the same direction as the momentum flux and the cross flow, (b) the development of negative buoyant plumes, and (c) the effect of the density stratified flow.

The summary of the results of the experimental investigation and the model development and calibration are given in Chapter 6. The statement of originality of the present investigation and recommendations for future work are also included in this final chapter.

The thesis has five appendices. Appendix A is a compilation of the video images obtained from the experimental investigation. Appendix B provides the concentration contours corresponding to the images given in appendix A. Appendix C is the line-thermal cross sections defined by the 20% contours interval concentration. Appendix D summarizes the data obtained from flow visualization. Appendix E is a computer program developed for the integral calculations of buoyant jets in cross flows.

Chapter 2

Line Thermal Experiments

2.1 Introduction

Line thermal experiments were conducted by releasing saline solution from a line source into a large tank of water of uniform density. The salinity concentration distribution in the thermals was determined by a video imaging method. Due to unstable convolution of the interface at the front of the thermal, and the formation of a stable interface at the back, the mixing across the front face of the thermal is significantly greater than the mixing across the back face. The asymmetry of the mixing processes has led to a lopsided density distribution for occasional overturning and bifurcation of the thermal. In one series of experiments, the thermal was produced with a small momentum impulse at the source. The small but non-zero impulse at the source did not change the initial development of the thermal but was observed to have a significant effect on the fine-grain turbulence and on the bifurcation processes as the thermal impinged on the bottom of the tank. Despite the difference in the bifurcation processes, the initial increases in the sizes of all thermals followed a linear relation with the distance from the source. The rate of the initial spreading was quite constant and, contrary to the suggestion of Richards (1963), was not dependent on the initial condition at the source.

The turbulent motion of a line thermal is produced by the instantaneous release of buoyant fluid along a line source. Figure 2.1 shows the cross sections of a line thermal as it advances through a tank of fluid. Through the process known as turbulent entrainment, the surrounding irrotational fluid is continuously incorporated into the turbulent region of the thermal. The result is an increase in the cross-sectional area

of the thermal with the distance from the source. Dimensional analysis shows that the radius of the cross section increases with the distance from the source following a linear spreading relation,

$$R = \beta z, \tag{2.1}$$

and the distance of the advancing front increases with time following a two-third power relation,

$$Z = K_f B_o^{\frac{1}{3}} t^{\frac{2}{3}}. (2.2)$$

The coefficients β and K_f are difficult to determine accurately. The previous experimental investigations (Richards, 1963; Tsang, 1971) were conducted in small tanks of narrow width. Measurements were primarily based on flow visualization. The present experiments however were conducted in a large tank. The width was three times greater than the tank used by Richards and twice as wide as the tank used by Tsang. The height of the tank is about the same as the tanks of Tsang and Richards, but was two-and-a-half times higher than the depth of the upper layer in experiment Noh et al. (1992). In analysing the experimental data, care was taken to isolate the effects of the side walls and the bottom of the tank. Dye was released with the source fluid and the concentration of the dye in the thermal was determined by video imaging method.

2.2 Experiment

The setup for the line thermal experiment is shown in Figure 2.2 (a). The tank dimensions were 2.4 m wide, 1.2 m high and 0.06 m thick. Table 2.1, summarizes the conditions of the experiments. The thermals were produced by the release of saline solution from a 5.2 cm × 6.4 cm rectangular box as shown in Figure 2.2b and 2.2c. The event was initiated by the opening of a set of flexible gates sliding on tracks. Side gates are connected to the bottom gates, and the entire gate assembly was attached to a weight through a system of strings and pulleys, as shown in Figure 2.2. The slide opening of the gates on the side, and on the bottom, is symmetrical and were

Test	Symbol	Tank	Source	Source Dye	Source	M_o/ ho	B_o/ ho
No.		Height	Volume	Concentration	Density		
		cm	cm ³	g/ℓ	$(\Delta ho)_o/ ho$	cm^3/s	cm^3/s^2
1	0	108	110	.20	.102	0	1834
2	Ø	108	110	.40	.105	0	1888
3	+	110.6	110	.40	.047	654	845
4	×	110.6	110	.40	.105	654	1888
5	8	108	110	.40	.047	0	845
6	⊕	108	110	.40	.173	0	3111

Table 2.1: Summary of test conditions.

activated by the dropping of the weight. Opening the gates exposed an unstable gravity-stratified interface at the bottom of the box. The convolution of this unstable interface from rest is not a deterministic process. To avoid uncertain action of the release, two of the experiments (tests no.3 and no.4) were performed with the solution in the box initially at a level 2.6 cm higher than the water in the tank, as shown in Figure 2.2b. The drop of the block over a distance of 2.6 cm produced a non-zero initial velocity at the source. This small initial impulse led to a more symmetrical action and hence more reproducible results. The initial velocity due to the impulse was estimated to be 35.7 cm/s, giving an initial Reynolds number of 22,000.

The tank was made of transparent Plexiglas for the convenience of flow visualization. The thermal in the tank was illuminated from behind. Dye was introduced to the source fluid as tracer and its concentration in the thermal was determined using a video camera. The video images of the thermals were initially recorded on tape using a camcorder (SONY CCD901) and subsequently digitized by a video frame grabber (NEW MEDIA GRAPHIC VIDEO WINDOW). Several blue and red dyes were tested. The tractive red dye (TRICHOMATIC DF-6BL) was found to be the most suitable. Three colour intensities, Red, Green and Blue, were obtained at each pixel of the digitized image. The concentration of the red dye was determined from the intensity of the Green by subtracting the background intensity.

2.2.1 Visualization and Data Collection

Figure 2.3 shows the sequence of digitized images of the thermal at 4 second intervals. The images of all six tests are presented in this figure. The images obtained from tests no.5, no.2 and no.6 are arranged from left to right along the middle row of the figure; the initial density difference between the source fluid and its surrounding fluid for these three tests in the middle row were 4.7%, 10.5% and 17.3%, respectively. The images obtained from tests no.3 and no.4, produced with an initial impulse, are arranged in an area of the figure above the images of tests no.5 and no.2. Tests no.1 and no.2 have the same source condition, but the results are not exactly the same. For comparison, and to show the variability, the images of test no.1 are arranged directly below the images of test no.2 in the figure.

Figure 2.4 shows the outlines of the same set of images shown in Figure 2.3. The outlines are defined by the region of the thermals where the dye concentration has exceeded 20 percent of the average within the thermal. Figure 2.5 shows the concentration contours of the images shown in Figure 2.3.

The shapes of the thermal cross section changed quite drastically as the thermal advanced through the tank. The thermal had a tendency to separate into two parts divided in the middle by a region of low turbulent intensity. Eight key coordinates, $(z_i, y_i; i = 1, 8)$ are used in the present analysis to characterize the thermal cross section. Figure 2.1 shows the definition of the key coordinates. The locations of the key coordinates for each of the thermal images obtained from the experiment are given in Figure 2.4. The size, shape and motion of the thermals are determined with these coordinates. For example, the coordinates of the vortex cores on the right-hand side are given by the formula

$$z_c = \frac{1}{2}(z_8 + z_2), y_c = \frac{1}{2}(y_4 + y_6),$$
 (2.3)

and on the core on left-hand-side, by

$$z_c = \frac{1}{2}(z_1 + z_7), y_c = \frac{1}{2}(y_3 + y_5).$$
 (2.4)

The widths of the turbulent core are determined by the formula

$$R_h^* = \frac{1}{2}(y_4 - y_6 + y_5 - y_3). \tag{2.5}$$

and the height of the core (Figure 2.9) by

$$R_{\nu} = \frac{1}{4}(z_7 + z_8 - z_1 - z_2). \tag{2.6}$$

Other characteristics of the thermal are the radius of the equivalent circle

$$R = \sqrt{R_h^* R_v} \tag{2.7}$$

and the width

$$R_h = \frac{1}{2}(y_4 - y_3). \tag{2.8}$$

The area of the elliptical cross section of the thermal is $\simeq \pi R_h^* R_v$. The radius of an equivalent circle of the same area is R.

2.2.2 Mass Centres and Skewness

Additional characteristics of the thermal are derived from the dye-concentration measurements. The parameters related to the tracer concentration distributions are (i) the maximum concentration C_m , (ii) the average concentration C_a , (iii) the location of the mass centre, (z_m, y_m) , (iv) the standard deviations, σ_h and σ_v , and (v) the skewness factors, γ_h and γ_v . The procedure to evaluate these parameters from the concentration measurement is described below.

The coordinates of the mass centres are obtained by the weighted averages:

$$z_m = \frac{\sum_i C_i z_i}{\sum_i C_i}, y_m = \frac{\sum_i C_i y_i}{\sum_i C_i}$$

$$(2.9)$$

where C_i is the dye concentration determined from the 640 × 480 pixel digitized images. The calculations for the mass centres are made separately for the turbulent cores by distinguishing the masses on the left hand side $(y_i < (y_5 + y_6)/2)$ from those on the right and side $(y_i > (y_5 + y_6)/2)$. The variances in y- and z-directions are

$$\sigma_h^2 = \frac{\sum_i C_i (y_i - y_m)^2}{\sum_i C_i}, \ \sigma_v^2 = \frac{\sum_i C_i (z_i - z_m)^2}{\sum_i C_i}.$$
 (2.10)

The skewness in z- and y-direction are

$$\gamma_z^3 = \frac{\sum_i C_i (z_i - z_m)^3}{\sum_i C_i}, \ \gamma_y^3 = \frac{\sum_i C_i (y_i - y_m)^3}{\sum_i C_i}.$$
 (2.11)

Again, these weighted averages are obtained separately by distinguishing the masses on the left hand side from those on the right hand side. The standard deviations, σ_h and σ_v , define an ellipse of area = $\pi \sigma_h \sigma_v$. The radius of an equivalent circle of the same area is $\sigma = \sqrt{\sigma_h \sigma_v}$.

The positions of the mass centres (x_m, y_m) and the geometric centres (x_c, y_c) of the turbulent cores are shown in Figure 2.6. The magnitude and the direction of the skewness vector, $(z_m, y_m) \to (z_m + \gamma_z, y_m + \gamma_y)$, are shown in Figure 2.7. The mass centres are consistently located above the geometrical centre. This top-heavy situation is due to the absence of mixing across the stable interface on the top of the thermal and the enhanced mixing across the unstable interface at the bottom. The thermal with the top-heavy concentration distribution is unstable. Therefore, the tendency is for the thermal to overturn, generating vorticity rather suddenly. Figure 2.11 shows how vorticity is produced by the overturning of the thermal.

2.2.3 Size and Path of the Turbulent Cores

The initial trajectory of the core is given by the spreading rate $dy_c/dz_c \simeq dy_m/dz_m \simeq 0.18$. The initial separation of the core is primarily due to turbulent entrainment of the surrounding fluid. The rate of separation increases in the later stages as the thermal approaches the bottom of the tank. The tendency for the thermal to bifurcate is evident in the low dye concentration region observed at the middle of most of the thermal images. The absence of dye in the middle region is an indication that the exchange of mass and momentum by the fine-grain turbulence is negligible. The bifurcation of the thermal is observed for some to occur as early as the thermal passed the mid-depth of the tank. Otherwise, the bifurcation would certainly take place upon impingement of the thermal on the bottom of the tank.

The size of the turbulent cores increases continuously due to entrainment of the surrounding fluid into the cores. Figure 2.8, shows the widths of the core, R_h^* and

 σ_h , and Figure 2.9, the height of the core, R_v and σ_v . The ratio, R_h^*/R_v , is shown in Figure 2.10. R_h^* , R_v and R are plotted with

$$\zeta_c = \int_0^t \sqrt{(dz_c)^2 + (dy_c)^2},\tag{2.12}$$

which is the distance measured along the locus of the geometric centre. For σ_h, σ_v and σ , the data are plotted with

$$\zeta_m = \int_0^t \sqrt{(dz_m)^2 + (dy_m)^2},\tag{2.13}$$

which is the distance along the mass centre. The distances ζ_c and ζ_m obtained from the above formulae are not significantly different from each other (see Figure 2.16).

The variations in the radius of the equivalent circles, R and σ , with distance, ζ , from the source are shown in Figure 2.12. Initially, the increase in the size of the thermals is approximately linear with the distance from the source.

The best fit of the initial data in Figure 2.8, Figure 2.9 and Figure 2.12 gives the following initial spreading rates

$$\frac{dR_h}{d\zeta} \simeq 0.37, \frac{dR_v}{d\zeta} \simeq 0.22, \text{ and } \frac{dR}{d\zeta} \simeq 0.29,$$
 (2.14)

$$\frac{d\sigma_h}{d\ell} \simeq 0.12$$
, and $\frac{d\sigma}{d\ell} \simeq 0.10$. (2.15)

These are the rates of spreading of the free thermals that are not affected by the tank's bottom and side walls.

2.2.4 Overturning

Following the initial linear spreading, there is an erratic increase in the size of the thermals. The variation in the vertical thickness, R_{ν} , is particularly dramatic (see Figure 2.9). Sudden increases in the vertical thickness are observed to occur at locations identified in the figure with arrows pointing to the beginning of the event. Preceding the event is a reduction in vertical thickness, R_{ν} , and the peaking of the ratio R_h^*/R_{ν} as shown in Figure 2.10.

Inspecting the images in Figure 2.3 leads to the conclusion that the changes in the shape of the thermal are associated with an overturning motion of the thermal.

Figure 2.11 describes the mechanism of the overturning event. Figure 2.11a shows the top-heavy density distribution in the thermal proceeding the event. The top-heavy distribution is an unstable configuration as the mass centre of the thermal is now above its geometric centre. The natural tendency is for this top-heavy element to tip over. The result is the rapid production of the counter rotating vorticity shown in Figure 2.11b.

The lopsided density distribution preceding the overturning event is due to enhanced mixing across the unstable density-stratified interface at the front of the thermal and the absence of mixing across the stable interface at the back. If the tank were very large, the overturning event may occur repeatedly, since the asymmetry between the mixing at the front and at the back would continue to produce the lopsided density distribution required for the overturning event.

In most of the present experiments, the overturning event was observed only once before the impingement of the thermal onto the bottom of the tank. The exception is test no. 6, which had the highest initial density difference, $(\Delta \rho_o)/\rho = 17.3\%$. The overturning of the thermal in this test occurred twice during its advancement towards the bottom of the tank.

The burst of turbulent activities associated with the overturning motion increases the spreading rate. With the occasional enhancement of turbulent entrainment by the overturning, the average spreading rate of the line thermal is expected to be greater than the initial value of $dR/d\zeta = 0.29$. In fact, the average spreading rate of $\beta_n = dR/d\zeta = 0.34$, recommended by Chu (1994) for jets and plumes in cross flows, appears to be an acceptable rate if accelerated entrainment due to overturning is included as part of the overall process (see the long dash lines in Figure 2.12).

2.2.5 Dilution

The dilution of the thermal is directly determined from the dye-concentration measurements. Figure 2.13 shows the maximum concentration, C_m , and the average concentration, C_a plotted against the distance, ζ_m from the source. Figure 2.14 is a

plot of the maximum-to-average concentration ratio, C_m/C_a along the distance, ζ_m . Figure 2.15 provides the ratio of the visual radius to the standard deviation, R/σ . Fitting the data in the initial stage of the development gives

$$\sqrt{\frac{\gamma_o}{C_m}} = 0.44\zeta + 5,\tag{2.16}$$

$$\sqrt{\frac{\gamma_o}{C_a}} = 0.61\zeta + 6. {(2.17)}$$

Since the maximum-to-average concentration ratio ranges from 1.3 to 2.1, the average ratio, as shown in Figure 2.14, is

$$\frac{C_m}{C_a} \simeq 1.61,\tag{2.18}$$

and the visual radius to standard deviation ratio, as shown in Figure 2.15, is

$$\frac{R}{\sigma} \simeq 3. \tag{2.19}$$

The dye mass per unit length of the line thermal is γ_o . The ratios γ_o/C_m and γ_o/C_a , are characteristic areas, while $\sqrt{\gamma_o/C_m}$ and $\sqrt{\gamma_o/C_a}$ are the characteristic radii of the thermal cross section. In the initial stage of the development, the thermals are not affected by the tank's bottom. Therefore, the characteristic radii initially increase linearly with the distance from the source. It should be pointed out that C_a is an average value obtained in an area where $C_i > 0.2C_a$.

2.3 Two Stages of Development

The movement of the thermal element along its geometric centre, (z_c, y_c) , and its mass centre, (z_m, y_m) , is defined by the distances ζ_c and ζ_m (Equation 2.12 and Equation 2.13). These are plotted versus time, $B_o^{1/2}t$, in Figure 2.16a and Figure 2.16b. The data are fitted with two sets of curves for the initial development $(\zeta_c < 0.55H)$ and the final movement of the bifurcation element along the floor $(\zeta_c > 0.7H)$.

2.3.1 Free Thermal $(\zeta_c < 0.55H)$

The initial development is relatively unaffected by the side walls and the bottom of the tank. Hence, the two-third power laws

$$\zeta_c = \zeta_{co} + K_c B_o^{\frac{1}{3}} t^{\frac{2}{3}}, \text{ and } \zeta_m = \zeta_{mo} + K_m B_o^{\frac{1}{3}} t^{\frac{2}{3}},$$
 (2.20)

are proposed. The best fit to the experimental data for pure thermals, tests nos. 5, 2, 1, and 6. gives the path coefficients

$$K_m \simeq K_c = 1.35.$$
 (2.21)

For thermals with an initial impulse, tests nos.3 and 4. the path coefficient are

$$K_m \simeq K_c = 1.45.$$
 (2.22)

The path coefficient obtained for the locus of the geometric centre, K_c , is not different from the coefficient for the mass centre, K_m . The mass centres are generally located at a position slightly above the geometric centre. Hence, the virtual origins are selected at $\zeta_{co} = -7$ cm and $\zeta_{mo} = -5$ cm.

The difference of about 7 percent between the path coefficients given by Equation 2.21 and Equation 2.22 is due to the impulse at the source. In tests no.5, no.2, no.1 and no.6, the source fluid was started from at rest. The block of the source fluid in tests no. 3 and no.4, however, was 2.6 cm above the water surface. The dropping of the block of source fluid over a distance of 2.6 cm produced an initial impulse, $M_o \simeq 654 \text{ cm}^3/\text{s}$ (see Table 2.1). The momentum of the thermal increased linearly with time as $M = M_o + B_o t$; the proportionality constant is the source buoyancy, B_o . For tests no.3 and no.4, the time scale, M_o/B_o , is 0.76 second and 0.34 seconds, respectively. Therefore, the momentum produced by the buoyancy force, $B_o t$, would become comparable to the initial impulse in a fraction of second. Much greater momentum would be acquired as the thermals travel from the source to the mid-depth of the tank over a period of about 8 to 12 seconds. At mid-depth the initial impulse would be about 4 to 6 percent of the total, which is negligible compared with the momentum produced by the buoyancy force.

2.3.2 Velocity Along the Floor $(\zeta_c > 0.70H)$

Although the initial impulse represents only a small fraction of the thermal's momentum, its effect on the velocity of the thermal along the floor is not negligible. For the pure thermals (tests no.5, no.2, no.1 and no.6) best fit of the data in the later stage of the development, ($\zeta_c > 0.7H$), gives

$$\zeta_m \simeq \zeta_c = 0.055 B_o^{\frac{1}{2}} t + 44.$$
 (2.23)

For thermals with an initial impulse (tests no.3 and no.4) the best fit gives

$$\zeta_m \simeq \zeta_c = 0.071 B_o^{\frac{1}{2}} t + 38.$$
 (2.24)

Normalizing the data with the height of the tank, H, the above linear relations lead to the dimensionless velocity along the floor

$$V_m \simeq V_c \simeq \frac{d\zeta_c}{dt} \frac{H^{\frac{1}{2}}}{B_o^{\frac{1}{2}}} = 0.57,$$
 (2.25)

for the pure thermals, and

$$V_m \simeq V_c \simeq \frac{d\zeta_c}{dt} \frac{H^{\frac{1}{2}}}{B_o^{\frac{1}{2}}} = 0.75,$$
 (2.26)

for thermal with an initial impulse.

The small increase of the momentum by the initial impulse has produced a 30 percent increase in the velocity of the thermal along the floor. The initial impulse has led to a more symmetrical delivery of the thermal at the source. This seems to have delayed the overturning and bifurcation of the thermal and has led to a reduced mixing of the thermal with its surrounding fluid which results in greater velocity along the floor.

2.3.3 Front and Back

Similar two-stage relations are derived for the front face and the back face of the thermals. The positions of the front and the back of the thermals are defined by the key coordinates as follows:

$$z_f = \frac{1}{2}(z_7 + z_8), \ y_f = \frac{1}{2}(y_4 - y_3),$$
 (2.27)

$$z_b = \frac{1}{2}(z_1 + z_2). \ y_b = \frac{1}{2}(y_6 - y_5)$$
 (2.28)

The distances along the locus of these coordinates are

$$\zeta_f = \int_0^t \sqrt{(dz_f)^2 + (dy_f)^2},\tag{2.29}$$

$$\zeta_b = \int_0^t \sqrt{(dz_b)^2 + (dy_b)^2}.$$
 (2.30)

These are plotted against $B_o^{1/2}t$ in Figure 2.17 and Figure 2.18. Again, the data are fitted for the two stages of development. For the initial stage, $\zeta_f < 0.55H$,

$$\zeta_f = K_f B_0^{\frac{1}{3}} t^{\frac{2}{3}}, \text{ and } \zeta_b = K_b B_0^{\frac{1}{3}} t^{\frac{2}{3}}.$$
 (2.31)

The constants that best fit the experimental data are

$$K_f = 1.65$$
, and $K_b = 1.05$, (2.32)

for the pure thermals (tests no.5, no.2, no.1 and no.6), and

$$K_f = 1.75$$
, and $K_b = 1.15$, (2.33)

for the thermals with an initial impulse (tests no.3 and no.4). These results are consistent with the data of Tsang (1971) presented in Figure 2.21 and Figure 2.22. The value of the coefficient $K_f = 1.65$ obtained for the pure plume is to be compared with the range of values for the coefficient, K_f , shown in Table 1.4, obtained from the previous experimental investigations. The range of values obtained by Richards (1963) and Tsang (1971) was $1.03 < K_f < 2.22$ and $1.42 < K_f < 1.74$, respectively. Noh, Fernando and Ching (1992) proposed a value of $K_f = 2.03$. The fitting of the data of the six tests in present experiment led to a range of values $1.39 < K_f < 1.65$, which is very close to the range of values obtained by Tsang (1971). Although the scatter among the six tests was not large, fitting the data of each test by different spreading coefficients and path constants tends to produce a range of variability that is more apparent than real. The spreading coefficient obtained by Tsang (1971) is in the range $.27 < \beta < .32$. The range of values obtained from the present experiment would be $0.26 < \beta < 0.45$ if the data of each test were fitted with different constants.

Despite the variability, the spreading rate $\beta = dR/d\zeta \simeq 0.29$ is a good approximation to all the initial data shown in Figure 2.12.

Figure 2.21 compares R_h from the present experiment with the radius R_T of Tsang (1971); $2R_h$ is the width of the thermal as defined in Figure 2.1 while R_T is the radius of the circle that Tsang used to fit the cross section of his thermal, which is not the radius $R = \sqrt{R_h^* R_v}$ of the equivalent circle. It appears that the thermal in Tsang's experiment has a slightly greater spreading coefficient. The forward motion of the thermal produces a reverse flow that, in a small tank, increases the velocity difference between the thermal and its surrounding fluid; one possible consequence is the greater spreading coefficient of the thermals observed in Tsang's experiment.

The spreading velocity after the impingement of the thermal on the floor is constant. The data for the final stage of the development (that is, for $\zeta_c > H - R \simeq 0.7H$) in Figures 2.17 and 2.18, can be fitted with the *linear* relations:

$$\zeta_f = 0.076 B_o^{\frac{1}{2}} t + 54$$
, and $\zeta_b = 0.034 B_o^{\frac{1}{2}} t + 32$, (2.34)

for the pure thermals (tests no.5, no.2, no.1 and no.6), and

$$\zeta_f = 0.089 B_o^{\frac{1}{2}} t + 54$$
, and $\zeta_b = 0.053 B_o^{\frac{1}{2}} t + 22$, (2.35)

for thermals with an initial impulse (tests no.3 and no.4). Normalizing the data with the height of the tank, H, the above linear relations lead to the following dimensionless horizontal spreading velocity along the floor:

$$V_f \simeq \frac{d\zeta_f}{dt} \frac{H^{\frac{1}{2}}}{B_o^{\frac{1}{2}}} = 0.79$$
, and $V_b \simeq \frac{d\zeta_b}{dt} \frac{H^{\frac{1}{2}}}{B_o^{\frac{1}{2}}} = 0.35$, (2.36)

for the pure thermals, and

$$V_f \simeq \frac{d\zeta_f}{dt} \frac{H^{\frac{1}{2}}}{B_o^{\frac{1}{2}}} = 0.94$$
, and $V_b \simeq \frac{d\zeta_b}{dt} \frac{H^{\frac{1}{2}}}{B_o^{\frac{1}{2}}} = 0.56$, (2.37)

for the thermals produced by an initial impulse. With only a small percentage of momentum from the initial impulse, the increases in the velocities along the floor area, 19 % for the front and 60 % for the back of the thermals, are much greater than expected.

The horizontal velocity of the bifurcated thermal along the floor is comparable to the vertical velocity of the thermal approaching the floor. Before the impingement of the thermal on the floor, the position of the mass centre is

$$\zeta_c \simeq K_c B_o^{\frac{1}{3}} t^{\frac{2}{3}}.$$
 (2.38)

According to this relation, the vertical velocity approaching the floor is

$$\frac{d\zeta_f}{dt} = \frac{2}{3} K_c B_o^{\frac{1}{3}} t^{-\frac{1}{3}} = \frac{2}{3} \frac{K_c^{\frac{3}{2}} B_o^{\frac{1}{2}}}{\zeta_f^{\frac{1}{2}}},\tag{2.39}$$

which if evaluated at $\zeta_f = H$, is

$$W = \frac{2}{3} \frac{K_c^{\frac{3}{2}} B_o^{\frac{1}{2}}}{H^{\frac{1}{2}}},\tag{2.40}$$

which, for $K_c = 1.35$, is

$$\frac{WH^{\frac{1}{2}}}{B_{c}^{\frac{1}{2}}} = 1.05 \tag{2.41}$$

This vertical impingement velocity, W, is higher than the velocities along the floor, given by Equations 2.36 and 2.37, but it is in the same order of magnitude.

The horizontal floor velocity obtained from the present series of experiments is consistent with the measurement by Noh, Fernando and Ching (1992), who measured the spreading velocity due to the impingement of a line thermal on a density stratified interface. Their experimental data gives a range of

$$\frac{V_f H^{\frac{1}{2}}}{B_o^{\frac{1}{2}}} = 0.4 \sim 0.6 \tag{2.42}$$

for a range of interfacial Richardson number $Ri = g(\Delta \rho)_i H/W^2 = 5 \sim 900$ where $(\Delta \rho)_i$ is the density difference across the density interface. The solid floor of the present experiment is the limiting case of high interfacial Richardson number, $Ri \rightarrow \infty$.

2.4 Integral Analysis

The problem of the line thermal is analyzed for two stages. In the initial stage of development, before the impingement of the thermal on the floor, the momentum

increases linearly with time, proportional to the buoyancy B_o at the source; i.e.,

$$M = \rho(1+k)\pi R^2 \frac{d\zeta_c}{dt} = B_o t + M_o,$$
 (2.43)

where $M_o = \rho \pi R_o^2 W_o$ is the initial momentum. The cross-sectional area of the thermal is πR^2 , the velocity of thermal is $d\zeta_c/dt$ and the momentum associated with the motion is $(1+k)\rho\pi R^2 d\zeta_c/dt$ where k is an added-mass coefficient introduced to account for the effect of the irrotational motion of the surrounding fluid. In the initial stage of development, the radius, R, is assumed to increase linearly with distance from the source; i.e.,

$$R = \beta \zeta_c + R_o, \tag{2.44}$$

where β is a spreading coefficient and R_o is the initial radius of the source. For a point source (letting $R_o \to 0$), the solution of the above equations is

$$\zeta_c = \left[\frac{3}{2\pi\beta^2(1+k)}\right]^{\frac{1}{3}} \left[\frac{B_o}{\rho}t^2\right]^{\frac{1}{3}},\tag{2.45}$$

which becomes

$$\zeta_c = 1.37 \left[\frac{B_o}{\rho} t^2 \right]^{\frac{1}{3}} \tag{2.46}$$

if $\beta = 0.29$ and $k = R_h^*/R_v \simeq 1.2$. The point-source solution given by Equation 2.46 is in good agreement with the formula,

$$\zeta_c = 1.35 \left[\frac{B_o}{\rho} t^2 \right]^{\frac{1}{3}},\tag{2.47}$$

obtained from fitting the experimental data in Figures 2.16. The added-mass coefficient is a necessary ingredient in the integral formulation of the line thermal. If the added-mass effect were ignored by setting k=0, the analysis would produce the formula, $\zeta_c = 1.78[B_o/\rho t^2]^{\frac{1}{3}}$, for the advancement of the thermal at a significantly higher rate (34 %) than the experimental observation (see Figure 2.23).

In the second stage of development, after the impingement of the thermal on the floor, the thermal is assumed to move along the floor with the same momentum in the horizontal direction as it had approaching the floor in the vertical direction. A semi-empirical procedure has been adopted to obtain from the integral analysis the movement of the thermal covering both the initial and final stages of the development. In the semi-empirical formulation, the calculation is conducted in two stages. The momentum increases initially with time and buoyancy as in Equation 2.43 but remains constant once the position of the thermal passes the initial stage. In the calculation, B_o is set to zero once $\zeta > 0.55H$. The radius of the thermal is assumed to be given by the two-stage relation

$$R = 0.29\zeta + 1.7 \qquad \text{if } \zeta < 0.55H,$$

$$R = -26 + 0.8\zeta - 0.000016\zeta^3 \text{ if } \zeta > 0.55H, \tag{2.48}$$

which is selected to fit the experimental data in Figure 2.19. The added-mass coefficient is $k = R_h^*/R_v$ if $\zeta < .7H$ and $k = R_v/R_h^*$ if $\zeta > .7H$. The ratio R_h^*/R_v is given by the empirical relation

$$\frac{R_h^*}{R_n} = 1.2 + 0.000001\zeta^3,\tag{2.49}$$

which fits the experimental data shown in Figure 2.20. Using the above empirical relations, the path of the thermal is obtained from integration of the momentum equation. The results of the integration for the advancement of the thermal, $\zeta_c(t)$, shown as a set of dashed lines in Figure 2.23, are in good agreement with the experimental data. The path of the thermal, $\zeta_c(t)$, is obtained by numerical integration of the above set of equations.

The calculation was also conducted including the wall friction, but the effect was negligible so the results are not presented here. With the friction, the momentum equation is

$$\frac{dM}{dt} = B_o - \frac{c_f}{2h} (\frac{d\zeta_c}{dt})^2. \tag{2.50}$$

where c_f is the friction coefficient and 2h is the distance between the walls at front and at the back of the tank. As before, the integration is carried out in two stages.

The integral calculations have demonstrated the significance of the added-mass effect on the motion of the thermal. Neglecting the added mass effect would lead to over prediction of ζ_c in the initial development of the thermal, as shown in Figure

2.23. It would also lead to a slow-down of the thermal on the floor, which was not observed in the experiments.

It is important to note that the thermal moves horizontally with a constant velocity, which is a feature of the thermal motion that requires an explanation. Despite the stable density stratification, the thermal on the floor continues to entrain fluid from its surroundings (see Figure 2.12 and Figure 2.13). The entrainment of the surrounding fluid into the thermal should reduce the velocity of the thermal. However, this retardation of the motion by entrainment is offset by the acceleration of the thermal through the added-mass effect. As the thermal moves horizontally along the floor, the added-mass coefficient is continuously reduced due to the elongation of the thermal element. Figure 2.20 shows that the ratio of horizontal to vertical dimension of the thermal increases from a value of about 1.2 to a value as high as 3.5 at the end of the thermal motion on the floor. The added-mass coefficient, $k = R_v/R_h^*$, is inversely proportional to the ratio, R_h^*/R_v . The elongation of the element on the floor leads to rapid reduction of the added-mass coefficient. The result is acceleration of the thermal element. The velocity of the thermals in tests no.3 and no.4 is observed in Figure 2.18 to increase slightly as the thermal moves along the floor.

2.5 Concluding Remarks

The turbulent flow of a thermal is characterized by the formation of a vortex pair and occasional overturning. Due to unstable stratification at the front and stable stratification at the back, the mixing across the boundary of the thermal is not symmetrical. The asymmetrical process leads to a lopsided density distribution and overturning of the thermals. Mixing is enhanced due to the occasional release of the potential energy associated with overturning. The spreading of the line thermal is generally greater than the initial spreading rate $dR/d\zeta \simeq 0.29$ because of the additional mixing. Analysis of line thermals produced by buoyant plumes in cross flow has suggested a spreading rate of $dR/d\zeta \simeq 0.34$ (Chu, 1994) which is consistent with the overall spreading rate found from the present experiment (see Figure 2.12).

The lateral dimension of the thermal, varying from 5 to 70 cm in the present experiment, was large compared with the 6 cm thickness of the tank. The large-scale turbulence in the small space between the tank walls restricted motion to a direction essentially parallel to the walls. The space between the tank walls, however, was large enough so that the wall friction was negligible compared with the momentum of the thermals (see section 2.4). The present simulation was made with the understanding that the entrainment process is decided primarily by the two-dimensional structure of turbulent motion. The experiments could have been performed in a tank of greater thickness. The selection of the 6 cm thickness was a compromise to permit visualization of the turbulent motion by the video imaging method.

For a line thermal of infinite length, the convolution of the unstable interface at the front of the thermal can be a three dimensional process. In the process of overturning, the top-heavy element can rotate in all three directions. However, in the present experiment, this rotation is restricted essentially to the plane parallel to the front and back walls of the tank. In previous experiments of line thermals, the tank width varied from 87 cm to 150 cm and the tank thickness from 30 cm to 90 cm (see Table 1.4). In Tsang's experiment the diameter of the thermals at mid-depth of the tank, varying from 50 cm to 60 cm, was comparable in magnitude to both the depth and the width of the tank. It is not clear under these circumstance how the thermal element may rotate while overturning.

Line thermals of great length are observed in nature. An example is chimney plumes in a cross wind (see Figure 1.1). Scorer (1968, p.45 and p. 88) observed that the bifurcation of the thermals "is always seen in a smooth wind but is often disrupted by the more intense eddies in the surrounding air". The bifurcation of the chimney plume in a smooth wind is similar to the overturning and bifurcation processes observed in the present experiment.

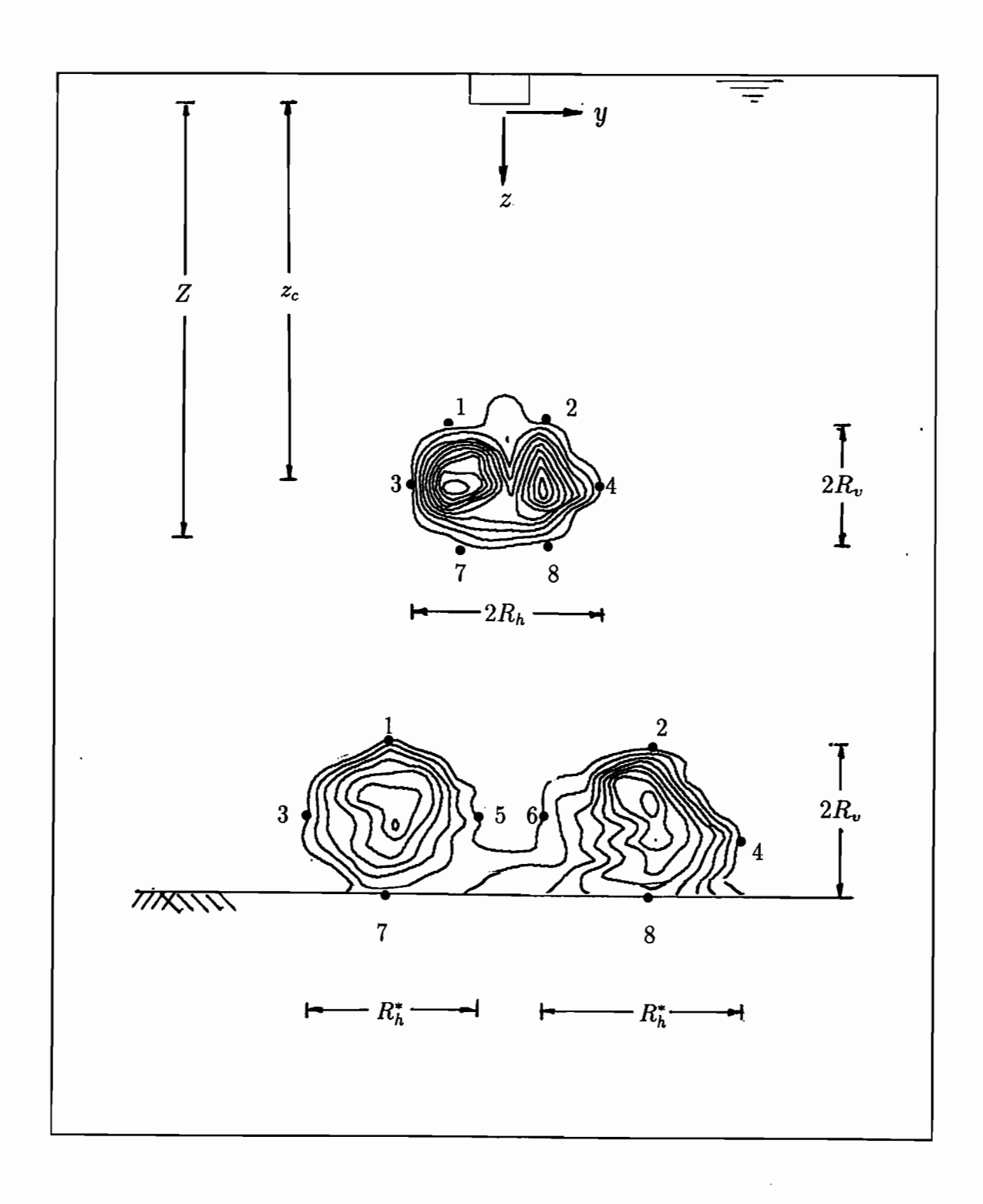
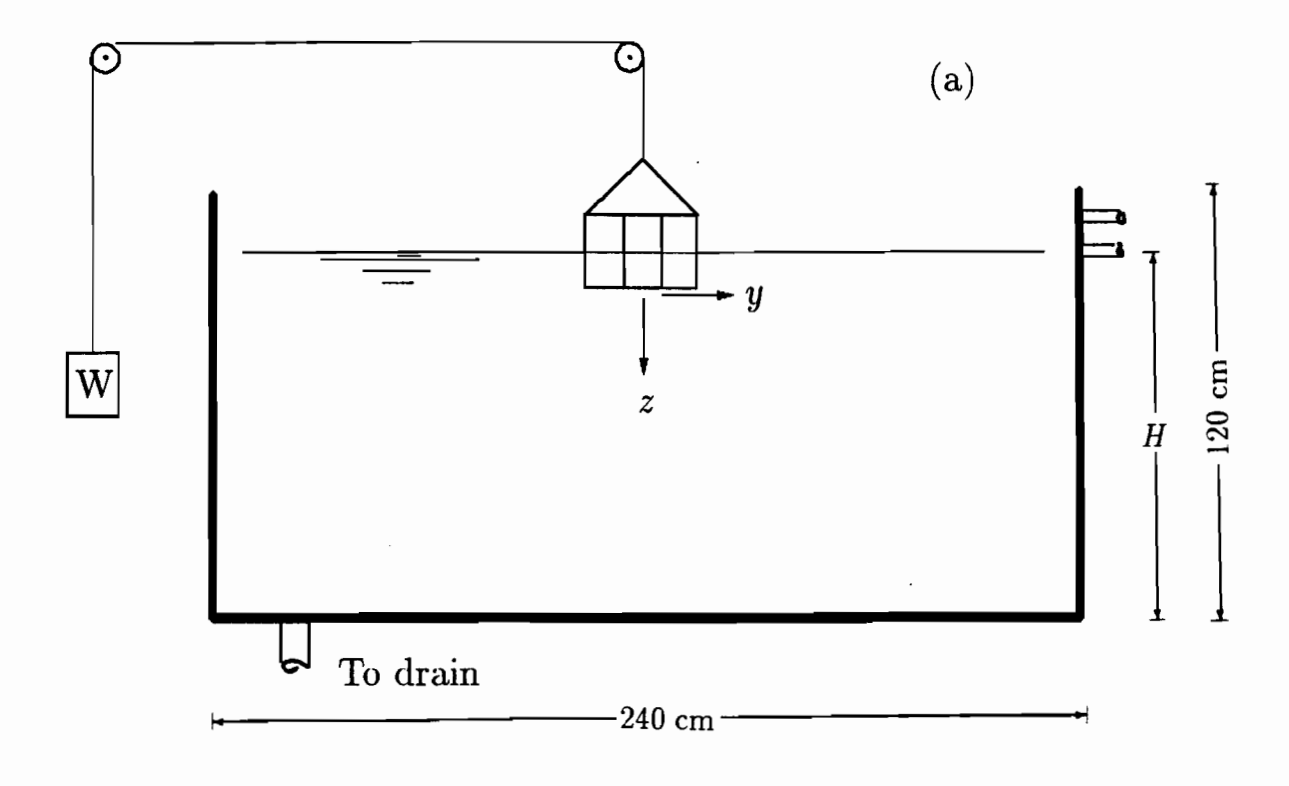


Figure 2.1: Definition sketch. The location and the dimensions of the thermal are defined by a set of key coordinates, 1 through 8, as shown in the figure.



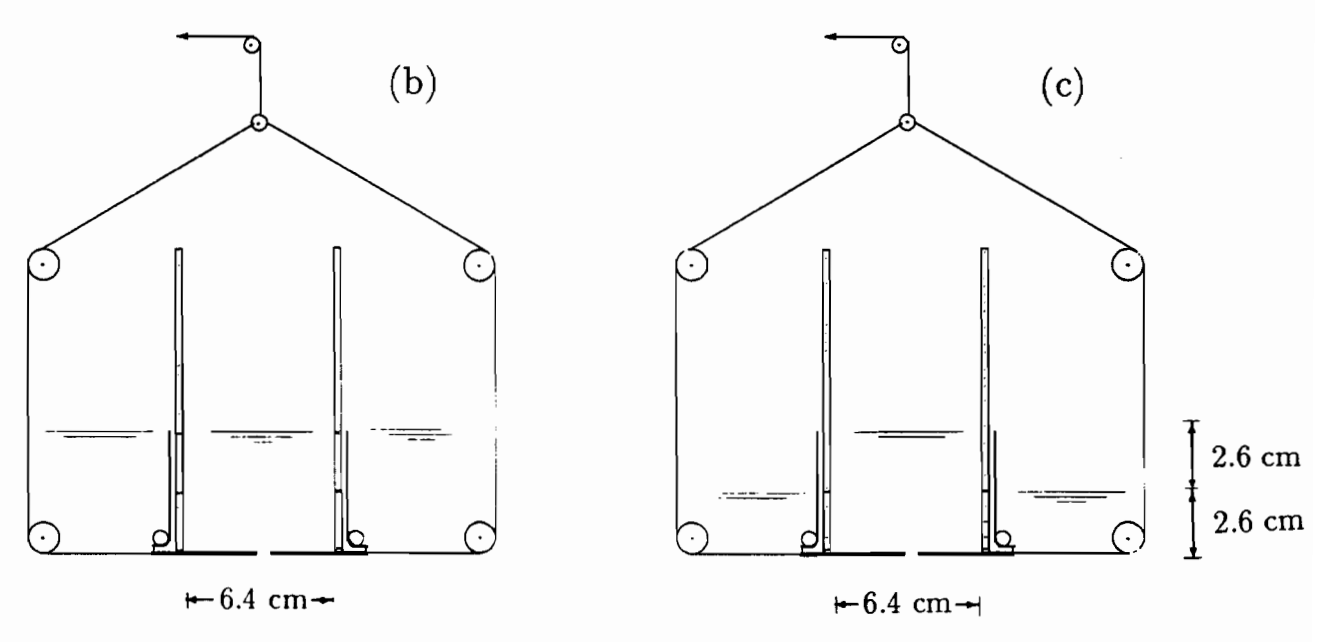


Figure 2.2: Experiment apparatus: (a) 2.4 m wide, 1.2 m high and 0.06 m thick; (b) and (c) two arrangements for the release of source fluid from a 5.2 cm × 6.4 cm enclosure; the initial impulse is produced by arranging the source fluid at a level 2.6 cm above the water level in the tank as shown in (c).

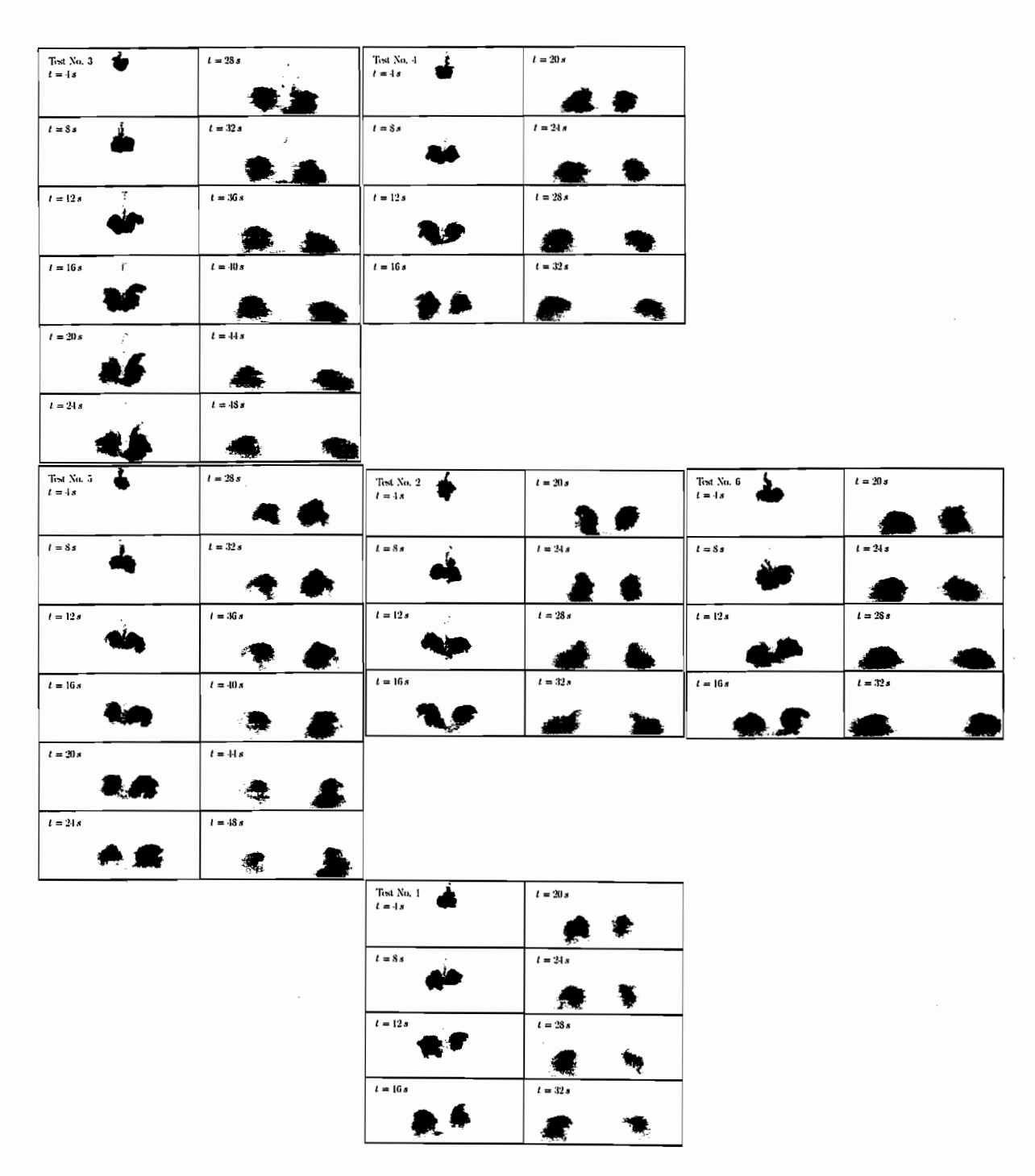


Figure 2.3: Images of the thermals at 4 second intervals. Tests no.5, no.2, and no.6 are arranged from left to right in the middle of the figure. Test no.1 is directly below test no.2, as the condition of this test is the same as test no.2 in the middle of the figure. Tests no.3 and no.4 are directly above test no.5 and no.2. Except for the initial impulse, the conditions of tests no.3 and no.4 are the same as those of tests no.5 and no.2, respectively.

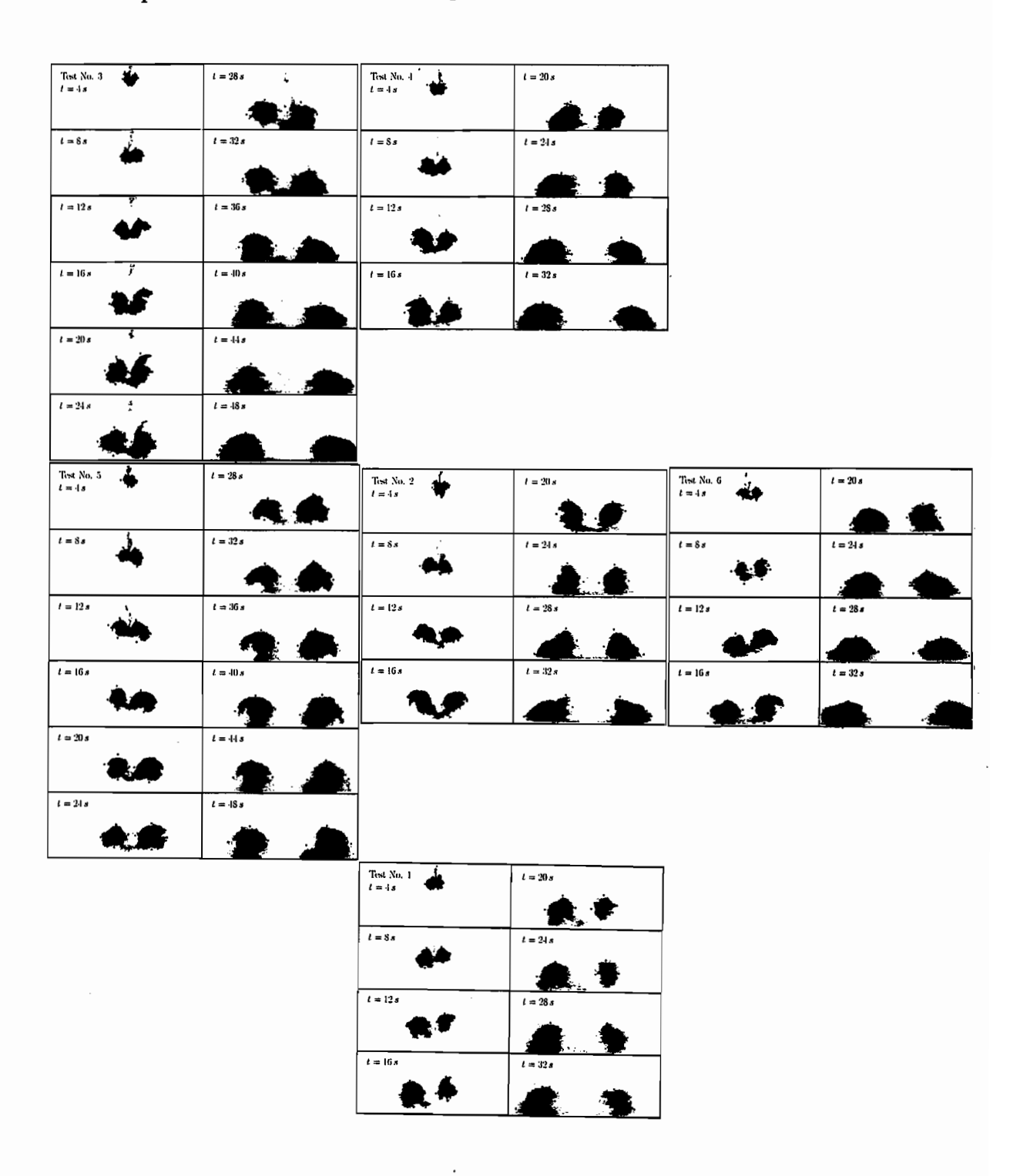


Figure 2.4: The shape of the thermal images in Figure 2.3 is defined by the cutoff at 20% concentration contours. The eight key coordinates, $(x_i, y_i; i = 1, 8)$, of the thermals are marked on the each of the images by the black dots. See Appendix C.

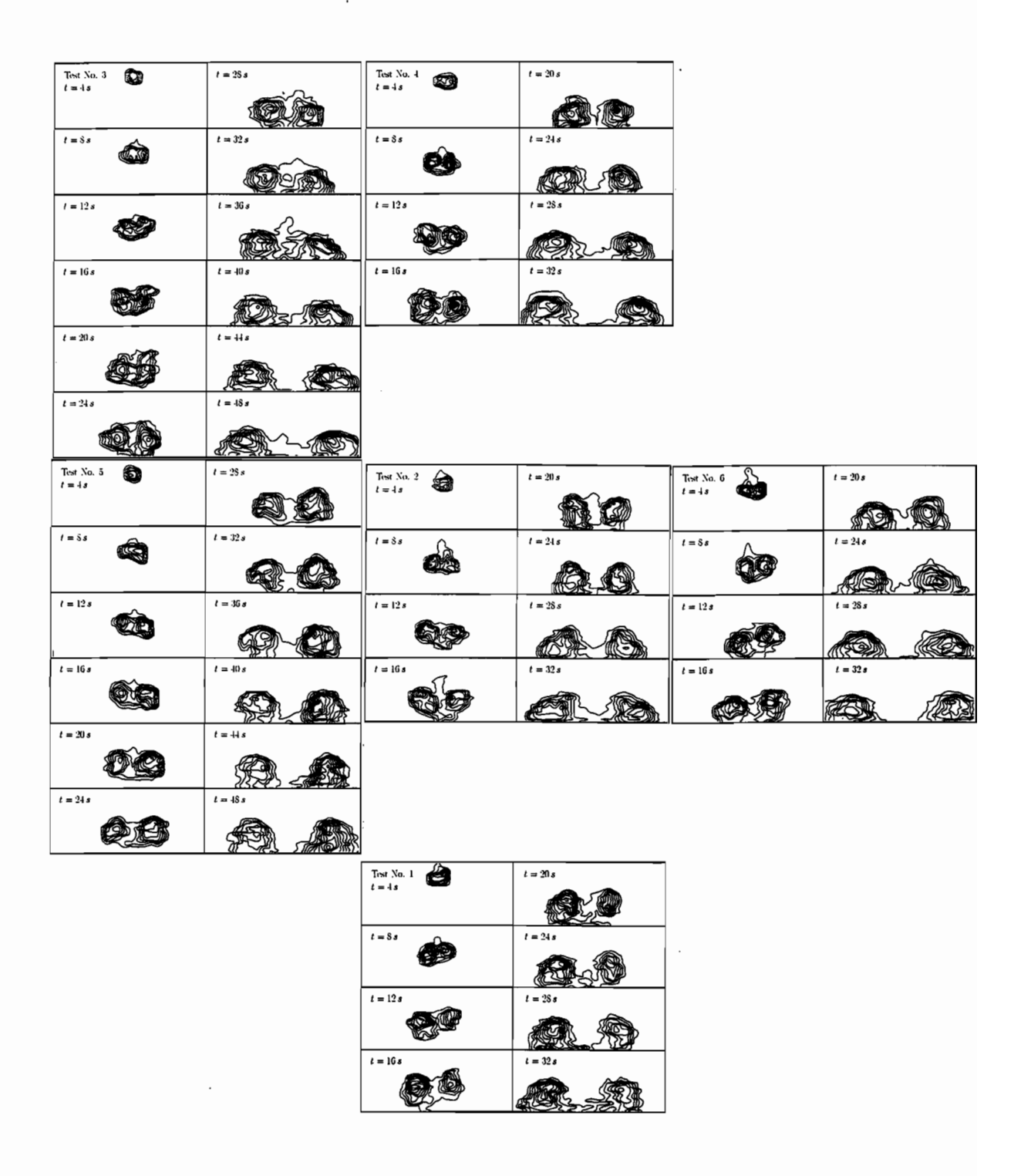


Figure 2.5: Concentration contours of the images at 4 second intervals.

Arrangement of the images are the same as those in Figure 2.3 and
Figure 2.4.

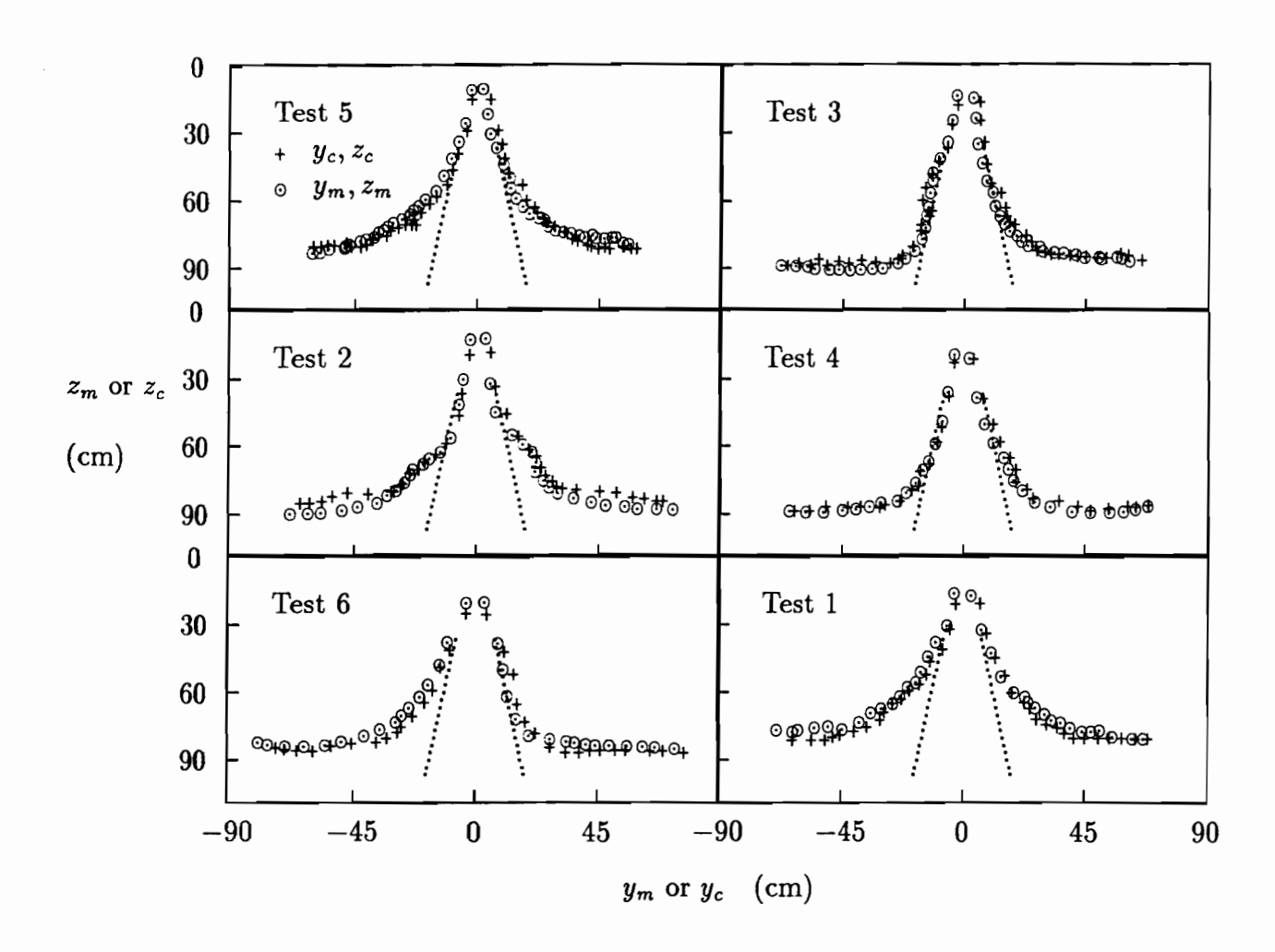


Figure 2.6: Locus of the turbulent core. The geometrical center, (z_c, y_c) , is denoted by the + symbol, and the mass center, (z_m, y_m) , by \odot . The dotted lines delineate the initial spreading rate of $dy_c/dz_c \simeq dy_m/dz_m \simeq 0.18$. Upon impingment of the thermal on the bottom of the tank, the cores move in opposite directions along the floor.

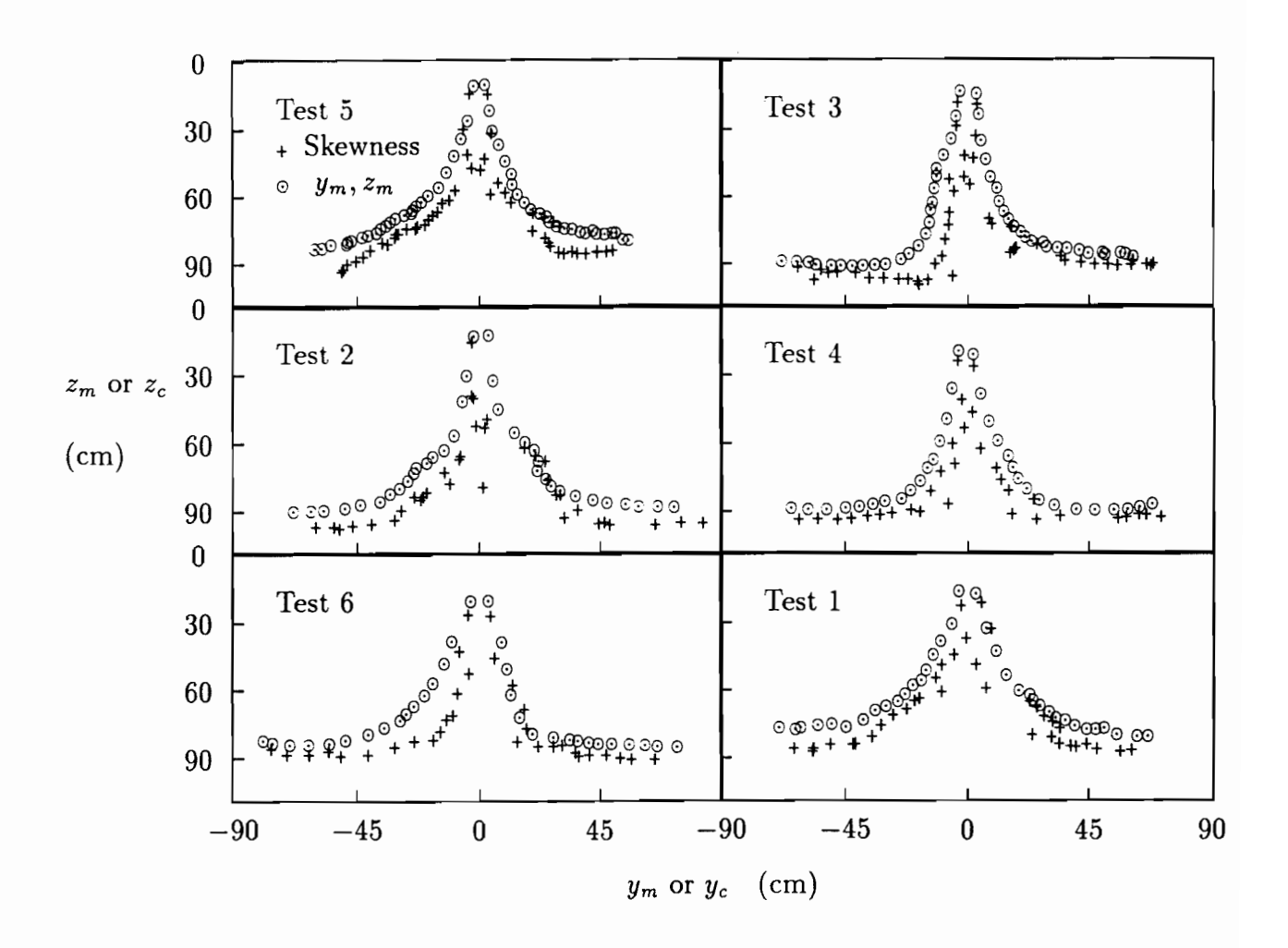


Figure 2.7: Skewness center and mass center; the symbol \odot denotes the position of the mass center, (z_m, y_m) , and the symbol + the skewness center, $(z_m + \gamma_z, y_m + \gamma_y)$.

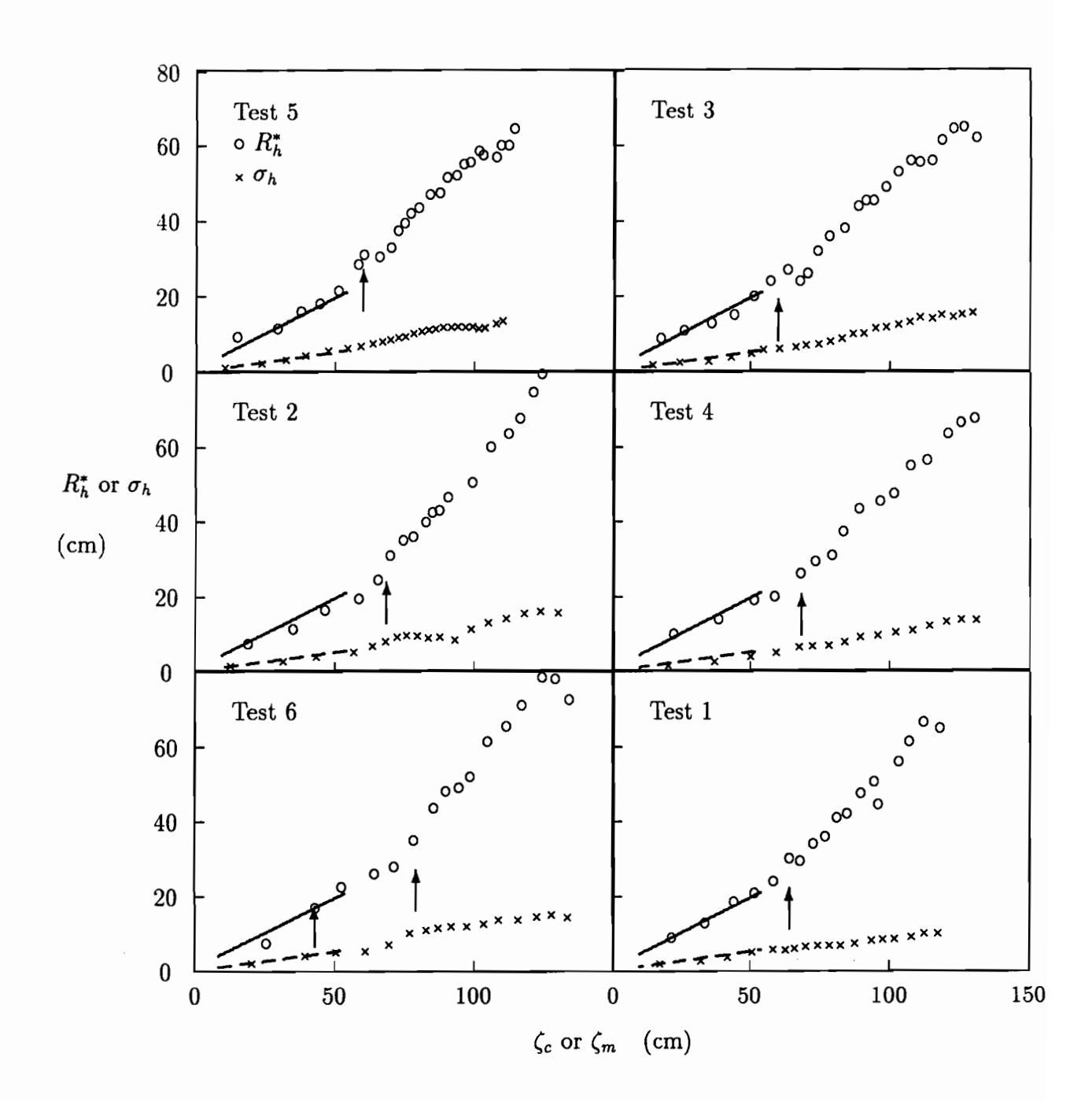


Figure 2.8: Variation of R_h^* and σ_h with distance, ζ_c or ζ_m , from the source; the initial spreading rate $dR_h^*/d\zeta = 0.37$ for R_h^* is denoted by the solid line, and the spreading rate $d\sigma_h^*/d\zeta = 0.12$, by the dashed line; the arrows point to overturning events.

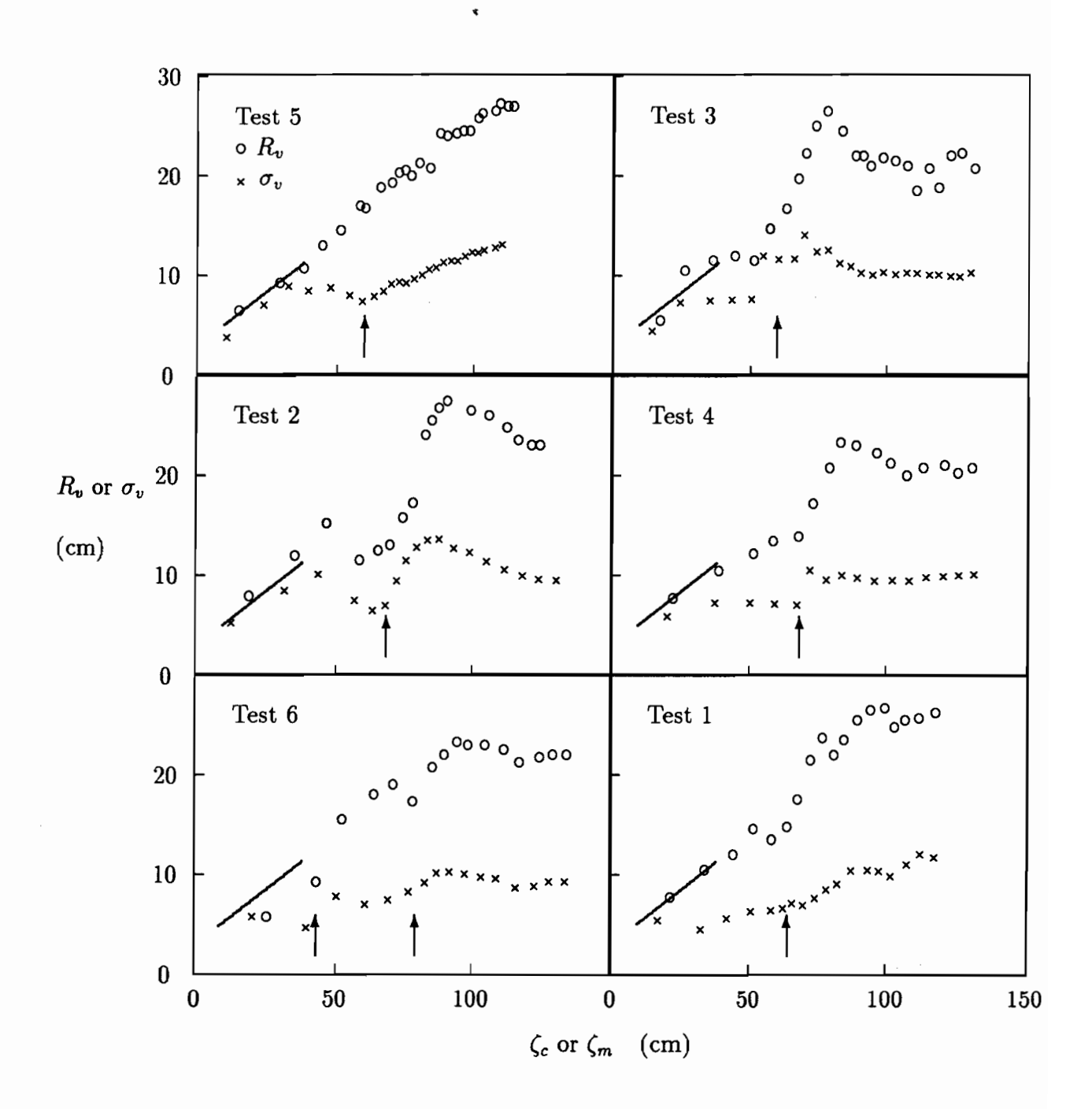


Figure 2.9: Variation of R_v and σ_v with distance, ζ_c or ζ_m , from the source; the initial spreading rate, $dR_v/d\zeta=0.22$, is denoted by the solid line; the arrows point to the overturning events where the vertical radii are reduced.

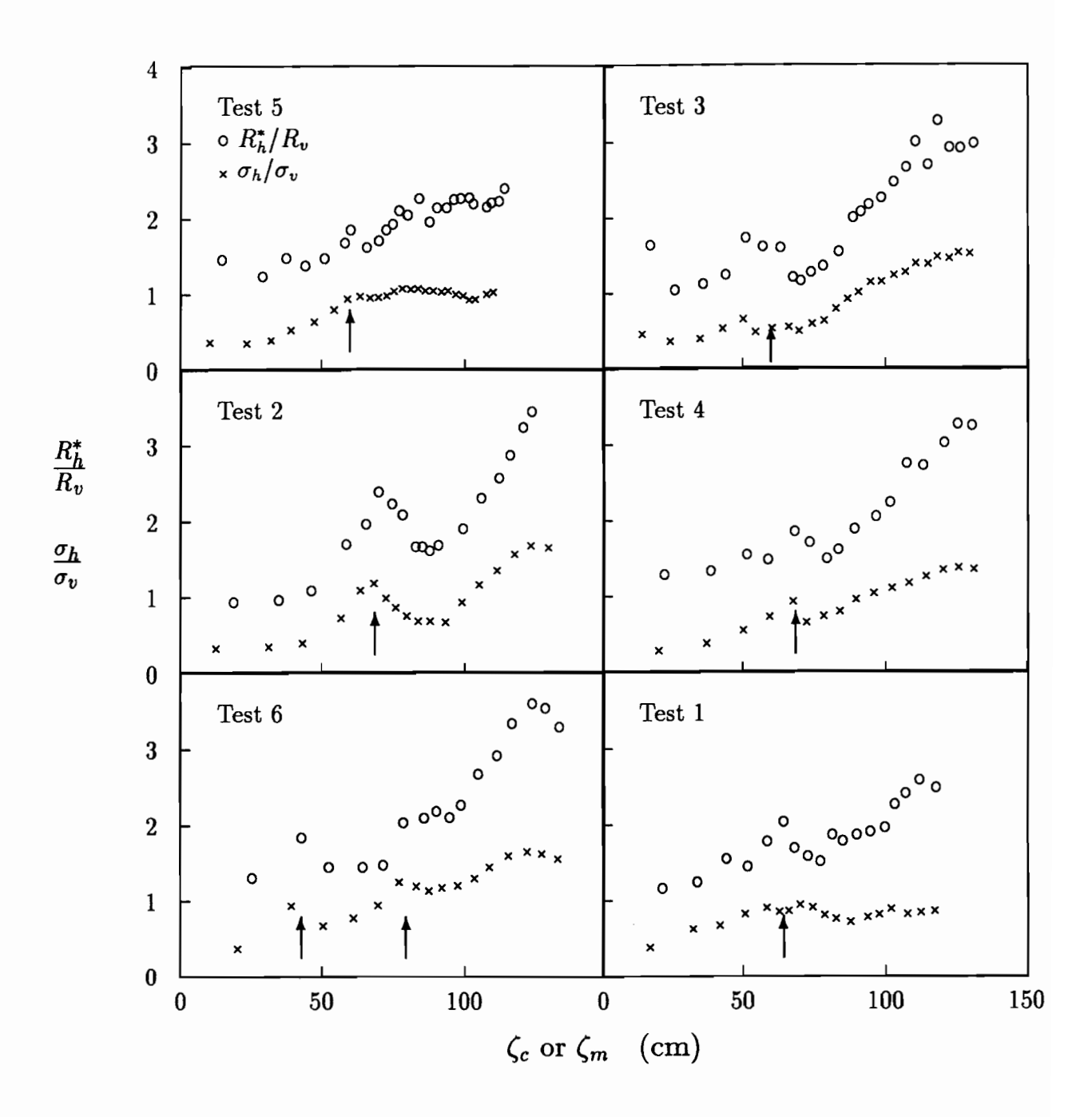


Figure 2.10: The shape of the thermal cross section defined by the ratios R_h^*/R_v and σ_h/σ_v ; the arrows point to the overturning events where this ratio is maximum.

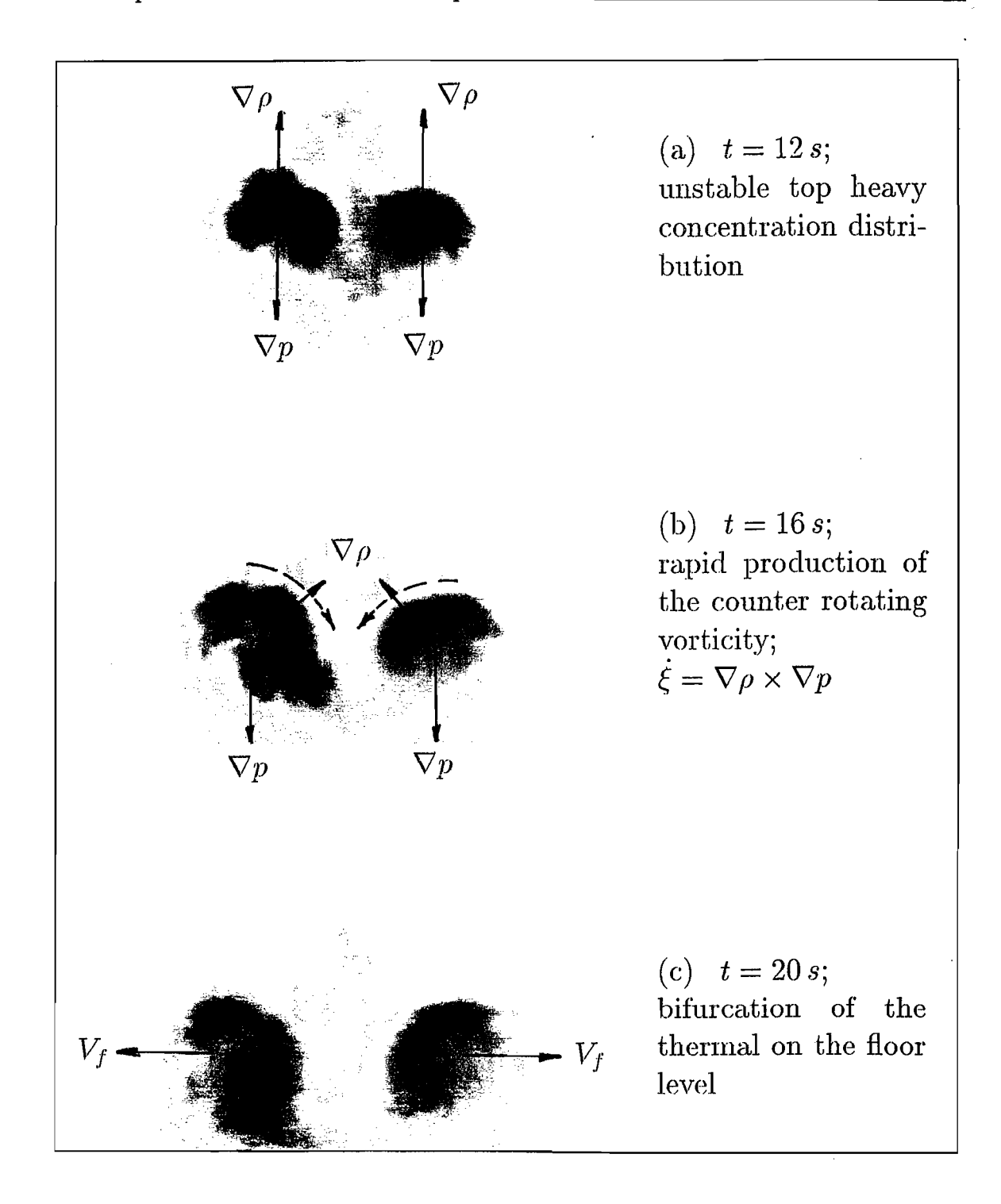


Figure 2.11: The mechansim of overturning; the images are those from test no.6.

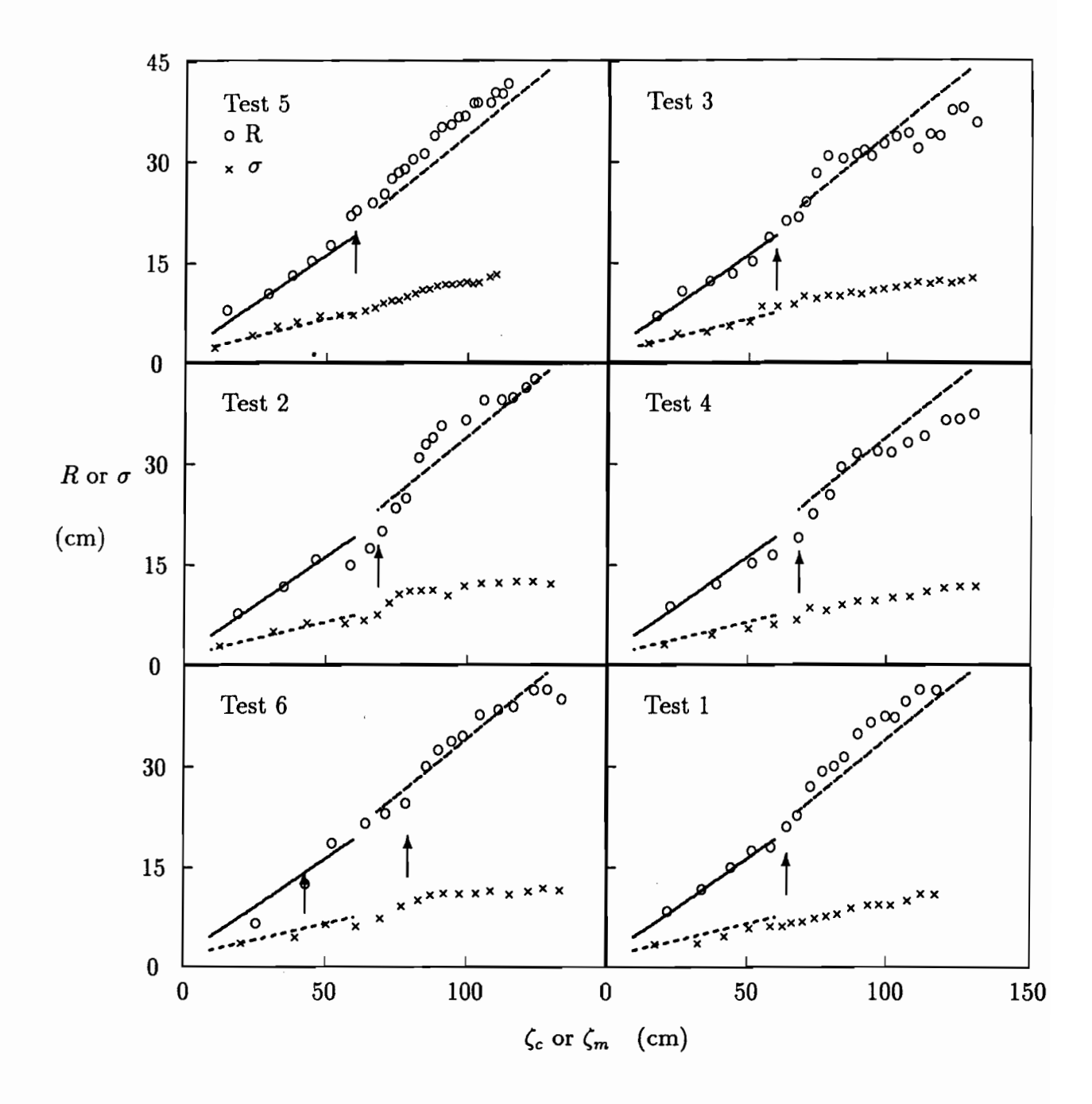


Figure 2.12: Variation of R and σ with distance, ζ_c or ζ_m , from the source; the initial spreading rates, $dR/d\zeta = 0.29$ and $d\sigma/d\zeta = 0.10$ are denoted the the solid lines and the short desh lines; the long dashlines denotes the rate, $dR/d\zeta = 0.34$, of the later development. R and σ are the radii of the equivalent circles that have the same areas as the elliptical cross section of the turbulent cores.

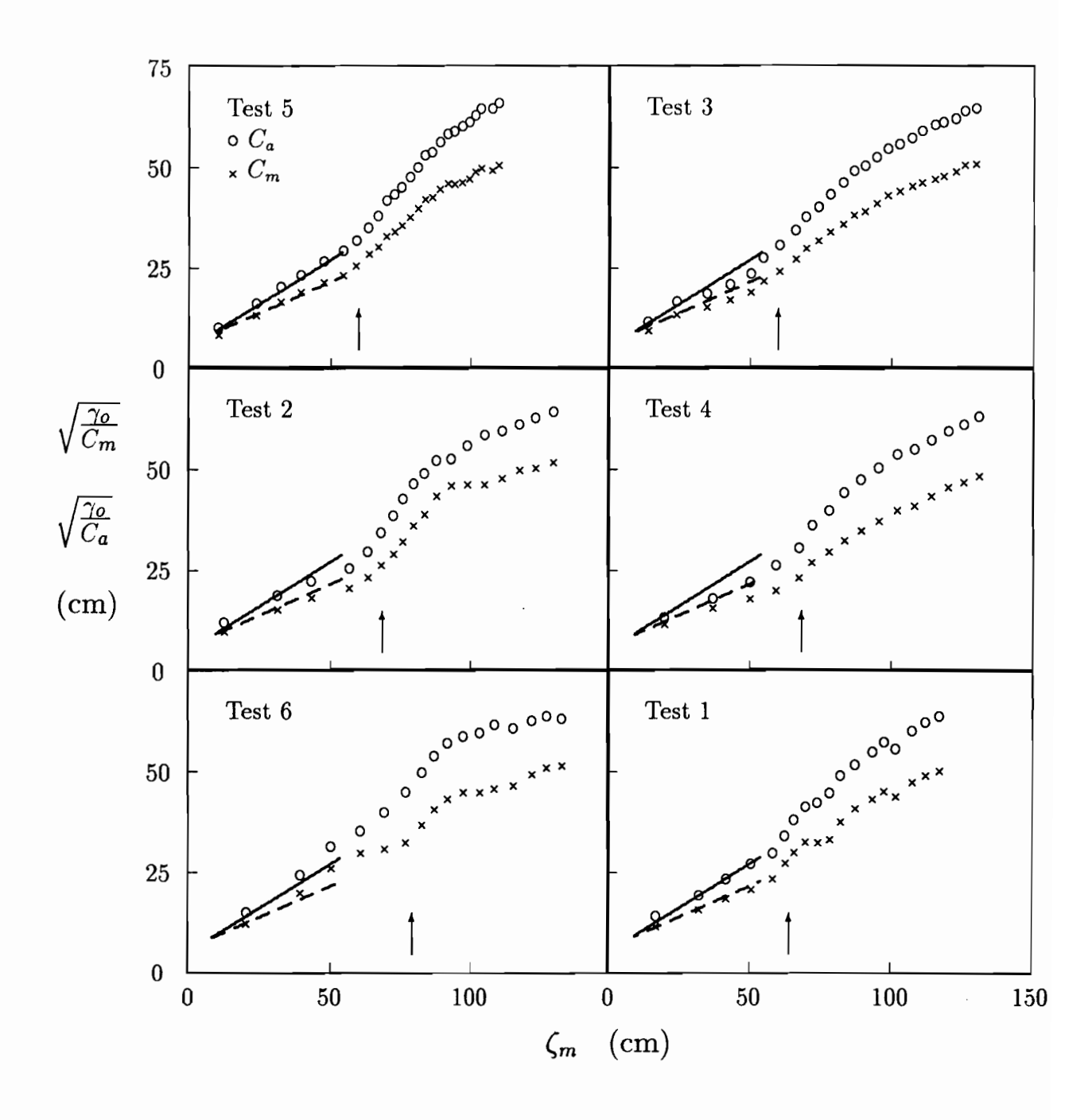


Figure 2.13: Dye concentration maximum, C_m , and dye concentration averaged over the thermal cross section, C_a . The data are normalized by the total dye mass per unit length of the thermal, γ_o , initially released from the source.

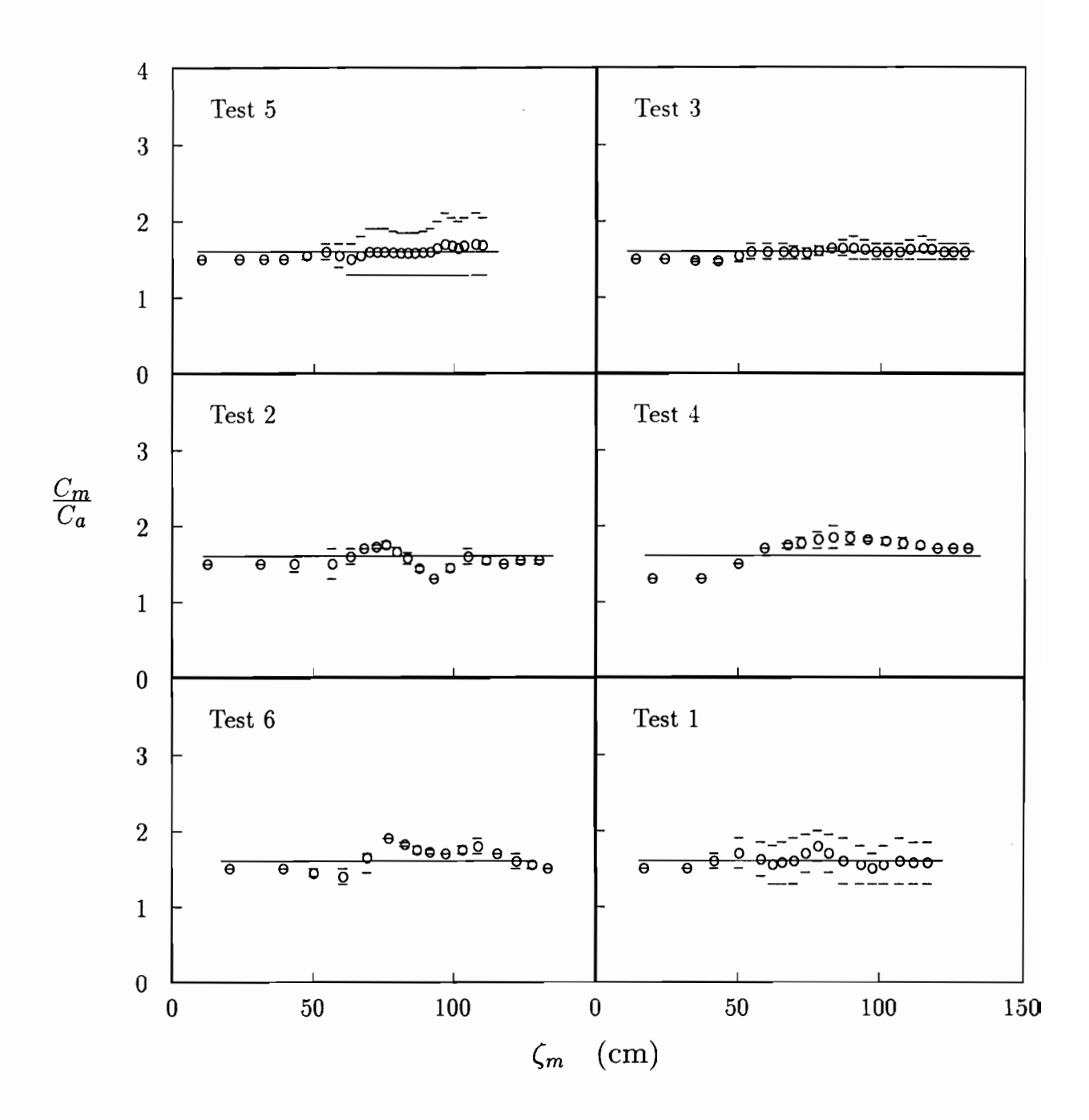


Figure 2.14: The maximum-to-average concentration ratio, C_m/C_a =1.61; bars denote values on the left hand side and the right hand side of the cores.

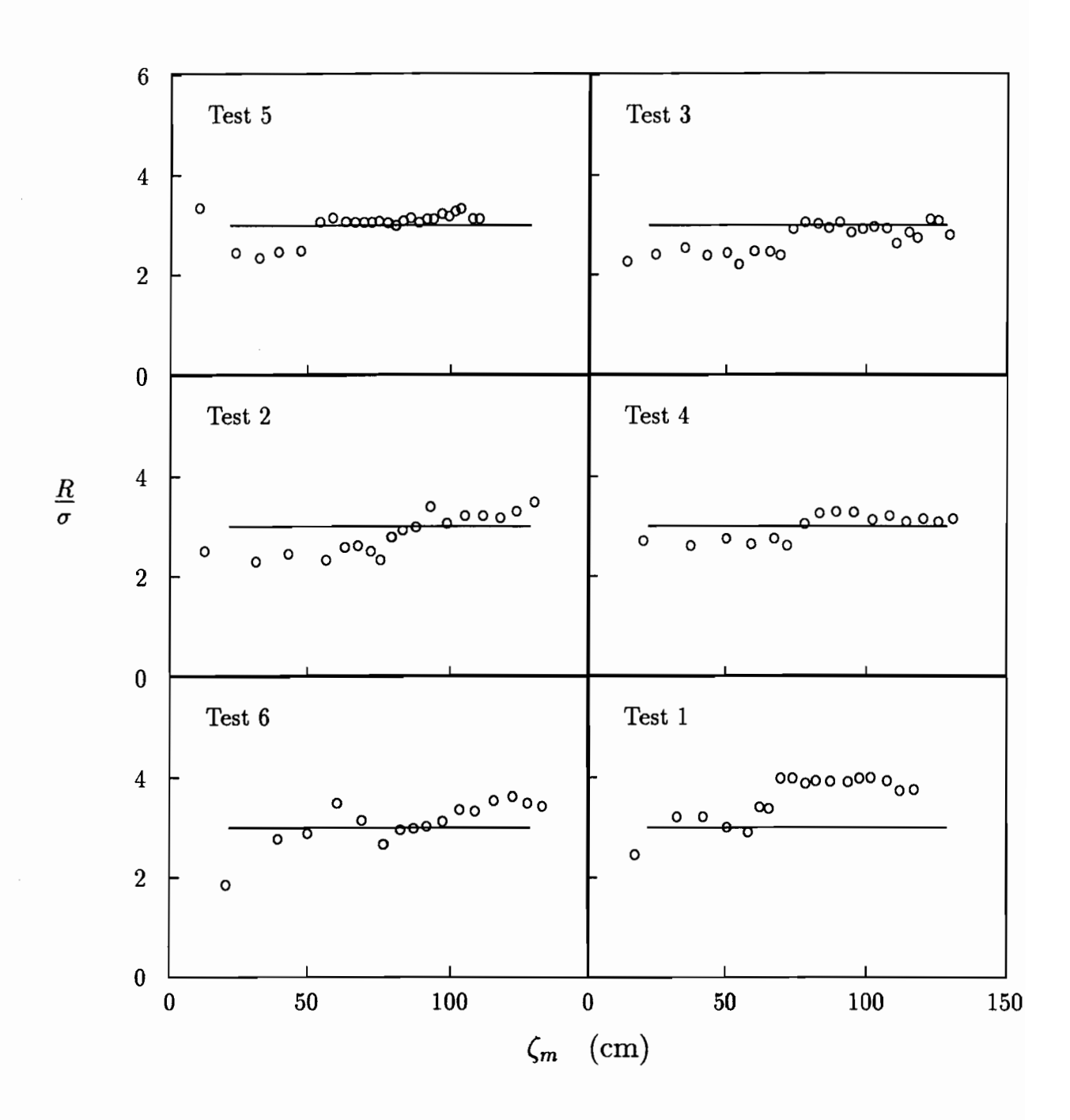


Figure 2.15: The visual radius to standard deviation ratio, $R/\sigma=3$.

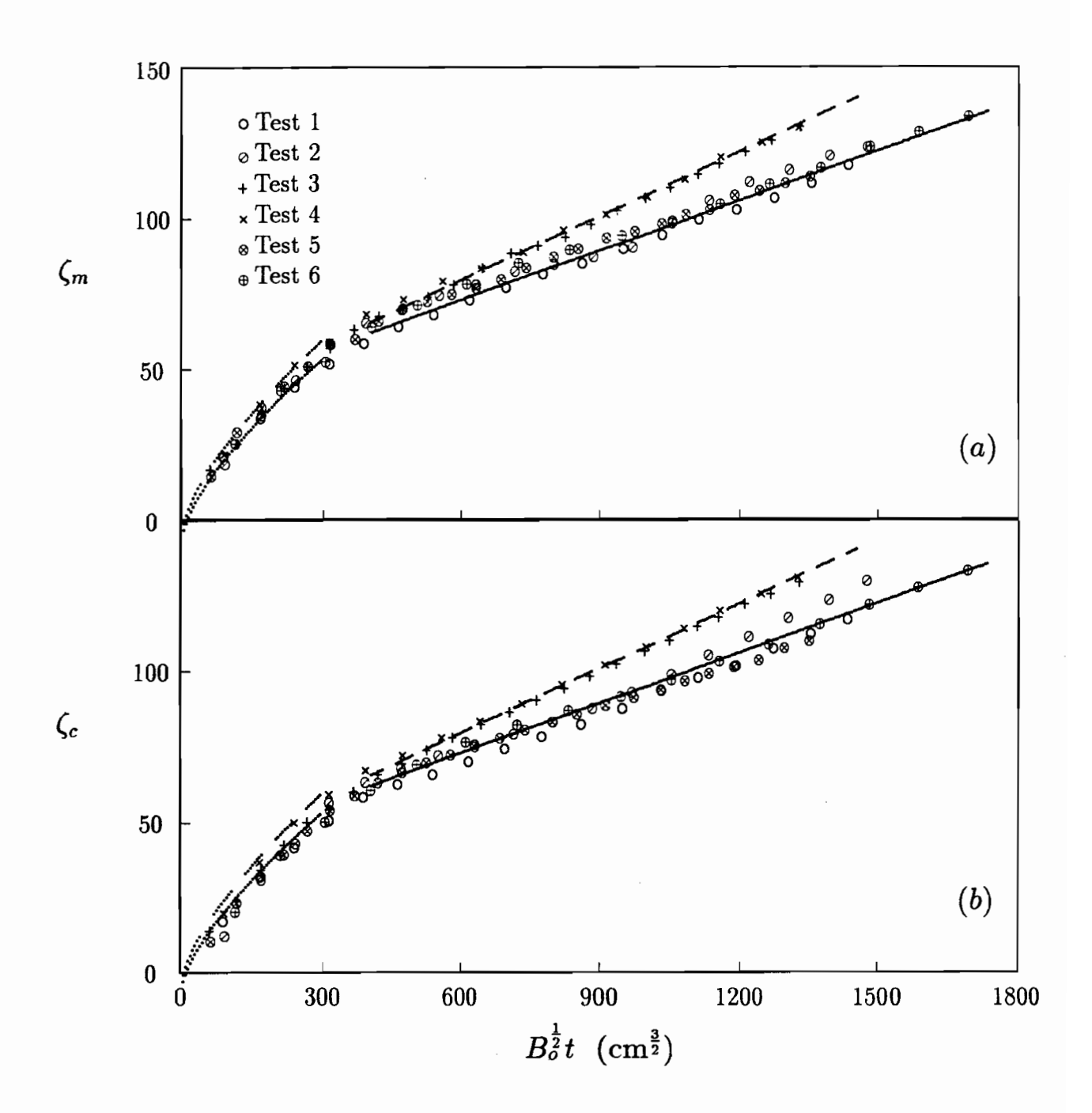


Figure 2.16: Two stages of development of the thermals; (a) geometric center; (b) mass center; both sets of data are fitted with the same curves except that the virtual origins are $\zeta_{co} = 5$ cm and $\zeta_{mo} = 10$ cm.

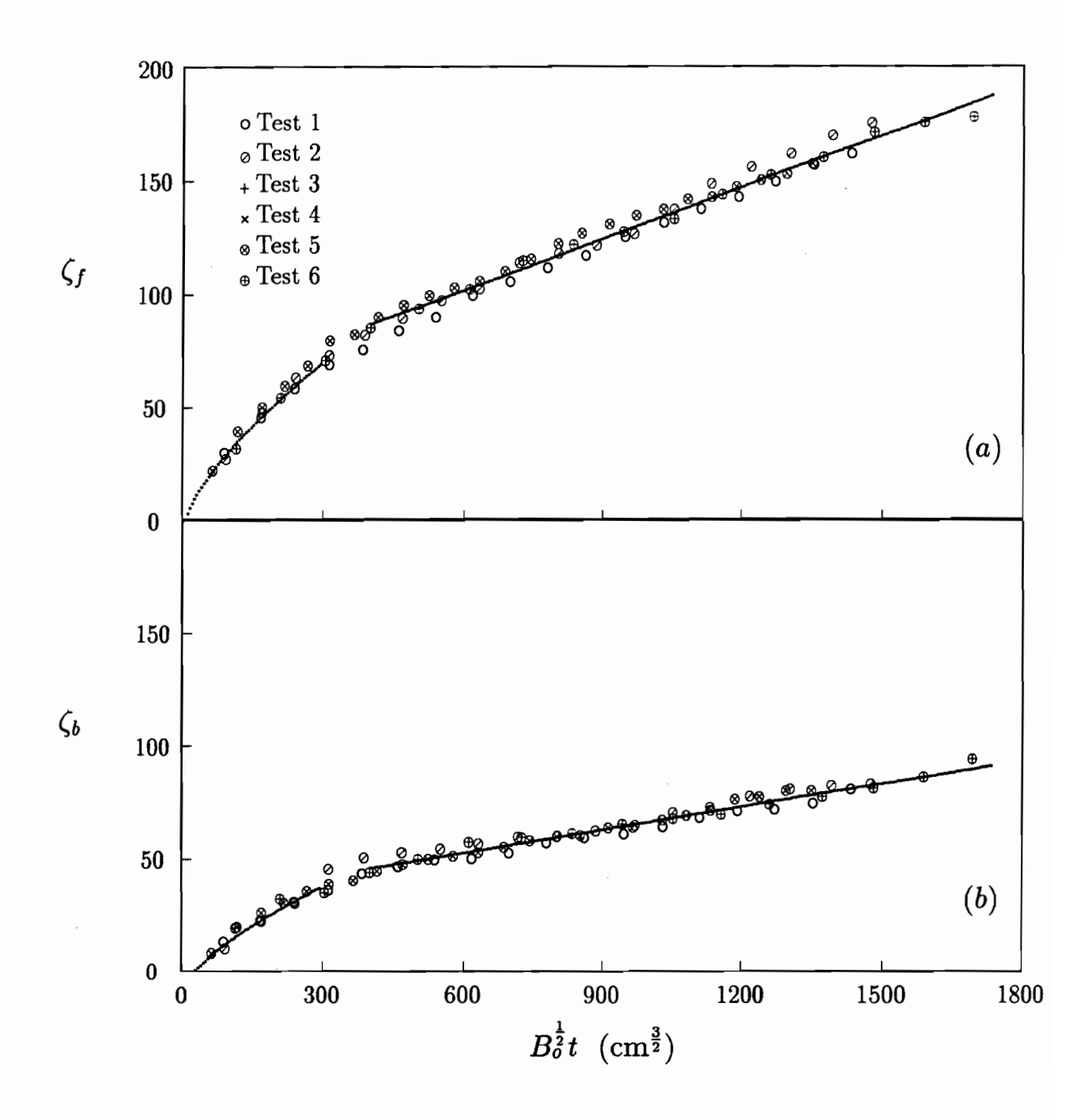


Figure 2.17: Two stages of development for (a) front and (b) back of the thermals; the data, ζ_f and ζ_b , are plotted versus time, $B_o^{\frac{1}{2}}t$.

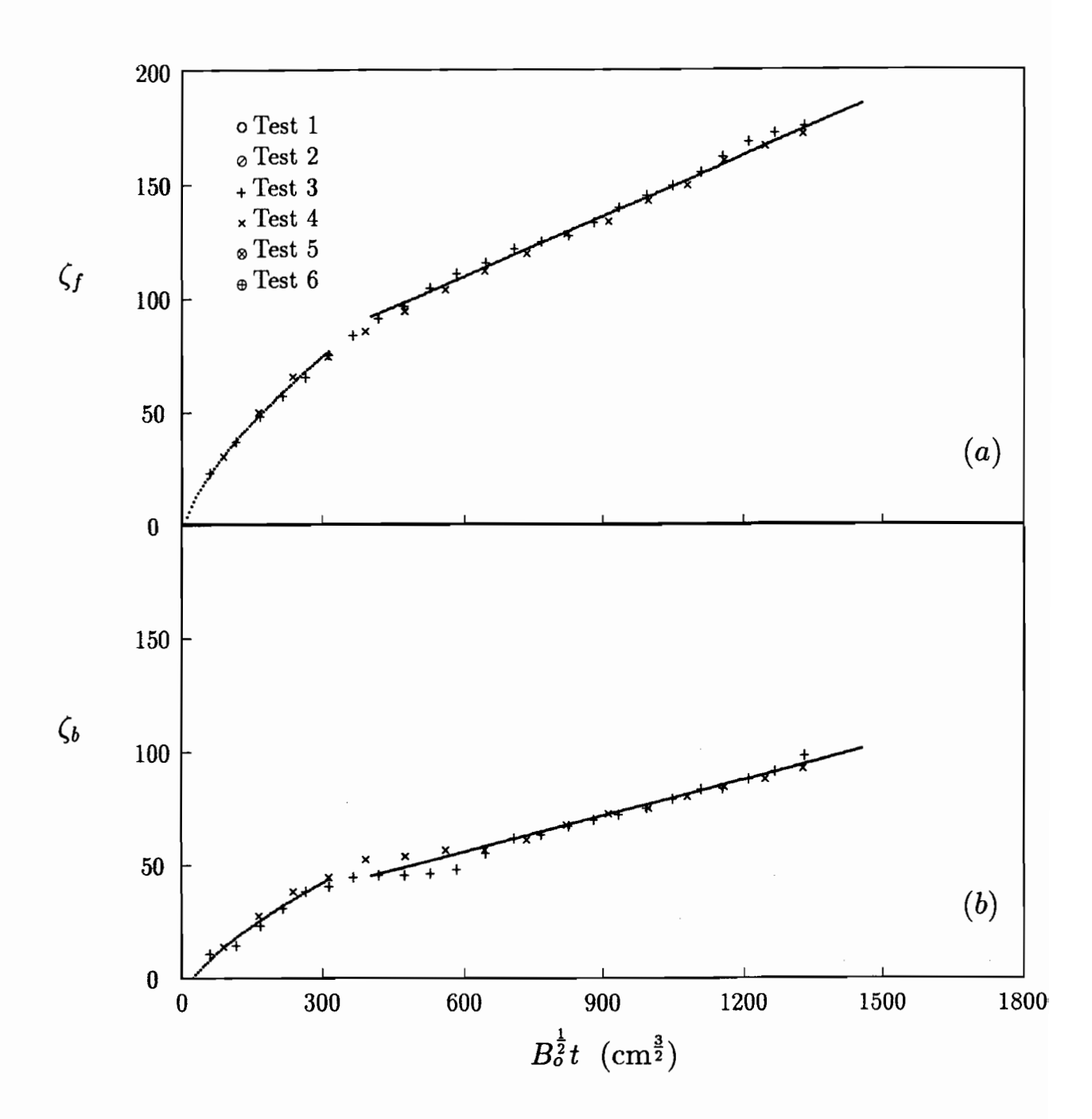


Figure 2.18: Two stages of development for the thermals of test no.3 and no.4; the effect of the initial impulse is negligible in the initial development but is significant to the velocity along the floor.

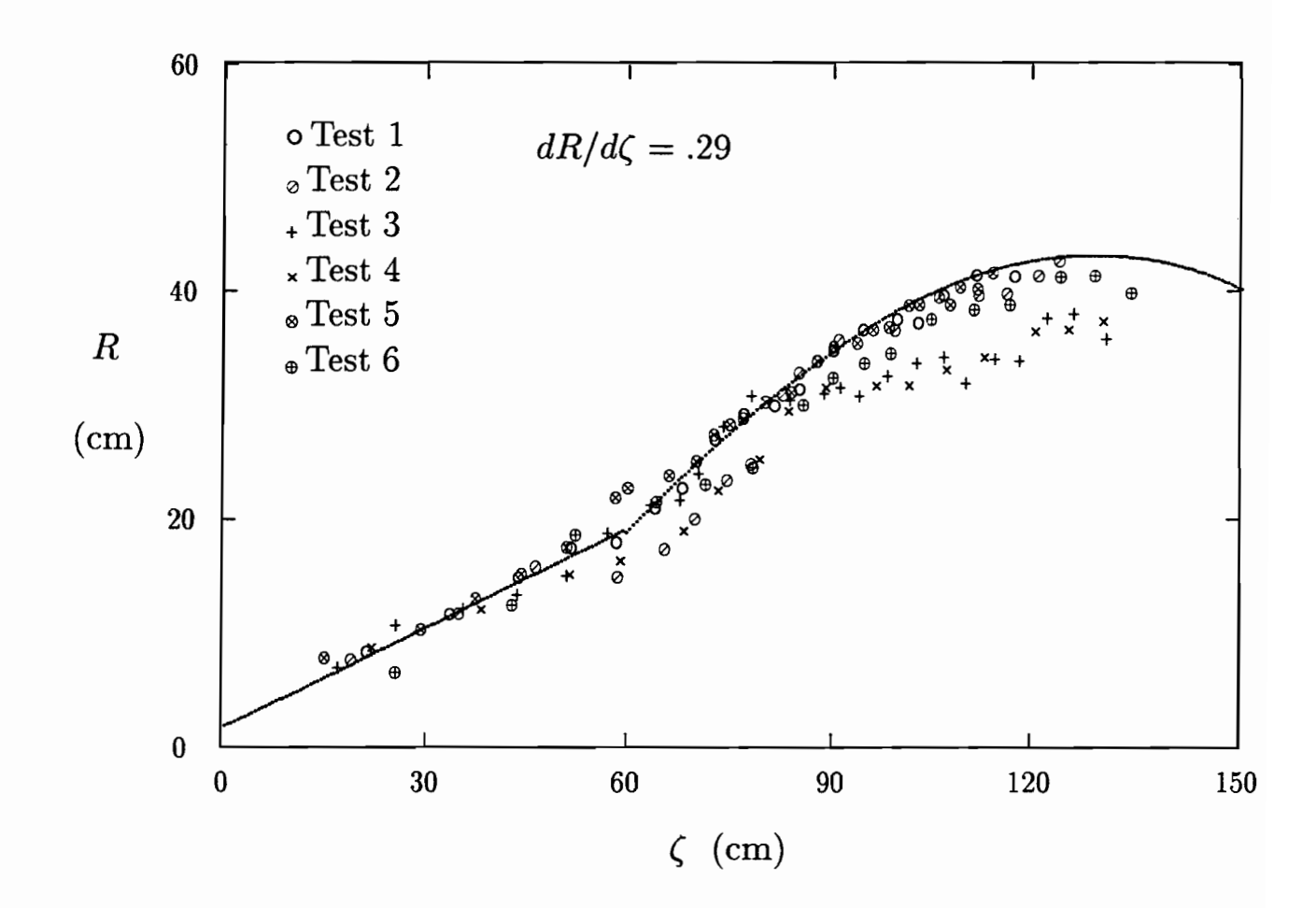


Figure 2.19: Fitting of the radius, $R(\zeta)$, of the thermal by the empirical formulae; note that the data of test no.3 and no.4 are lower suggesting a lower dilution for these tests.

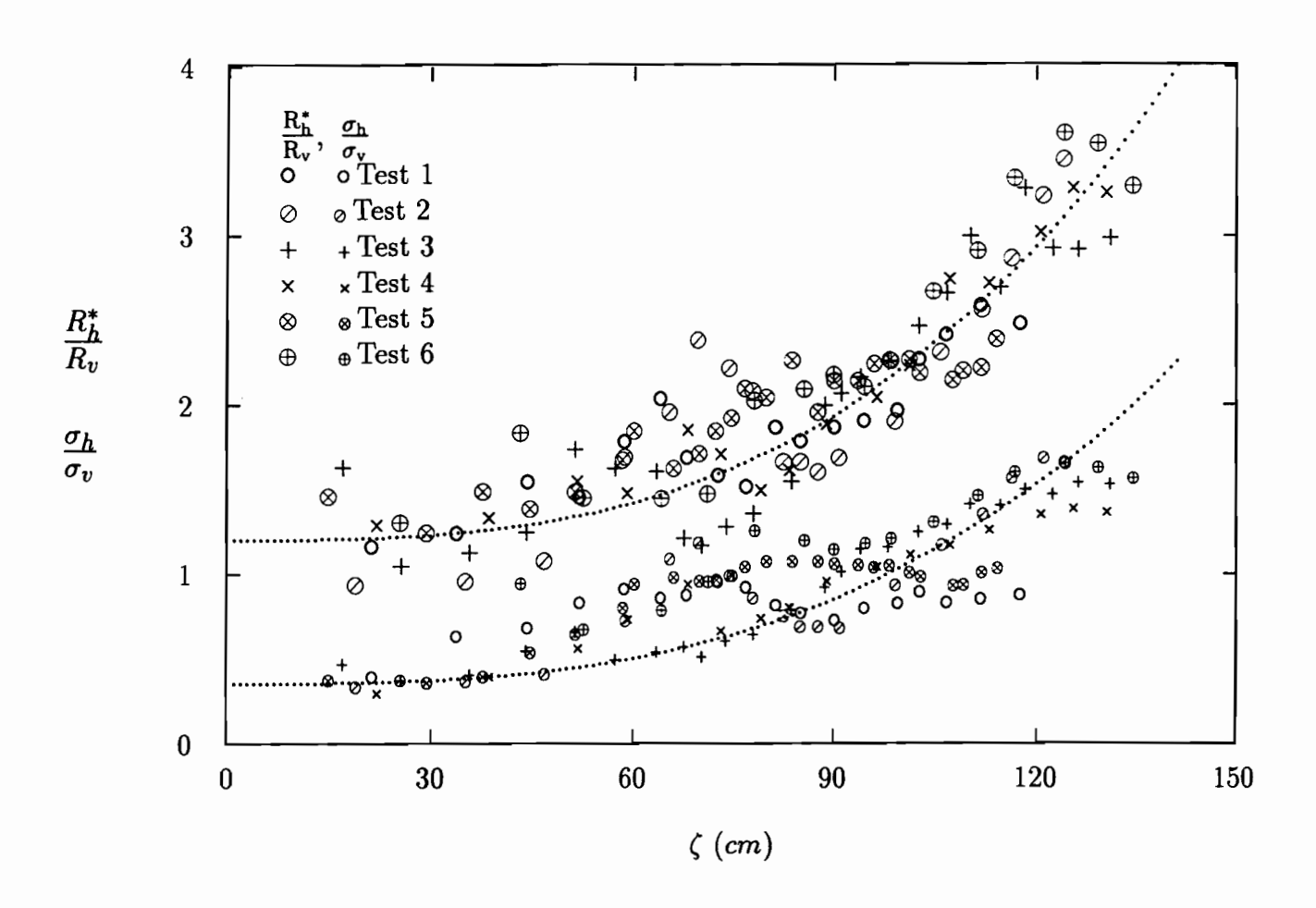


Figure 2.20: Fitting the width-to-height ratios, R_h^*/R_v and σ_h/σ_v , by emprirical formulae.

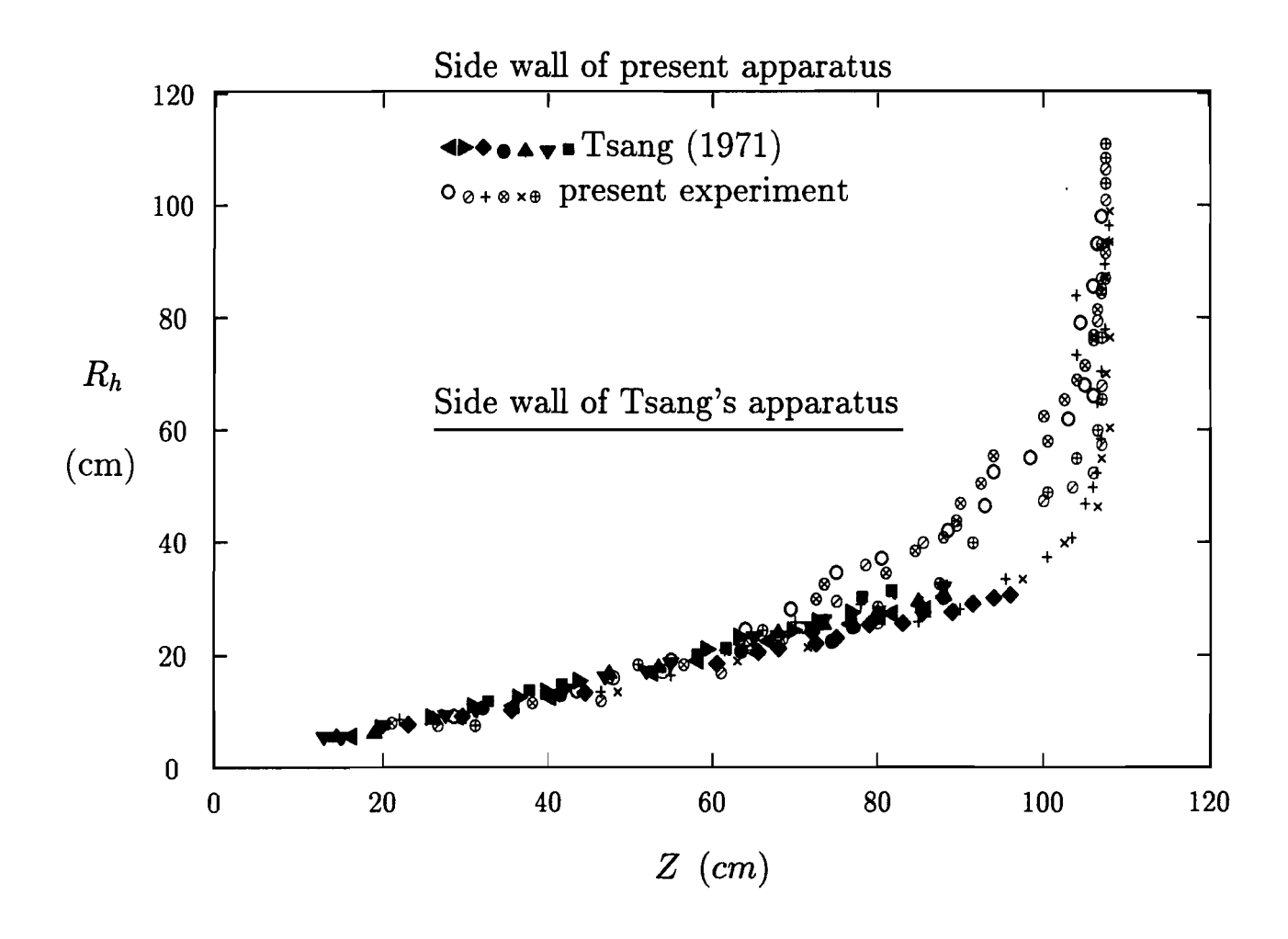


Figure 2.21: Width of the thermal compared with the experimental data of Tsang (1971); the data of Tsang are denoted by the solid symbols; data of test no.3 and no.4 are denoted by the symbols + and ×.

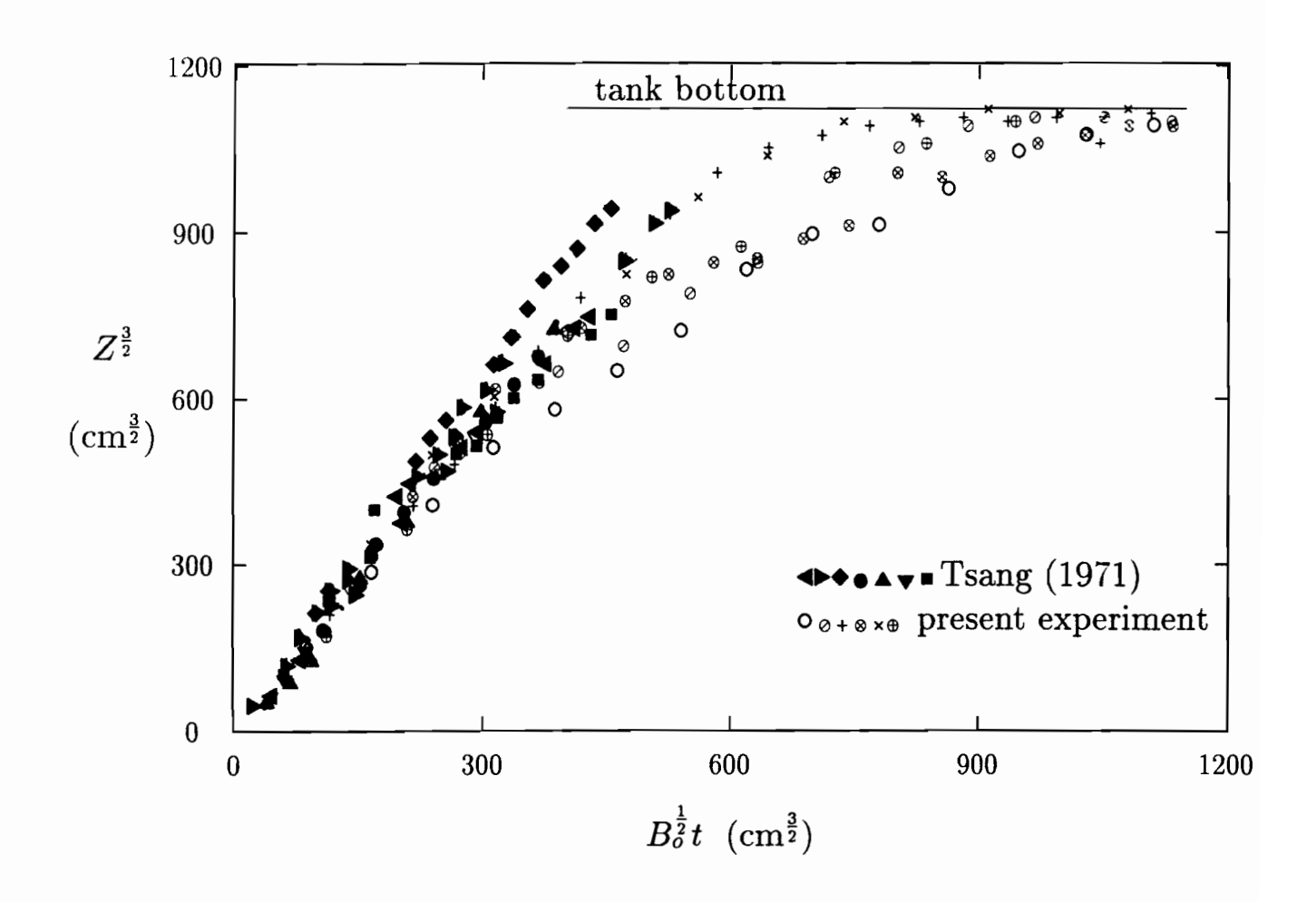


Figure 2.22: The data of $Z^{\frac{3}{2}}$ versus $B_o^{\frac{1}{2}}t$ compared with the data of Tsang (1971); data of test no.3 and no.4 are denoted by the symbols + and \times .

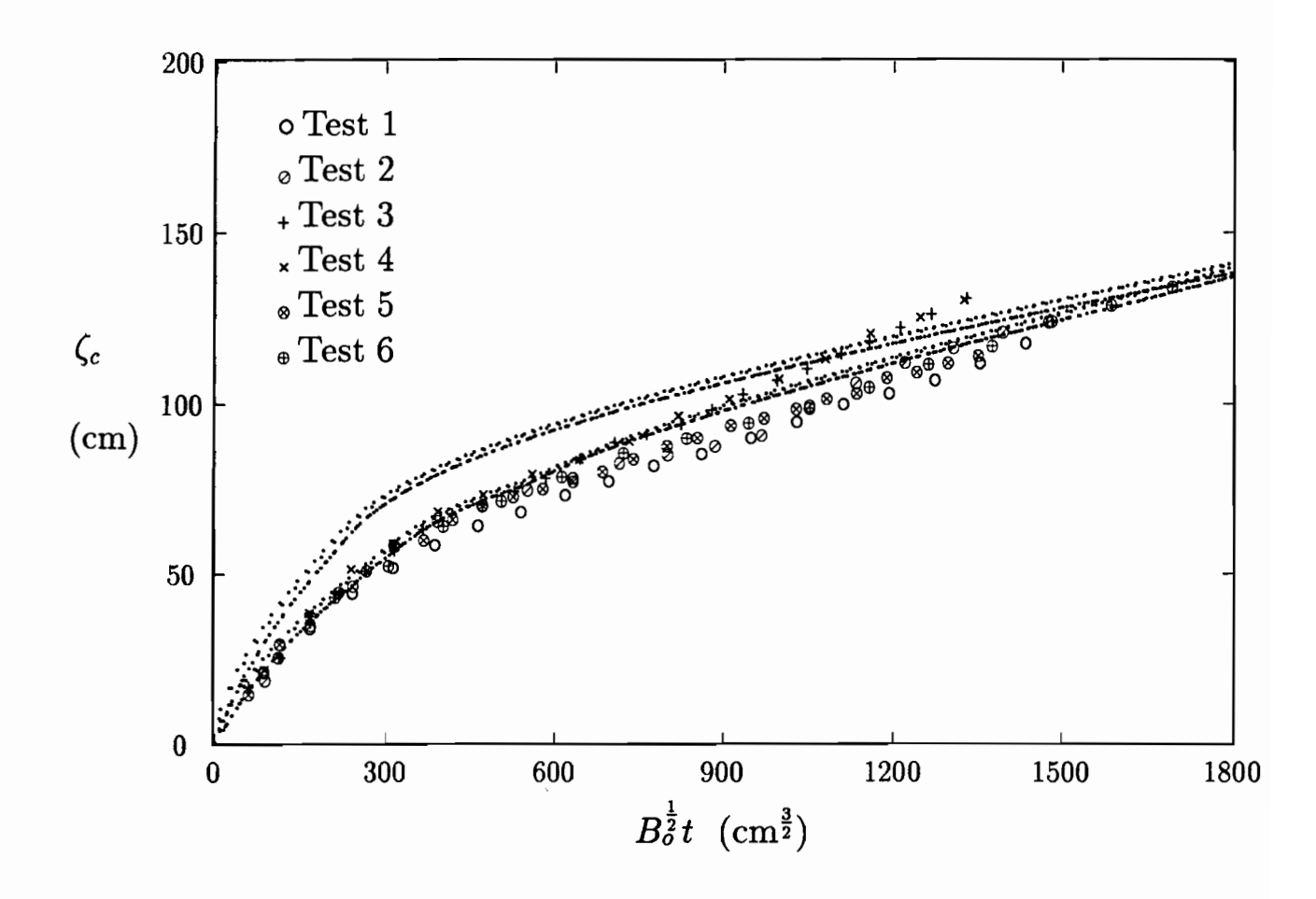


Figure 2.23: Path of the thermal obtained from integral model and the comparison of the path with the experimental data; the short dashed lines are the predictions by the model that includes the added-mass effect; the dotted lines are the model prediction obtained by setting k=0.

Chapter 3

Integral Analysis

3.1 Dominant Eddy Hypothesis

The formulation for buoyant jets in cross flows is conducted in this chapter using a Lagrangian method based on the dominant eddy hypothesis proposed recently by Chu (1994). The dominant eddy is the large coherent structure of the turbulent motion that, according to the hypothesis, is responsible for the transport of mass, momentum and buoyancy along the path of the turbulent jet. A control volume AB is selected between the dominant eddies A and B along the path of the jet so that B leaves the source one time unit earlier than A. The vector connecting A to B is therefore equal to the velocity of the dominant eddy along the path, $\tilde{\mathbf{U}}$, as shown in Figure 3.1. The velocity of the cross flow is \mathbf{U}_a . Therefore, the velocity of the dominant eddy relative to the cross flow is

$$\tilde{\mathbf{u}} = \tilde{\mathbf{U}} - \mathbf{U}_a. \tag{3.1}$$

The characteristic radius of the cross section of the jet is \tilde{b} . Due to turbulent entrainment into the path of the jet, the radius of the jet cross section is assumed to increase at a rate proportional to the relative velocity. The rate is defined by the spreading coefficients, β_s and β_n , as follows:

$$\frac{\delta \tilde{b}}{\delta t} = \beta_s |\tilde{\mathbf{u}}_s| + \beta_n |\tilde{\mathbf{u}}_n| \tag{3.2}$$

where $\tilde{\mathbf{u}}_s$ and $\tilde{\mathbf{u}}_n$ are the components of the relative velocity in the tangential and normal directions, respectively.

3.1.1 Buoyancy and Momentum Equation

As the turbulent jet moves relative to the cross flow, mass and momentum are entrained into the jet from the cross flow. The result is the dilution of the fluid in the jet and bending of the jet towards the cross flow. The motion of the dominant eddies along the path of the jet is governed by the equations of buoyancy and momentum. The derivation of these equations is made considering the collision problem between a volume of fluid in the jet, \tilde{V} , and a small volume of the fluid entraining from the cross flow, $\delta \tilde{V}$. Since the element AB (shown in Figure 3.1) is selected as the control volume, the volume associated with the turbulent part of the control volume, \tilde{V} , is $\pi \tilde{b}^2 |\tilde{\mathbf{U}}|$. Before the collision, the mass is $\rho \tilde{V} + \rho_a \delta \tilde{V}$. After the collision, the mass is $\rho \tilde{V} + \delta(\rho \tilde{V})$. The mass is unchanged before and after the collision. Hence,

$$\rho \tilde{V} + \delta(\rho \tilde{V}) - (\rho \tilde{V} + \rho_a \delta \tilde{V}) = 0. \tag{3.3}$$

Multiplying by g and re-arranging gives the buoyancy equation

$$\delta \tilde{\mathbf{F}} = \mathbf{g} \tilde{V} \delta \rho_a, \tag{3.4}$$

where $\tilde{\mathbf{F}} = \mathbf{g}(\rho_a - \rho)\tilde{V} = \rho_a \mathbf{g}'\tilde{V}$ is buoyancy force, $\mathbf{g}' = \mathbf{g}(\rho_a - \rho)/\rho_a$ is the reduced gravity equal to the buoyancy forces per unit mass of fluid, and $\mathbf{g} = (0, 0, -g)$ is the vector of gravity. The derivation is made here for incompressible fluid.

The momentum equation is derived using a similar procedure. Before the collision, the momentum is the sum of the momentum of the volume of fluid in the jet and the momentum of the entraining fluid from the cross flow, that is $\rho \tilde{V}\tilde{\mathbf{U}} + \rho_a(\delta \tilde{V})\mathbf{U}_a$. After the collision, the momentum of the combined volume is $\rho(\tilde{V} + \delta \tilde{V})(\tilde{\mathbf{U}} + \delta \tilde{\mathbf{U}})$. The change in momentum is equal to the impulse of buoyant forces acting on the system, that is,

$$\rho(\tilde{V} + \delta \tilde{V})(\tilde{\mathbf{U}} + \delta \tilde{\mathbf{U}}) - (\rho \tilde{V}\tilde{\mathbf{U}} + \rho_a(\delta \tilde{V})\mathbf{U}_a) = \tilde{\mathbf{F}}\delta t$$
(3.5)

where $\tilde{\mathbf{F}}$ is the buoyancy force acting on the control volume. Using the mass conservation relation, the above momentum equation may be re-written into the more compact form

$$\delta \tilde{\mathbf{m}} = -\rho \tilde{V} \delta \mathbf{U}_a + \tilde{\mathbf{F}} \delta t, \tag{3.6}$$

where $\tilde{\mathbf{m}} = \rho \tilde{V} \tilde{\mathbf{u}}$ is the momentum of the control volume based on the relative velocity. The inertia effect due to density variation is ignored in this derivation. This is the Boussinesq approximation assuming that density of the fluid is uniform but the specific weight is not.

The path and the dilution of the jet in the cross flow are determined by the momentum and buoyancy equations, Equations 3.4 and 3.6, and by the spreading hypothesis, Equation 3.2. Integration of these equations was carried out by a fourth order Runge-Kutta method. The calculations were conducted in two stages, first for the flow in the zone of established flow (see Figure 3.1) and then the flow in the potential core (see Figure 3.2).

3.2 Zone of Established Flow

The procedure for the zone of established flow is straight forward and is described first in this section. The control volume in this case is the element AB, shown in Figure 3.1, which is defined as an element of the turbulent jet produced over a period of one time unit. With this definition, the initial momentum associated with the element is equal to the momentum flux of the jet at the source. As the fluid from the cross flow is entrained into the turbulent jet, the magnitude and the direction of the velocity, $\tilde{\mathbf{U}}$, change and gradually approach the velocity of the cross-flow, \mathbf{U}_a . The change in velocity is determined by the momentum equation, Equation 3.6.

The goal of the numerical integration is to find the path of the motion along the turbulent jet. The vector that defines the position of the dominant eddy depends on time: $\tilde{\mathbf{s}} = \tilde{\mathbf{s}}(t)$. The position of the jet is known at the beginning of the time interval. The position at the subsequent time interval is determined by numerical integration. The increment in position along the path is

$$\delta \tilde{\mathbf{s}} = \tilde{\mathbf{U}} \delta t, \tag{3.7}$$

where δt is the time increment (in the numerical integration). The absolute velocity vector, $\tilde{\mathbf{U}}$, of the dominant eddy is in a direction tangential to the path. The growth

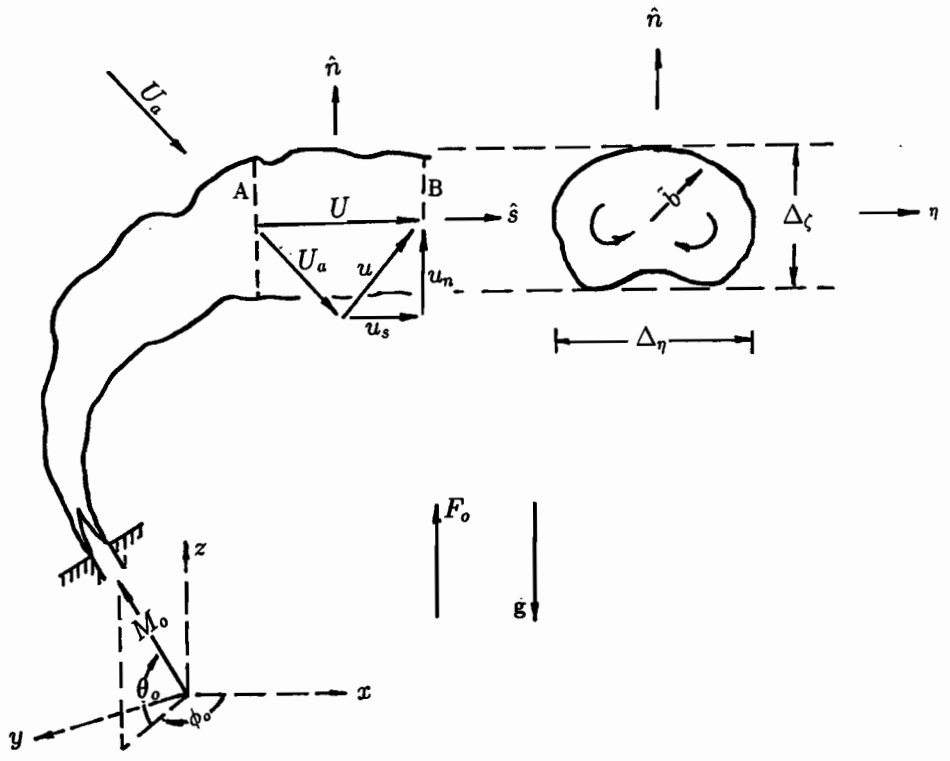


Figure 3.1: Buoyant jets in a non-uniform cross-flow. The control volume, AB, is defined by the movement of the dominant eddies and is produced at the source over a period of one time unit.

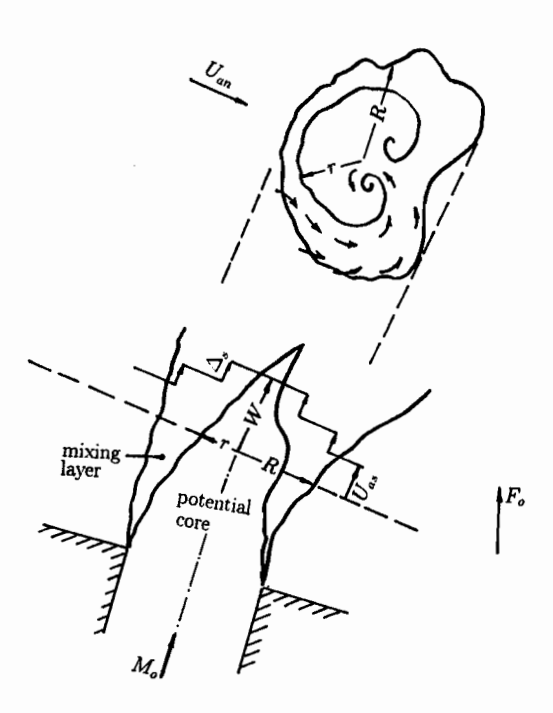


Figure 3.2: The development of the mixing layer in the potential core region near the source.

in the width of the jet is related to the relative velocity,

$$\tilde{\mathbf{u}} = \tilde{\mathbf{U}} - \mathbf{U}_a. \tag{3.8}$$

The relative velocity may be resolved into a component tangential to the path and a component normal to the path as follows:

$$\tilde{\mathbf{u}}_s = \tilde{\mathbf{u}} \cdot \hat{\mathbf{s}} \quad \text{and} \quad \tilde{\mathbf{u}}_n = \tilde{\mathbf{u}} \cdot \hat{\mathbf{n}}. \tag{3.9}$$

The tangential unit vector is

$$\hat{\mathbf{s}} = \frac{\tilde{\mathbf{U}}}{|\tilde{\mathbf{U}}|}.\tag{3.10}$$

The normal unit vector is

$$\hat{\mathbf{n}} = \frac{\tilde{\mathbf{u}}_n}{|\tilde{\mathbf{u}}_n|} = \frac{\tilde{\mathbf{u}} - \tilde{\mathbf{u}}_s}{|\tilde{\mathbf{u}} - \tilde{\mathbf{u}}_s|}.$$
(3.11)

The increment in the width of jet, \tilde{b} , is determined by the spreading hypothesis

$$\delta \tilde{b} = \beta_s |\tilde{\mathbf{u}}_s| \delta t + \beta_n |\tilde{\mathbf{u}}_n| \delta t \tag{3.12}$$

(see Equation 3.2). The increments in buoyancy and momentum are governed by the buoyancy and momentum equations:

$$\delta \tilde{\mathbf{F}} = \tilde{\mathbf{g}} \tilde{V} \delta \rho_a, \tag{3.13}$$

$$\delta \tilde{\mathbf{m}} = -\rho_a \tilde{V} \delta \mathbf{U}_a + \tilde{\mathbf{F}} \delta t \tag{3.14}$$

(see Equations 3.4 and 3.6).

The momentum associated with the control volume, \tilde{V} , has two parts. Part of the momentum comes from the turbulent part of the jet and part of it from the induced irrotational motion surrounding the turbulent jet. The part with the turbulent fluid is $\tilde{V} = \pi \tilde{b}^2 |\mathbf{U}|$. The added-mass effect due to the irrotational motion depends on the orientation of the jet relative to the cross flow. A pair of added-mass coefficients are introduced to account for the relative motion in the tangential and normal directions perpendicular to the path of the cross flow as follows:

$$m_s = \rho(1+k_s)\tilde{V}u_s$$
, and $m_n = \rho(1+k_n)\tilde{V}u_n$ (3.15)

where (m_s, m_n) are the components of the momentum and (u_s, u_n) are the components of the relative velocity in the tangential and normal directions, respectively.

A summary of the equations and procedure used in the calculation of the flow in the zone of the established flow is given in Table 3.1.

3.3 Potential Core

The flow at the source is characterized by a potential core relatively unaffected by the cross flow. A mixing layer develops around the core due to the exchange of momentum between the fluid in the core and the cross flow. The core and the mixing layer is defined by the inner and outer radii, r and R, as shown in Figure 3.2. The inner radius, r, decreases and the outer radius, R, increases with distance, \tilde{s} , from the source. The inner radius reduces to zero at the end of the potential core. The calculation for the flow in the potential core follows a slightly different procedure, the details of which are given below.

The fluid in the core is lighter than the fluid in the cross flow. The increase in velocity due to buoyancy is assumed to be given by the Bernoulli equation:

$$W^2 - g_o'z = W_o^2 (3.16)$$

where W_o and $g'_o = g(\rho_a - \rho)/\rho_a$ are the velocity and the reduced gravity at the source, respectively.

The dominant eddies in the mixing layer move along the shear layer in the tangential direction. The velocity of the eddies is the average of the velocities in the core and the cross flow: $\tilde{U}_c = \frac{1}{2}(W + U_{as})$. In the tangential direction, the difference in velocity across the mixing layer is $\tilde{\Delta}_s = \frac{1}{2}(W - U_{as})$. In normal direction, the difference is $\tilde{\Delta}_n = U_{an}$. The components of the cross flow velocity in tangential and normal directions are U_{as} and U_{an} , respectively. The part of the fluid entrained into the mixing layer due to the tangential shearing is $3_s\tilde{\Delta}_s 2\pi(R+r)$ while the part due to shearing in the normal direction is $\beta_n\tilde{\Delta}_n 2\pi(R+r)$. The total entrained volume divided by the circumference, $2\pi(R+r)$, gives the entrainment velocity $v_e = \beta_s\tilde{\Delta}_s + \tilde{\beta}_n\Delta_n$.

Table 3.1: Summary of Equations in the Zone of Established Flow.

$$\hat{s} = \frac{\tilde{\mathbf{U}}}{|\tilde{\mathbf{U}}|}, \quad \tilde{\mathbf{u}}_s = \mathbf{u} \cdot \hat{\mathbf{s}}, \quad \tilde{\mathbf{u}}_n = \mathbf{u} - \tilde{\mathbf{u}}_s, \quad \hat{\mathbf{n}} = \frac{\tilde{\mathbf{u}}_n}{|\tilde{\mathbf{u}}_n|}$$

$$\delta \rho_a = \frac{\partial \rho_a}{\partial t} \delta t + (\delta \mathbf{s} \cdot \nabla) \rho_a, \ \delta \mathbf{U}_a = \frac{\partial \mathbf{U}_a}{\partial t} \delta t + (\delta \mathbf{s} \cdot \nabla) \mathbf{U_a}$$

$$\delta \tilde{\mathbf{F}} = \mathbf{g} \tilde{V} \delta \rho_a, \ \delta \tilde{\mathbf{m}} = -\rho_a \tilde{V} \delta \mathbf{U}_a + \tilde{\mathbf{F}} \delta t$$

$$\tilde{\mathbf{m}}_n = \tilde{\mathbf{m}} \cdot \hat{\mathbf{n}}, \ \tilde{\mathbf{m}}_s = \tilde{\mathbf{m}} \cdot \hat{\mathbf{s}}$$

$$\tilde{\mathbf{u}}_s = \frac{\tilde{\mathbf{m}}_s}{\rho(1+k_s)V}, \ \tilde{\mathbf{u}}_n = \frac{\tilde{\mathbf{m}}_n}{\rho(1+k_n)V}$$

$$\delta \tilde{b} = \beta_s |\tilde{\mathbf{u}}_s| \delta t + \beta_n |\tilde{\mathbf{u}}_n| \delta t$$

$$\tilde{\mathbf{u}} = \tilde{u}_s \hat{\mathbf{s}} + \tilde{u}_n \hat{\mathbf{n}}, \ \tilde{\mathbf{U}} = \tilde{\mathbf{u}} + \mathbf{U}_a, \ \delta \tilde{\mathbf{s}} = \tilde{\mathbf{U}} \delta t$$

$$\tilde{\mathbf{s}} = \tilde{\mathbf{s}} + \delta \tilde{\mathbf{s}}, \ \tilde{b} = \tilde{b} + \delta \tilde{b}, \ \tilde{\mathbf{F}} = \tilde{\mathbf{F}} + \delta \tilde{\mathbf{F}}, \ \tilde{\mathbf{m}} = \tilde{\mathbf{m}} + \delta \tilde{\mathbf{m}}$$

$$ilde{V}=\pi ilde{b}^2 ilde{U}_s$$

Table 3.2: Summary of Equations in the Potential Core Region.

$$\hat{\mathbf{s}} = \frac{\tilde{\mathbf{U}}}{|\tilde{\mathbf{U}}|}, \ \ \tilde{\mathbf{u}}_s = \tilde{\mathbf{u}} \cdot \hat{\mathbf{s}}, \ \ \tilde{\mathbf{u}}_n = \tilde{\mathbf{u}} - \tilde{\mathbf{u}}_s, \ \ \hat{\mathbf{n}} = \frac{\tilde{\mathbf{u}}_n}{|\tilde{\mathbf{u}}_n|}$$

$$\delta \rho_a = \frac{\partial \rho_a}{\partial t} \delta t + (\delta \tilde{\mathbf{s}} \cdot \nabla) \rho_a, \ \delta \mathbf{U}_a = \frac{\partial \mathbf{U}_a}{\partial t} \delta t + (\delta \tilde{\mathbf{s}} \cdot \nabla) \mathbf{U}_a$$

$$\tilde{Q} = \pi r^2 W + \pi (R^2 - r^2) \tilde{U}_c, \ \mathbf{B} = \pi r^2 W \mathbf{g}_o' + \pi (R^2 - r^2) \tilde{U}_c \frac{\mathbf{g}_o'}{2}$$

$$\delta \tilde{\mathbf{m}} = -\rho_a \tilde{V} \delta \mathbf{U}_a + \tilde{\mathbf{B}} \delta t$$

$$\tilde{m}_{\textit{n}} = \tilde{m} \cdot \hat{n}, \ \tilde{m}_{\textit{s}} = \tilde{m} \cdot \hat{s}, \ U_{\textit{an}} = U_{\textit{a}} \cdot \hat{n}, \ U_{\textit{as}} = U_{\textit{a}} \cdot \hat{s}$$

$$\tilde{\mathbf{u}}_s = \frac{\tilde{\mathbf{m}}_s}{\rho(1+k_s)V}, \ \tilde{\mathbf{u}}_n = \frac{\tilde{\mathbf{m}}_n}{\rho(1+k_n)V}$$

$$\tilde{\mathbf{u}} = \tilde{u}_s \hat{\mathbf{s}} + \tilde{u}_n \hat{\mathbf{n}}, \quad \tilde{\mathbf{U}} = \tilde{\mathbf{u}} + \mathbf{U}_a, \quad \delta \tilde{\mathbf{s}} = \tilde{\mathbf{U}} \delta t$$

$$W^2 = W_o^2 + 2g'z, \ \delta W = \frac{g'_o dz}{W}$$

$$v_e = \beta_s \tilde{\Delta}_s + \beta_n \tilde{\Delta}_n, \quad \tilde{\Delta}_s = \frac{1}{2}(W - U_{as}), \quad \tilde{\Delta}_n = U_{an}, \quad \tilde{U}_c = \frac{1}{2}(W + U_{as})$$

$$\tilde{m}_s = 2\pi \rho r^2 W \tilde{\Delta}_s + \pi \rho (1 + k_s) (R^2 - r^2) \tilde{U}_c \tilde{\Delta}_s$$

$$\delta \tilde{m}_s = f_1 \delta r + f_2, \ \delta r = \frac{\delta \tilde{m}_s - f_2}{f_1}, \ \text{see Equation 3.25}.$$

$$\tilde{U}_c \frac{\delta(R-r)}{\delta s} = v_e, \ \delta s = \frac{\tilde{U}_c}{v_e} \delta(R-r), \ \delta t = \frac{\delta s}{\tilde{U}_s}$$

$$s = s + \delta s$$
, $r = r + \delta r$, $R = R + \delta R$, $W = W + \delta W$

$$\tilde{\mathbf{B}} = \tilde{\mathbf{B}} + \delta \tilde{\mathbf{B}}, \ \tilde{\mathbf{m}} = \tilde{\mathbf{m}} + \delta \tilde{\mathbf{m}}$$

The thickness of the mixing layer, (R-r), is assumed to increase at a rate proportional to the entrainment velocity:

$$\frac{\delta(R-r)}{\delta t} = \tilde{U}_c \frac{\delta(R-r)}{\delta s} = \beta_s \tilde{\Delta}_s + \beta_n \tilde{\Delta}_n. \tag{3.17}$$

The change in momentum follows a similar relation,

$$\delta \tilde{\mathbf{m}} = -\rho \tilde{Q} \delta \mathbf{U}_a + \tilde{\mathbf{B}} \delta t \tag{3.18}$$

(see Equation 3.6), except that the volume flux and the body force terms due to buoyancy now have slightly difference expressions:

$$\tilde{Q} = \pi r^2 W + \pi (R^2 - r^2) \tilde{U}_c, \tag{3.19}$$

$$\tilde{\mathbf{B}} = \pi r^2 W \mathbf{g}' + \pi (R^2 - r^2) \tilde{U}_c \frac{\mathbf{g}'}{2}.$$
 (3.20)

The relative momentum flux, $\tilde{\mathbf{m}}$, can be resolved into s- and n-components as before. The s-component is

$$\tilde{m}_s = 2\rho \pi r^2 W \tilde{\Delta}_s + \rho (1 + k_s) \pi (R^2 - r^2) \tilde{U}_c \Delta_s. \tag{3.21}$$

The calculation for the potential core ends when r=0. The variation δW is determined by the relation,

$$W\delta W - g_o'\delta z = 0, (3.22)$$

which is obtained from the differentiation of Equation 3.16. The variation δr is calculated by the relation,

$$\delta \tilde{m}_s = f_1 \delta r + f_2, \tag{3.23}$$

which is obtained from the differentiation of Equation 3.21. Hence,

$$\delta r = \frac{\delta \tilde{m}_s - f_2}{f_1},\tag{3.24}$$

where

$$f_{1} = 4\pi \rho r W \tilde{\Delta}_{s} + 2\pi \rho (1 + k_{s})(R - r)U_{c} \tilde{\Delta}_{s},$$

$$f_{2} = -\pi \rho [2r^{2}W \delta W + r^{2}W \delta U_{as} - r^{2}U_{as} \delta W]$$

$$-\frac{1}{4}\pi \rho (1 + k_{s})[8RU_{c}\Delta_{s} + (R^{2} - r^{2})(2W \delta W - 2U_{as} \delta U_{as})]. \tag{3.25}$$

The calculation for the development of the mixing layer follows essentially the same procedure as in the zone of established flow. The variation $\delta \tilde{\mathbf{m}}$ is determined by Equation 3.18, the variation δW by Equation 3.22, the variation $\delta (R-r)$ by Equation 3.17, and δr by Equation 3.24. The equations involved in the calculations in the core region are summarized in Table 3.2.

3.4 Source Condition and Model Coefficients

Finally, some details related to the specification of the condition at the source must be specified. As shown in Figure 3.1, the z-axis of the Cartesian coordinate system is defined to be in the upward direction. The gravity force is in the negative z-direction. The initial orientation of the jet is defined by the angles, θ and ϕ , as shown in the figure. The cross flow velocity, \mathbf{U}_a , can be any magnitude and direction and may in fact vary with both time and space. The reduced gravity, g'_o , the discharge, Q_o , and the jet radius, r_o , are specified at the source. Therefore, the source momentum flux, $M_o = \rho W_o Q_o$, and the buoyancy flux, $F_o = \rho_a g'_o Q_o$ are given at the source. In terms of the angle, θ and ϕ , the source velocities are

$$U_{xo} = W_o \cos \theta \cos \phi,$$
 $U_{yo} = W_o \cos \theta \sin \phi,$ $U_{zo} = W_o \sin \theta.$ (3.26)

A computer program was developed to calculate numerical integration of jets in cross flows. Calculation was conducted for a variety of cases with different discharge configurations and orientations of the cross flow. The numerical results for the non-buoyant jets are given in Chapter 4. The results obtained for the buoyant jets, including the effects of density stratification, are presented in Chapter 5. The calculations were primarily conducted to compare results with the data obtained from experimental investigations. The values of the model coefficients are fixed in all the cases computed. The values selected for the coefficients are derived from asymptotic properties of the jets in the limiting cases. For, example, the spreading coefficient

$$\beta_s = 0.17 \tag{3.27}$$

is selected to give the correct behaviour of the model in the limiting case of the free jet. On the other hand, the model coefficient

$$\beta_n = 0.34,\tag{3.28}$$

is selected to obtain correct simulation for the line puffs and line thermals. The added-mass coefficient depends on the orientation of the element relative to the cross flow. The selections are:

$$k_s = 0.18,$$
 (3.29)

for the free jets and plumes, and

$$k_n = 1.00,$$
 (3.30)

for line puffs and line thermals.

Chapter 4

Model Verification for Non-buoyant Jets

Numerical computations were conducted using the integral model for non-buoyant jets and buoyant jets in cross flows. The results obtained for the non-buoyant jets are presented in Chapter 4 and for the buoyant jets in Chapter 5.

The discharge conditions selected for model verification are the same as the conditions of the available experimental data. Table 4.1 lists the experiments for non-buoyant jets in cross flows. The results of the calculations conducted for jets discharged in a direction normal to the cross flow are compared with the available experimental data obtained by Chassaing et al. (1974), Pratte and Baines (1967), Fan (1967) and Wright (1977). The results obtained for jets at an oblique angle to the cross flow are compared with the data obtained by Chu (1985).

4.1 Jet Normal to the Cross-flow

The schematic diagram in Figure 4.1 shows the jet normal to the cross flow. The initial development of the jet in the potential core region is shown in Figure 4.2 (a), (b) and (c) for exit-to-crossflow velocity ratios $W/U_{a\infty} = 2.37$, 3.95 and 6.35, respectively. The results obtained from the integral calculations are generally in agreement with the experimental data obtained by Chassaing *et al.* (1974) provided that the momentum thickness of the cross flow is $\theta/d_o = 1$. In the calculation the velocity profile of the boundary layer was assumed to follow the one-seventh power law. The momentum thickness, $\theta \simeq d_o$ was in this case selected to account for the effect of horse shoe vortex that forms upstream of the jet in the cross flow.

Using the same momentum thickness of the cross flow, namely $\theta/d_o = 1$, the

Jet cases	Data	Section No.
Jet Normal to the Cross-flow	Chassaing et al. (1974) Pratte and Baines (1967) Fan (1967) Wright (1977)	4.1
Jet Oblique to the Cross-flow	Chu (1985)	4.2

Table 4.1: Summary of available experiments and flow conditions for non-buoyant jets in cross flow.

length of the potential core, ℓ_p , is computed for exit-to-crossflow velocity ratios varying from $W_o/U_a=2\simeq 50$. The results, shown in Figure 4.3 are in general agreement with the experimental data obtained by Pratte and Baines (1967).

The model predictions for the path of the turbulent jets in the far field region are given in Figure 4.4. The prediction normalized by the momentum length scale $\ell_m = \sqrt{M_o/U^2}$ are compared with the experimental data of Pratte and Baines (1967). The pair of curves in each of the figures denotes the upper and lower boundaries of the jets. The data of Pratte and Baines were obtained by flow visualization of the turbulent smoke jets in a wind tunnel. The data for the width of the jets, $\Delta \eta$, and for the thickness, $\Delta \zeta$, of the jets are given in Figure 4.6 and Figure 4.5, respectively. The definition for $\Delta \eta$ and $\Delta \zeta$ are provided in the sketch in Figure 4.1. Agreement of the data of the model and the experiment is obtained if values $\Delta \eta/\tilde{b}=1.11$ and $\Delta \zeta/\tilde{b}=0.90$ are selected.

The present formulation is based on the top-hat velocity profile. Hence, the average dilution is determined by the model. Figure 4.8 shows the minimum dilution ratio obtained on the centre plane of symmetry by Wright (1977) and Fan (1967). The model predictions, nevertheless, follow the trend of the experimental data. Best

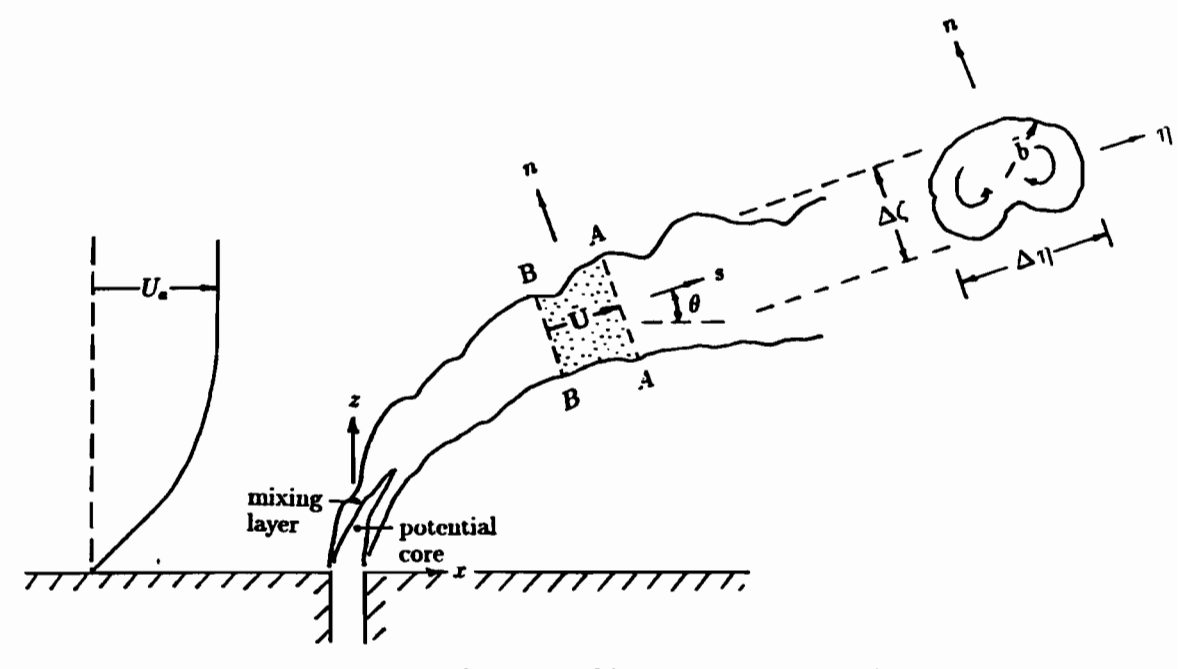


Figure 4.1: A schematic diagram of buoyant jets normal to cross flow.

fit to the experimental data is obtained by selecting $\delta_v/\tilde{b}=0.62$ and $S_c/\overline{S}=0.85$; δ_v is the half-width and S_c is the minimum dilution of the concentration profile on the centre plane of the symmetry. The average dilution ratio is $\overline{S}=\overline{Q}/Q_o$, where Q is given by Equation 3.19 in the potential core and by $Q=\tilde{V}=\pi\tilde{b}^2\tilde{U}_s$ in the established flow.

The model predictions for the half-width and the centre-line dilution ratios of the non-buoyant jets are compared with only some of the experimental data of Fan (1967) in Figure 4.7. The jets in Fan's experiment were buoyant jets produced by the discharge of brine into the cross flow. However, the buoyancy effect is negligible in these tests. The densimetric Froude number Fr = 40 is selected for comparison with the non-buoyant model predictions in Figure 4.7.

The average dilution obtained from the model, multiplied by the factor 0.85, is compared with the data of Fan (1967) in Figure 4.7. The data of Wright (1977) in Figure 4.8 also support the selection $S_c/\overline{S} = 0.85$.

4.2 Oblique Jets in Cross-flows

The oblique jet is one of the most complex configurations of turbulent jets in cross-flows. The jet is produced in the laboratory by discharging at an angle to the cross flow. The model predictions for the oblique jets are compared with the experimental data of Chu (1985) in Figure 4.9.

The experiment by Chu (1985) was conducted in a flume 30 cm wide, 45 cm deep and 900 cm long. The injection pipe was 80 cm long and 1.42 cm in diameter. In the experiment, tests with oblique angles of θ_o equal to 45, 67.5, 90, 112.5 and 135 degrees and exit-to-cross velocity ratios of 2, 4, 6, 8 and 10 were performed. Ambient velocity was 10.1 cm/s and the Reynolds numbers, based on jet exit velocity, were 3000 to 14000. The trajectories of oblique jets in cross flow are shown in Figure 4.9.

The model predictions follow closely the experimental data for almost the entire range of jet inclination ranging from 0 to 135° and exit-to-cross flow velocity ratios from $2 \simeq 10$. The agreement of the oblique jets data with the model predictions is significant. This is the first clear indication that the integral model is capable of handling very complex discharge configurations.

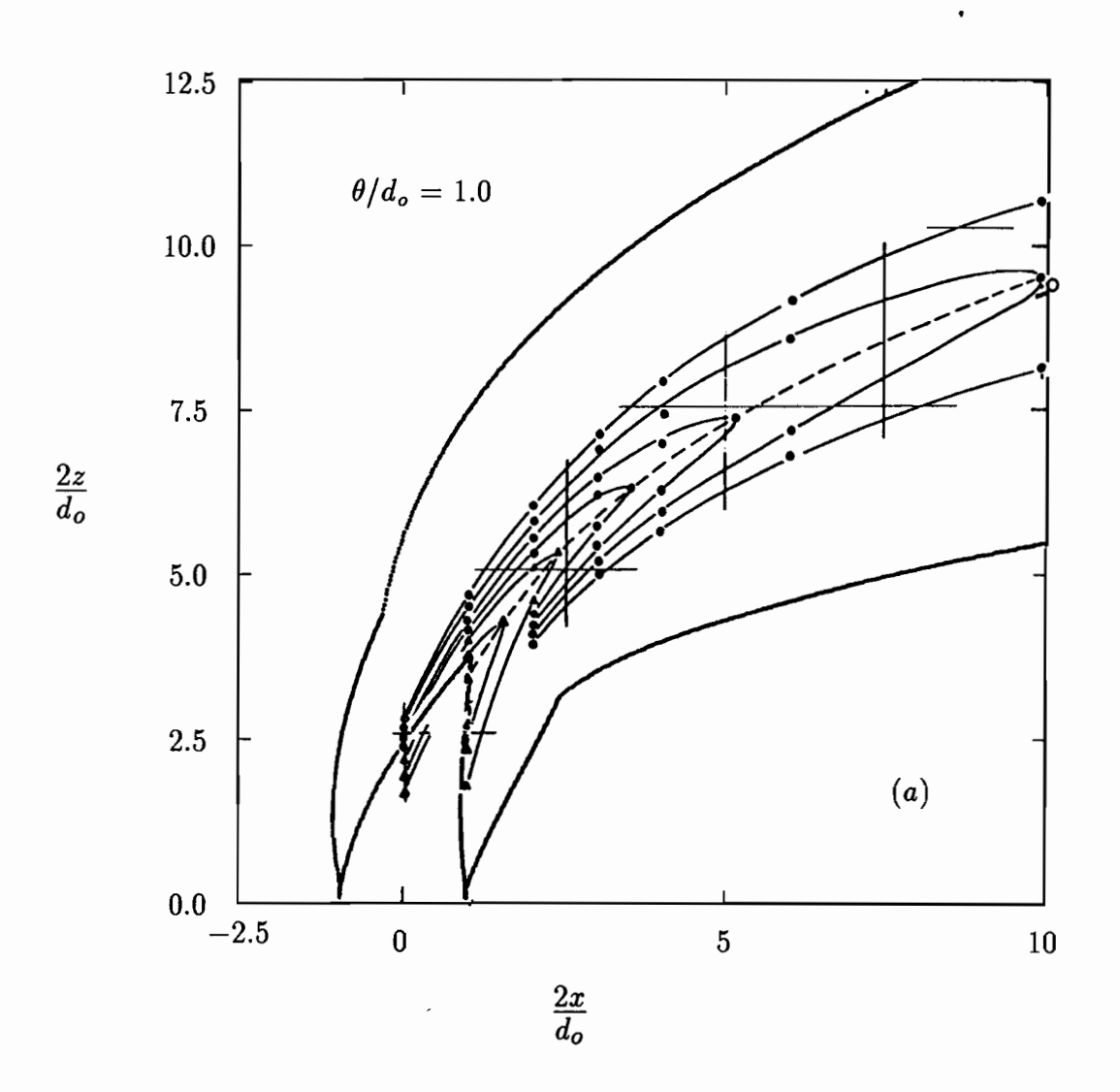


Figure 4.2: The development of the jet in the near field region; (a) $W_o/U_{a\infty}=2.37$, (b) $W_o/U_{a\infty}=3.95$, (c) $W_o/U_{a\infty}=6.35$. The contours of constant velocity in (a), (b) and (c) are reproduced from Chassaing *et al.* (1974). The dots indicates the locations where the velocity are measured by hot-wire anemometry.

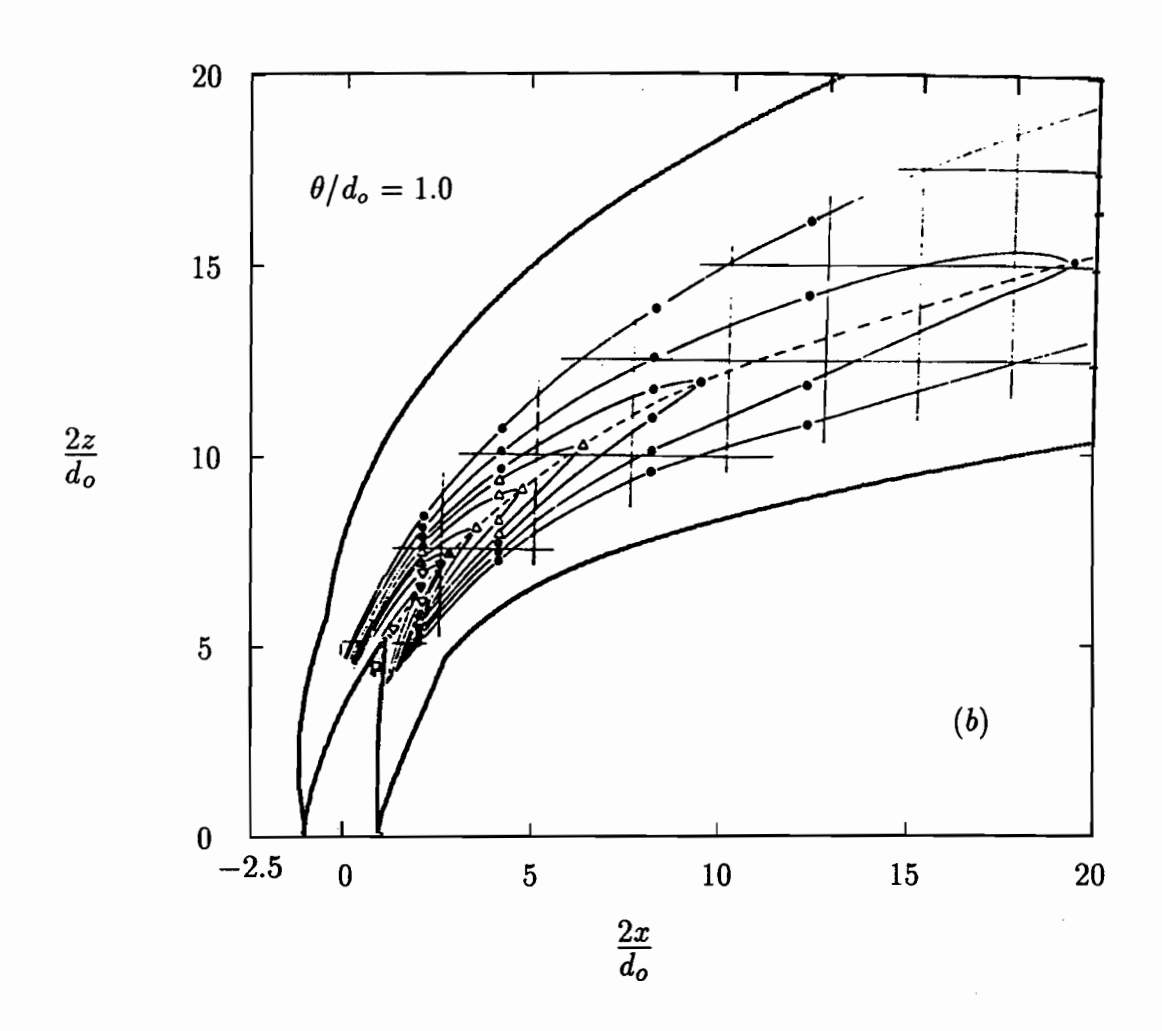


Figure 4.2: Contd.

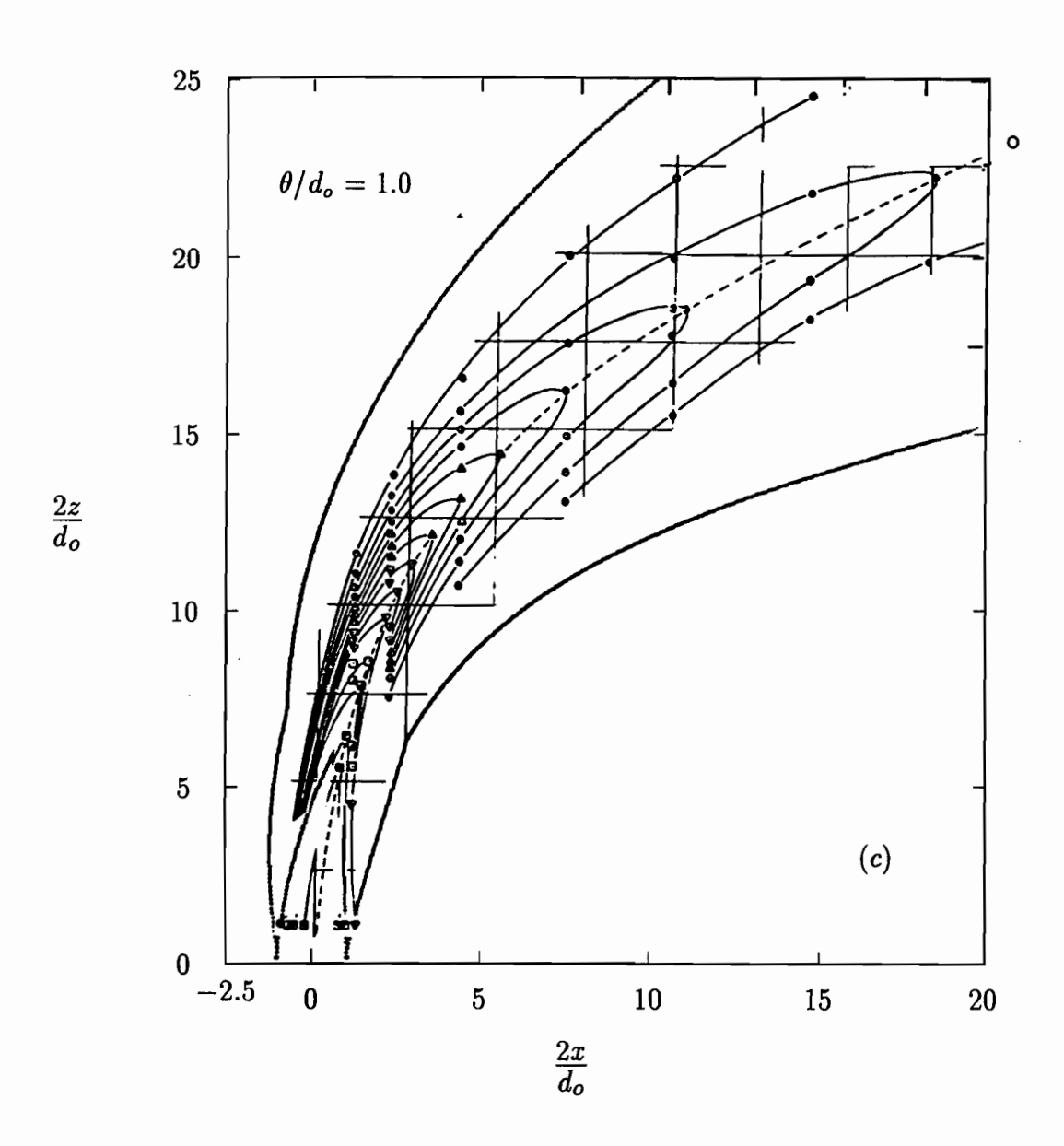


Figure 4.2: Contd.

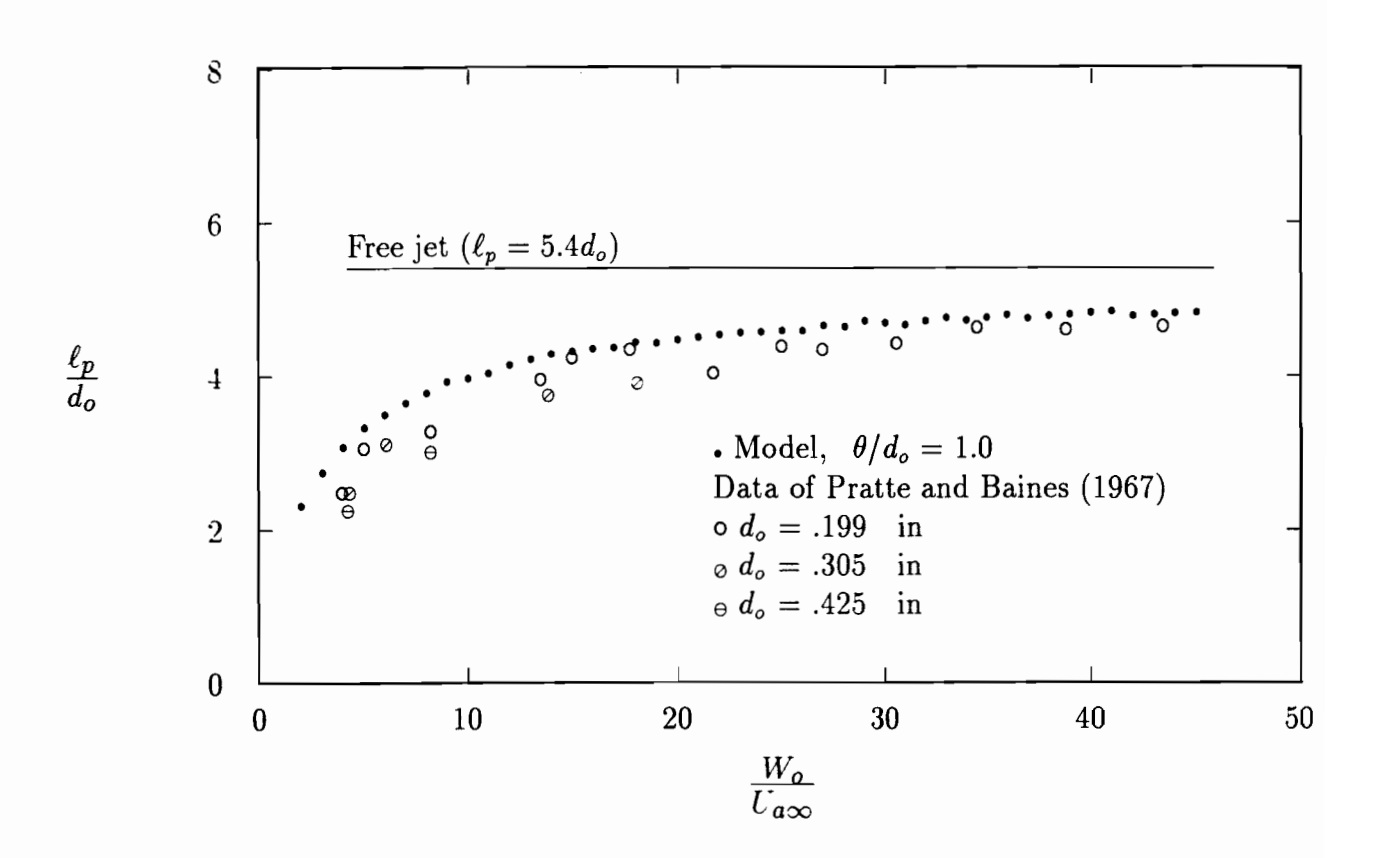


Figure 4.3: Length of the potential core in cross flow; data are obtained by Pratte and Baines (1967).

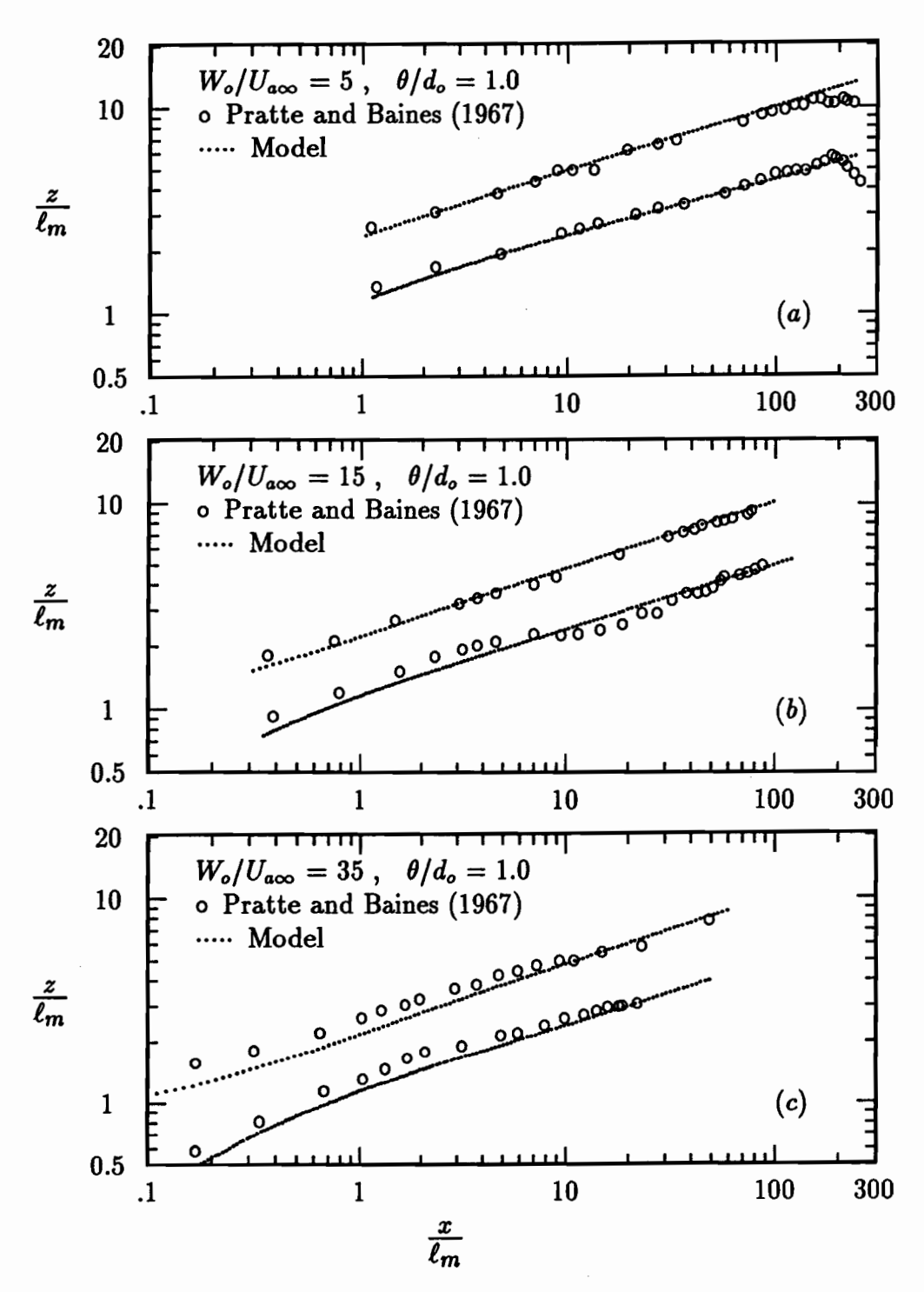


Figure 4.4: The development of the jet in the far field region; (a) $W_o/U_{a\infty}=5$, (b) $W_o/U_{a\infty}=15$ and (c) $W_o/U_{a\infty}=35$. The pair of curves in each figure denote the upper and lower boundaries of the turbulent jet. The experimental data of Pratte and Baines (1967) were obtained by flow visualization of smoke jets in a wind tunnel.

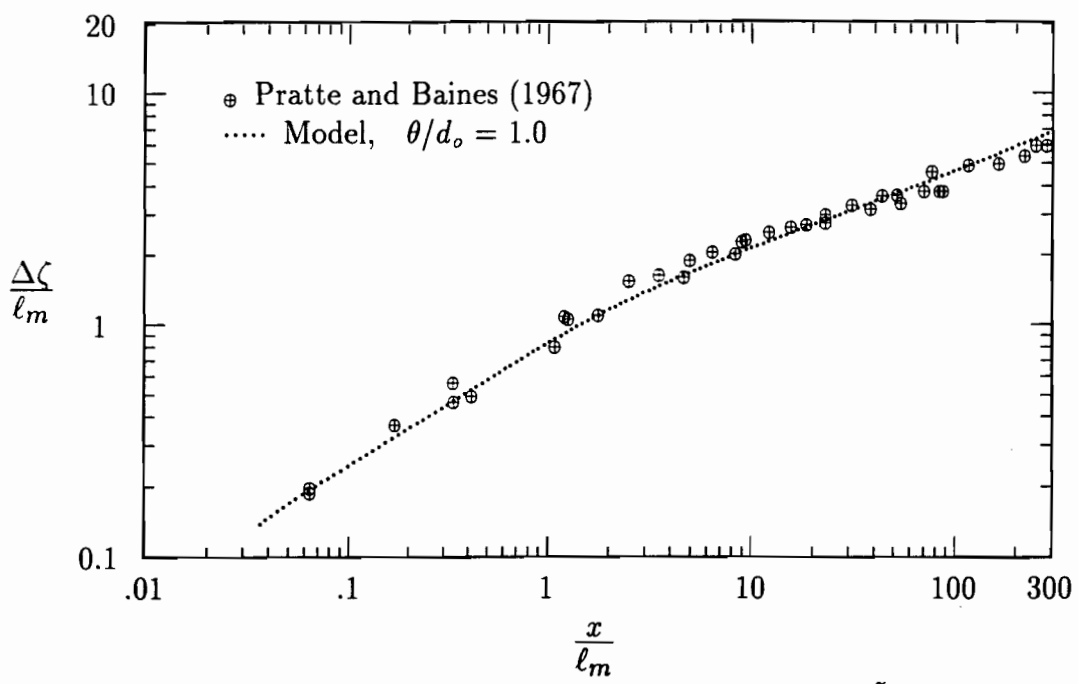


Figure 4.5: Thickness, $\Delta \zeta$, of jets in cross flow; $\Delta \zeta/\tilde{b}=0.90$.

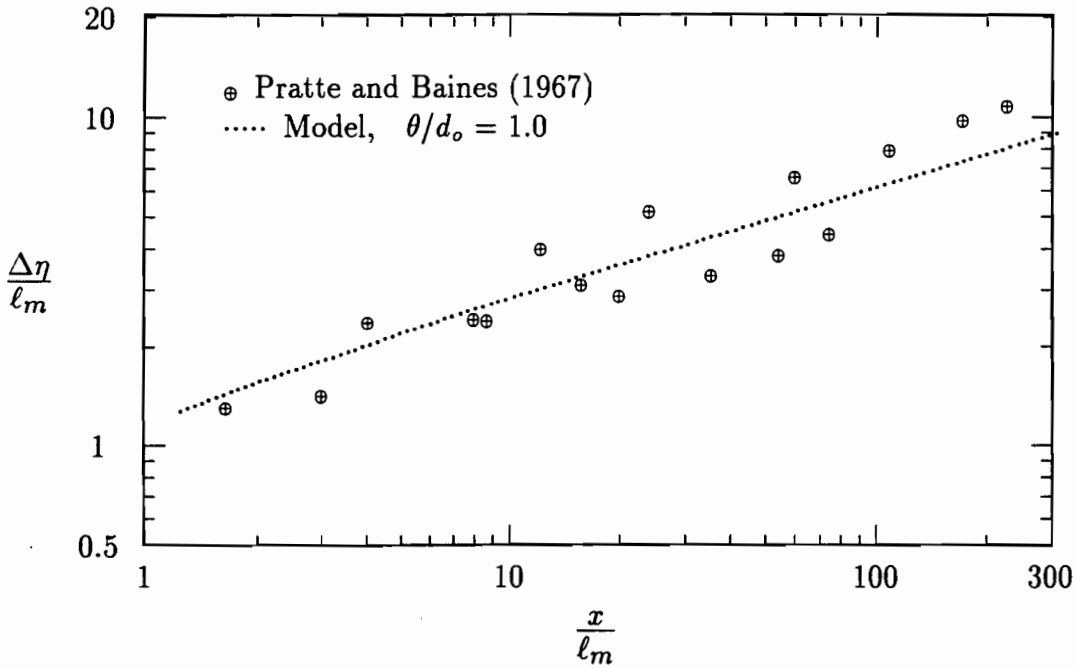


Figure 4.6: Width, $\Delta \eta$, of jets in cross flow; $\Delta \eta/\tilde{b}=1.11$.

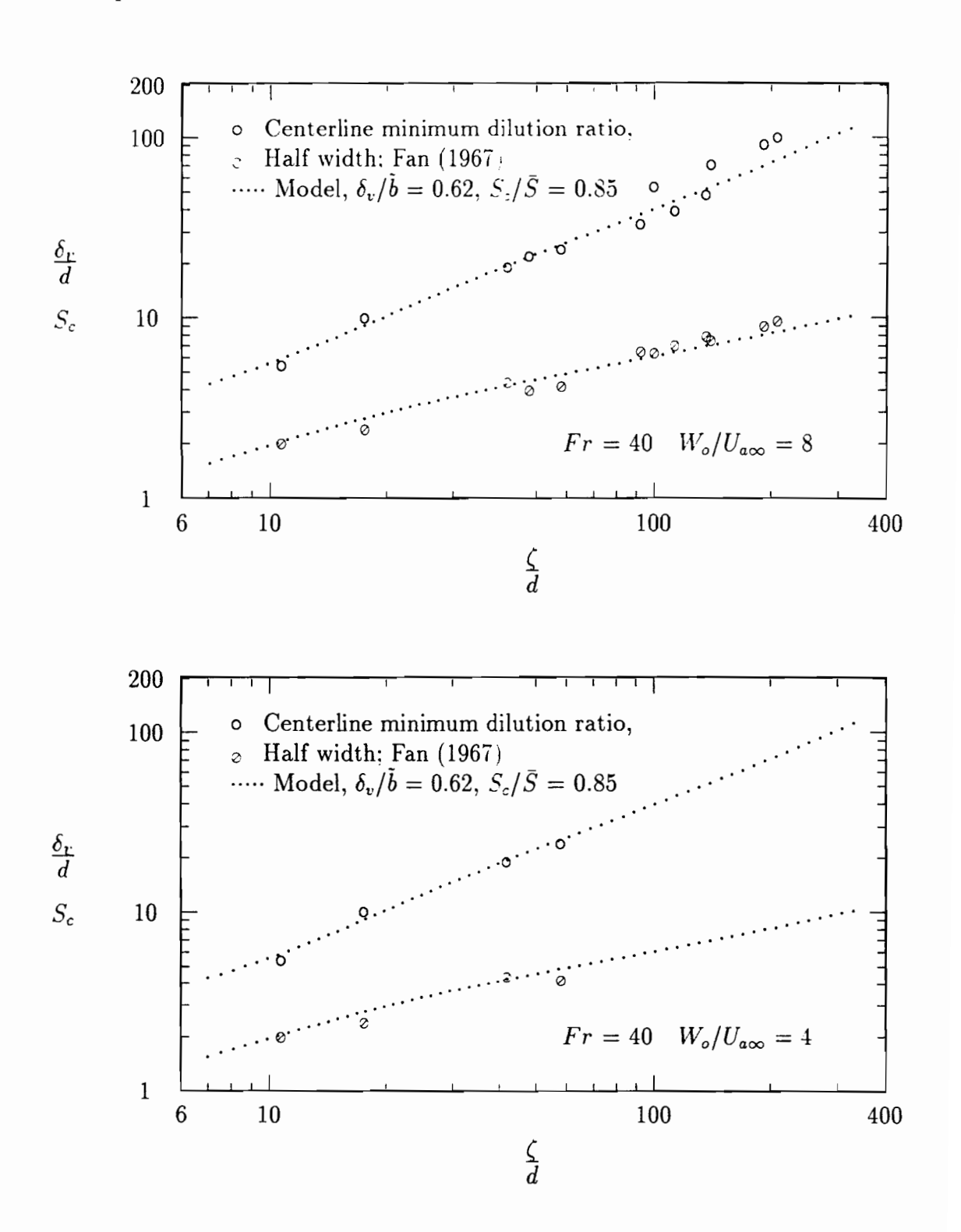


Figure 4.7: comparison of observed and model predictions for the half-widths and the center-line dilution ratios of non-buoyant jets in cross flow.

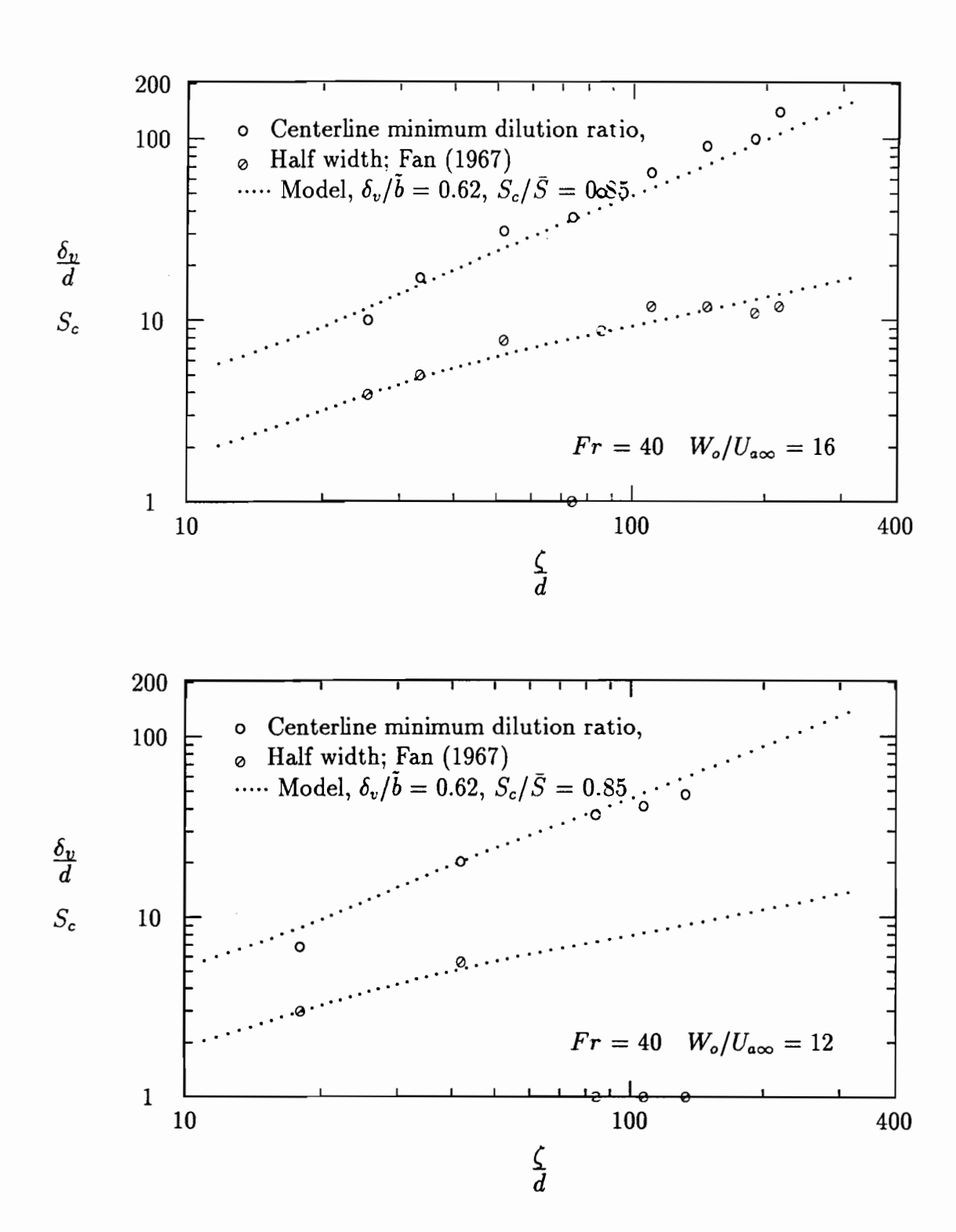


Figure 4.7: Contd.

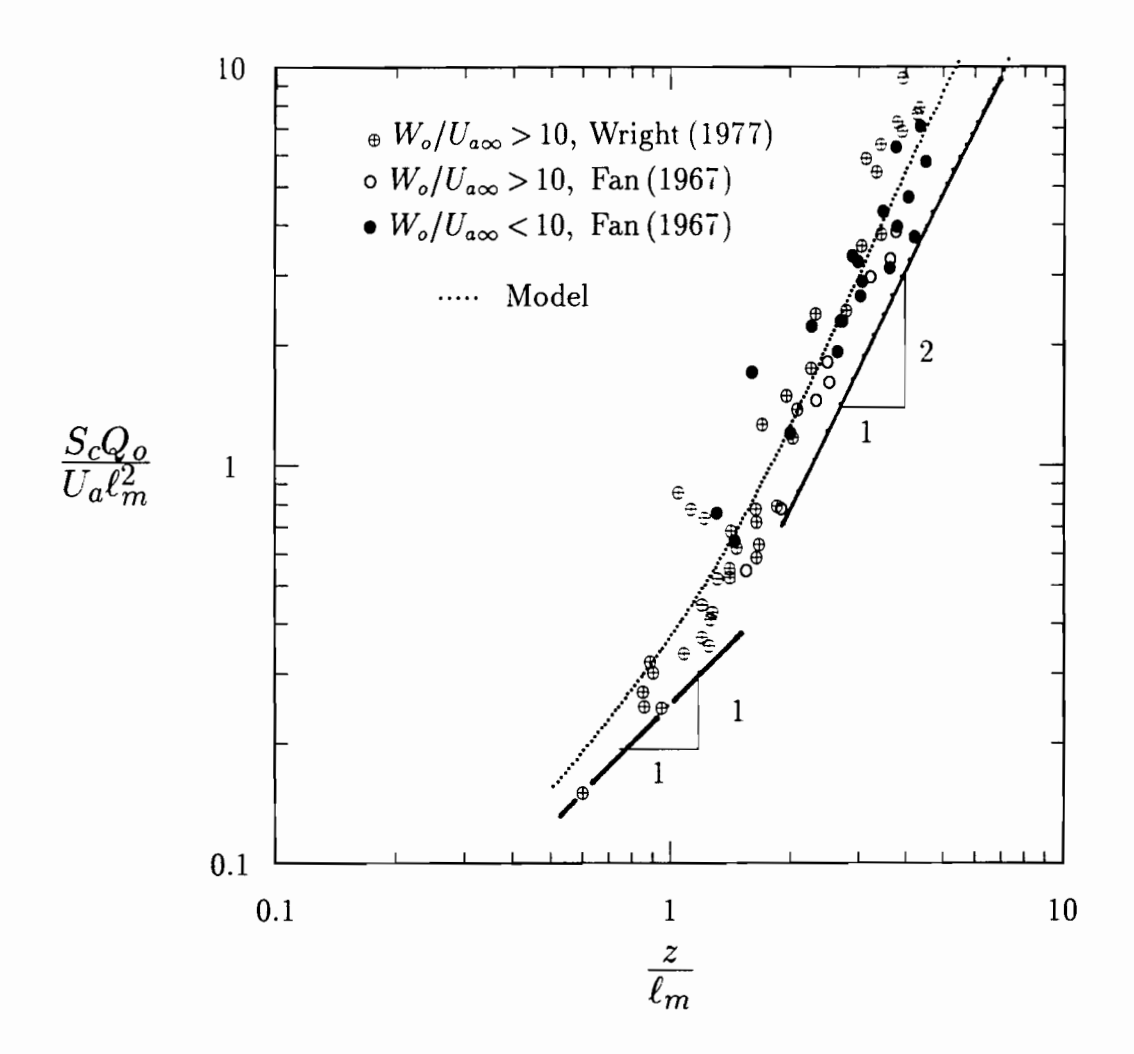


Figure 4.8: Jet dilution as a function of vertical elevation; the momentum length scale is $\ell_m = (M_o/U_a^2)^{\frac{1}{2}}$. S_c is the minimum dilution ratio obtained from the concentration profile on the plane of symmetry. The model prediction is the average value multiplied by a factor of 0.85, i.e., $S_c = 0.85\overline{S}$.

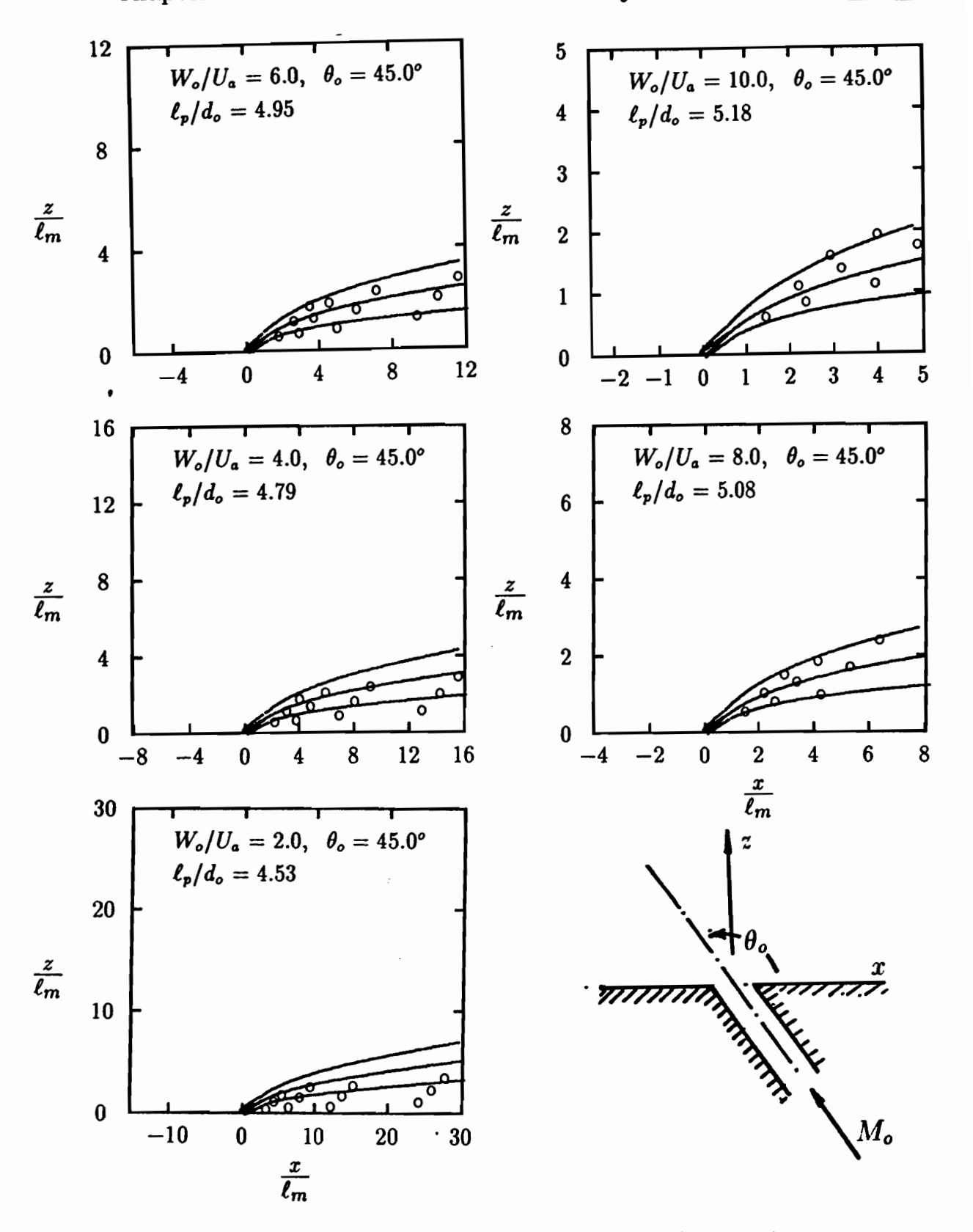


Figure 4.9: Comparison between the model prediction (solid line) and experimental data (denoted by symbol o) in the oblique jets in cross flow.

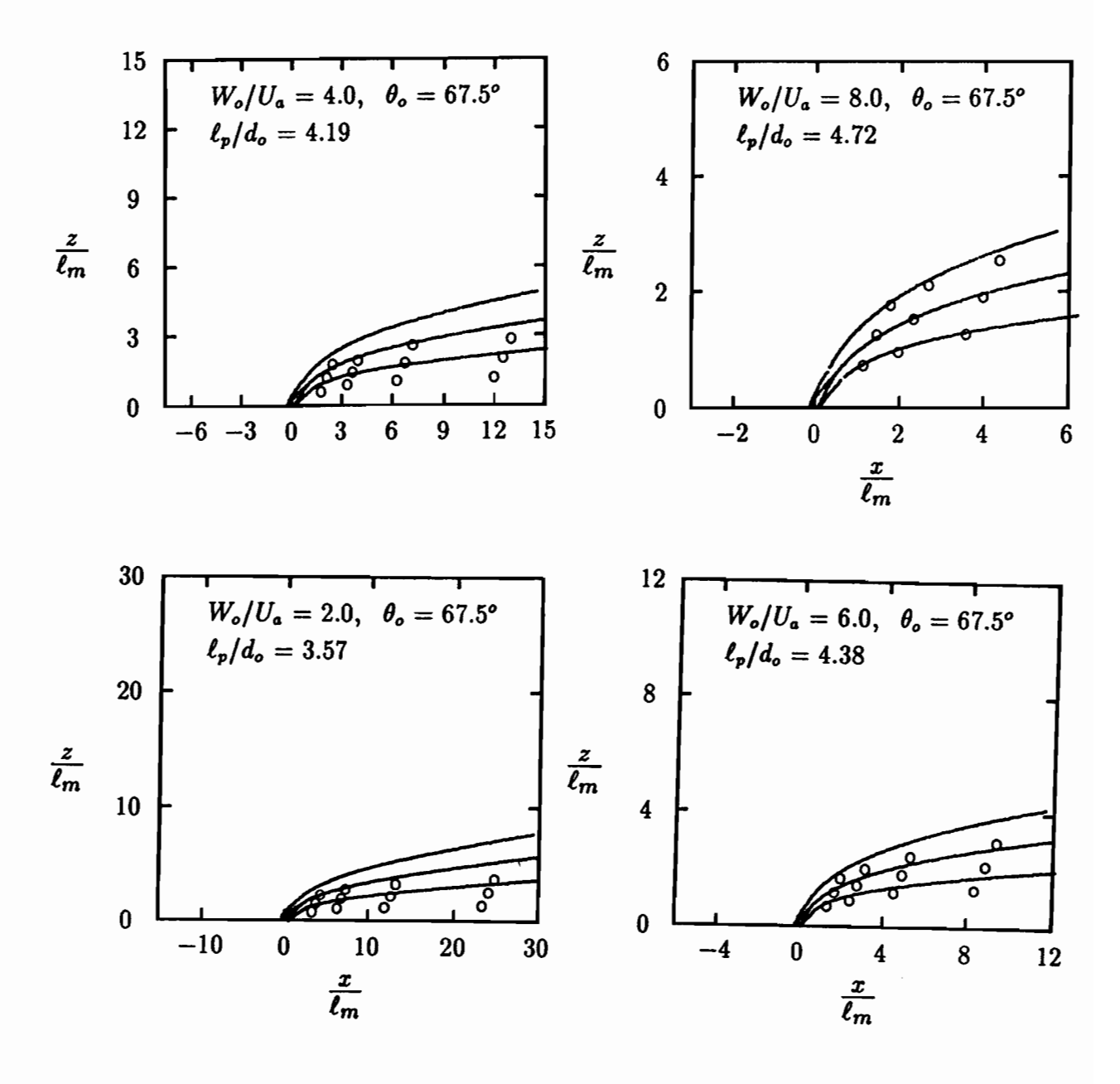


Figure 4.9: Contd

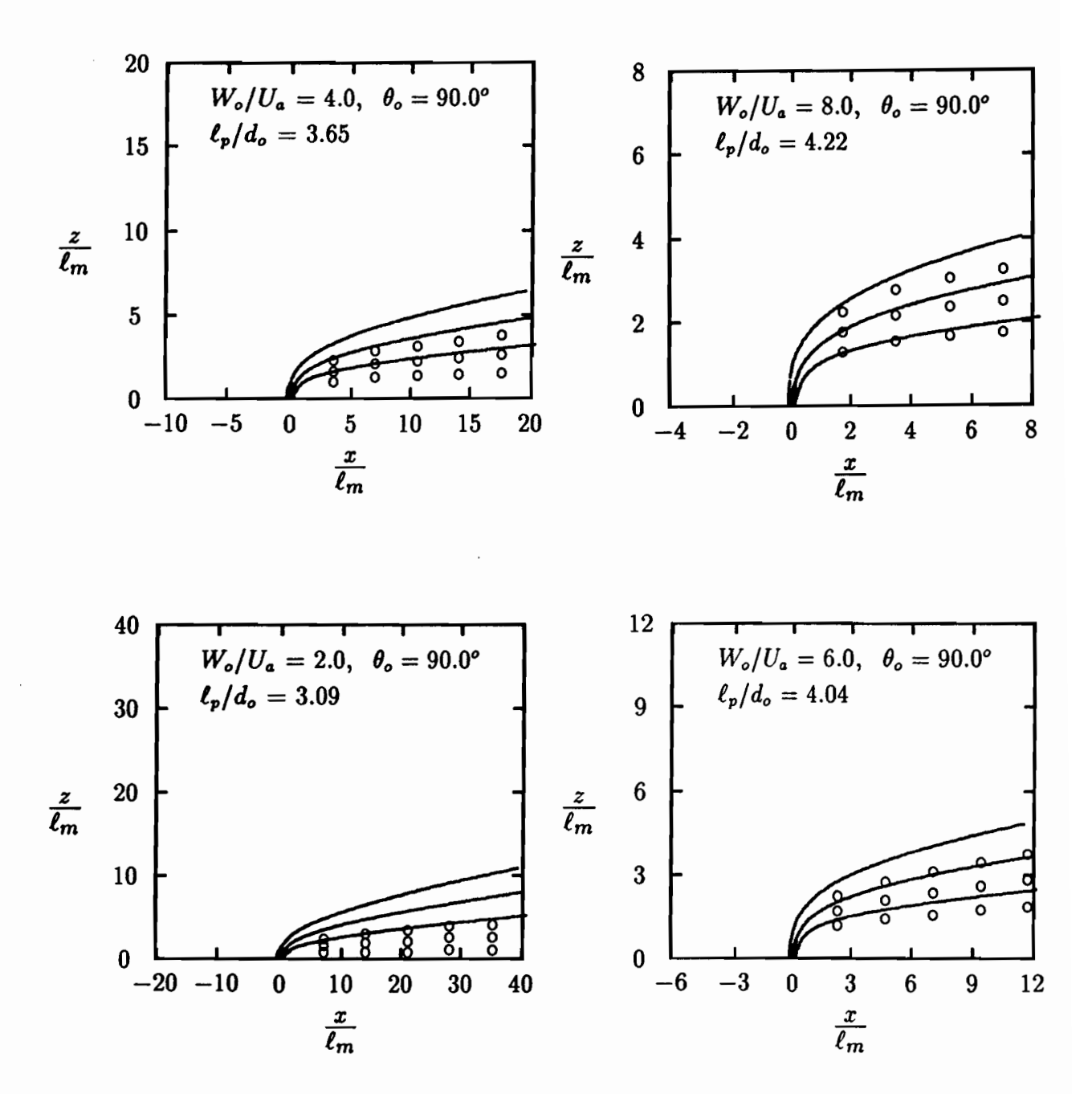


Figure 4.9: Contd

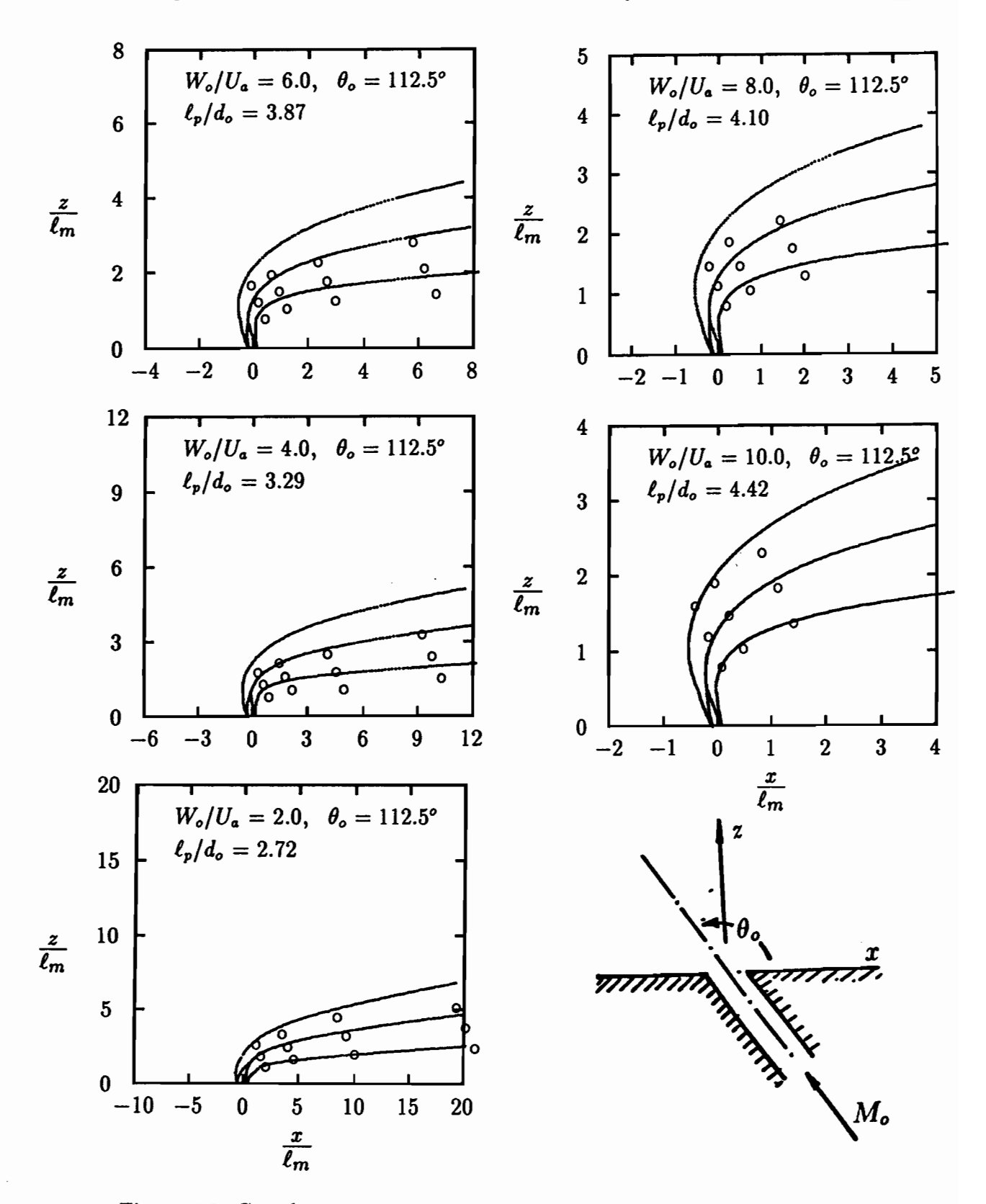


Figure 4.9: Contd

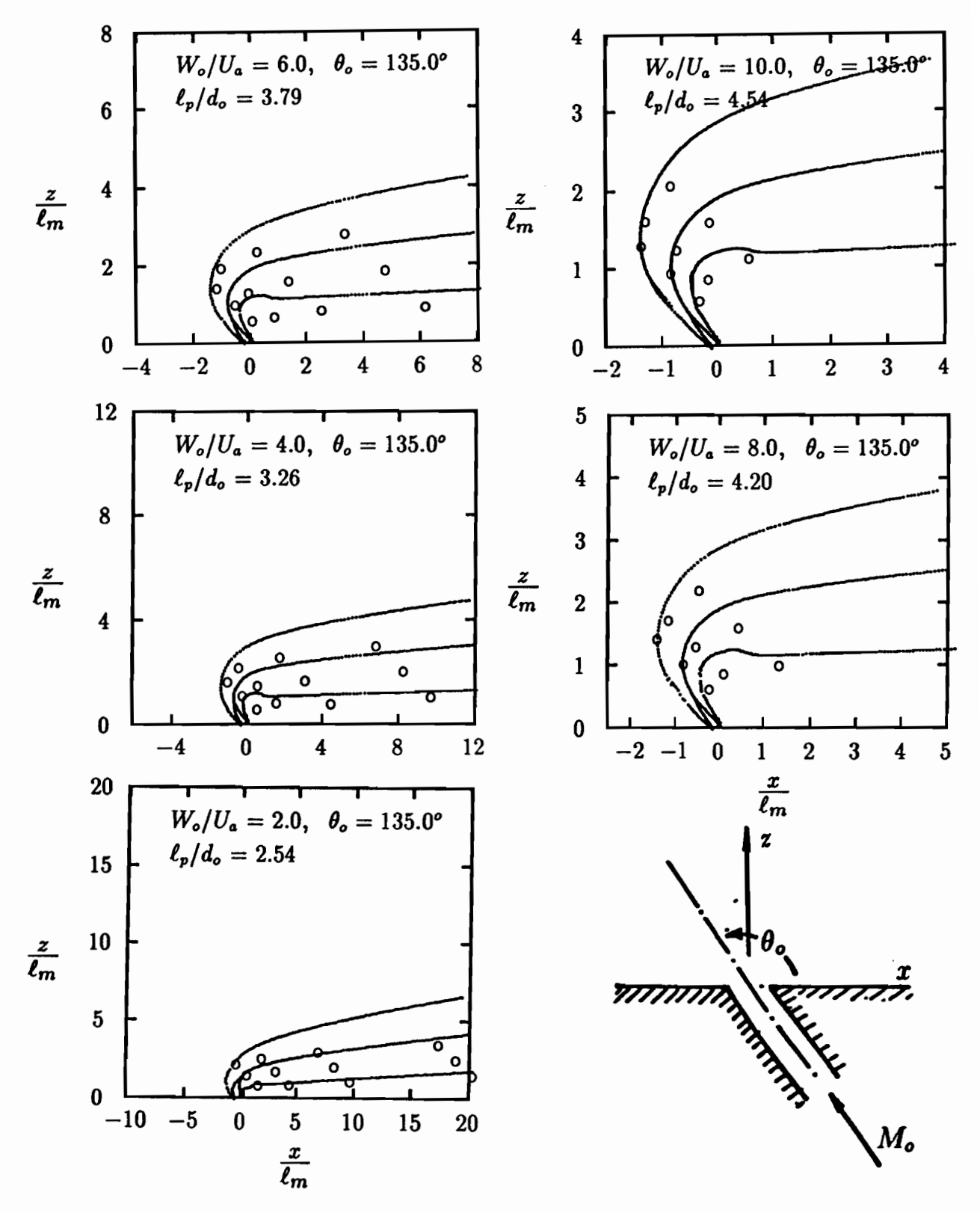


Figure 4.9: Contd

Chapter 5

Model Verification for Buoyant Jets

The calculation of non-buoyant jets, presented in the previous chapter, demonstrated the ability of the integral model to handle complex discharge conditions and particularly the validity of the model in the potential core region near the source. The inclusion of the buoyancy effect leads to even more complex flow geometry. A buoyant jet in a cross flow generally follows a three-dimensional trajectory. The momentum of the buoyant jet may increase or decrease, depending on the direction of the buoyancy force relative to the surrounding fluid. The buoyancy effect is examined in this chapter for five flow cases and compared with available data. Table 5.1 lists the cases under consideration. The cases examined are (a) buoyant jets in a stagnant environment (Fan, 1967), (b) buoyant jets normal to the cross flow (Fan, 1967), (c) buoyant jets with three-dimensional trajectories (Chu, 1975; Ayoub, 1971), (d) negative buoyant jets (Zeitoun et al, 1970; Baines et al., 1990; Fan, 1967, and Wright, 1977), and (e) buoyant jets in a stratified environment (Fan, 1967; Wright, 1977; and Briggs, 1969).

5.1 Buoyant Jets in Stagnant Environment

In a series of experiments conducted by Fan (1967), brine solution was discharged in a horizontal direction in a tank of stagnant water. The tank dimension of his experiments was 226 cm long, 107 cm wide and 61 cm deep. The path of the buoyant jets, as shown in Figure 5.1, depends on the relative effect between source momentum and buoyancy. The measurement of this relative effect is the densimetric Froude

Buoyant Jet cases	Data	Section No.
Buoyant Jets in Stagnant Fluid	Fan (1967)	5.1
Buoyant Jet Normal the Cross-flow	Fan (1967)	4.1 5.2
Buoyant Jets With 3D Trajectories	Chu (1975) Ayoub (1971)	5.3
Negative Buoyant Jets	Zeitoun et al. (1970) Baines et al. (1990) Fan (1967) Wright (1977)	5.4
Buoyant Jets in Density Stratified Flow	Fan (1967) Wright (1977) Briggs (1969)	5.5

Table 5.1: Summary of available experiments and flow conditions for buoyant jets.

number

$$Fr = \frac{W_o}{\sqrt{g_o'd_o}} \tag{5.1}$$

where W_o = velocity of the jet, $g'_o = g(\rho_o - \rho_a)/\rho_a$ = reduced gravity, and d_o = diameter of the discharge at the source; the subscript 'o' denotes the condition at the source. The model predictions are compared with Fan's experimental data in Figure 5.1 for source densimetric Froude numbers varying from Fr = 10 to 130. The agreement of the model prediction with the experimental data again validated not only the integral model but also the selection of the model coefficients as specified in Equations 3.27, 3.28, 3.29, and 3.30 ($\beta_s = 0.17$, $\beta_n = 0.34$, $k_s = 0.17$. $k_n = 1$).

5.2 Buoyant Jets Normal to the Cross-flow

Buoyant jets discharged in a direction perpendicular to the velocity of the cross flow are computed for a range of exit-to-crossflow velocity ratios $W_o/U_a=4$ to 16, and densimetric Froude numbers Fr=10 to 80. The jets are initially in the z-direction while the cross flow is in the x-direction. The model predictions are compared with the experimental data in Figure 5.2 and Figure 5.3. Figure 5.2 shows the jets trajectory and Figure 5.3 the half-width and the minimum dilution ratio. In Figure 5.7, the half-width δ_v is normalized by ℓ_s . Both the half-width, δ_v , and the minimum dilution ratio, S_c , are obtained based on the concentration measurement at the centre plane of symmetry. The integral model gives the visual width of the top-hat profile, \tilde{b} , and the average dilution, \overline{S} . For comparison, the ratios of $\delta_v/\tilde{b}=0.62$ and $S_c/\overline{S}=0.85$ are selected to fit the experimental data.

The experimental data by Fan (1967), is most accurate. His experiments were conducted in a 110-cm wide, 61-cm deep and 40-m long flume. These width and the depth of the flume are large for this type of experiment. However, the data were still affected by the bottom and side walls of the tanks similar to the situation with the line thermal experiments discussed in Chapter 2. The present calculations were obtained based on the selection of a spreading coefficient $\beta_n = 0.34$. This value is believed

to have include the overturning and bifurcation effects mentioned in Chapter 3. In Figure 5.4, the experimental data of Fan (1967) and the field data of Lee and Neville Jones (1987) are normalized by the buoyant length scale. $\ell_b = F_o/U^3$. Both set of the data are in agreement with the model prediction using the coefficient $\beta_n = 0.34$.

The experimental data of Fan and others (Chu and Goldberg, 1974; Chu, 1979; Wright, 1977) have been analyzed by a number of different methods. One procedure including the effect of the source momentum is to introduce length and time scale based on the momentum per unit length, M_o/U , and the buoyancy force per unit length, F_o/U , of the line element as follows:

$$\ell_s = (\frac{M_o}{\rho U})^{\frac{2}{3}} (\frac{F_o}{\rho U})^{-\frac{1}{3}} = (\frac{M_o^2}{\rho F_o U})^{\frac{1}{3}}.$$
 (5.2)

The time scale is

$$t_s = (\frac{M_o}{U})(\frac{F_o}{U})^{-1} = \frac{M_o}{F_o}.$$
 (5.3)

In Figures 5.6, 5.5 and 5.6, the experimental data are normalized using these length and time scales. Both the diluation data and the path of the buoyant jets collapse onto the curves of the model predictions. The dilution increases with distance from the source follows approximately a quadratic power law. The initial development of the path follows a one-third power law and then two-third power law in the far field. These asymptotic behaviours are consistent with the dimensional analysis discussed in Chapter 1.

5.3 Negative Buoyant Jets

Further testing of the integral model was made by conducting calculations for the negative buoyant jets. In this case the source fluid is heavier than the surrounding fluid and is initially directed in an upward direction against the gravity. This negative buoyant jet, sometimes referred as a dense plume, rises to a maximum height and then falls back on the jet. If the discharge is at an angle slightly deviated from the vertical, the falling-back fluid will not re-entrain into the rise jet. Under this condition, the integral model is applicable.

The experimental data obtained by Zeitoun et al. (1970) and Baines et al. (1990) for the maximum rises of the dense plume are compared with the model predictions in Figures 5.8 and 5.9. The agreement of the model prediction with the data of Baines et al. (1990) is quite good, but not so good with the data of Zeitoun (1970). The re-entrainment of the falling fluid may have had an influence on the dense plumes of Zeitoun. The effect of re-entrainment could be included in the integral model but that has not been implemented in the current calculation.

5.4 Buoyant Jets With Three Dimensional Trajectories

Buoyant jets with three-dimensional trajectories can be produced by discharging the buoyant fluid in a horizontal direction perpendicular to the cross flow. Experiments with this arrangement were conducted by Chu (1975) and Ayoub (1971). The model predictions for a series of tests with a wide range of exit-to-crossflow velocity ratios and densimetric Froude numbers are compared with the experimental data of the same conditions in Figure 5.10 and Figure 5.11. The jet trajectories on the (x, y) plane and the (x, z) plane are provided in the figures. In the experiments, brine solution was discharged in a horizontal direction. The jets at the source were in the y-direction, the buoyant force in the z-direction and the cross flow in the x-direction. The exit-to-crossflow velocity ratios varied from 2 to 8 in Chu's experiments and from 5 to 20 in Ayoub's experiment. The densimetric Froude number varied from 1.4 to 12.4 in Chu's experiments and from 15 to 90 in Ayoub's experiments.

The agreement of the model predictions with both sets of experimental data is quite good. The results confirm again the ability of the model to handle flows with complex discharge configurations.

5.5 Buoyant Jets in Fluids With Stratification

Perhaps the most complex of all discharge configurations is the release of buoyant fluid in a stratified fluid. In a stratified environment, the buoyancy flux of the discharge changes continuously with elevation. In a stable stratified environment, the buoyancy flux becomes zero as the density of the fluid in the jet reduces to the same as its surrounding fluid. The fluid in the buoyant jet, or plume, then oscillates about this equilibrium level of zero buoyancy. The photograph and the sketch in Figure 5.12 show how the plume rises and then oscillates about its equilibrium level in a stably stratified atmosphere.

The parameter for a stable density stratification is the Brunt - Väisälä frequency.

$$N = \left[-\frac{g}{\rho_a} \frac{d\rho_a}{dz} \right]^{\frac{1}{2}},\tag{5.4}$$

where $d\rho_a/dz$ is the density gradient in the vertical direction. The period of oscillation, $2\pi/N$, varies from a few minuets in the atmosphere to a few hours in deep oceans. N is constant in a linear stratification. The variation of the buoyancy flux is related to the Brunt-Väisälä frequency and the volume flux of the jet

$$\frac{dF}{dz} = -N^2 \tilde{Q}. ag{5.5}$$

Calculations using the integral model have been conducted in a stagnant fluid and a moving cross flow with stable density stratification. The results of the stagnant cases are compared with the experimental data of Fan (1967) in Figure 5.13. The results for the cross-flow case are compared with the data of Wright (1977) in Figure 5.14. The maximum rises were determined for a range of linear stratifications and are compared with the field and laboratory data collected by Briggs (1969) in Figure 5.15. In all cases, the agreement between model predictions and experimental data is quite acceptable.

5.6 Summary

The model simulations for the various jets and plumes in stagnant fluid and cross flows, both with and without density stratification were conducted using the same set of model coefficients ($\beta_s = 0.17$, $\beta_n = 0.34$, $k_s = 0.18$, $k_n = 1$). The momentum thickness of the cross flow in all of the simulations presented in Chapters 4 and 5 are specified to be one jet diameter at the source. All simulations were made using the same computer program. The excellent agreement between model predictions and experimental data has validated the model and the selection of the model coefficients. It has also shown that the computer program is sufficiently versatile for routine engineering calculations.

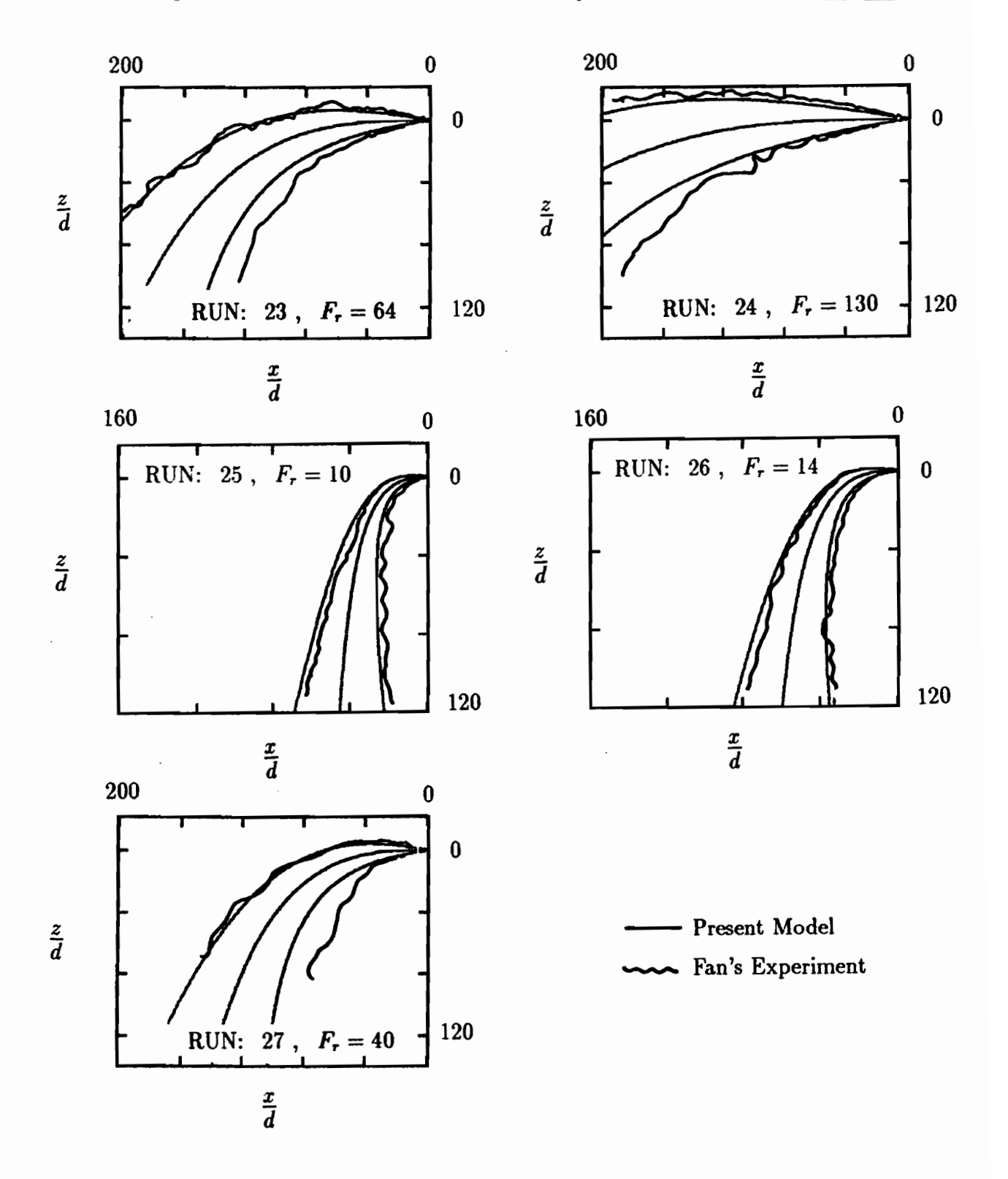


Figure 5.1: Trajectories of buoyant jets discharged into stagnant and homogeneous ambient fluid. Data due to Fan (1967).

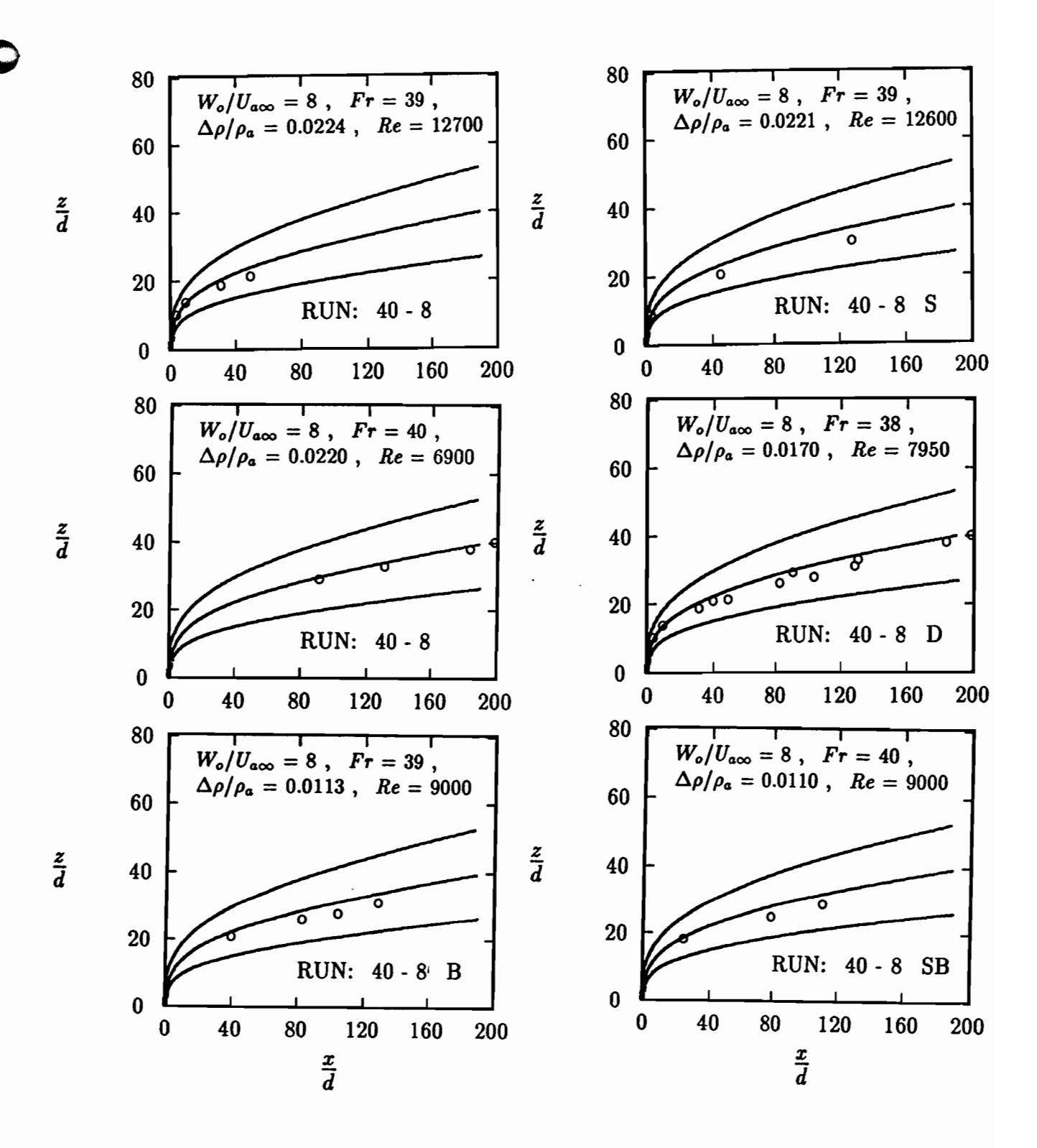


Figure 5.2: Trajectories for buoyant jets discharged into homogeneous cross-flows. Data obtained by Fan (1967).

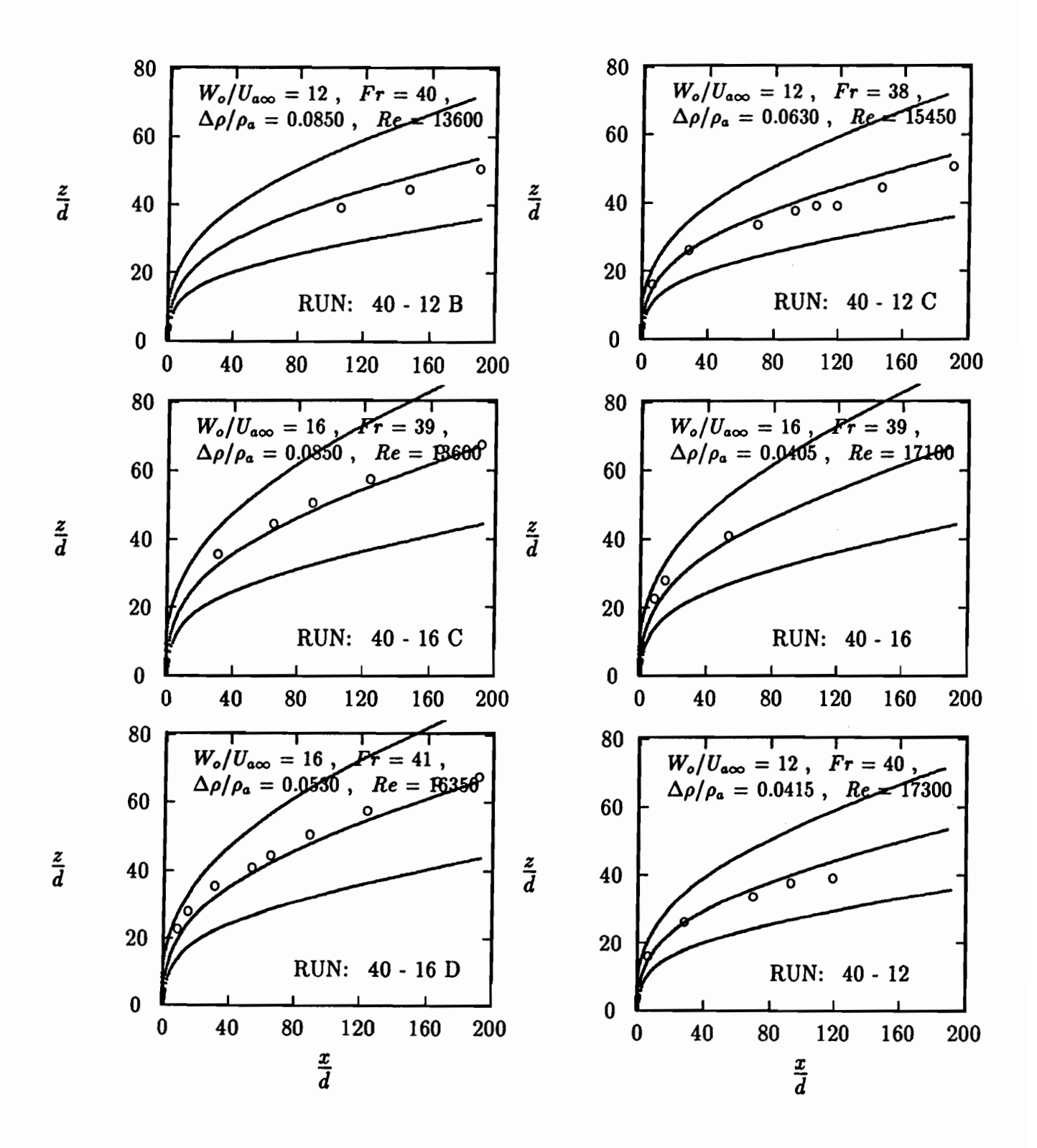


Figure 5.2: Contd.

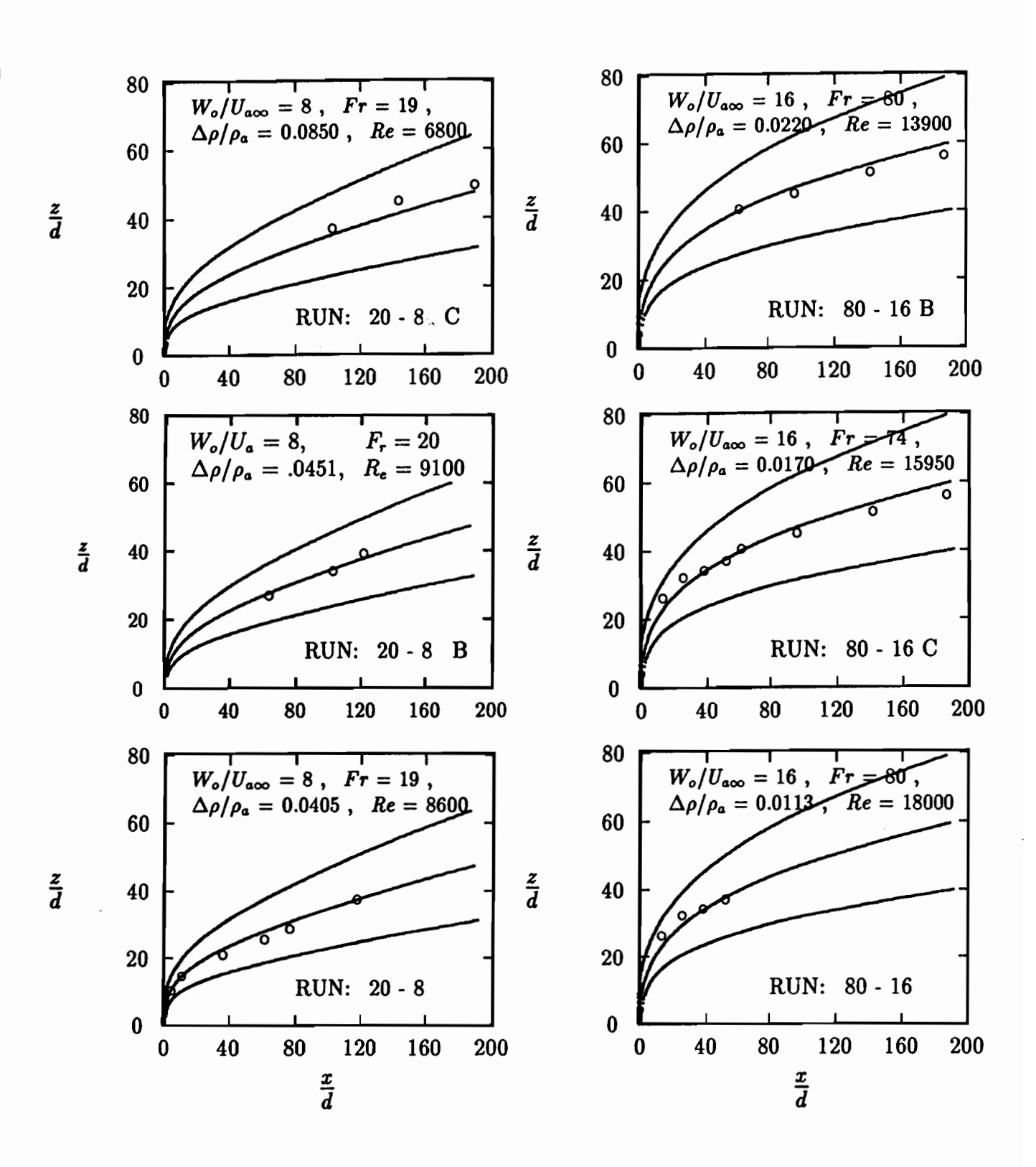


Figure 5.2: Contd.

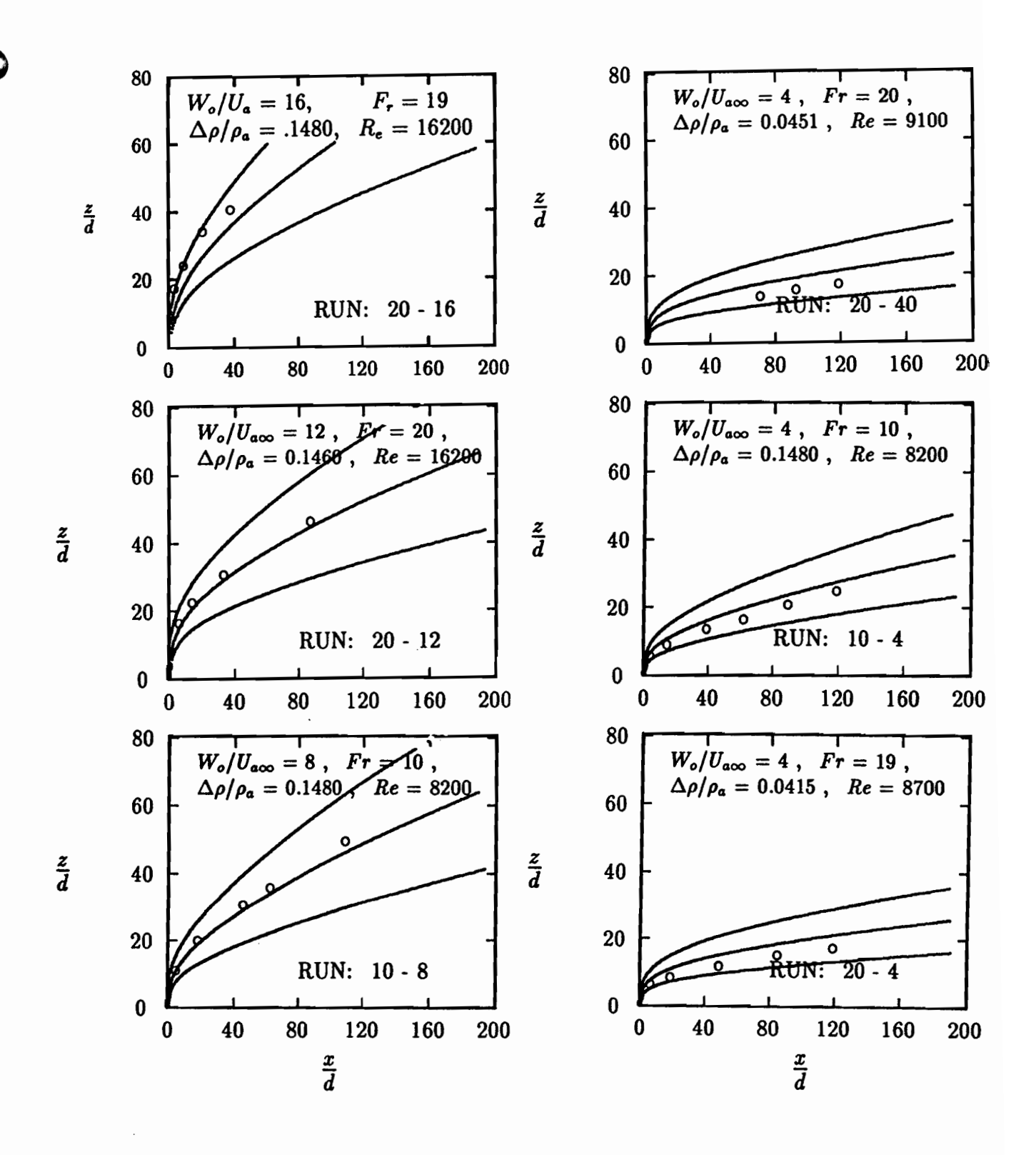


Figure 5.2: Contd.

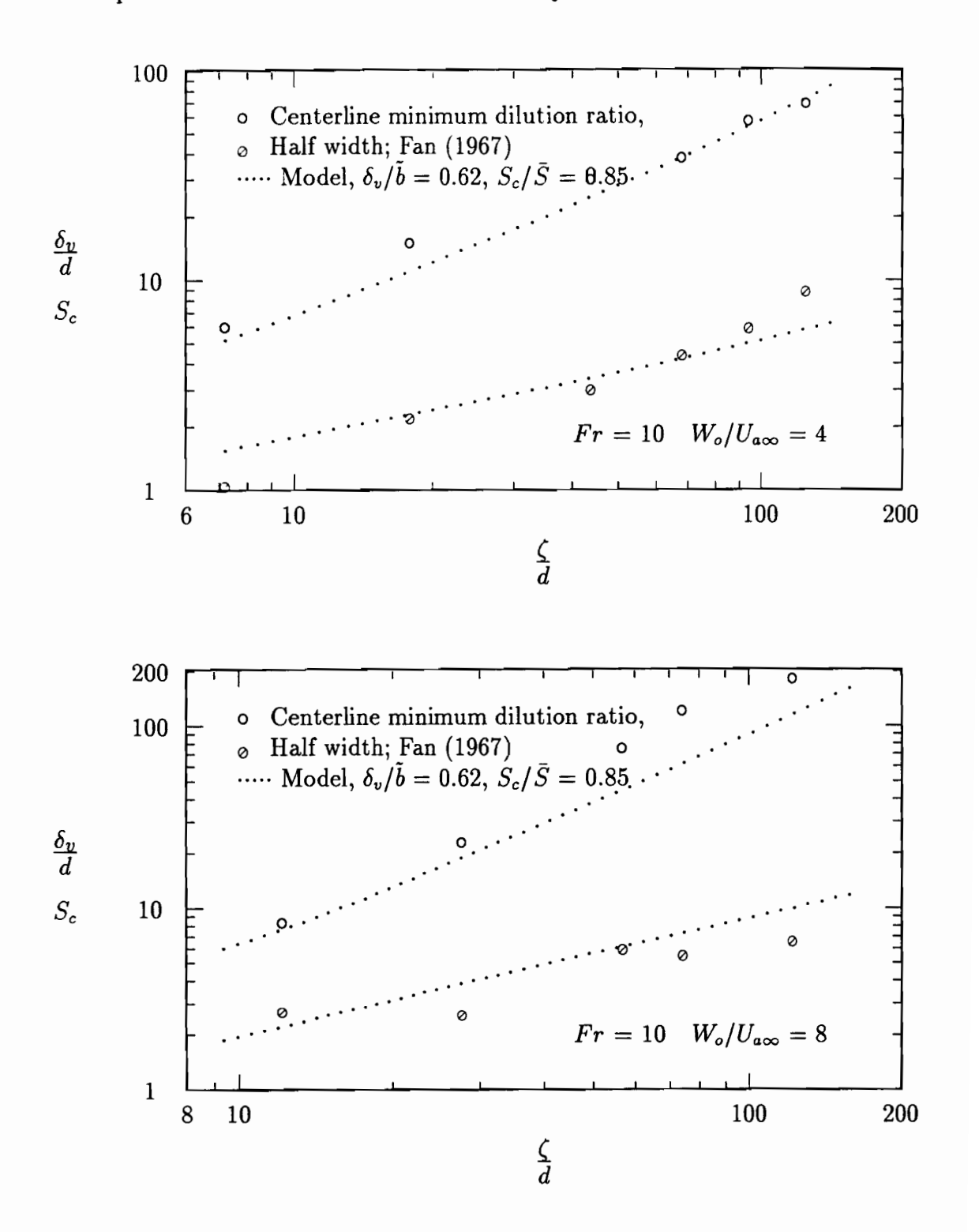


Figure 5.3: comparison of observed and model predictions for the half-widths and the center-line dilution ratios of buoyant jets in cross flow; $\delta_v/\tilde{b}=.62$, $S_c/\overline{S}=0.85$.

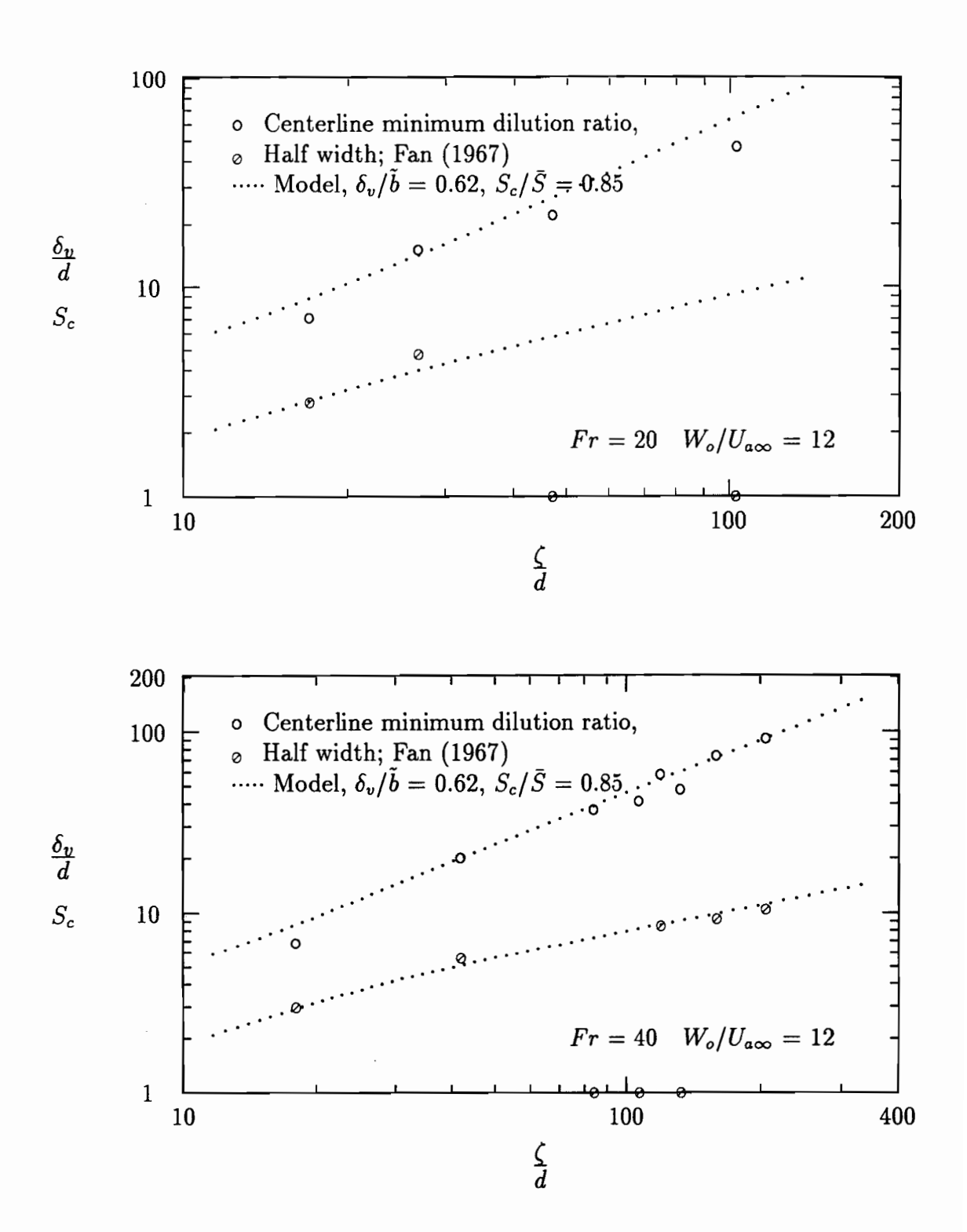


Figure 5.3: Contd.

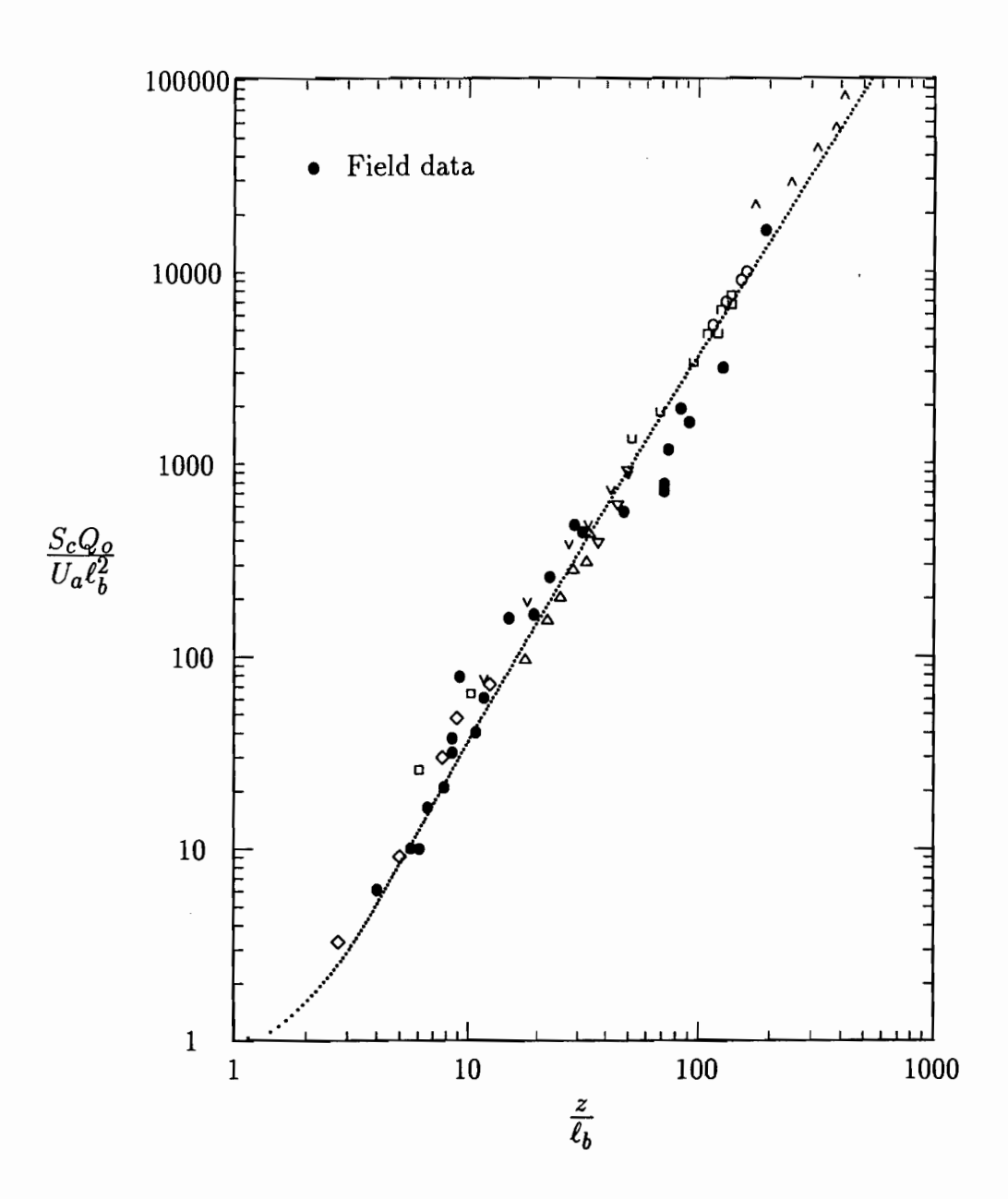


Figure 5.4: Dilution ratio as a function of the vertical elevation for buoyant jets discharged into homogeneous cross-flow. Experimental data are due to Fan (1967). The model prediction is $S_c = 0.85\overline{S}$. • Field data in Gasport, Bridport and Hasting outfall in the U.K. (Reproduced from Lee and Neville Jones, 1987).

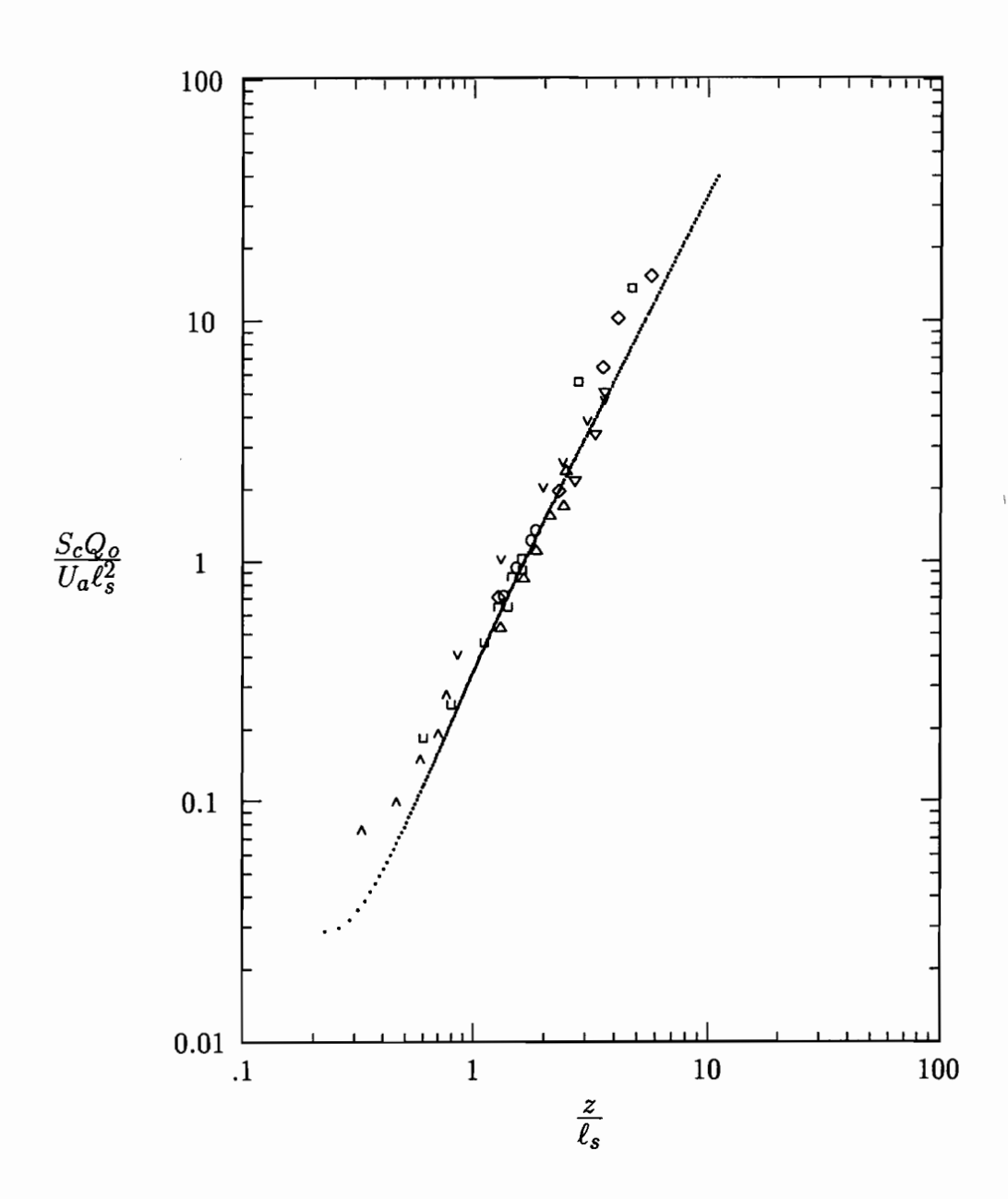


Figure 5.5: Dilution ratio of buoyant jets in homogeneous cross flow. Experimental data were obtained on the plane of symmetry. Model predictions are $S_c = 0.85\overline{S}$.

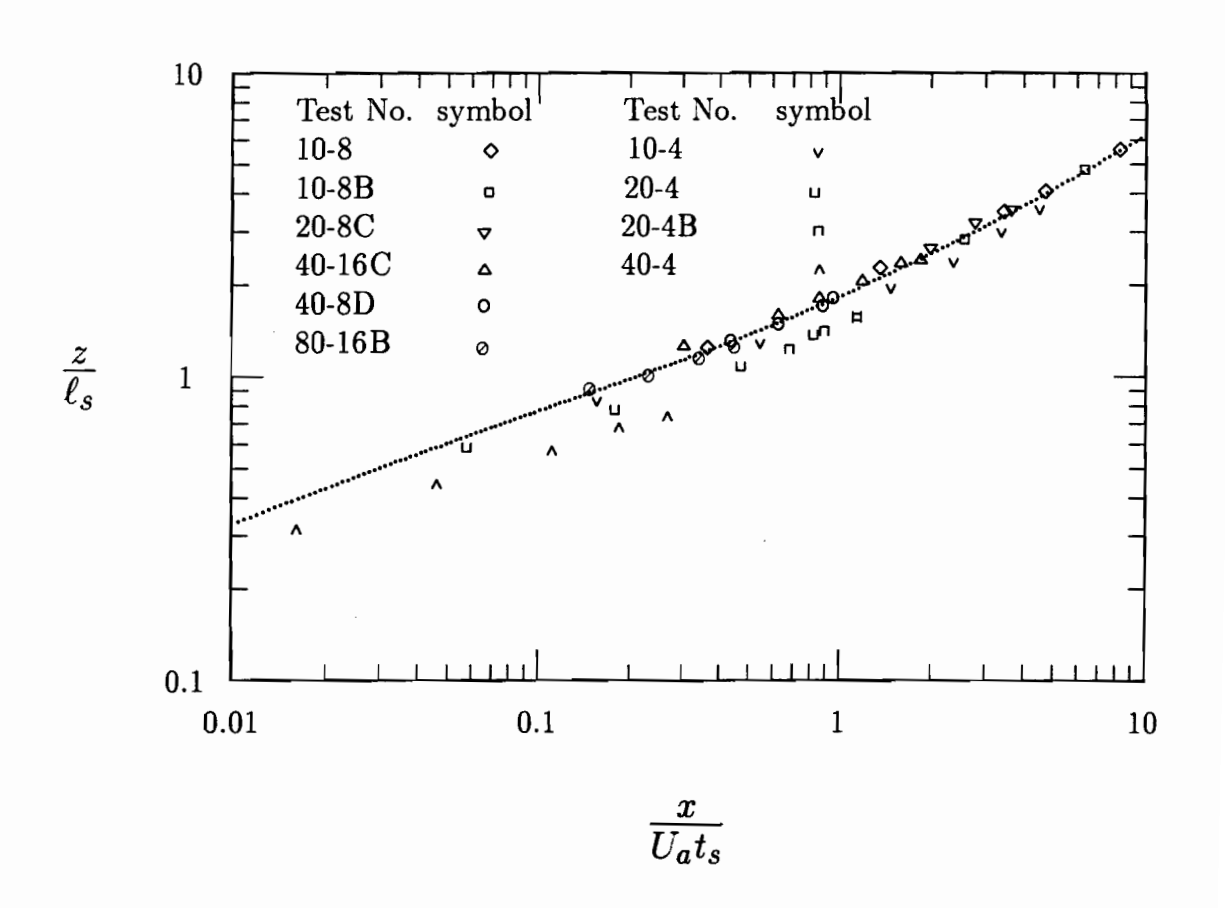


Figure 5.6: Normalized path of buoyant jets discharged into homogeneous cross flow. Experimental data are due to Fan (1967).

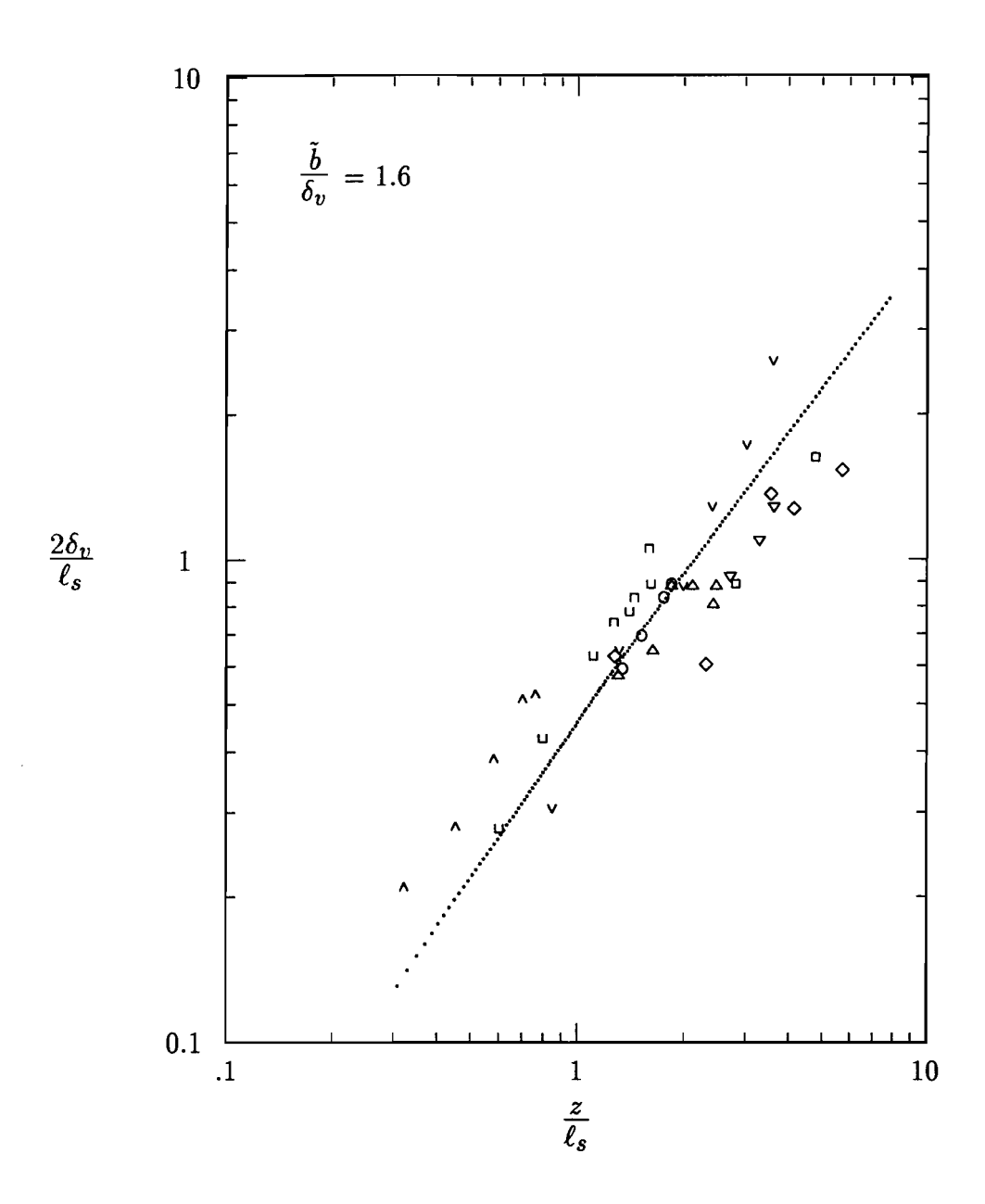


Figure 5.7: Trend of buoyant jet thickness in a homogeneous cross flow; $\delta_v/\tilde{b}=.62$, $\ell_s=13$.

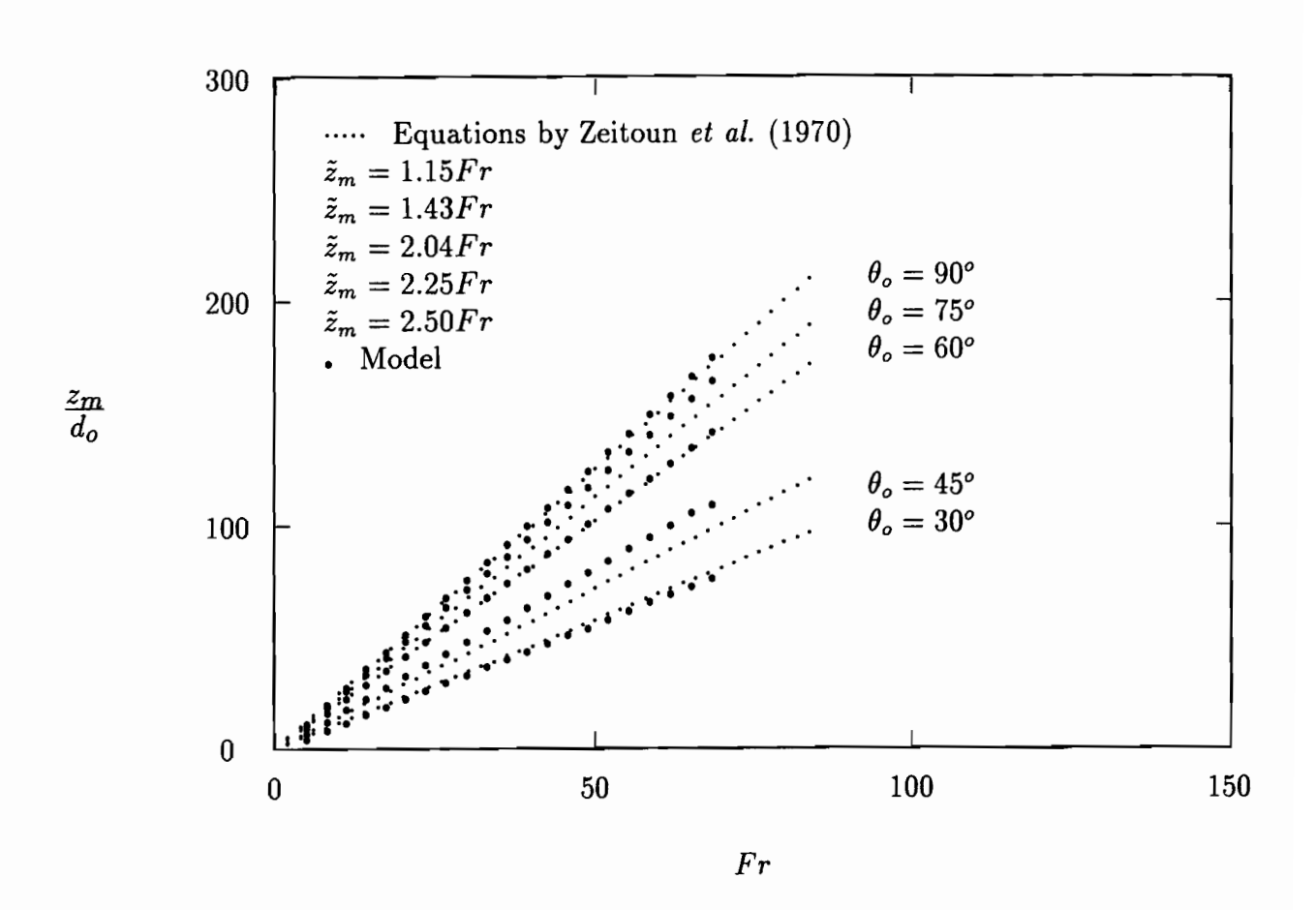


Figure 5.8: Negative buoyant jets. Model results in a stagnant fluid are compared with Zeitoun's data.

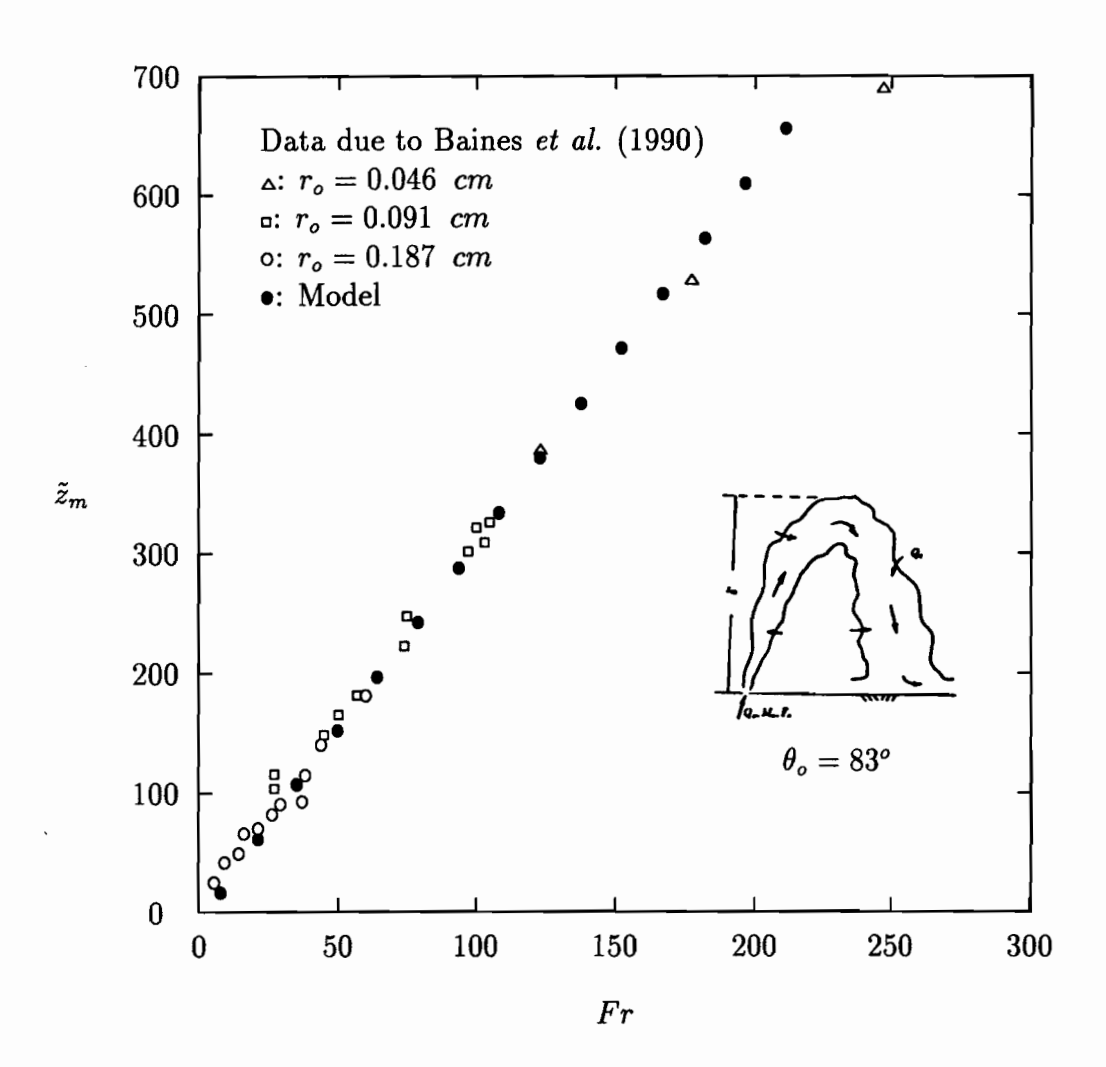


Figure 5.9: Negative buoyant jets. Model results in a stagnant fluid are compared with Baines's data.

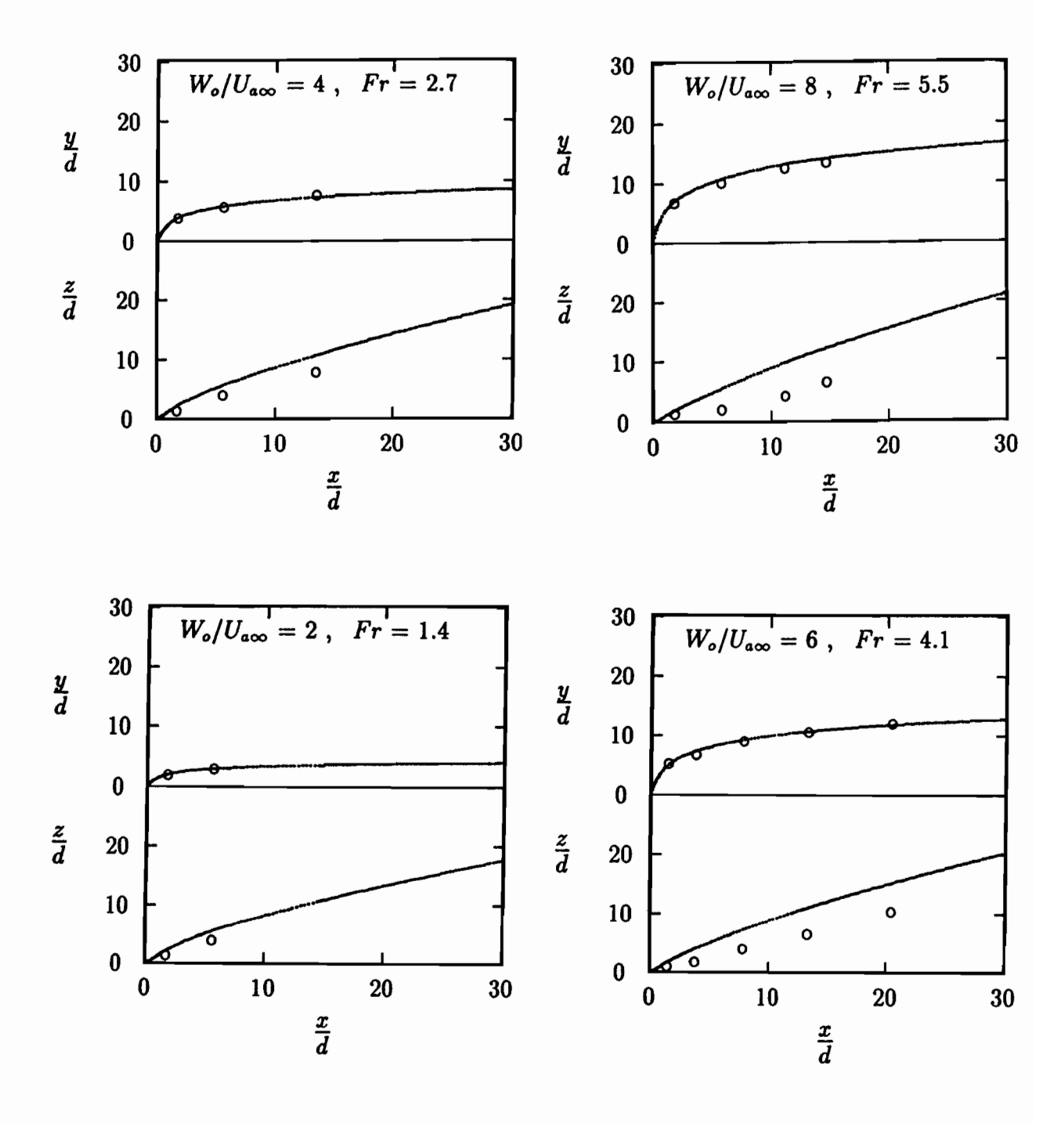


Figure 5.10: Buoyant jets with three-dimensional trajectories. The jets are initially in a horizontal direction perpendicular to the cross flow. The experimental data are obtained from the experiments by Chu (1975).

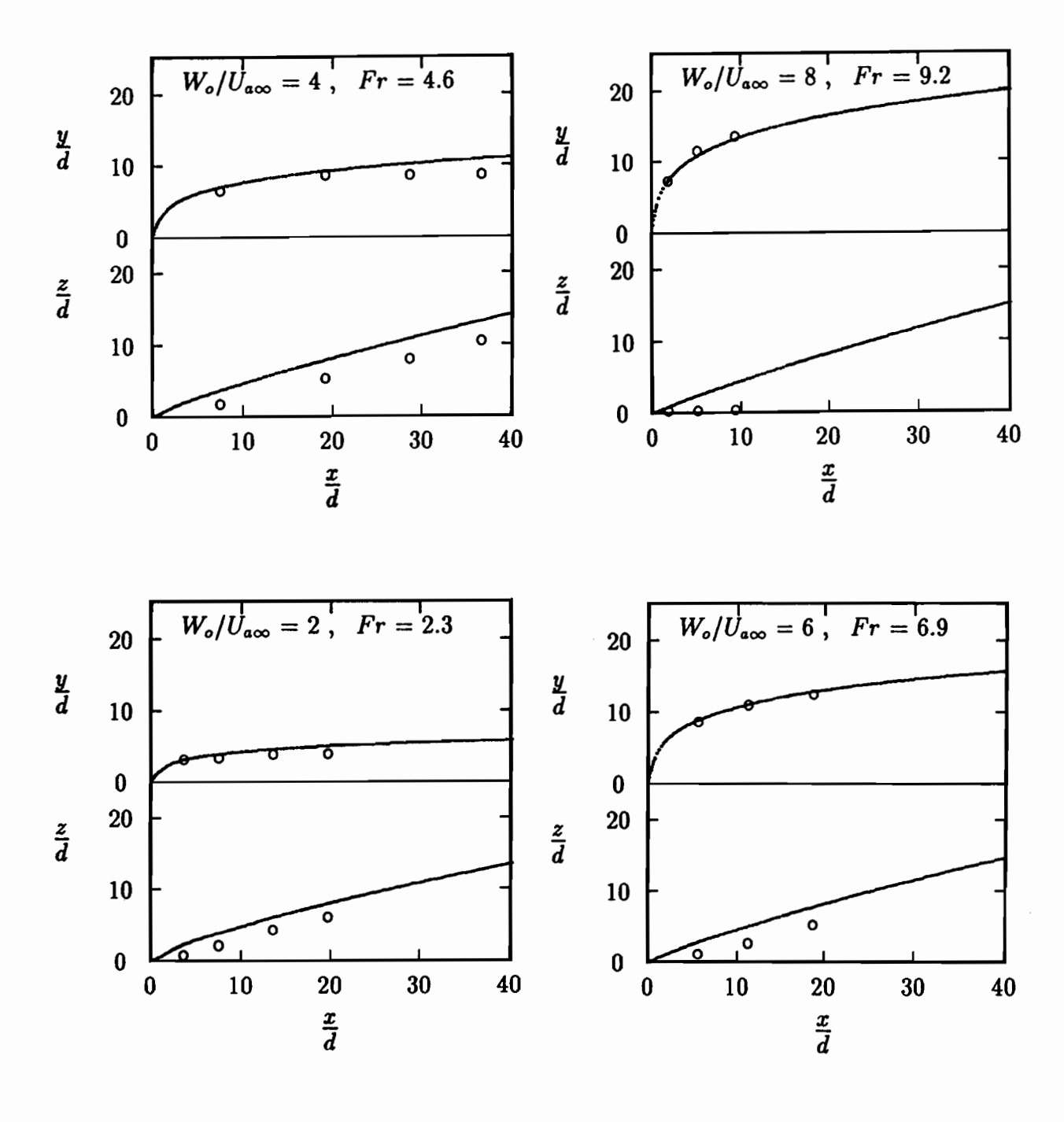


Figure 5.10: Contd.

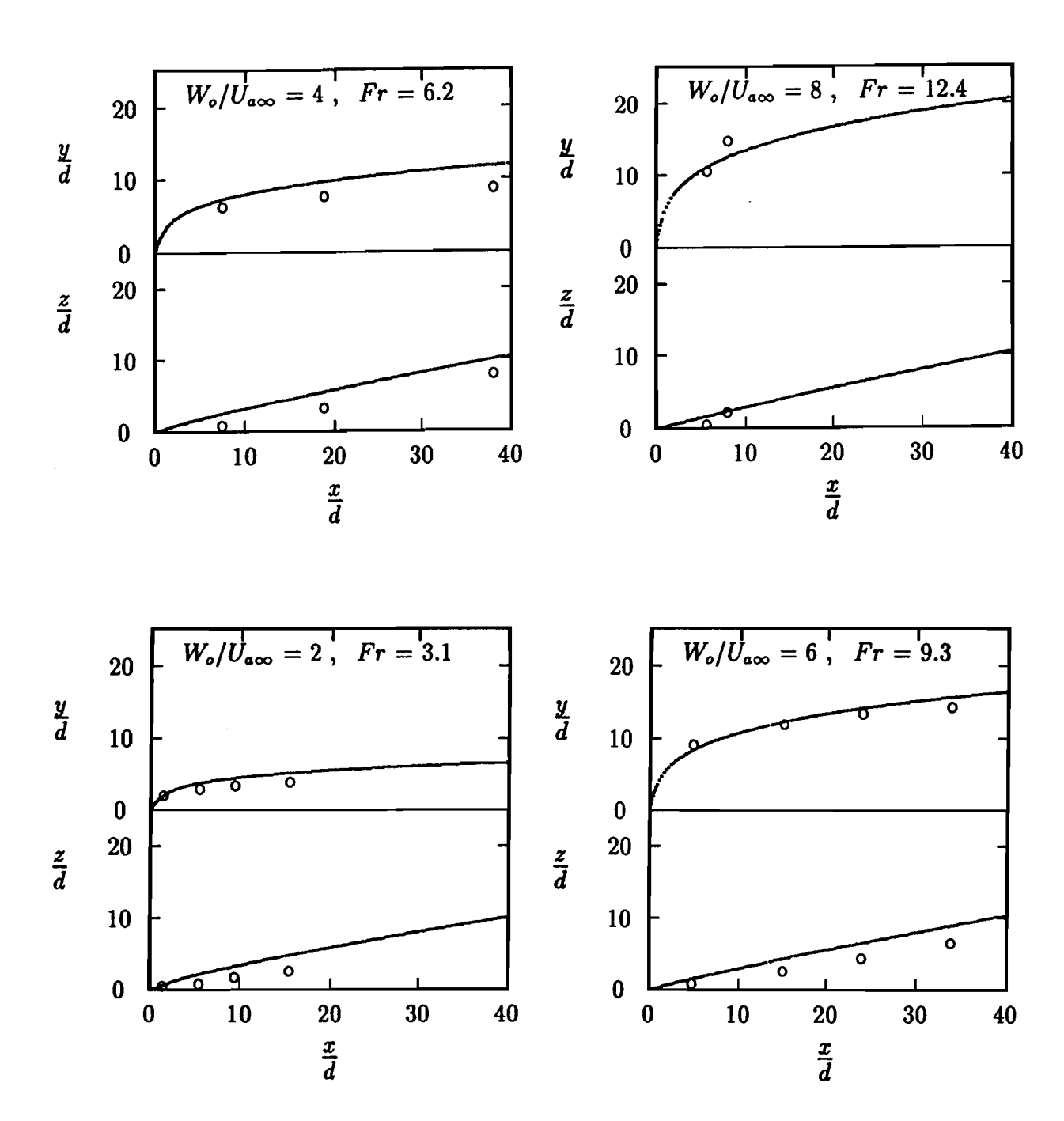


Figure 5.10: Contd.

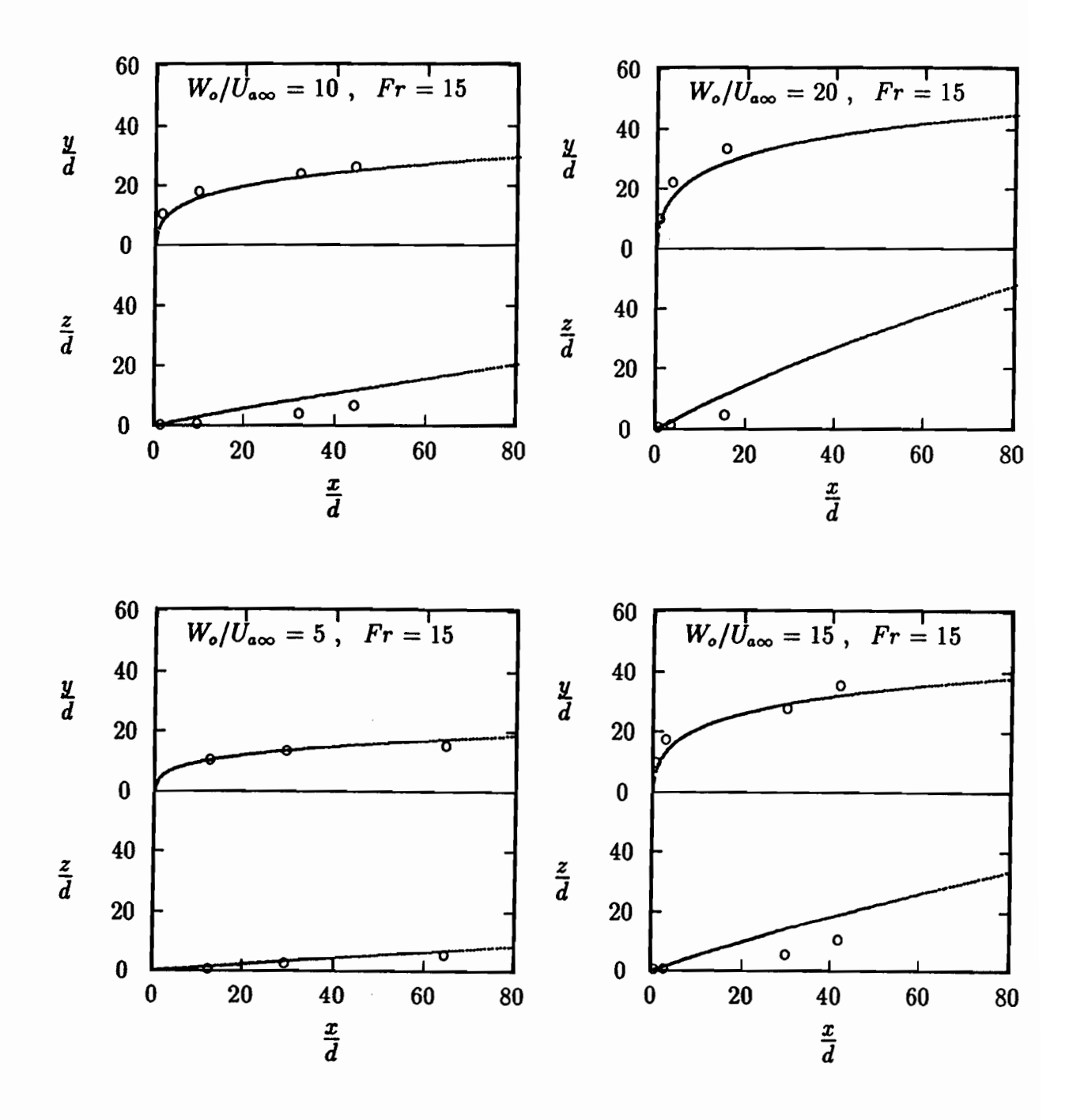


Figure 5.11: Buoyant jets with three-dimensional trajectories. Experimental data of Ayoub(1971) are compared with the model prediction.

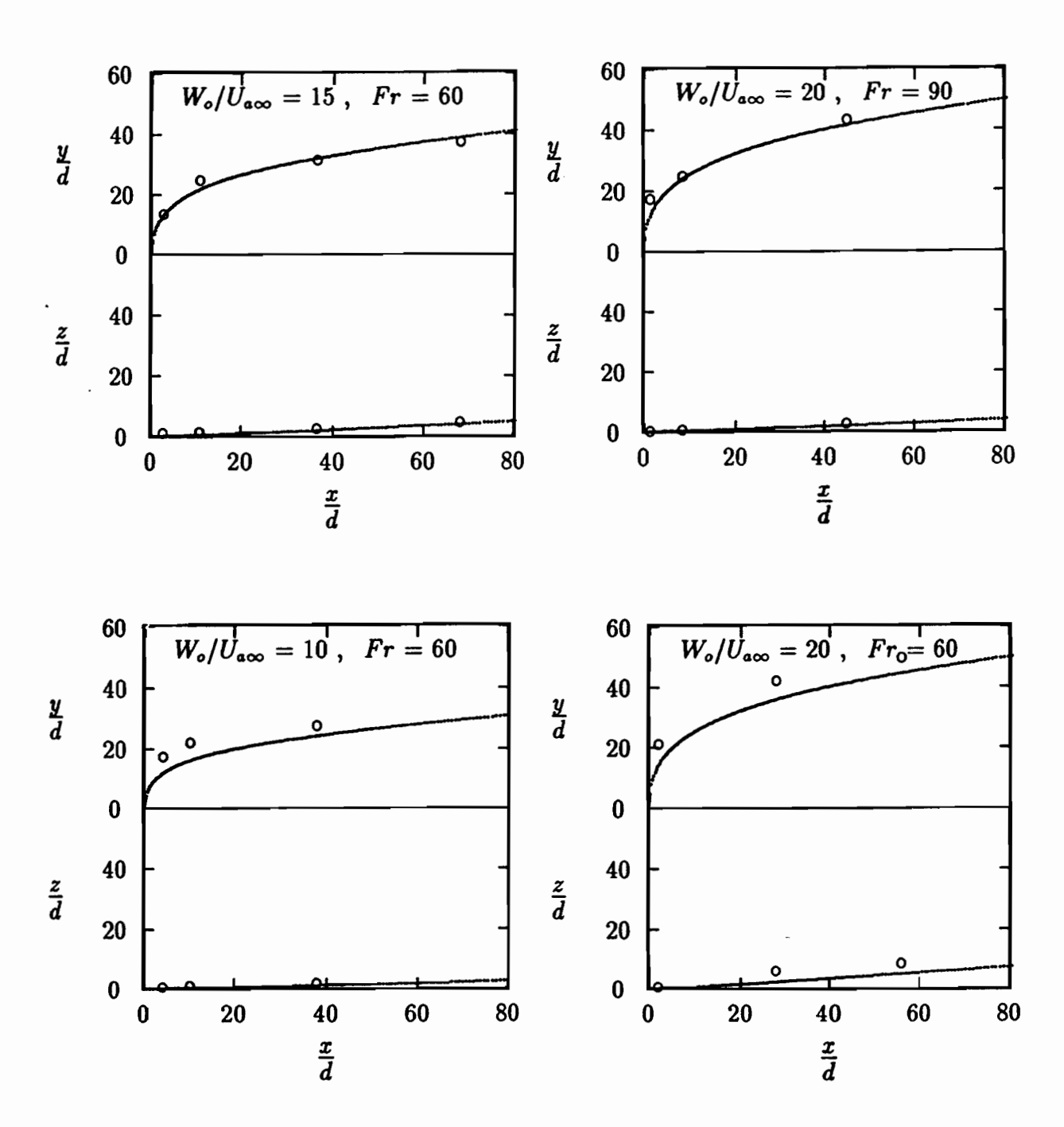


Figure 5.11: Contd.

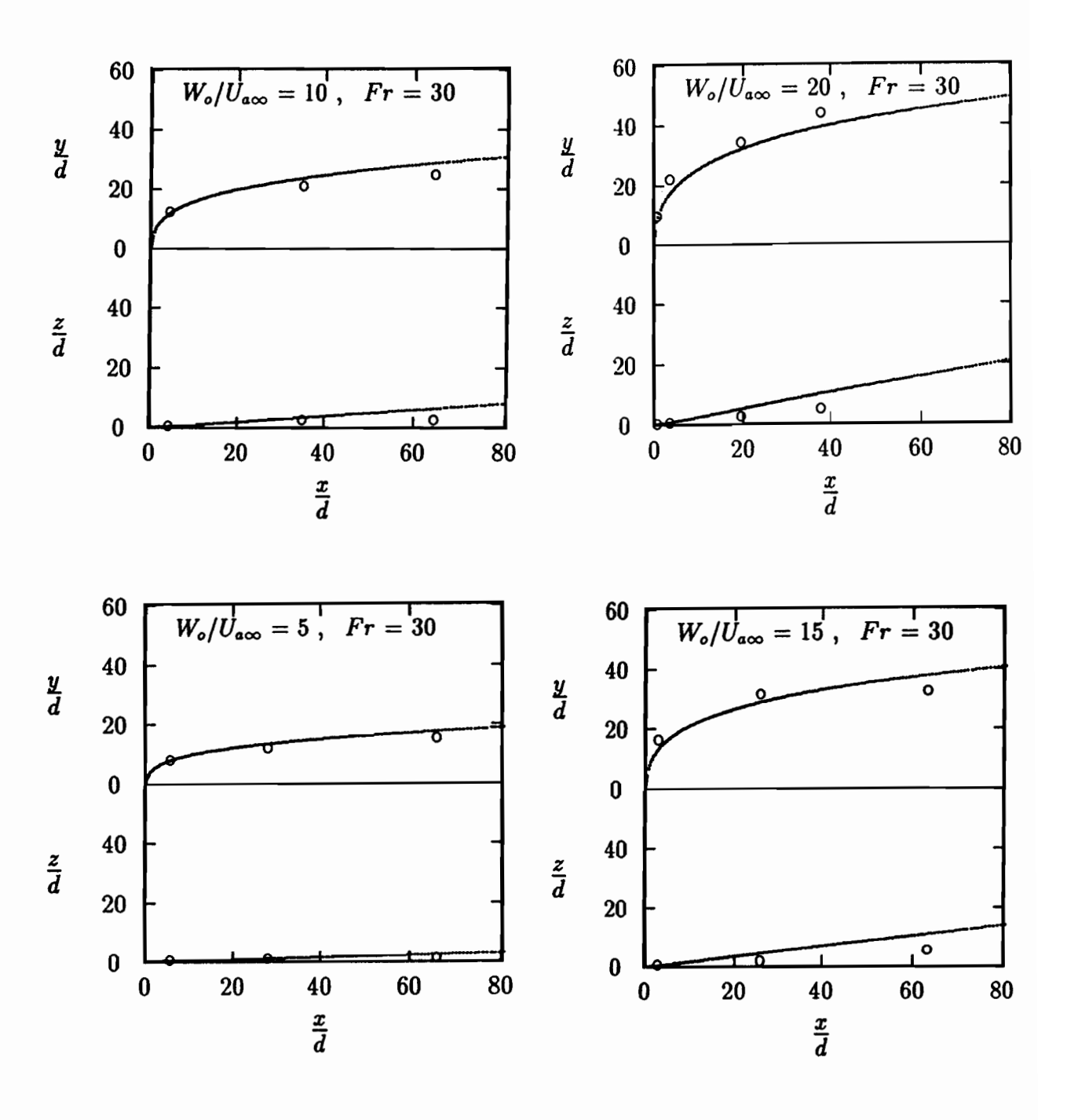


Figure 5.11: Contd.



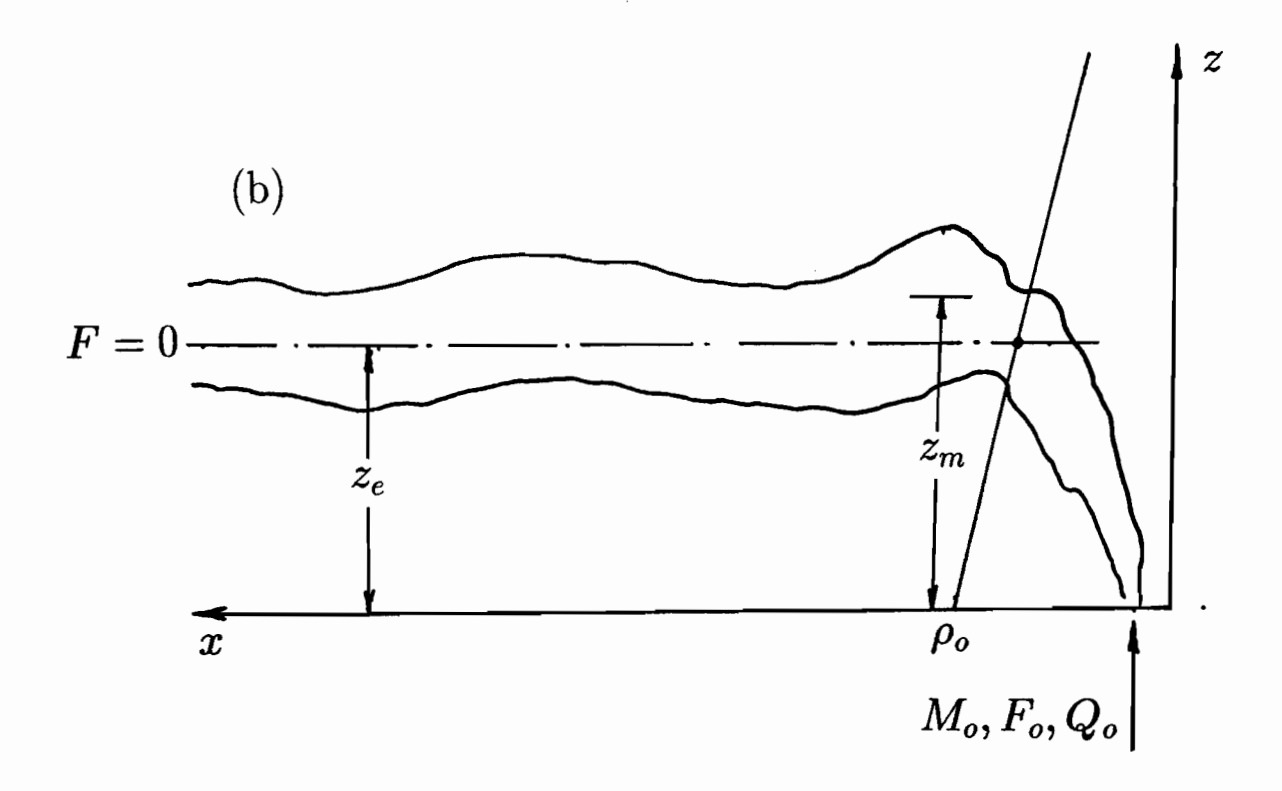


Figure 5.12: (a) Smoke plume generated by large oil tank fire in a stable density stratified environment; Photo courtesy of Los Angeles Times. (b) Schematic diagram of the plume in a linearly stratified fluid.

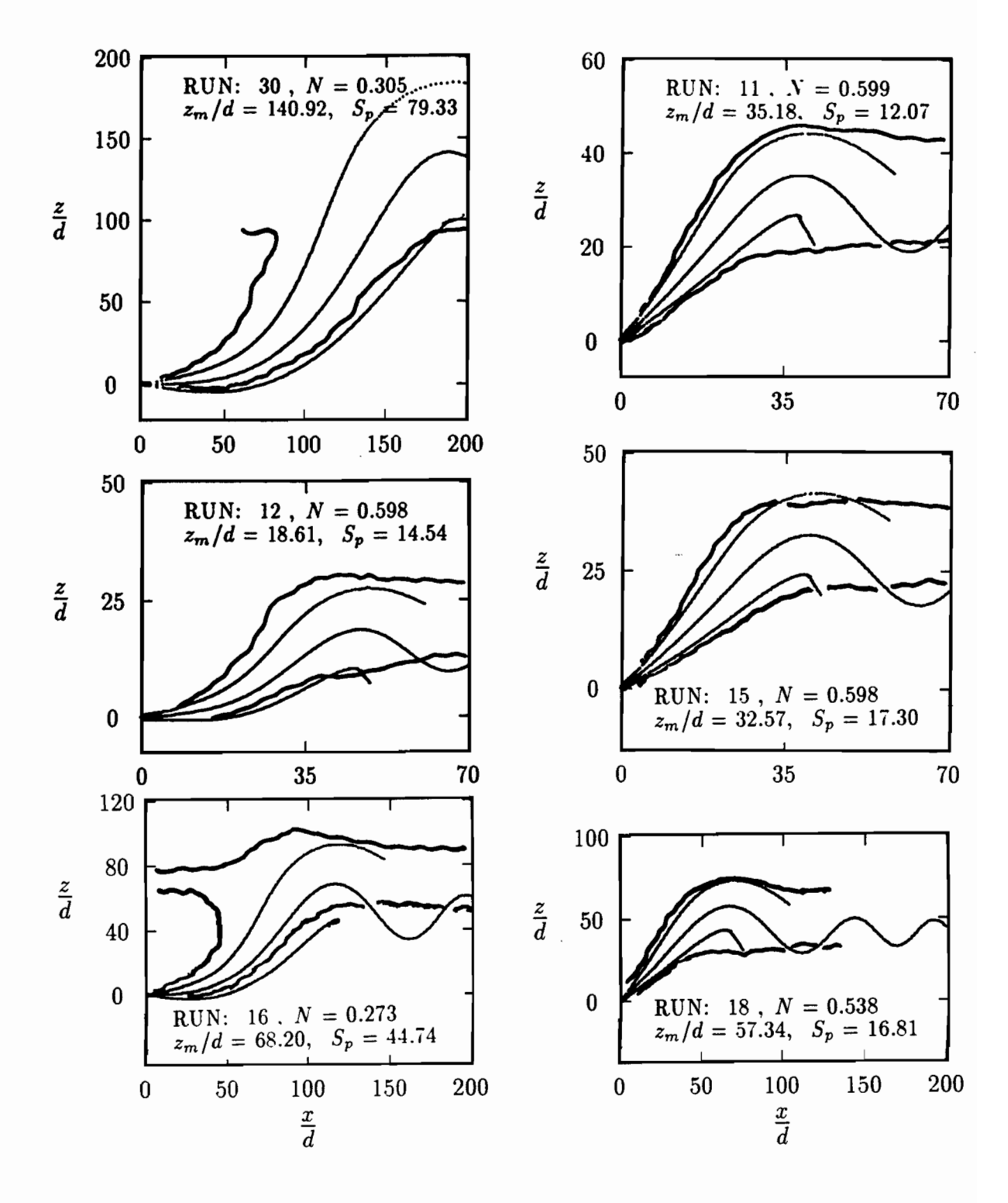


Figure 5.13: Model predictions compared with data of Fan (1967) for inclined and horizontal buoyant jets in stagnant stratified fluid; S_p is the model prediction of the averaged dilution at the peak of the buoyant jet.

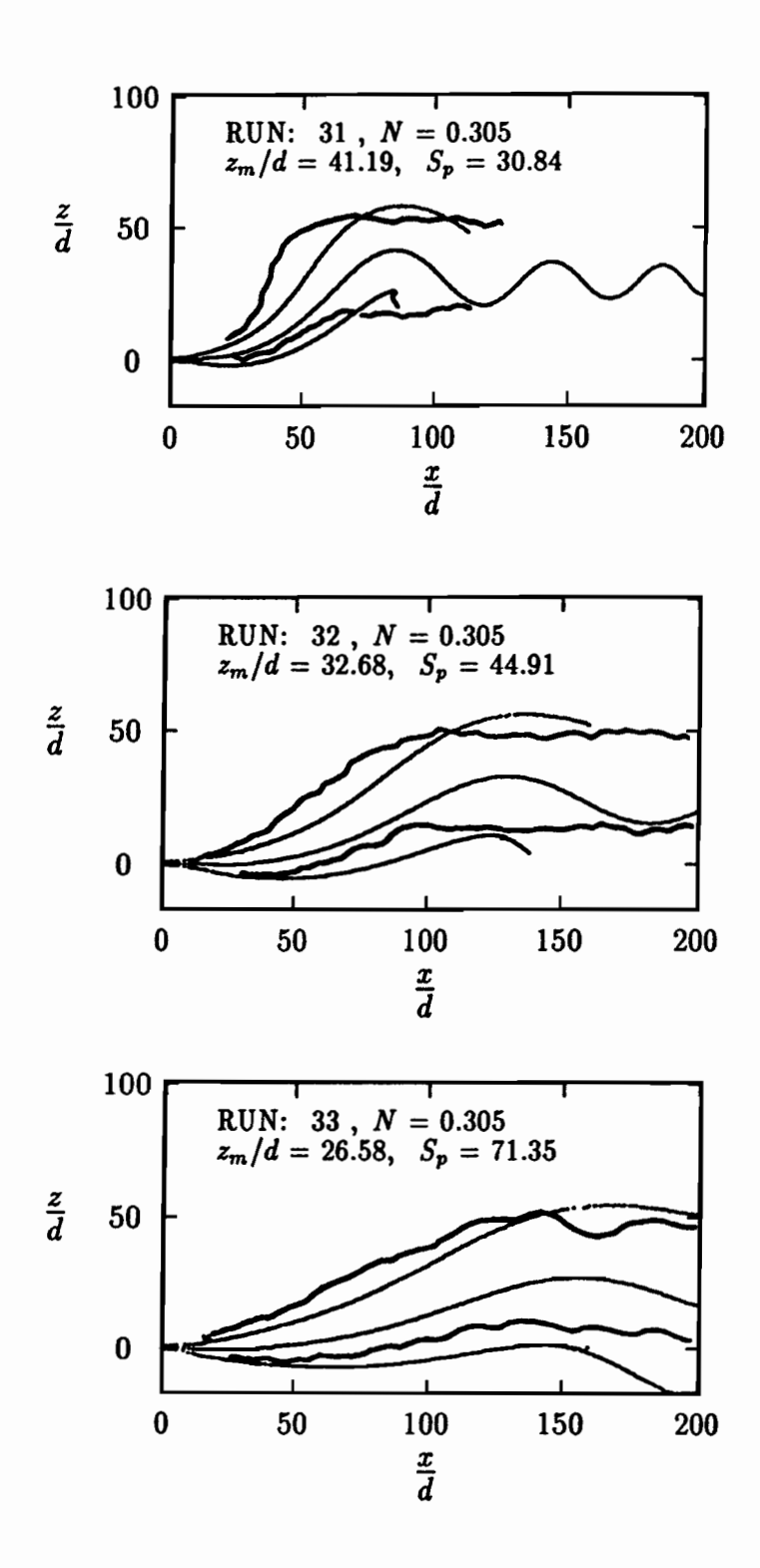


Figure 5.13: Contd.

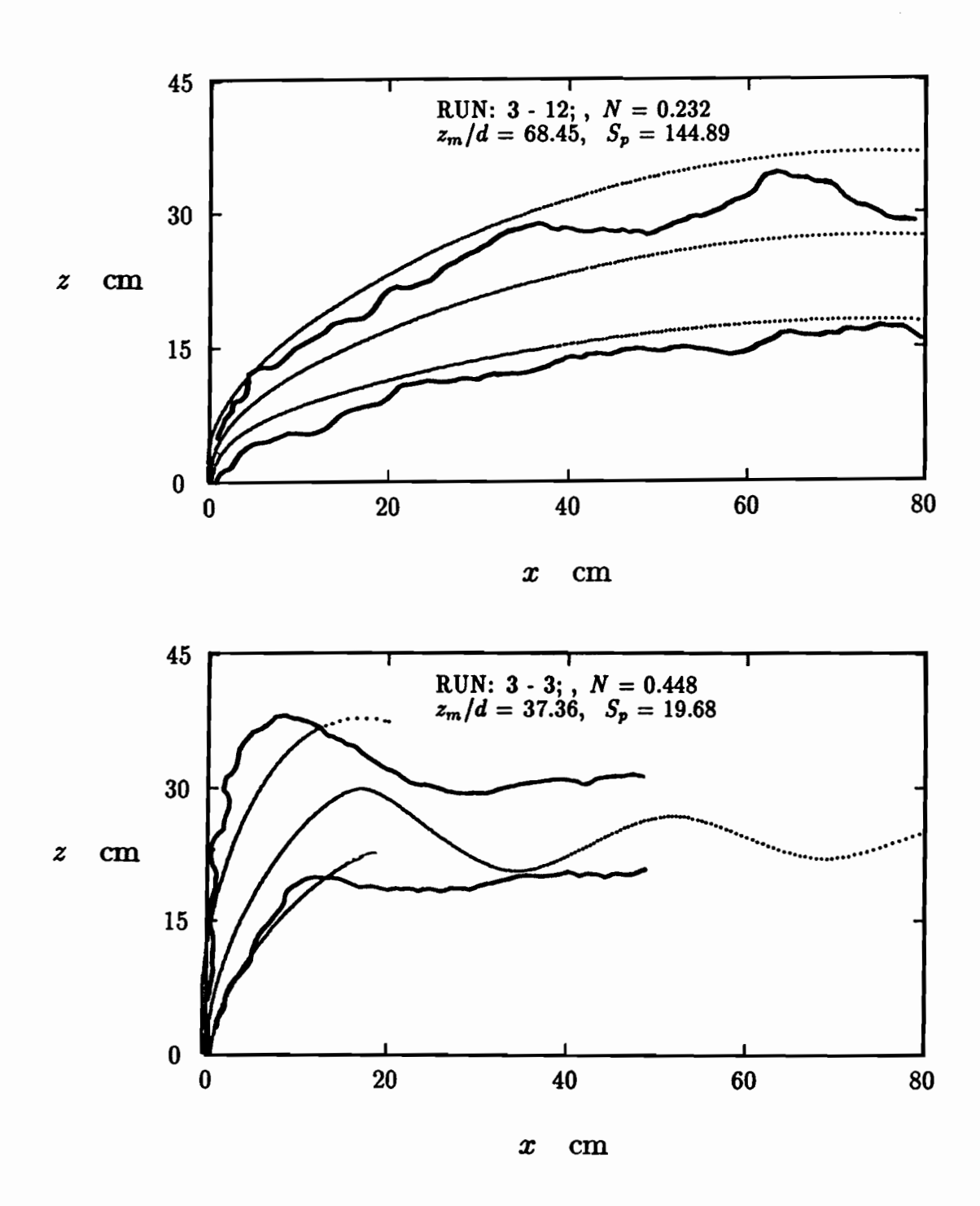


Figure 5.14: Model predictions compared with experimental data by Wright (1977) for vertical buoyant jets in a stratified cross-flow: S_p is the averaged dilution ratio obtained by the model for the buoyant jet at the peak.

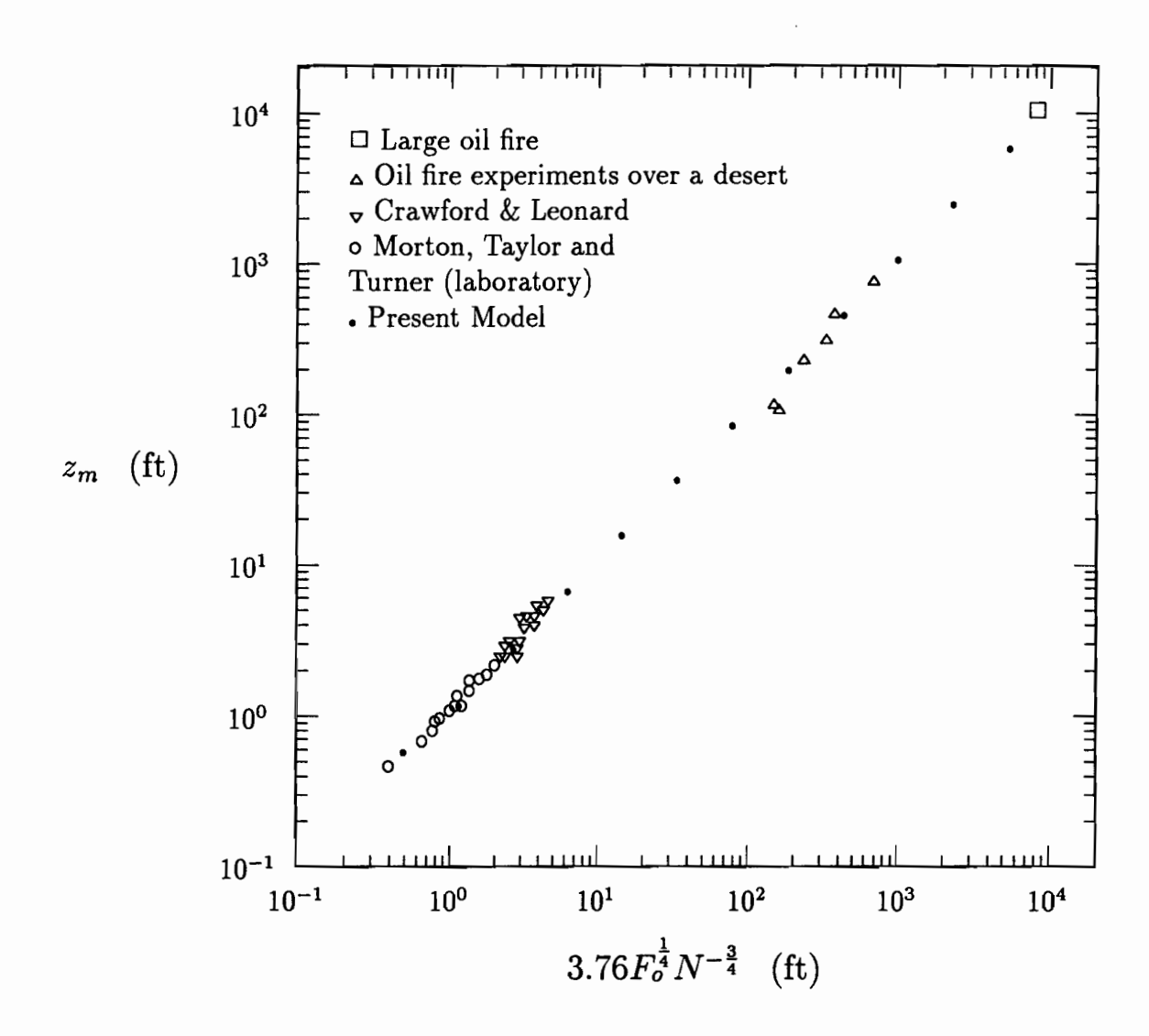


Figure 5.15: Maximum rise of the buoyant plume in a stratified stagnant and stratified fluid. Model results are compared with Briggs's data (1969).

Chapter 6

Conclusions

6.1 Summary and Conclusions

Buoyant jets in cross flows were examined in this thesis based on a series of linethermal experiments and an integral analysis of the flow for a wide range of discharge conditions.

The laboratory experiments provided the opportunity to observe the bifurcation and overturning phenomena of line thermals. The tracer concentration distributions through cross sections of the line thermals were determined using a video imaging method. The density distributions were observed to be top-heavy due to the formation of an unstable interface at the front and a stable interface at the back. This observation of the lopsided density distribution in the line thermal has provided, for the first time, the correct interpretation for the overturning and bifurcation phenomena, as well as a connection of these phenomena to the process of turbulent entrainment. Measurements of the tracer concentration in the line thermals showed the maximum concentration at the vortex core to be equal to about 1.61 times the average over the thermal cross section.

The experimental investigation for the line thermals was complemented by an integral analysis of buoyant jets in cross flows. The integral formulation, based on a Lagrangian method, is for the general problem of a buoyant jet in a cross flow with non-uniform density and velocity distributions. The integral model is developed based on a set of model coefficients. These coefficients, evaluated by experimental

observation of the flow in limiting cases, are

$$\beta_s = 0.17, \quad \beta_n = 0.34, \quad k_s = 0.18 \quad \text{and} \quad k_n = 1.00.$$
 (6.1)

Calculations were conducted for a variety of discharge configurations including (a) jet normal to the cross flow, (b) oblique jets in a uniform cross flow, (c) buoyant jets in stagnant fluid, (d) buoyant jets normal to the cross flow, (e) buoyant jets with three-dimensional trajectories, (f) negatively buoyant jets, and (g) buoyant jets in a stably stratified flow. The results of these calculations suggest that the model coefficients specified in Equation 6.1 are very close to optimal.

6.2 Recommendations for Future Research

It is significant to note that most of experimental investigations conducted in the past were concerned with buoyant jets that were essentially point sources in uniform cross flow. Therefore, the model verification efforts in Chapter 4 and Chapter 5 are limited to situations of rather simple discharge configuration. However, the integral model developed from the present investigation is applicable to more general situations when the velocity of the cross flow is not uniform and when the size of source is not small compared with the depth of the flow.

To examine the more general problem, calculations were conducted for a wider range of discharge conditions. The results obtained for flows with two very different source densimetric Froude numbers are presented in Figure 6.1 and Figure 6.2. Figure 6.1 shows the results obtained for cases of plumes with a small densimetric Froude number (Fr = 0.1) at the source. Figure 6.2 shows the results obtained for the cases of jets with a large densimetric Froude number (Fr = 10) at the source. The source densimetric Froude number is $Fr = W_o/g_o^{\frac{1}{2}}A_o^{\frac{1}{2}} = M_o^{\frac{5}{4}}/(F_o^{\frac{1}{2}}Q_o)$.

Figure 6.3 shows how the height of the jet is affected by the boundary layer thickness. In this figure, the height of the jet centre-lines, z_6/ℓ_s , obtained at a downwind location of $x = 6 \ell_s$ from the source are plotted against the momentum thickness, θ , of the cross flow. The plume (with a source densimetric Froude number, Fr = 0.1) is

found to be most sensitive to the boundary layer thickness. The height of the plumes is observed in this case to change significantly as the momentum thickness-to-source diameter ratio varies from $\theta/d_o = 0$ to $\theta/d_o = 8$.

Figure 6.4 shows the effect of the velocity ratio, W_o/U_a , on the potential core length. The results of these calculations show that the near field of the buoyant jet is affected by the exit velocity-to-cross flow velocity ratio, W_o/U_a , and the densimetric Froude number, Fr, in a rather complex manner.

The flow of the plumes is characterized by a small upward velocity at the ground level. The profiles of the plumes in Figure 6.1 show how the plume cross section contracts, due to the upward acceleration of the flow by buoyancy force. The velocity in the upward accelerating region is small, therefore the velocity of cross flow, U_a , at the ground level is significant.

Most buoyant discharges into oceans and the atmosphere are in the plume regime. The coastal discharge from the power plant in Figure 1.2 is an example. A large fire over an oil field is another example. The results presented in Figures 6.1 through 6.4 have provided some interesting insight into the effect of non-uniformity in the cross flow. Unfortunately, data available at the present time dose not permit model verification of these effects. Therefore, future experimental investigations should be devoted to examining a wider range of discharge conditions. Special attention should be given to studying the profile effect of the cross flow, particularly in the plume regime.

6.3 Statement of Originality

The research reported in this thesis consists of two related parts: an experimental investigation of line thermals and an integral formulation of buoyant jets in cross flows.

1. The line thermal experiments were conducted in a large tank. The width of the tank used in the present setup was three times wider than the tank used by Richards (1967) and twice as wide as the tank used by Tsang (1971). The height of the tank

was about the same as the tanks of Tsang and Richards but was two-and-a-half times higher than the depth of the upper layer in the experiments reported by Noh et al. (1992). In analysing the experimental data, special care was taken to isolate the effects of the side walls and the bottom of the tank.

- 2. During the experiment, dye was released with the source fluid. The concentration of the dye in the thermal was measured using a video imaging method. The measurement of the concentration field provided a precise description turbulence flow that was not attempted in any of the previous experimental studies of the line thermal.
- 3. In present experiments, the overturning event was observed before impingement of the thermal onto the bottom of the tank. The lopsided density distribution preceding the overturning event is due to enhanced mixing across the unstable density-stratified interface at the front of the thermal and the absence of mixing across the stable interface at the back. If the tank were very large, the overturning event may occur repeatedly, since the asymmetry between the mixing at the front and at the back would continue to produce the lopsided density distribution required for the overturning event.
- 4. The integral formulation was conducted for the general flow problem of buoyant jets in a non-uniform cross flow. The governing equations were derived using vector notations, and are generally applicable to buoyant jets with a three-dimensional trajectory.
- 5. The present formulation includes a procedure to calculate the flow in the potential core, which was not attempted by any of the previous formulations.
- 6. Numerical solutions of the buoyant jet problem were conducted for a wide range of discharge conditions including discharge from very large sources. The model predictions were compared with a comprehensive set of experimental data and many

Chapter 6	Conclusions	12	27
CHAPICI O	Concidenti		, 1

previous experimental investigations. This is the first time that an integral model has gone through an extensive calibration against experimental observation.

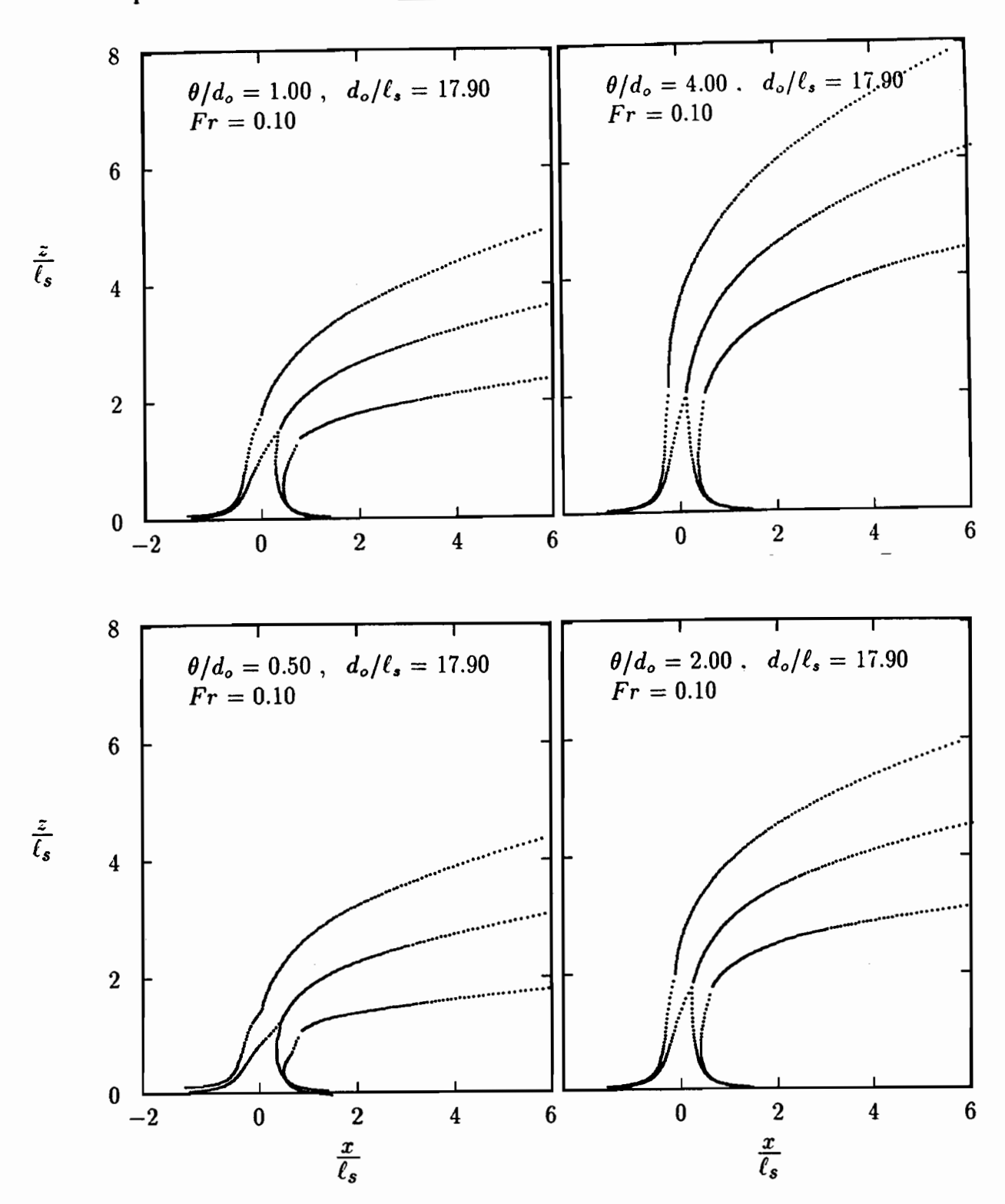


Figure 6.1: Plumes in non-uniform cross flows; Fr = 0.1; (a) $\theta/d_o = 0.5$, (b) $\theta/d_o = 1.0$, (c) $\theta/d_o = 2.0$, (d) $\theta/d_o = 0.5$; $\ell_s = [M_o^2/F_oU_a]^{\frac{1}{3}}$.

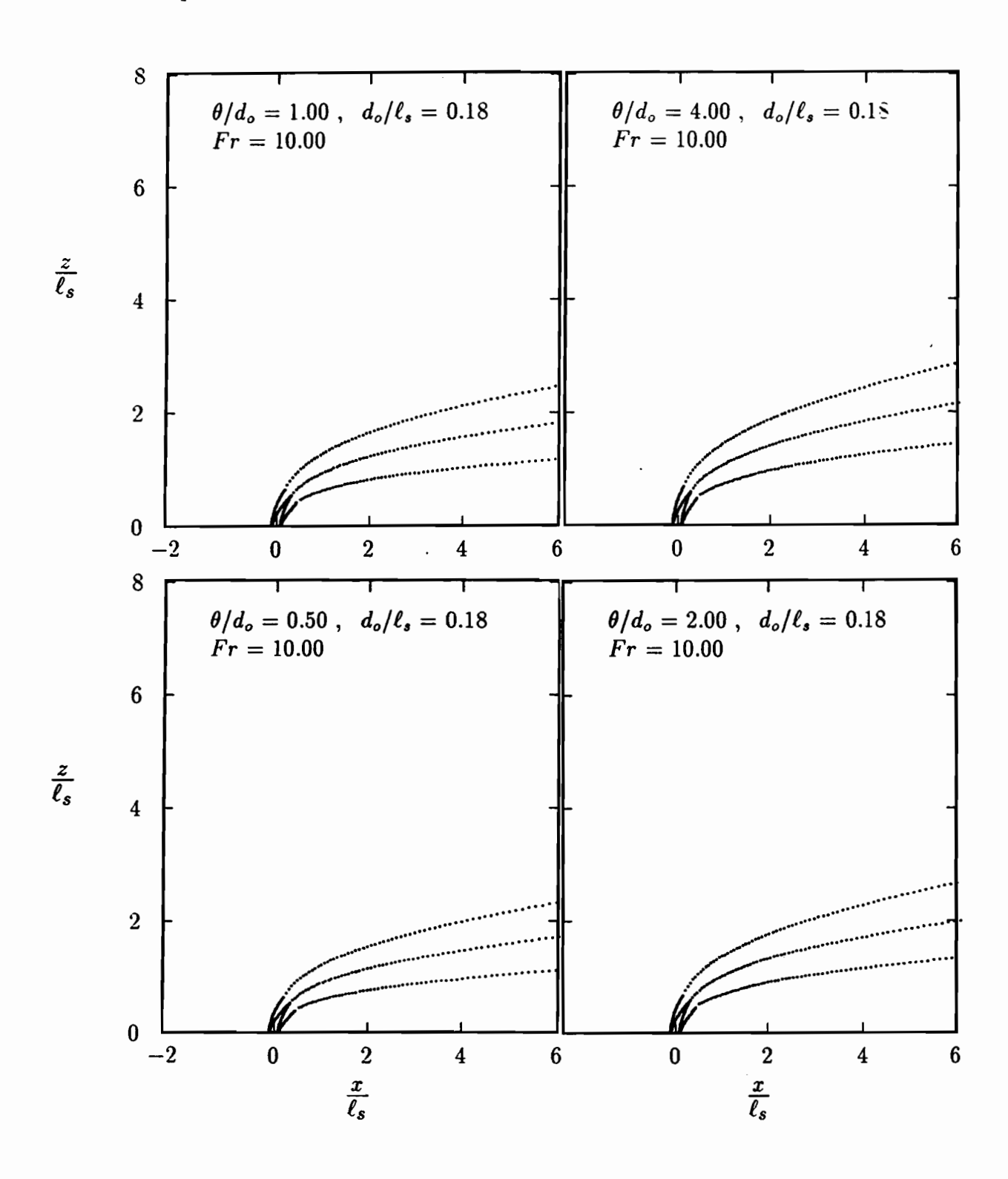


Figure 6.2: Jets in non-uniform cross flows; Fr = 10; (a) $\theta/d_o = 0.5$, (b) $\theta/d_o = 1.0$, (c) $\theta/d_o = 2.0$, (d) $\theta/d_o = 0.5$.

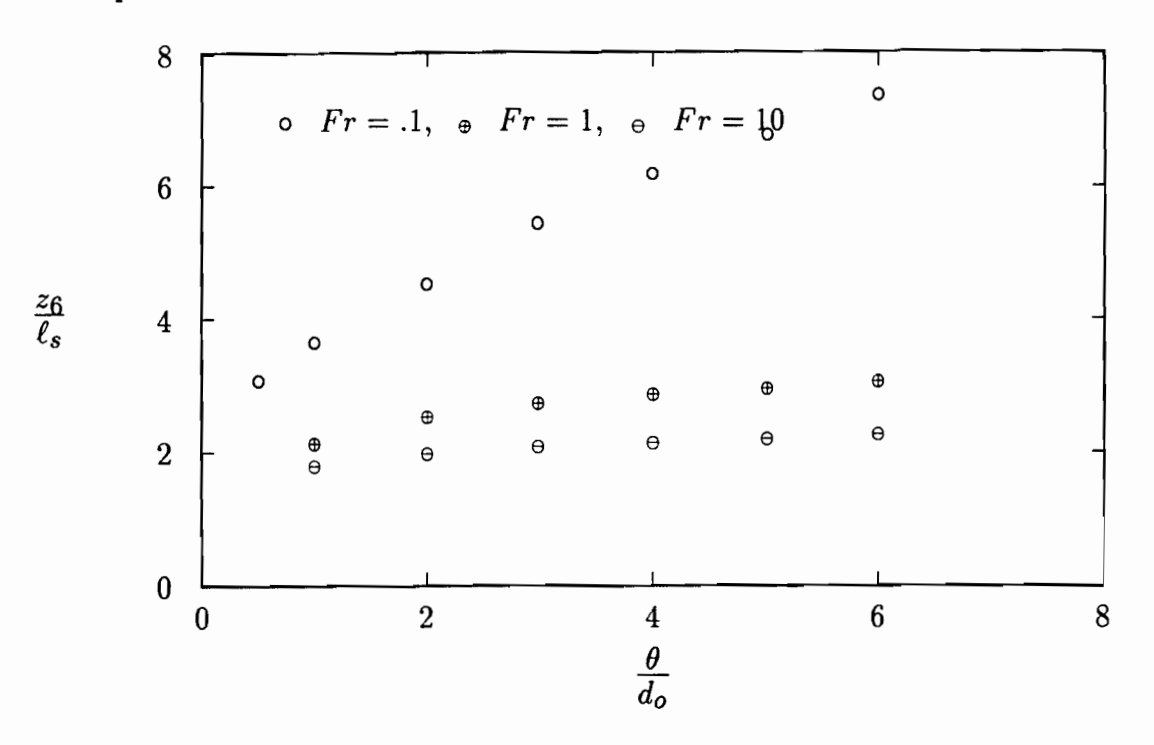


Figure 6.3: Height of the buoyant jet, z_6/ℓ_s , obtained at a downwind location where $x = 6\ell_s$.

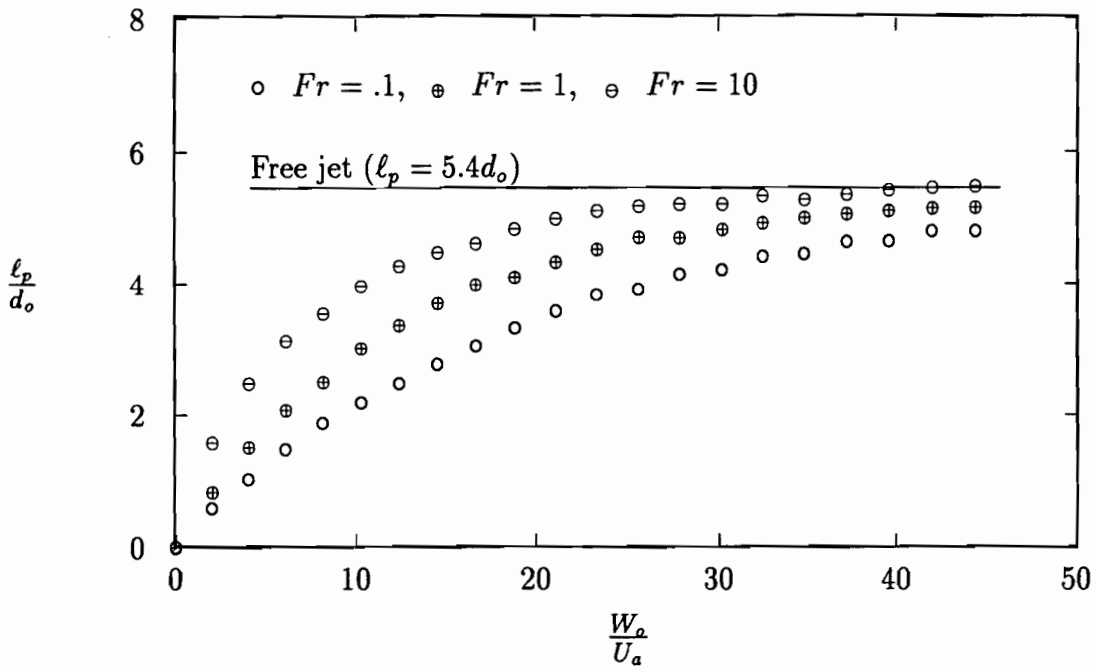


Figure 6.4: Length of the potential core, ℓ_p/d_o , obtained for three densimetric Froude numbers, Fr = 0.1, 1.0 and 10.0.

References

- Abdelwahed M. S. T. and Chu V. H. (1978) "Bifurcation of buoyant jets in cross flow," Technical Report No. 78-1, Fluid Mechanics Laboratory, Department of Civil Engineering and Applied Mechanics, McGill University, Montreal, Canada.
- Abraham, G. and Eysink, W. D. (1969) "Jets issuing into fluid with a density gradient," *Journal of Hydraulic Research*, Vol. 7(2), pp 145-175.
- Abraham, G., (1967) "Jets with negative buoyancy in homogeneous fluid," *Journal* of Hydraulic Research, Vol. 5(4), pp 235-248.
- Abraham, G. (1965) "Entrainment principle and its restrictions to solve problems of jets," J. Hydr. Research, Vol. 3(2), pp 1-23.
- Albertson, M. L., Dai, Y. B., Jensen, R. A., and Rouse, H. (1950) "Diffusion of submerged jets," Trans. Am. Soc. Civ. Eng., Vol. 115, pp 639-644.
- Anderson, J. L., Parker, F. L. and Benedict, B. A. (1972) "Negatively buoyant jets in a cross-flow," *International Symposium on Stratified Flows*, Vol. 7(2), pp 467-472.
- Antonia, R. A. and Bilger, R. W. (1973) "An experimental investigation of an axisymmetric jet in a co-flowing air stream," J. Fluid Mech., Vol. 61, pp 805-822.
- Anwar, Habib O. (1969) "Behavior of buoyant jet in calm fluid," J. Hydr. Div. ASCE. vol. 95, pp 1289-1303.

- Ayoub, G, M. (1971) "Dispersion of buoyant jets in a flowing ambient fluid," thesis presented to Imperial College, University of London, at London, England, in partial fulfilment of the requirements for the degree of Doctor of Philosophy.
- Baines, W. D. (1983) "A technique for the direct measurement of volume flux of a plume," J. Fluid Mech., Vol. 132, pp 247-256.
- Baines, W. D., Corriveau, and Reedman, T. J. (1993) "Turbulent fountains in a closed chamber," J. Fluid Mech., Vol. 255, pp 621-646.
- Baines, W. D. and Murphy, T. M. (1986) "The temperature distribution in an enclosed space produced by a forced plume," *Proc. 8th Intl. Heat Transfer Conf.*, San Francisco, Hemisphere, pp 1507-1512.
- Baines, W. D. and Turner, J. S. (1969) "Turbulent buoyant convection from a source in a confined region," J. Fluid Mech., Vol. 37, pp 51-
- Baines, W. D. and Hopfinger, E. J. (1984) "Thermals with Large Density Difference," Atmospheric Environment, Vol. 18, No. 6, pp 1051-1057.
- Baines, W. D., Turner, J. S. and Campbell, I. H. (1990) "Turbulent fountains in an open chamber," J. Fluid Mech., Vol. 212, pp 557-592.
- Barker S. J. and Crow S. C. (1977) "The motion of two-dimensional vortex pairs in a ground effect," J. Fluid Mech., Vol. 82, pp 659-671.
- Bradbury L. J. S. (1965) "The structure of a self-preserving turbulent plane jet," J. Fluid Mech., Vol. 23, pp 31-64.
- Bradbury L. J. S. (1967) "The spread of a turbulent plane jet issuing into a parallel moving airstream," J. Fluid Mech., Vol. 27, pp 381-394.
- Briggs, G. A. (1969) *Plume Rise*, U.S. Atomic Energy Commission Critical Review Series, 81 pp.

- Bringfelt, B. (1969) "A study of buoyant chimney plumes in neutral and stable atmospheres," Atmospheric Environment, Vol. 3, pp 609-623.
- Brown, G. L. (1974) "On density effects and large structure in turbulent mixing layers." J. Fluid Mech., Vol. 64, pp 775-816.
- Cantwell. B. J. (1981) "Organized motion in turbulent flow," Ann. Rev. Fluid Mech., Vol. 13, pp 457-515.
- Chassaing. P., George, J., Claria, A. and Sananes (1974) J. Fluid Mech., Vol. 62, part 1, pp 41-64.
- Cheung, V. (1991) "Mixing of a round buoyant jet in a current," thesis presented to the Department of Civil and Structural Engineering, University of Hong Kong, at Hong Kong, in partial fulfilment of the requirements for the degree of Doctor of Philosophy.
- Chu, V. H., (1975) "Turbulent dense plumes in a laminar cross flow," J. Hydr. Research, Vol. 13(3), pp 263-279.
- Chu, V. H. (1977) "A line-impulse model for buoyant jets in a cross-flow," Heat Transfer and Turbulent Buoyant Convection, Spalding, D. B. and Afgan, N, H. Editors, 850 pp.
- Chu, V.H. (1979) "L.N. Fan's data on buoyant jets in cross-flow," J. of Hydr. Division, ASCE, Vol. 105, No. HY5, pp 612-617.
- Chu V. H. (1985), "Oblique turbulent jets in a cross-flow," J. of Eng. Mechanics, ASCE, Vol. 111, No. 11. 20121.
- Chu, V. H. (1994) "Lagrangian scalings of jets and plumes with dominant eddies," in Recent Research Advances in the Fluid Mechanics of Turbulent Jets and Plumes, NATO ASI Series E: Applied Sciences, Vol. 255, Davies P. A. and Valente Neves, M. J. (ed.), Kluwer Academic Publishers, Dordrecht, pp. 45-72.

- Chu, V. H. and Baines, W. D. (1989) "Entrainment by a buoyant jet between confined walls," J. of Hydraulic Engineering, ASCE, Vol. 115, No. 4, pp 475-492.
- Chu V. H. and Goldberg M. B. (1974) "Buoyant forced plumes in cross-flow," J. Hydr. Div. ASCE. Vol. 100, pp 1203-1214.
- Chu, V. H. and Lee, J. H. W. (1996) "A general integral formulation of turbulent buoyant jets in cross flow," J. of Hydraulic Engineering, ASCE, (in press).
- Crowe, C. T. and Riesebieter, H. (1967) "An analytical and experimental study of jet deflection in a cross flow," Fluid Dynamics of Rotor and Fan Supported Aircraft at Subsonic Speeds, AGARD Reprints.
- Dimotakis, P. E., Miake-Lye, R. C., and Papantoniou, D. A. (1983) "Structure and dynamics of round turbulent jets," *Phys. Fluid*, Vol. 26, no. 11, pp 3185-3192.
- Dimotakis, P. E. (1986) "Two-dimensional shear-Layer entrainment," American Institute of Aeronautics and Astronautics, AIAA, pp 1791-1796.
- Escudier, M. P. and Maxworthy, T. (1973) "On the motion of turbulent thermals," J. Fluid Mech., Vol. 61, pp 541-552.
- Fan, L. N. (1967) "Turbulent buoyant jets into stratified or flowing ambient fluids," Report No. KH-R-15, W. M. Keck Laboratory of Hydraulics and Water Resources, California Institute of Technology, Pasadena, Calif.
- Fisher, H. B., List, E. J., Koh, R. C. Y., Imberger, J., and Brooks, N. H. (1979) "Mixing in inland and coastal waters," Academic Press, NY.
- Forstall, W. and Shapiro, A. H. (1950) "Momentum and mass transfer in coaxial gas jets," Trans. A. S. M. E, J. Appl. Mech., pp 399-408.
- Fox, D. G. (1970) "Forced plume in a stratified fluid," J. Geophysical Research., Vol. 75, pp 6818-6835.

- Fric, T. F. and Roshko. A. (1994) "Vortical structure in the wake of a transverse jet," J. Fluid Mech.. Vol. 279, pp 1-47.
- Gaster, M., Kit, E. and Wygnanski, I. (1985) "Large scale structures in a forced turbulent mixing layer," J. Fluid Mech., Vol. 150, pp 23-39.
- Germeles, A. E. (1975) "Forced plumes and mixing of liquids in tanks," J. Fluid Mech., Vol. 71. pp 601-625.
- Gosman, A. D., Lui, R. and McGuirk. J. J. (1993) "Second-moment closure predictions of buoyant jets in neutral and stratified cross flows," Ninth Symp. on Turbulent Shear Flows, Kyoto, Japan, paper 6.3, pp.1-6.
- Hinze, J. O. (1959) "Turbulence An introduction to its mechanism and theory," McGraw Hill, 586 pp.
- Hirst, E. (1972) "Buoyant jets with three-dimensional trajectories," J. Hydr. Engineering, ASCE, Vol. 98, pp 1999-2014.
- Hoult, D. P., Fay, J. A. and Forney, L. J. (1969) "A theory of plume rise compared with field observations," J. Air. Pollut. Control Ass., Vol. 19, pp 585-590.
- Hoult, D. P. and Weil, J. C. (1969) "Turbulent plume in a laminar cross flow,"

 Atmospheric Environment, Vol. 6, pp 513 531.
- James, W. P., Vergara, I. and Kim, K. (1983) "Dilution of a dense vertical jet," J. Env. Engineering, ASCE, Vol. 109(6), pp 1273-1283.
- Jirka, G. H. and Fong, H. L. M. (1981) "Vortex dynamics and bifurcation of buoyant jets in cross-flow," J. Hydr. Engineering, ASCE, Vol. 107, pp 479-499.
- Jordinson, R. (1956) "Flow in a jet directed normal to the wind," Aeronautical Research Council, London, R and M, 3074.
- Keffer, J. F. and Baines, W. D. (1963) "The round turbulent jet in a cross wind,"
 J. Fluid Mech., Vol. 15, pp 481-496.

- Killworth, P. D. and Turner, J. S. (1982) "Plumes with time varying buoyancy in a confined region," Gephys. Astrophys. Fluid Dynamics, Vol. 20, pp 265-291.
- Lee, J. H. W. and Cheung, V. W. L. (1986) "Inclined plane buoyant jet in stratified fluid," J. Hydr. Engineering, ASCE. Vol. 112(7), pp 580-589.
- Lee, J. H. W. and Neville-Jones, P. (1987a) "Initial dilution of horizontal jet in crossflow," J. of Hydr. Engrg., Vol. 113, No. 5, pp 615-629.
- Lee, J. H. W. and Neville-Jones, P. (1987b) "Sea outfall design prediction of initial dilution," *Proc. Inst. of Civil Engineers*, Vol. 82, No. 1, pp 981-994.
- Lin, S. C., Tsang, L. and Wang, C. P. (1972) "Temperature field structure in strongly heated buoyant thermals." *Phys. Fluids*, Vol. 12, pp 2118-2128.
- Linden, P. F. (1975) "The deepening of a mixed layer in a stratified fluid," J. Fluid Mech., Vol. 71, pp 385-405.
- List, E, J. and Imberger, J. (1973) "Turbulent entrainment in buoyant jets," J. Hydr. Division, ASCE, Vol. 99. pp 1461-1474.
- Malin, M. R. and Younis, B. A. (1990) "Calculation of Turbulent Buoyant Plumes with a Reynolds Stress and Heat Flux Transport Closure," Int'l J. Heat and Mass Transfer, Vol. 33, pp. 2247-2264.
- Margason, R. J. (1968) "The path of a jet directed at large angle to subsonic stream," NASA, TN.D.-4919, Langley Research Center, Hampton, Virginia.
- Morton, B. R. (1957) "Buoyant plumes in a moist atmosphere," J. Fluid Mech., Vol. 2, pp 127-144.
- Morton, B. R. (1956) "Buoyant plumes in a moist atmosphere," J. Fluid Mech., pp 127-144.
- Morton, B. R. (1959) "Forced plumes," J. Fluid Mech., Vol. 5, pp 151-163.

Morton, B., Taylor, G. I. and Turner, J. S. (1956) "Turbulent gravitational convection from maintained and instantaneous sources." Proc. R. Soc. London, Ser. A 234, PP 1-23.

- Muellenhoff, W. P., et al. (1985) "Initial mixing characteristics of municipal ocean discharges," Report EPA-600/3-85-073, U. S. Envir. Protection Agency, Newport, Oreg.
- Moussa, Z. M., Trischka, J. W., Eskinazi, S. (1977) "The near field in the mixing of a round jet with a cross-stream," J. Fluid Mech., Vol. 80, pp 48-80.
- Noh, Y., Fernando, H. J. S. and Ching, C. Y. (1992) "Flows induced by the impingement of a two-dimensional thermal on a density interface," *J. Physical Oceanography*, Vol. 22, pp 1207-1220.
- Ooms, G. (1972) "A new method for the calculation of the plume path of gas emitted by a stack," Atmospheric Environment, Vol. 6, pp 899-900.
- Pincinnee, A. B. and List, E. J. (1973) "Disposal of brine into an estuary," J. of the Water Pollution Control Federation, Vol. 45, pp 2335-2344.
- Platten, J. L. and Keffer, J. F. (1970) "Deflected turbulent jet flows," J. Applied Mechanics, ASME, pp 756-758.
- Pratte, B. D. and Baines, W. D. (1967) "Profiles of the round turbulent jet in a cross flow," J. Hydr. Division, ASCE, Vol. 92, No. HY6, pp 53-64; see also 1968 correction, Vol. 93, No. HY3, pp 815-816.
- Rajaratnam, N. (1972) "Turbulent compound annular shear layers," J. Hydr. Engineering, ASCE, Vol. 98, pp 1101-1115.
- Rajaratnam, N., (1976) "Turbulent jets," Elsevier, Amsterdam, The Netherlands.
- Rajaratnam, N. (1984) "Non-buoyant and buoyant circular surface jets in coflowing streams," J. Hydr. Research, Vol. 22(2), pp 117-140.

- Raymond, D. J., Libersky, L. and Petschek, A. G. (1989) "The development of thermals from rest," *Atmospheric Environment*. Vol. 46, pp 2280 2292.
- Richards, J. M. (1961) "Experiments on the penetration of an interface by buoyant thermals." J. Fluid Mech., Vol. 11. pp 369-384.
- Richards, J. M. (1963) "Experiments on the motions of isolated cylindrical thermals through unstratified surroundings." *Int. J. Wat. poll.*, Vol. 7, pp 17-34.
- Richards, J. M. (1965) "Puff motions in unstratified surroundings," J. Fluid Mech., Vol. 21, pp 97–106.
- Ricou, F. P. and Spalding, D. B. (1961) "Measurements of entrainment by axisymmetrical turbulent jets," J. Fluid Mech., Vol. 11, pp 21-32.
- Roberts, Philip, J. W., and Toms, G. (1987) "Inclined dense jets in flowing current,"

 J. Hydr. Engineering, ASCE, Vol. 113(3), pp 323-341.
- Roberts, J. W. P., Snyder, W. H. and Baumgartner, D. J. (1989) "Ocean outfalls. I: Submerged wasstefield formation." J. Hydr. Engineering, ASCE. Vol. 115(1), pp 1-25.
- Rodi, W. (1980) "Turbulence models and their application in hydraulics." International Association of Hydraulic Research, Monograph, Delft, the Netherlands.
- Rodi, W. and Srivatsa, S. K. (1985) "A locally elliptic calculation procedure for three-dimensional flows and its application to a jet in a cross-flow." J. Fluid Mech., Vol. 150, pp 23-39.
- Saffman, P. G. (1979) "The approach of a vortex pair to a plane surface in inviscid fluid," J. Fluid Mech., Vol. 92, pp 497-503.
- Schatzmann, M. (1978) "The integral equations for round buoyant jets in stratified flow," Z. angew, Math, Phys, Vol. 29, pp 608-630.

- Schatzmann, M. (1979) "An integral model of plume rise," Atmospheric Environment. Vol. 13, pp 721 - 731.
- Schatzmann, M. and Eduard, N. (1980). "Design criteria for cooling-water outlet structures," J. of Hyd. Div., ASCE, Vol. 106, No. HY3
- Schlichting, H., (1986) "Boundary-layer theory," McGraw-Hill BookCompany, U.S.
- Slawson, P. R. and Csanady, G. T. (1967) "On the mean path of buoyant, bent over chimney plumes," J. Fluid Mech., Vol. 28, pp 311-322.
- Slawson, P. R. and Csanady, G. T. (1971) "The effect of atmospheric conditions on plume rise," J. Fluid Mech., Vol. 47, pp 33-49.
- Tong, S. S. and Stolzenbach, K. D. (1979) "Submerged discharges of dense effluent," Rept. No. 243, Ralph M. Parsons Laboratory, Massachusetts Institute of Technology, Cambridge, Mass.
- Tsang, G. (1971) "Laboratory study of line thermals" Atmospheric Environment, Vol. 5, pp 445 471.
- Tsang, G. (1972) "Stack exit velocity distribution for higher effective stack height,"

 Atmospheric Environment, Vol. 6, pp 815 828.
- Turner, J. S. (1960) "A comparison between buoyant vortex rings and vortex pairs,"

 J. Fluid Mech., Vol. 7, pp 419-433.
- Turner, J. S. (1966) "Jets and plumes with negative or reversing buoyancy," J. Fluid Mech., Vol. 26, pp 779-792.
- Turner, J. S. (1986) "Turbulent entrainment: The development of the entrainment assumption, and its application to geophysical flows," J. Fluid Mech., Vol. 173, pp 431-471.
- Turner, J. S. (1979) Buoyancy Effects in Fluids, Cambridge University Press.

- Wang, C. P. (1971) "Motion of an isolated buoyant thermals," Phys. Fluids, Vol. 8. pp 1643-1647.
- Wong, C. F. (1991) "Advected line thermals and Puffs," M. Phil. thesis, Department of Civil and Structural Engineering, University of Hong Kong, 126 pp.
- Wood, I. R., Davidson. M. J. and Knudsen, M. (1991) "The behaviour of a single, horizontally discharged, buoyant flow in a non-turbulent coflowing ambient fluid," J. Hydr. Research, Vol. 29(99), pp 545-566.
- Wright. S. J. (1977) " Effect of ambient cross-flows and density stratification on the characteristic behaviour of round turbulent buoyant jets," Report No. KH-R-36, W. M. Keck Laboratory of Hydraulics and Water Resources, California Institute of Technology. Pasadena, Calif.
- Wright, S. J. (1984) "Buoyant jets in density-stratified crossflow," J. Hydr. Engineering, ASCE, Vol. 110(5), pp 643-656.
- Wygnanski, I. J. and Fiedler, H. (1969) "Some measurement in the self-preserving jet." J. Fluid Mech., Vol. 38, no.3, pp 577-612.
- Yih, C. S. (1977) "Turbulent buoyant plumes," *Physics of Fluids*, Vol. 20, pp 1234-1237.
- Yih, C. S. (1969). Fluid Mechanics, McGraw Hill, Inc.
- Yoda, M., Hesselink, L. and Mungal, M. G. (1992) "The evolution and nature of large-scale structure in the turbulent jet," *Phys. Fluids*, Vol. 4(4), pp 803-811.
- Zeitoun. M. A., et al. (1970). "Conceptual designs of outfall systems for desalting plants," Research and Development Progress Rept. No. 550, Office of Saline Water, U. S. Dept. Of Interior.

Appendix A

Line Thermal Images

The line-thermal cross section at 4 second intervals obtained from the video imaging method is given in this appendix. Images obtained for all six tests are provided. The tracer concentration is linearly proportional to the grey scale level.

Test No. 1 $t = 4 s$	t = 20 s
t = 8 s	t = 24 s
t = 12 s	t = 28 s
t = 16 s	t = 32 s

Figure A.1: Images of test no. 1 at 4 second intervals.

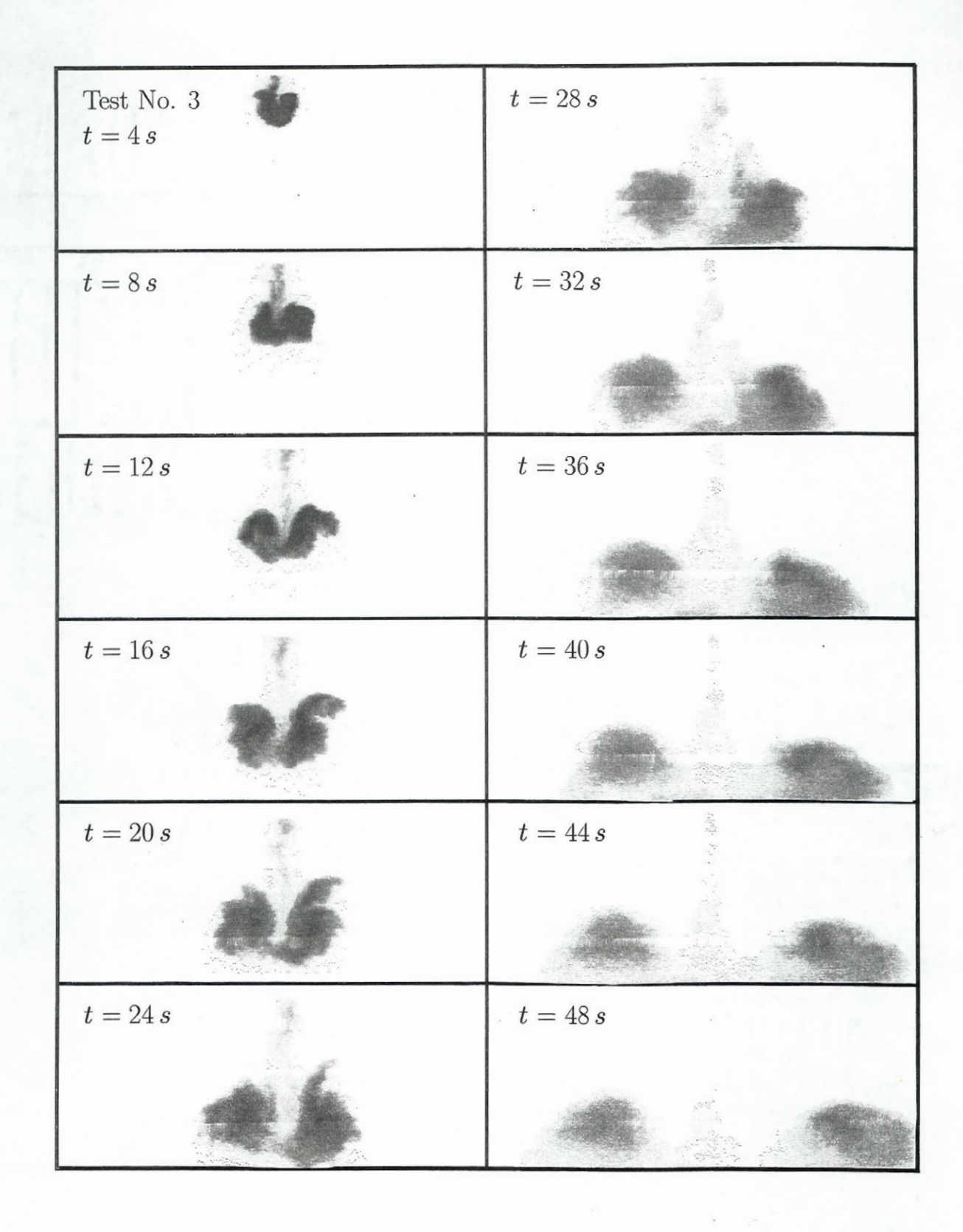


Figure A.3: Images of test no. 3 at 4 second intervals.

Appendix A

_ 145

Test No. 4 $t = 4s$	t = 20 s
t = 8 s	t = 24 s
t = 12 s	t = 28 s
t = 16 s	t = 32 s

Figure A.4: Images of test no. 4 at 4 second intervals.

Appendix A _______146

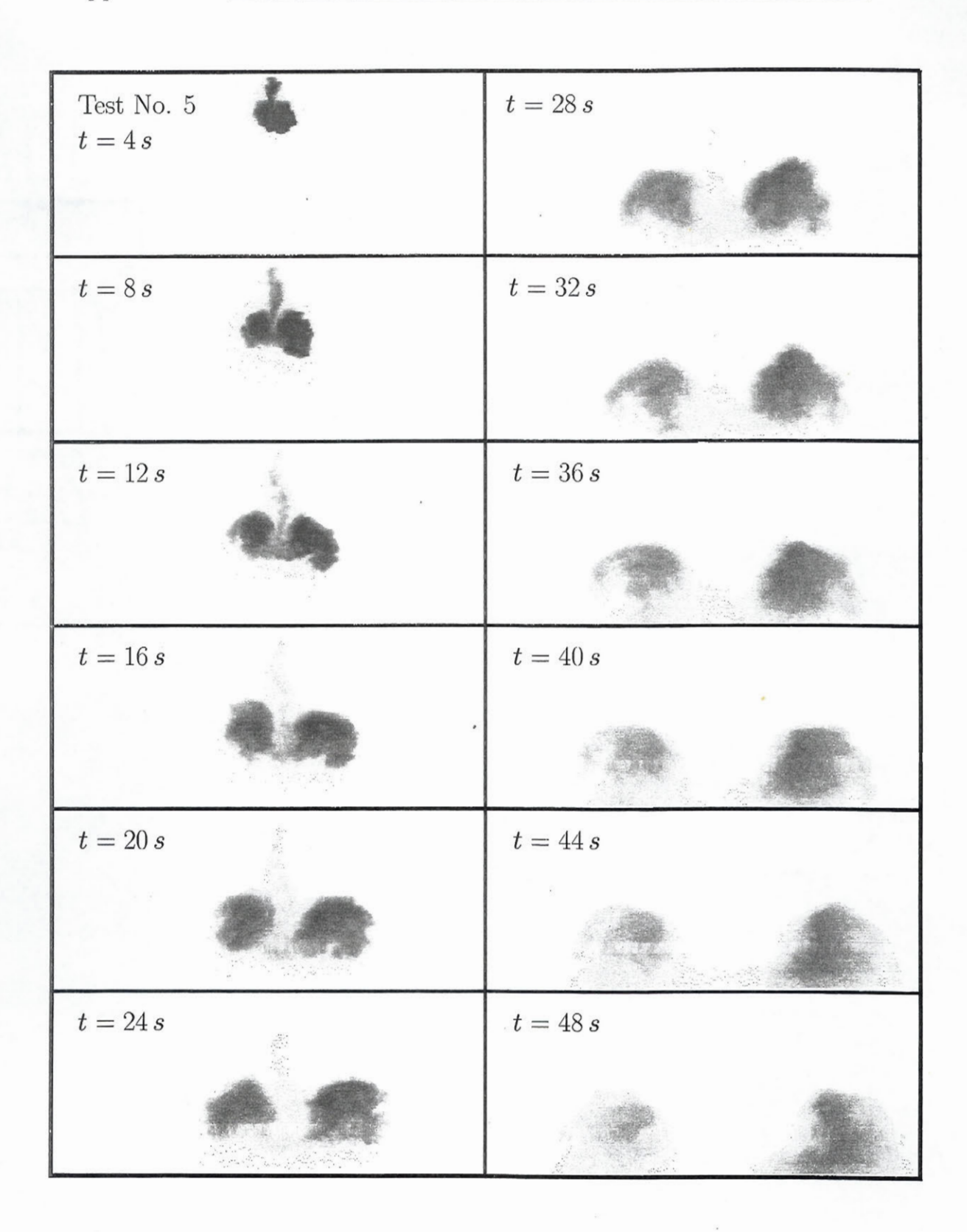


Figure A.5: Images of test no. 5 at 4 second intervals.

Appendix A _______147

Test No. 6 $t = 4 s$	t = 20 s
t = 8 s	t = 24 s
t = 12 s	t = 28 s
t = 16 s	t = 32 s

Figure A.6: Images of test no. 6 at 4 second intervals.

Appendix B

Concentration Contours

The concentration contours of the line-thermal cross sections obtained at 4 second intervals from the video imaging method is given in this appendix. Images obtained for all six tests are provided. The contour interval is equal to 20% of the averaged concentration over the cross section, that is $\Delta C = 0.2C_a$. The concentration of the first contour line is $0.2C_a$.

Test No. 1 $t = 4s$	t = 20 s
t = 8 s	t = 24 s
t = 12 s	t = 28 s
t = 16 s	t = 32 s

Figure B.1: Concentration contours of the images in test no.1 at 4 sec intervals.

Test No. 2 $t = 4 s$	t = 20 s
t = 8s	t = 24 s
t = 12 s	t = 28 s
t = 16 s	t = 32 s

Figure B.2: Concentration contours of the images in test no.2 at 4 sec intervals.

Appendix B _______ 151

Test No. 3 $t = 4 s$	t = 28 s
t = 8 s	t = 32 s
t = 12 s	t = 36 s
t = 16 s	t = 40 s
t = 20 s	t=44s
t = 24 s	t = 48 s

Figure B.3: Concentration contours of the images in test no.3 at 4 sec intervals.

Appendix B _______ 152

Test No. 4 $t = 4s$	t = 20 s
t = 8 s	t = 24 s
t = 12 s	t=28 s
t = 16 s	t=32s

Figure B.4: Concentration contours of the images in test no.4 at 4 sec intervals.

Test No. 5 $t = 4s$	t = 28 s
t = 8 s	t = 32 s
t = 12 s	t = 36 s
t = 16 s	t=40s
t = 20 s	t = 44 s
t = 24 s	t = 48 s

Figure B.5: Concentration contours of the images in test no.5 at 4 sec intervals.

		· · .
Test No. 6 $t = 4s$	t=20 s	•.
t = 8 s	t=24s	
t = 12 s	t = 28 s	
t = 16 s	t=32s	

Figure B.6: Concentration contours of the images in test no.6 at 4 sec intervals.

Appendix C

Cross Sections defined by the 20% Contours

The line-thermal cross sections defined by 20% of average concentration, $(0.2C_a)$, are presented for all six tests. The key coordinates $(x_i, y_i; i = 1, 8)$ marked on cross sections obtained by visual observation are identical to those of images in Appendix A.

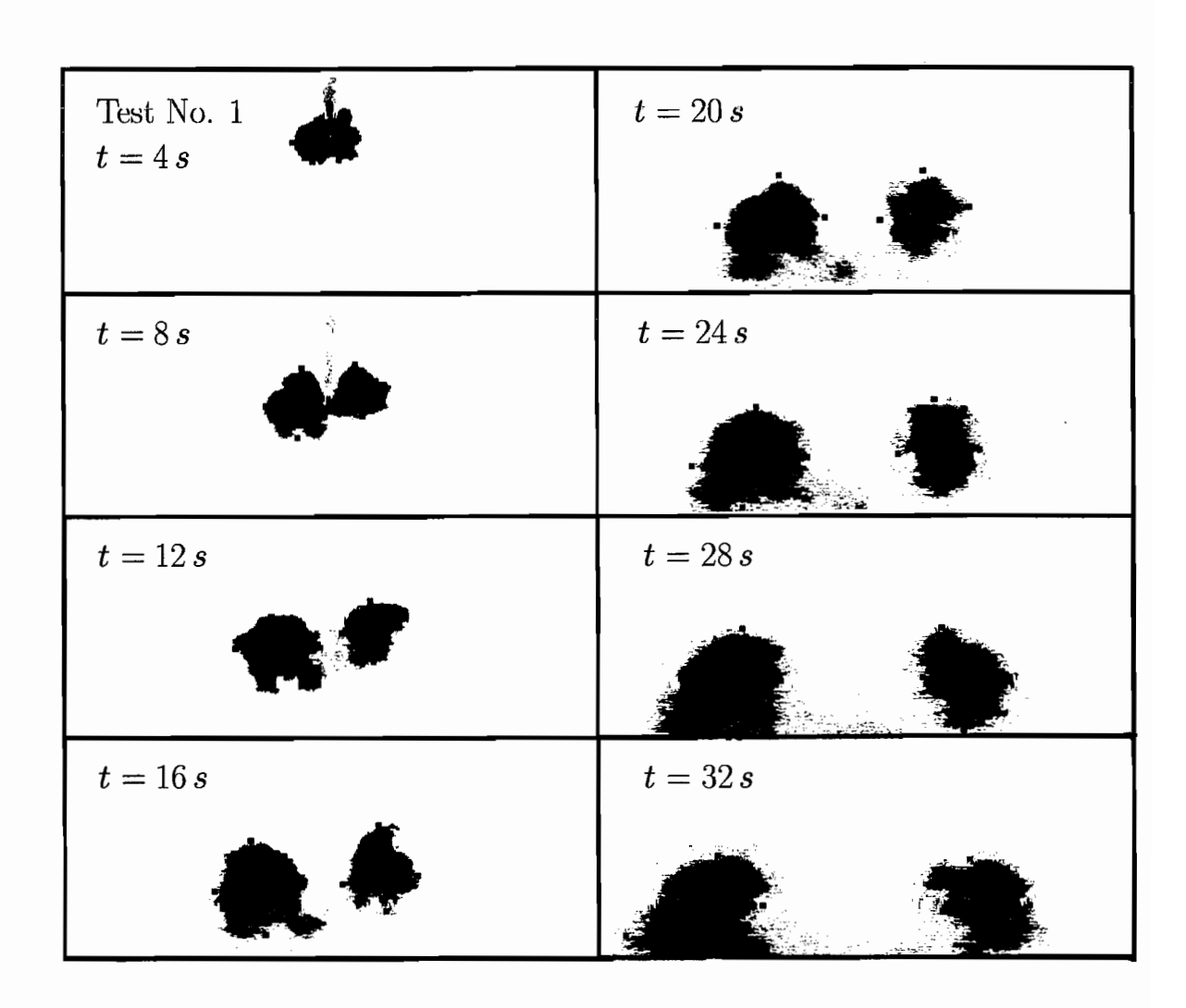


Figure C.1: Images of test no.1 defined by the 20% contour; the key coordinates are marked.

Test No. 2 $t = 4s$	t = 20 s
t = 8 s	t=24 s
t = 12 s	t = 28 s
t = 16 s	t = 32 s

Figure C.2: Images of test no.2 defined by the 20% contour; the key coordinates are marked.

158

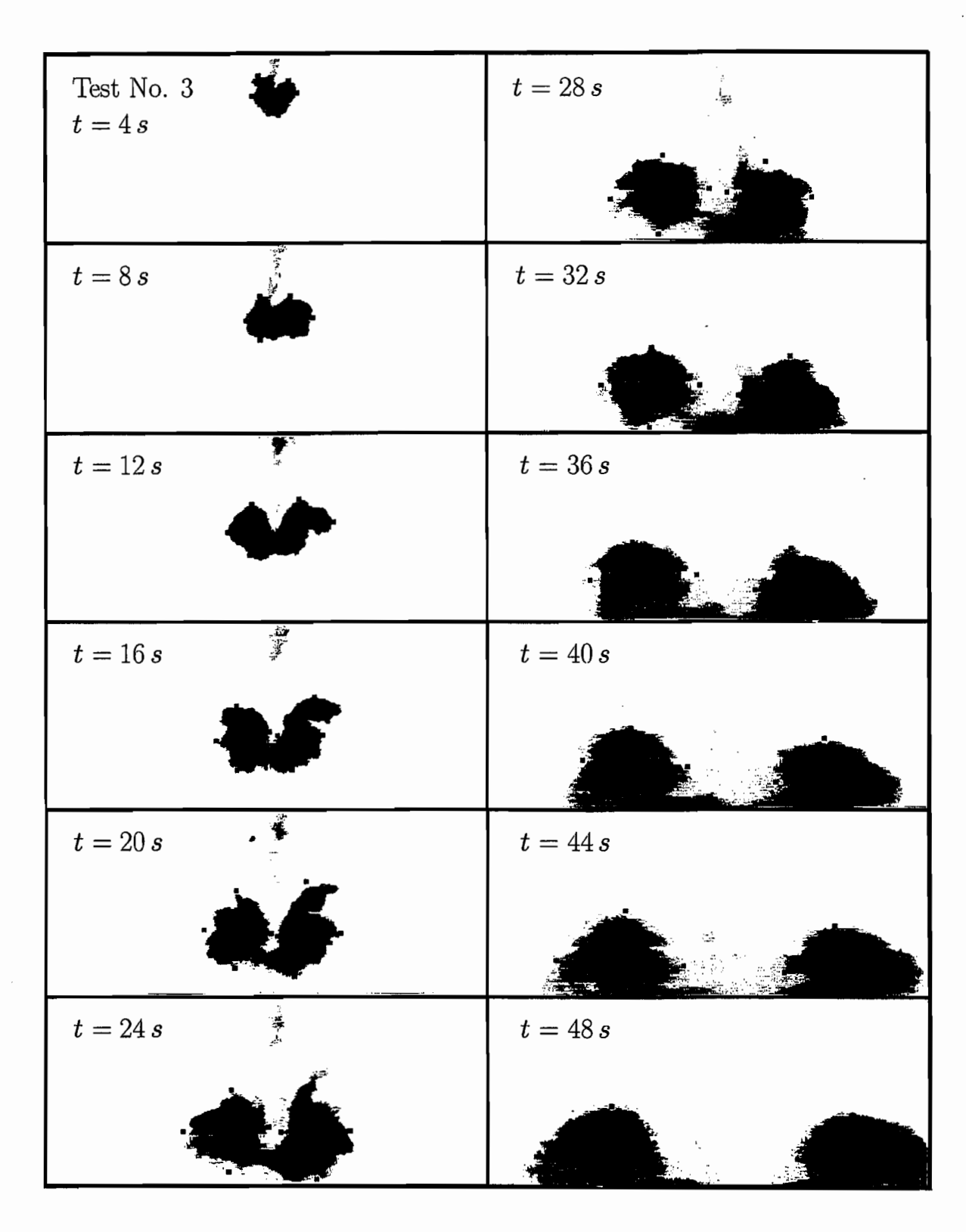


Figure C.3: Images of test no.3 defined by the 20% contour; the key coordinates are marked.

______159

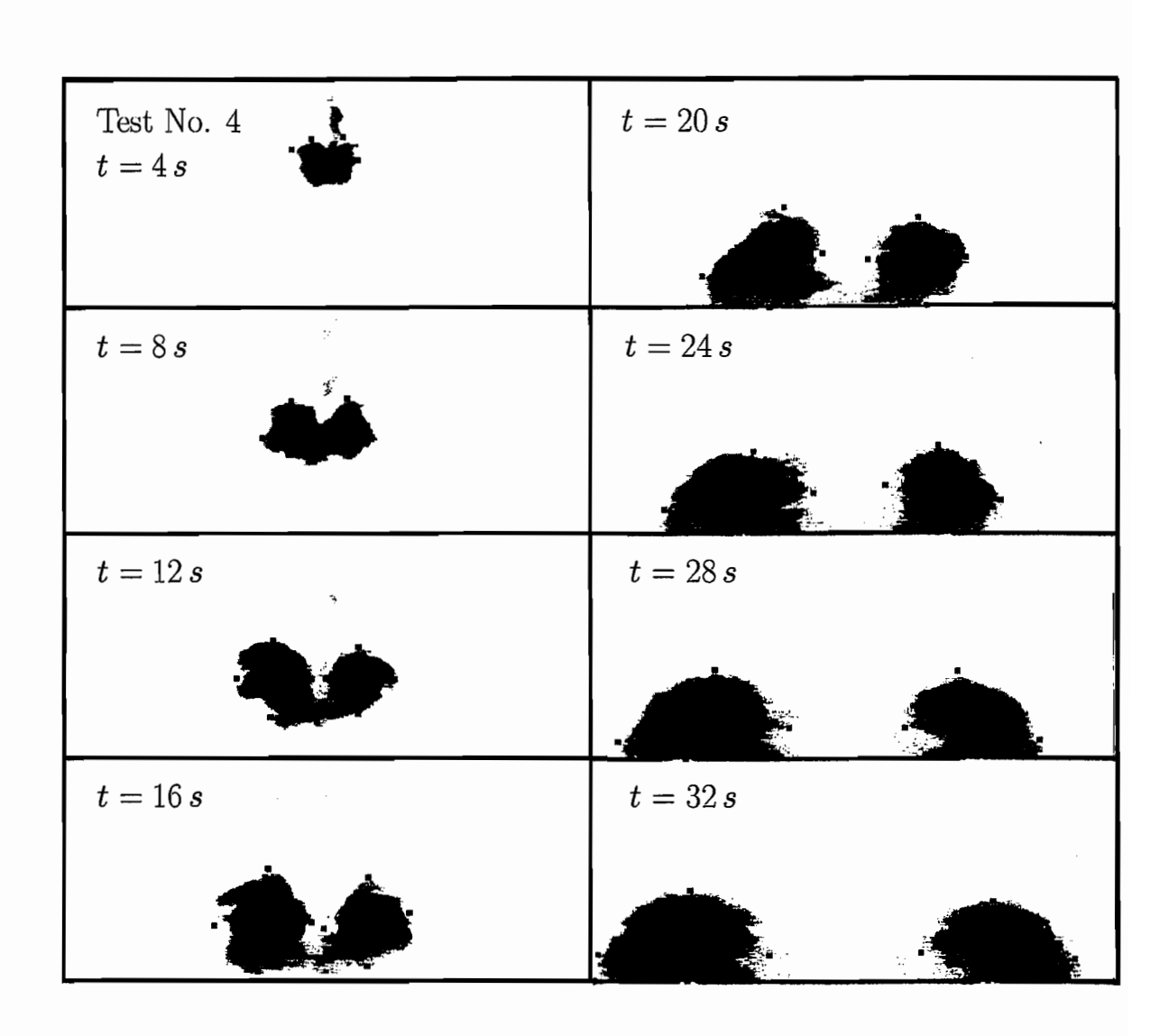


Figure C.4: Images of test no.4 defined by the 20% contour; the key coordinates are marked.

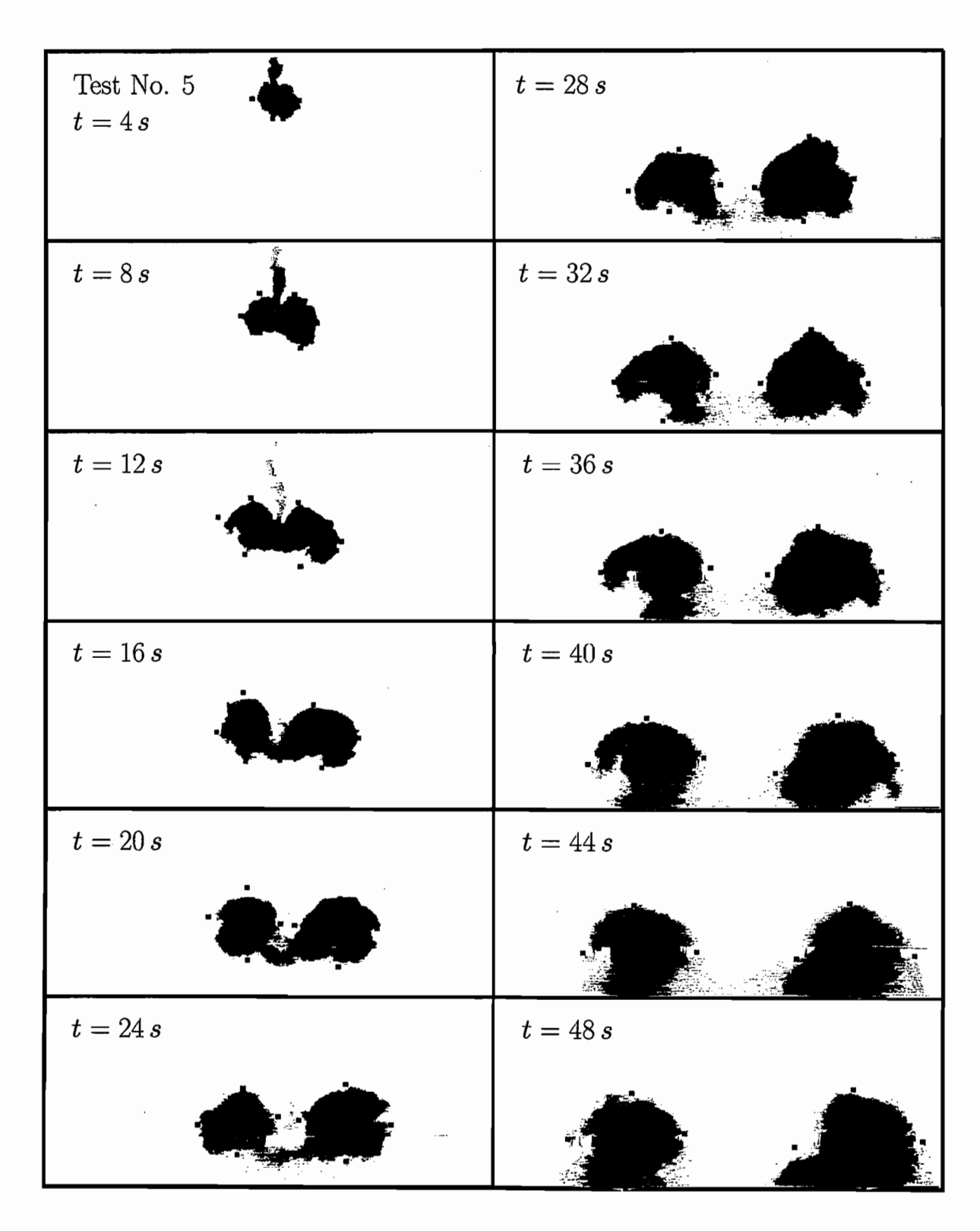


Figure C.5: Images of test no.5 defined by the 20% contour; the key coordinates are marked.

Appendix C ______ 161

Test No. 6 $t = 4s$	t = 20 s
t = 8 s	t=24s
4.5	
t = 12 s	t = 28 s
t = 16 s	t = 32 s

Figure C.6: Images of test no.6 defined by the 20% contour; the key coordinates are marked.

Appendix D

Experimental Data

This appendix provides the experimental data. Location of the source (x_o, y_o) and locations of the key coordinates $(x_i, y_i; i = 1, 8)$ are given in Tables D.1. The maximum concentration data obtained at cores of vortex pair are provided in Tables D.2.

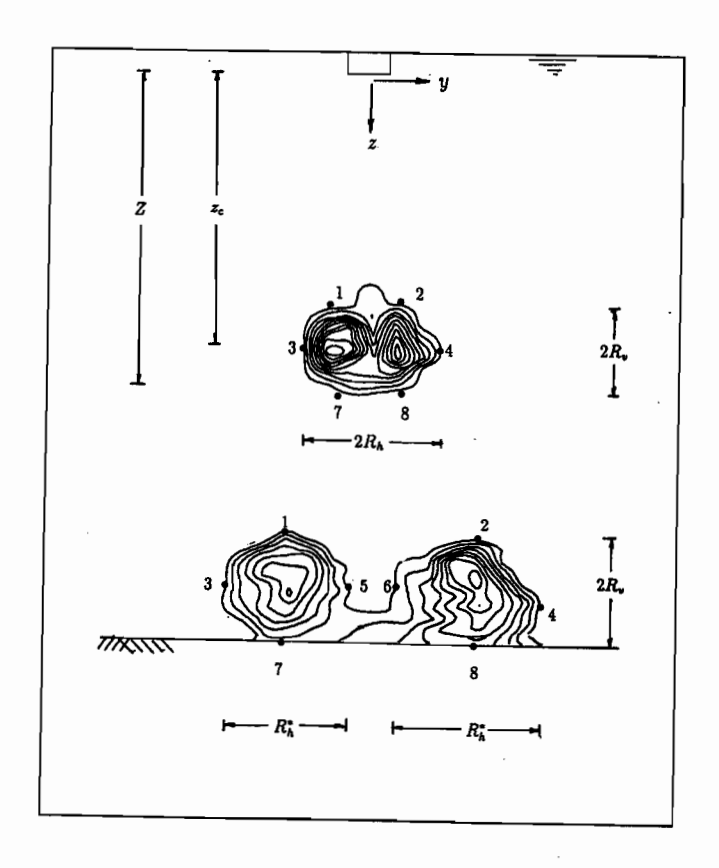


Figure D.1: Definition for the location of the key coordinates $(x_i, y_i; i = 1, 8)$.

image	t	x_o	y_o	$\overline{x_1}$	y_1	x_2	y_2	x_3	y_3
No.	sec	cm	cm	cm	cm	cm	cm	cm	cm
1001	2	125	157	121	13	128	13	114	20
1002	4	125	157	119	24	129	21	109	35
1003	6	125	157	113	32	131	30	103	46
1004	8	125	157	112	36	134	34	97	54
1005	10	125	157	104	46	134	39	92	57
1006	12	125	157	99	49	140	42	84	64
1007	14	125	157	95	49	142	42	80	62
1008	16	125	157	90	49	143	42	75	73
1009	18	125	157	89	49	142	42	70	77
1010	20	125	157	88	51	148	49	62	75
1011	22	125	157	84	54	148	49	58	78
1012	24	125	157	79	54	151	50	51	85
1013	26	125	157	75	54	155	50	45	80
1014	28	125	157	74	54	157	51	38	87
1015	30	125	157	72	54	156	56	31	87
1016	32	125	157	64	54	171	56	22	90
1017	34	125	157	63	54	172	56	17	85
1018	36	125	157	54	54	172	55	13	92
2001	2	125	157	120	10	129	11	117	16
2002	4	125	157	118	22	131	23	113	32
2003	6	125	157	116	31	132	30	105	50
2004	8	125	157	110	43	135	48	98	56
2005	10	125	157	107	48	137	52	93	61
2006	12	125	157	101	51	142	54	88	66
2007	14	125	157	98	52	145	56	84	68
2008	16	125	157	94	54	150	56	81	64
2009	18	125	157	92	50	152	54	77	67
2010	20	125	157	91	51	155	54	74	75
2011	22	125	157	90	51	156	54	71	81
2012	24	125	157	89	51	157	53	63	90
2013	26	125	157	88	53	160	55	53	93
2014	28	125	157	88	54	157	55	42	97
2015	30	125	157	88	58	163	57	35	92
2016	32	125	157	88	59	166	61	27	96
2017	34	125	157	85	61	164	62	20	91
2018	36	125	157	69	61	170	62	15	87

Table D.1: Source coordinates (x_o, y_o) and key coordinates $(x_i, y_i, i = 1, 8)$.

image	x_4	y_4	x_5	y_5	x_6	y_6	x_7	y_7	x_8	y_8
No.	cm									
1001	132	18	125	14	125	13	120	28	126	29
1002	136	33	124	29	125	30	117	44	128	43
1003	141	41	124	43	125	41	112	58	134	52
1004	146	49	120	50	127	48	110	69	137	59
1005	148	49	119	55	127	55	106	74	137	65
1006	153	49	119	64	128	57	99	79	141	71
1007	154	64	113	64	128	64	97	85	141	76
1008	159	66	112	70	128	70	96	94	146	83
1009	163	65	109	74	130	68	87	99	146	87
1010	167	66	107	71	130	72	80	100	147	88
1011	168	70	105	74	131	67	80	102	154	95
1012	175	78	102	79	131	80	75	106	159	100
1013	181	79	98	78	133	78	70	106	157	104
1014	186	78	93	77	136	78	66	106	166	106
1015	189	77	91	77	137	76	63	106	169	103
1016	193	83	89	78	137	78	56	106	171	106
1017	203	86	89	79	142	79	50	107	175	106
1018	209	86	81	78	147	79	46	107	182	107
2001	132	17	125	11	125	11	122	26	126	27
2002	137	32	124	26	125	26	119	44	126	49
2003	139	51	124	40	125	42	114	60	129	62
2004	144	64	120	56	127	59	107	68	140	69
2005	152	66	120	65	130	63	107	75	140	75
2006	160	68	120	67	130	69	104	78	147	79
2007	164	68	120	75	130	72	107	87	147	84
2008	167	71	116	79	130	77	104	92	148	87
2009	172	71	116	71	131	73	102	101	148	99
2010	174	69	116	75	131	82	103	105	148	102
2011	176	77	113	75	132	81	93	106	154	106
2012	178	80	113	82	135	84	87	107	158	107
2013	189	89	107	81	142	77	81	107	163	107
2014	201	97	104	74	143	84	71	107	169	106
2015	209	97	101	79	148	83	66	107	177	107
2016	213	93	98	79	149	84	69	107	167	107
2017	222	95	98	83	151	88	57	107	188	108
2018	228	94	97	81	151	85	51	107	194	108

Source coorindates (x_o, y_o) and key coordinates $(x_i, y_i, i = 1, 8)$, contd.

im	1				46				2/-
image No.	t	x _o	y_o	x_1	y ₁	$\begin{array}{c c} x_2 \\ \text{cm} \end{array}$	$\frac{y_2}{\mathrm{cm}}$	x ₃ cm	y_3 cm
_	sec	cm	cm 167	119	cm	128	11	116	16
3001	2	124	l	l	11	I	ı	l	ı
3002	4	124	167	118	13	133	16	115	25
3003	6	124	167	117	22	131	25	113	35
3004	8	124	167	118	31	133	31	111	45
3005	10	124	167	115	40	136	37	107	52
3006	12	124	167	114	42	137	39	102	58
3007	14	124	167	112	46	140	43	98	56
3008	16	124	167	107	48	145	43	97	68
3009	18	124	167	107	48	144	43	95	68
3010	20	124	167	107	48	141	43	91	71
3011	22	124	167	106	52	148	43	83	81
3012	24	124	167	104	55	143	54	80	78
3013	26	124	167	101	60	144	62	76	85
3014	28	124	167	99	60	150	64	73	85
3015	30	124	167	94	61	157	68	70	82
3016	32	124	167	93	61	162	66	68	82
3017	34	124	167	90	62	163	65	64	83
3018	36	124	167	83	63	162	67	62	85
3019	38	124	167	83	63	164	71	60	85
3020	40	124	167	82	63	178	69	58	81
3021	42	124	167	78	63	181	70	50	93
3022	44	124	167	78	59	182	68	44	88
3023	46	124	167	78	60	187	67	41	90
3024	48	124	167	73	64	192	69	36	92
4001	2	124	167	120	13	127	15	115	22
4002	4	124	167	115	28	128	27	107	33
4003	6	124	167	113	.37	129	40	100	53
4004	8	124	167	107	45	130	44	95	63
4005	10	124	167	103	51	133	54	88	61
4006	12	124	167	99	52	134	55	84	70
4007	14	124	167	99	53	136	59	83	71
4008	16	124	167	97	54	138	58	75	82
4009	18	124	167	93	58	141	63	71	82
4010	20	124	167	92	60	148	65	58	93
4011	22	124	167	91	65	152	66	49	94
4012	24	124	167	79	69	156	66	42	97
4013	26	124	167	67	67	162	66	35 1	00
4014	28	124	167	64	65	165	66	24 1	00
4015	30	124	167	57	66	172	69	20	97
4016	32	124	167	53	64	179	69	15	95
	102	/	101	100	- 1		/ 00		9) -

Source coordinates (x_o, y_o) and key coordinates $(x_i, y_i, i = 1, 8)$, contd.

x_5	y_5	x_6	y_6	x_7	y_7	m o	A1-
cm.				1		x_8	y_8
	cm	cm	cm	cm	cm	cm	cm
1	13	125	13	120	21	128	23
							36
125	1	ı	I .	1 1			47
123	40		l .				54
123	50			l '			59
123	58	127	57			1 1	69
123	60	127	60	l .			76
123	63	127	65	107			85
123	71	127	71	107			90
124	73	127	75	106			98
124	71	127	74	104	98	139	103
122	76	128	79	102	101	145	106
122	85	128	83	105	104	153	106
122	79	131	81	97	105	150	107
118	82	132	85	94	106	160	107
117	82	136	88	92	106	165	108
116	83	140	90	91	106	168	107
115	82	144	91	83	106	171	108
112	89	148	91	80	106	183	102
110	85	154	94	76	107	186	108
108	88	153	95	76	107	130	101
107	91	157	95	73	107	190	108
103	90	160	95	71	108	198	108
96	91	165	94	70	108	201	108
123	22	120	22	120	29	126	30
121	34	120	34	117	49	127	48
120	52	120	52	109	63	126	63
117	57	120	60	106	71	131	72
117	66	121	65	101	79	133	82
115	70	121	70	98	89	134	87
115	74	120	79	94	99	131	96
115	80	120	83	93	104	138	101
115	87	121	86	88	108	138	105
108	82	127	85	86	108	148	106
106	87	132	85	82	108	154	108
104	89	134	85	73	108	159	107
100	88	140	90	65	108	167	108
95	93	143	93	52	108	173	107
1	96	145	92	54	108	181	108
	95	149	94	52	108	177	108
86122060860186168768867607661620087	3 125 4 123 4 123 2 123 2 123 3 123 4 123 5 124 6 124 122 122 4 122 4 122 5 116 8 108 107 103 4 96 8 123 120 107 117 115 115 115 115 115 106 106 109 95 3 91 7 86	3 125 22 4 125 35 4 123 40 2 123 50 2 123 60 3 123 61 4 123 63 6 123 71 7 122 76 8 124 71 9 122 76 1 122 78 1 122 78 1 122 78 1 122 78 1 122 78 1 122 78 1 122 78 1 115 82 1 112 89 1 103 90 1 103 90 1 103 90 1 123 22 1 115 70 1 115 70 1 115 80 1 106 87	3 125 22 125 4 125 35 126 4 123 40 126 2 123 50 125 2 123 58 127 3 123 60 127 4 123 63 127 5 123 71 127 6 124 71 127 7 122 76 128 8 122 79 131 8 122 79 131 8 122 79 131 8 112 85 128 9 124 71 127 9 124 71 127 9 124 72 136 117 82 136 110 83 140 115 82 144 12 89 148 13 103 90 160 14 103 90 160<	3 125 22 125 22 4 125 35 126 34 4 123 40 126 41 2 123 50 125 49 2 123 58 127 57 3 123 60 127 60 4 123 63 127 65 5 123 71 127 71 6 123 71 127 74 7 124 71 127 74 8 124 73 127 75 9 122 76 128 79 13 81 82 132 85 14 122 85 128 83 117 82 136 88 117 82 136 88 117 82 136 88 110 85 154 94 12 89 148 91 13	3 125 22 125 22 123 4 125 35 126 34 120 4 123 40 126 41 118 2 123 50 125 49 114 2 123 58 127 57 113 3 123 60 127 60 114 4 123 63 127 65 107 5 123 71 127 71 107 6 124 71 127 74 104 7 122 76 128 79 102 8 122 85 128 83 105 8 122 79 131 81 97 8 118 82 132 85 94 117 82 136 88 92 13 117 82 136 88 92 14 91 83 144 91 83	8 125 22 125 22 123 35 6 125 35 126 34 120 46 6 123 40 126 41 118 56 7 123 50 125 49 114 64 8 123 58 127 57 113 71 9 123 60 127 60 114 80 9 123 63 127 65 107 85 9 123 71 127 71 107 90 9 123 71 127 75 106 93 9 124 73 127 75 106 93 9 122 76 128 79 102 101 9 122 76 128 79 102 101 9 122 76 128 83 105 104 9 122 79 131 81 97	8 125 22 125 22 123 35 128 6 125 35 126 34 120 46 130 8 123 40 126 41 118 56 134 8 123 50 125 49 114 64 136 9 123 60 127 60 114 80 137 9 123 63 127 65 107 85 134 9 123 71 127 71 107 90 133 9 123 71 127 71 107 90 133 9 123 71 127 74 104 98 139 124 71 127 74 104 98 139 122 76 128 79 102 101 145 13 122 76 128 83 105 104 153 13 122 79 <td< td=""></td<>

Source coordinates (x_o, y_o) and key coordinates $(x_i, y_i, i = 1, 8)$, cont'd.

image	t	x_o	y_o	x_1	<i>y</i> ₁	x_2	y_2	x_3	y_3
No.	sec	cm	cm	cm	cm	cm	cm	cm	cm
5001	2	123	164	118	8	125	8	114	14
5002	4	123	164	118	19	127	20	111	27
5003	6	123	164	117	26	129	26	108	35
5004	8	123	164	115	30	132	31	106	$\begin{vmatrix} 33 \\ 43 \end{vmatrix}$
5005	10	123	164	114	35	135	36	103	46
5006	12	123	164	111	37	134	40	95	48
5007	14	123	164	111	38	139	42	95	53
5008	16	123	164	108	40	142	47	95	62
5009	18	123	164	108	43	150	49	91	61
5010	20	123	164	108	44	153	51	89	61
5011	22	123	164	108	48	155	49	87	72
5012	24	123	164	107	51	157	49	85	71
5013	26	123	164	109	52	160	48	80	79
5014	28	123	164	99	56	163	49	74	79
5015	30	123	164	96	54	163	50	71	82
5016	32	123	164	96	54	165	50	68	79
5017	34	123	164	96	56	165	52	64	80
5018	36	123	164	91	56	168	54	61	79
5019	38	123	164	89	57	171	55	59	80
5020	40	123	164	84	55	178	54	55	81
5021	42	123	164	82	56	180	51	55	80
5022	44	123	164	77	54	183	53	52	82
5023	46	123	164	77	53	183	52	48	77
5024	48	123	164	77	54	186	53	46	80
5025	50	123	164	77	54	189	53	42	84
6001	2	127	153	123	20	131	19	122	24
6002	4	127	153	119	34	140	31	112	41
6003	6	127	153	117	36	146	34	108	50
6004	8	127	153	116	46	151	42	106	63
6005	10	127	153	115	54	149	45	102	74
6006	12	127	153	114	60	157	54	95	79
6007	14	127	153	107	65	157	53	84	84
6008	16	127	153	102	66	163	54	74	87
6009	18	127	153	93	66	163	54	65	90
6010	20	127	153	86	65	164	57	58	92
6011	22	127	153	83	64	169	58	50	89
6012	24	127	153	79	64	169	60	44	89
6013	26	127	153	76	64	183	65	39	86
6014	28	127	153	67	64	191	64	24	92
6015	30	127	153	62	64	200	63	18	90
6016	32	127	153	56	65	203	62	13	92

Source coorindates (x_o, y_o) and key coordinates $(x_i, y_i, i = 1, 8)$, cont'd.

	image	x_4	<i>y</i> ₄	x_5	<i>y</i> ₅	x_6	y_6	<i>x</i> ₇	y_7		y_8
	No.	cm	cm	cm	cm	cm	cm	cm	cm	cm	cm
	5001	130	14	124	14	121	13	122	21	125	21
	5002	134	28	124	28	124	26	121	3 8	126	38
-	5003	140	36	124	34	124	34	117	43	131	52
	5004	143	47	123	38	124	40	115	52	135	61
	5005	147	52	123	50	124	49	113	60	137	69
	5006	155	62	123	51	126	53	108	69	135	76
	5007	160	62	123	56	126	52	110	67	143	80
١	5008	164	66	121	63	129	65	109	79	146	83
	5009	168	64	120	63	131	68	107	82	150	87
	5010	171	68	124	65	131	66	108	86	152	90
	5011	175	69	125	66	134	71	106	87	153	92
١	5012	179	72	124	67	134	69	104	88	157	92
	5013	181	74	121	74	135	76	129	90	157	95
	5014	185	73	119	76	136	78	94	91	160	97
	5015	187	76	118	69	139	80	98	100	167	101
ļ	5016	193	80	118	75	140	80	92	101	166	99
	5017	195	79	116	75	143	80	92	103	170	102
	5018	199	80	115	77	143	81	87	104	170	104
	5019	202	79	114	79	146	82	90	105	176	105
	5020	207	82	112	78	147	87	86	106	178	106
	5021	209	82	111	77	150	88	85	106	184	106
ļ	5022	215	83	108	81	157	85	79	107	186	106
	5023	217	81	105	79	154	82	76	107	186	107
	5024	220	82	103	77	157	85	74	108	191	107
1	5025	225	93	103	86	157	78	71	108	192	107
	6001	137	24	128	24	128	24	125	31	131	31
1	6002	149	40	128	39	131	38	121	50	141	52
Į	6003	157	50	130	52	134	51	128	68	144	64
	6004	163	60	130	61	135	59	125	- 84	151	76
1	6005	167	67	128	69	137	66	114	92	151	83
ı	6006	175	70	127	74	137	72	107	96	152	87
	6007	182	69	126	78	137	77	106	104	153	97
	6008	184	72	125	80	139	77	100	107	157	101
	6009	185	75	118	86	140	80	91	107	165	106
	6010	189	80	114	86	141	80	87	107	169	107
	6011	203	92	110	89	140	82	79	107	174	107
	6012	214	92	106	86	145	86	74	107	178	107
	6013	225	97	104	90	148	85	67	107	186	107
	6014	232	95	100	90	151	92	57	108	194	107
	6015	235	92	94	95	155	93	53	108	202	107
	6016	235	90	88	94	165	95	48	108	208	107
_	urce coo	rindat	oc (r	<i>u</i>) :	and be	W COO	rdina	tac (r	. 11. i	- 1 R	cont

Source coorindates (x_o, y_o) and key coordinates $(x_i, y_i, i = 1, 8)$, cont'd.

image	C_o	C_a/C_o	(C_m/C_a)	$\overline{(C_m/C_a)}$	C_m/C_a
No.	g/liter	-	left	right	ave
1001	0.20	0.0370	1.50	1.50	1.50
1001	0.20	0.0260	1.50	1.50	1.50
1003	0.20	0.0190	1.70	1.50	1.60
1004	0.20	0.0161	1.90	1.50	1.70
1005	0.20	0.0142	1.85	1.40	1.62
1006	0.20	0.0130	1.80	1.30	1.55
1007	0.20	0.0123	1.85	1.30	1.58
1008	0.20	0.0112	1.90	1.30	1.60
1009	0.20	0.0105	1.95	1.45	1.70
1010	0.20	0.0098	2.00	1.60	1.80
1011	0.20	0.0094	1.95	1.45	1.70
1012	0.20	0.0091	1.90	1.30	1.60
1013	0.20	0.0088	1.80	1.30	1.60
1014	0.20	0.0081	1.70	1.30	1.60
1015	0.20	0.0076	1.80	1.30	1.60
1016	0.20	0.0077	1.90	1.30	1.60
1017	0.20	0.0075	1.85	1.30	1.60
1018	0.20	0.0072	1.85	1.30	1.60
2001	0.40	0.0600	1.50	1.50	1.50
2002	0.40	0.0255	1.50	1.50	1.50
2003	0.40	0.0187	1.60	1.40	1.50
2004	0.40	0.0168	1.70	1.30	1.50
2005	0.40	0.0153	1.70	1.50	1.60
2006	0.40	0.0137	1.70	1.70	1.70
2007	0.40	0.0124	1.75	1.70	1.73
2008	0.40	0.0110	1.80	1.70	1.75
2009	0.40	0.0103	1.72	1.60	1.66
2010	0.40	0.0095	1.65	1.50	1.58
2011	0.40	0.0096	1.47	1.40	1.44
2012	0.40	0.0089	1.30	1.30	1.30
2013	0.40	0.0090	1.50	1.40	1.45
2014	0.40	0.0087	1.70	1.50	1.60
2015	0.40	0.0083	1.60	1.50	1.55
2016	0.40	0.0080	1.50	1.50	1.50
2017	0.40	0.0077	1.55	1.50	1.55
2018	0.40	0.0076	1.55	1.50	1.55

Table D.2: Average concentration, C_a , and maximum concentration at the cores of the votex pair, C_m .

image	C_o	C_a/C_o	(C_m/C_a)	(C_m/C_a)	$C_m/\overline{C_a}$
No.	g/liter	-	left	right	ave
3001	0.40	0.1390	1.50	1.50	1.50
3002	0.40	0.0311	1.50	1.50	1.50
3003	0.40	0.0245	1.47	1.50	1.49
3004	0.40	0.0214	1.45	1.50	1.48
3005	0.40	0.0191	1.47	1.60	1.54
3006	0.40	0.0166	1.50	1.70	1.60
3007	0.40	0.0147	1.50	1.70	1.60
3008	0.40	0.0136	1.50	1.70	1.60
3009	0.40	0.0126	1.50	1.67	1.59
3010	0.40	0.0119	1.50	1.65	1.58
3011	0.40	0.0113	1.55	1.67	1.62
3012	0.40	0.0109	1.60	1.65	1.65
3013	0.40	0.0107	1.55	1.75	1.65
3014	0.40	0.0104	1.50	1.80	1.65
3015	0.40	0.0103	1.50	1.75	1.63
3016	0.40	0.0099	1.50	1.70	1.60
3017	0.40	0.0096	1.50	1.70	1.60
3018	0.40	0.0092	1.50	1.70	1.60
3019	0.40	0.0090	1.50	1.75	1.63
3020	0.40	0.0087	1.50	1.80	1.65
3021	0.40	0.0087	1.50	1.75	1.63
3022	0.40	0.0084	1.50	1.70	1.60
3023	0.40	0.0084	1.50	1.70	1.60
3024	0.40	0.0080	1.50	1.70	1.60
4001	0.40	0.0587	1.30	1.30	1.30
4002	0.40	0.0239	1.30	1.30	1.30
4003	0.40	0.0197	1.50	1.50	1.50
4004	0.40	0.0165	1.70	1.70	1.70
4005	0.40	0.0153	1.70	1.77	1.74
4006	0.40	0.0128	1.70	1.85	1.78
4007	0.40	0.0117	1.70	1.92	1.82
4008	0.40	0.0106	1.70	2.00	1.85
4009	0.40	0.0105	1.75	1.92	1.84
4010	0.40	0.0097	1.80	1.85	1.82
4011	0.40	0.0091	1.75	1.85	1.80
4012	0.40	0.0091	1.70	1.85	1.78
4013	0.40	0.0088	1.70	1.70	1.74
4014	0.40	0.0086	1.70	1.70	1.70
4015	0.40	0.0083	1.70	1.70	1.70
4016	0.40	0.0079	1.70	1.70	1.70

Average concentration, C_a , and maximum concentration at the cores of the votex pair, C_m , cont'd.

image	C_o	C_a/C_o	(C_m/C_a)	$\overline{(C_m/C_a)}$	C_m/C_a
No.	g/liter	-	left	right	ave
5001	0.40	0.1053	1.50	1.50	1.50
5002	0.40	0.0300	1.50	1.50	1.50
5003	0.40	0.0209	1.50	1.50	1.50
5004	0.40	0.0179	1.50	1.50	1.50
5005	0.40	0.0157	1.50	1.60	1.55
5006	0.40	0.0145	1.50	1.70	1.60
5007	0.40	0.0134	1.40	1.70	1.55
5008	0.40	0.0129	1.30	1.70	1.50
5009	0.40	0.0120	1.30	1.80	1.55
5010	0.40	0.0114	1.30	1.90	1.60
5011	0.40	0.0107	1.30	1.90	1.60
5012	0.40	0.0101	1.30	1.90	1.60
5013	0.40	0.0100	1.30	1.87	1.59
5014	0.40	0.0096	1.30	1.85	1.58
5015	0.40	0.0093	1.30	1.85	1.58
5016	0.40	0.0087	1.30	1.85	1.58
5017	0.40	0.0087	1.30	1.87	1.59
5018	0.40	0.0084	1.30	1.90	1.60
5019	0.40	0.0081	1.30	2.00	1.65
5020	0.40	0.0078	1.30	2.10	1.70
5021	0.40	0.0077	1.30	2.05	1.68
5022	0.40	0.0074	1.30	2.00	1.65
5023	0.40	0.0074	1.30	2.05	1.68
5024	0.40	0.0072	1.30	2.10	1.70
5025	0.40	0.0070	1.30	2.05	1.69
6001	0.40	0.0754	1.50	1.50	1.50
6002	0.40	0.0338	1.50	1.50	1.50
6003	0.40	0.0251	1.40	1.50	1.45
6004	0.40	0.0222	1.30	1.50	1.40
6005	0.40	0.0197	1.45	1.70	1.65
6006	0.40	0.0165	1.90	1.90	1.90
6007	0.40	0.0151	1.85	1.80	1.82
6008	0.40	0.0127	1.80	1.70	1.75
6009	0.40	0.0120	1.75	1.70	1.72
6010	0.40	0.0116	1.70	1.70	1.70
6011	0.40	0.0109	1.70	1.80 1.90	1.75 1.80
6012	0.40	0.0101	1.70	1.90 1.70	1.70
6013	0.40	0.0098	1.70	1.70	1.60
6014	0.40	0.0099	1.70	l	1
6015 6016	0.40 0.40	0.0098 0.0091	$1.60 \\ 1.50$	1.50 1.50	1.55 1.50
0010		0.0091		tration at	

Average concentration, C_a , and maximum concentration at the cores of the votex pair, C_m , cont'd.

Appendix E

Computer Program in Quick Basic

```
3D INTEGRAL ANALYSIS OF BUOYANT JETS IN A NON-UNIFORM FLOW.
       Jet path is defined in a rectangular Cartesian coordinate system
       The program has several sets of subroutines. These are
       for the calculation in the Potential Core, Zone of Flow
       Establishment, subroutines related to a experiment for
       program verification, AmbientEnvironment for the ambient
       conditions and Plot subroutines for presenting prediction verses
       experimental data, etc. All terms in the program has been defined
       in TermDefinition subroutine.
DECLARE SUB IniCondition ()
DECLARE SUB PlotChassa ()
DECLARE SUB Chassa ()
DECLARE SUB CoreIncrement ()
DECLARE SUB CoreRungeKutta ()
DECLARE SUB CoreVelocity ()
DECLARE SUB CoreWidth ()
DECLARE SUB AmbientEnvironment ()
DECLARE SUB ZfeIncrement ()
DECLARE SUB ZfeRungeKutta ()
DECLARE SUB ZfeVelocity ()
COMMON SHARED ks, kn, betas, betan
COMMON SHARED xmin, xmax, ymin, ymax, zmax, rho, rhoa, drhoa, pi, Mo, Qo, Fo
COMMON SHARED t, x, y, z, dt, dx, dy, dz
                                            'TIME AND POSITION
COMMON SHARED dx1, dy1, dz1, dx2, dy2, dz2, dx3, dy3, dz3, dx4, dy4, dz4
COMMON SHARED Bx, By, Bz, dBx, dBy, dBz
                                            'BUOYANCY-FORCE VECTOR
COMMON SHARED Bx1, dBy1, dBz1
COMMON SHARED dBx2, dBy2, dBz2, dBx3, dBy3, dBz3, dBx4, dBy4, dBz4
COMMON SHARED B, db, db1, db2, db3, db4, vol
                                            'WIDTH AND VOLUME
COMMON SHARED mx, my, mz, ms, mn
                                            'MOMENTUM DEFECT
COMMON SHARED dmx, dmy, dmz, dmx1, dmy1, dmz1
COMMON SHARED dmx2, dmy2, dmz2, dmx3, dmy3, dmz3, dmx4, dmy4, dmz4
COMMON SHARED UUx, UUy, UUz
                                            'VELOCITY AND DIRECTION
COMMON SHARED Ua, Uax, dUax, Uay, dUay, Uaz, dUaz, sx, sy, sz, nx, ny, nz
COMMON SHARED ux, uy, uz, us, un, usx, usy, usz, unx, uny, unz
COMMON SHARED a, R, RR, d, dd, ds
COMMON SHARED rc, drc, drc1, drc2, drc3, drc4
COMMON SHARED delta, deltas, deltan, W, Uc, Uas, Uan, ve, UUs, Wo
COMMON SHARED deg, thetao, phi, degPhi, degthetao
COMMON SHARED xx, zz, zzz, xxu, xxl, zzu, zzl
COMMON SHARED Fro, VR, yt, lm, zm, Re
COMMON SHARED drho, rhoo, rho1
```

```
COMMON SHARED gx, gy, gz, gg
COMMON SHARED dFs, s, ts, ls, Froud, lp
COMMON SHARED Uaxx, Uayy, Uazz, Ao
COMMON SHARED dR1, dW1, dR2, dW2, dR3, dW3, dR, dW
COMMON SHARED dUas, dUc, dDs, dms, term, lb, m.thick
kn = 1
betan = .34
betas = .17
ks = .18
pi = 3.14159
rho = 1
gx = 0
gy = 0
gz = 981
CALL Chassa
CALL IniCondition
DO
        CALL CoreWidth
        CALL CoreRungeKutta
        RR = SQR(vol / pi / UUs)
        CALL PlotChassa
LOOP UNTIL rc < 0
        B = RR
        dt = .001
        CALL ZfeVelocity
DO
        CALL ZfeRungeKutta
        CALL PlotChassa
LOOP UNTIL xx > xmax
END
SUB AmbientEnvironment STATIC
     rhoa = rho
     IF z < .01 * delta THEN
        Uax = Ua * 51.79 * z / delta
        dUax = 51.79 * Ua / delta * dz: dUay = 0: dUaz = 0
        ELSE
        IF z < delta THEN
          Uax = Ua * (z / delta) ^ (1 / 7): Uay = 0: Uaz = 0
           dUax = Ua / 7 / z * (z / delta) ^ (1 / 7) * dz: dUay = 0: dUaz = 0
              ELSE
          Uax = Ua
          dUax = 0: dUay = 0: dUaz = 0
        END IF
    END IF
END SUB
SUB Chassa STATIC
Ua = 429.1
d = 4
```

```
a = d / 2
m.thick = d
                                'momentum thickness
delta = m.thick * 72 / 7
'>>>>>> Test condition for the jet in crossflow
                               'SELECT VELOCITY RATIO
         VR = 2.37
         VR = 3.95
         VR = 6.35
        degthetao = 90
        degPhi = 0
        thetao = pi / 180 * degthetao
        phi = pi / 180 * degPhi
       Wo = VR * Ua
                              '/ 100
        Qo = Wo * d^2 * pi / 4
        Mo = Qo * Wo
        gg = 0
                              10000
        Fo = gg * Qo
       lm = SQR(Mo / Ua ^ 2)
IF VR = 2.37 THEN xmax = 10: ymax = 15
IF VR = 3.95 THEN xmax = 20: ymax = 20
IF VR = 6.35 THEN xmax = 20: ymax = 25
SCREEN 12
WINDOW (-.6 * xmax, -.3 * ymax) - (2 * xmax, 1.2 * ymax)
LINE (-2.5, 0)-(xmax, ymax), B
LOCATE 13, 6: PRINT "z/ro"
LOCATE 26, 19: PRINT "O"
LOCATE 26, 48: PRINT xmax
LOCATE 5, 5: PRINT ymax
LOCATE 27, 32: PRINT "x/ro"
LOCATE 26, 11: PRINT "-2.5"
LOCATE 25, 9: PRINT "O"
IF VR = 2.37 THEN OPEN "chassal.dat" FOR INPUT AS #1
IF VR = 3.95 THEN OPEN "chassa2.dat" FOR INPUT AS #1
IF VR = 6.35 THEN OPEN "chassa3.dat" FOR INPUT AS #1
i = 0
DO
       i = i + 1
       INPUT #1, x, z
       xx(i) = x * 25 / 14.5
       zz(i) = z * 30 / 7.08
       CIRCLE (xx(i), zz(i)), xmax / ymax / 6, VR / 3 + 1
LOOP UNTIL EOF(1)
LOCATE 4, 16: PRINT USING "delta = ##.## m.thickness=##.## "; delta; m.thick
END SUB
SUB CoreIncrement STATIC
dx = UUx * dt: dy = UUy * dt: dz = UUz * dt
CALL AmbientEnvironment
```

```
dmx = -rho * vol * dUax + Bx * dt
dmy = -rho * vol * dUay + By * dt
dmz = -rho * vol * dUaz + Bz * dt
END SUB
SUB CoreRungeKutta STATIC
       subroutine to produce the incremental changes over the period
       of time, dt. The calculation for the changes is carried out
       by four passes according to the Runge-Kutta method
'----- 1st pass ------
                             'evaluated at the beginning of the interval
CALL CoreIncrement
dx1 = dx: dy1 = dy: dz1 = dz
drc1 = drc
dR1 = dR
dW1 = dW
dmx1 = dmx : dmy1 = dmy : dmz1 = dmz
x = x + dx1 / 2: y = y + dy1 / 2: z = z + dz1 / 2
rc = rc + drc1 / 2
R = R + dR1 / 2
W = W + dW1 / 2
mx = mx + dmx1 / 2: my = my + dmy1 / 2: mz = mz + dmz1 / 2
CALL CoreVelocity
'----- 2nd pass -----
CALL CoreIncrement
                             'evaluated at the mid-interval
dx2 = dx: dy2 = dy: dz2 = dz: dmx2 = dmx: dmy2 = dmy: dmz2 = dmz
drc2 = drc
dR2 = dR
dW2 = dW
x = x - dx1 / 2 + dx2 / 2: y = y - dy1 / 2 + dy2 / 2
z = z - dz1 / 2 + dz2 / 2
rc = rc - drc1 / 2 + drc2 / 2
R = R - dR1 / 2 + dR2 / 2
W = W - dW1 / 2 + dW2 / 2
Bx = Bx - dBx1 / 2 + dBx2 / 2: By = By - dBy1 / 2 + dBy2 / 2
mx = mx - dmx1 / 2 + dmx2 / 2: my = my - dmy1 / 2 + dmy2 / 2
mz = mz - dmz1 / 2 + dmz2 / 2
CALL CoreVelocity
'----- 3rd pass ------
CALL CoreIncrement 'evaluated at the mid-interval
dx3 = dx: dy3 = dy: dz3 = dz: dmx3 = dmx: dmy3 = dmy: dmz3 = dmz
drc3 = drc
dR3 = dR
dW3 = dW
x = x - dx2 / 2 + dx3: y = y - dy2 / 2 + dy3
z = z - dz2 / 2 + dz3
rc = rc - drc2 / 2 + drc3
R = R - dR2 / 2 + dR3
W = W - dW2 / 2 + dW3
Bx = Bx - dBx2 / 2 + dBx3: By = By - dBy2 / 2 + dBy3
```

```
mx = mx - dmx2 / 2 + dmx3: my = my - dmy2 / 2 + dmy3
mz = mz - dmz2 / 2 + dmz3
CALL CoreVelocity
'----- 4th pass ------
                             'evaluated at the end of the interval
CALL CoreIncrement
drc4 = drc
dR4 = dR
dW4 = dW
dx4 = dx: dy4 = dy: dz4 = dz: drc4 = drc: dmx4 = dmx: dmy4 = dmy: dmz4 = dmz
                             'back to the beginning of the interval
x = x - dx3: y = y - dy3
                             'actual increment at the end of the routine
z = z - dz3
rc = rc - drc3
R = R - dR3
W = W - dW3
mx = mx - dmx3: my = my - dmy3: mz = mz - dmz3
CALL CoreVelocity
'----- actual weight-averaged increment ------
dx = (dx1 + 2 * dx2 + 2 * dx3 + dx4) / 6: x = x + dx
dy = (dy1 + 2 * dy2 + 2 * dy3 + dy4) / 6: y = y + dy
dz = (dz1 + 2 * dz2 + 2 * dz3 + dz4) / 6: z = z + dz
drc = (drc1 + 2 * drc2 + 2 * drc3 + drc4) / 6: rc = rc + drc
dR = (dR1 + 2 * dR2 + 2 * dR3 + dR4) / 6: R = R + dR
dW = (dW1 + 2 * dW2 + 2 * dW3 + dW4) / 6: W = W + dW
dBx = (dBx1 + 2 * dBx2 + 2 * dBx3 + dBx4) / 6: Bx = Bx + dBx
dBy = (dBy1 + 2 * dBy2 + 2 * dBy3 + dBy4) / 6: By = By + dBy
dmx = (dmx1 + 2 * dmx2 + 2 * dmx3 + dmx4) / 6: mx = mx + dmx
dmy = (dmy1 + 2 * dmy2 + 2 * dmy3 + dmy4) / 6: my = my + dmy
dmz = (dmz1 + 2 * dmz2 + 2 * dmz3 + dmz4) / 6: mz = mz + dmz
CALL CoreVelocity
END SUB
SUB CoreVelocity STATIC
CALL AmbientEnvironment
                       'for the ambient density and velocity
Uas = (Uax * sx + Uay * sy + Uaz * sz)
ms = (mx * sx + my * sy + mz * sz): us = ms / (1 + ks) / vol / rho
mn = (mx * nx + my * ny + mz * nz): un = mn / (1 + kn) / vol / rho
ux = us * sx + un * nx: uy = us * sy + un * ny: uz = us * sz + un * nz
UUx = ux + Uax: UUy = uy + Uay: UUz = uz + Uaz
UUs = SQR(UUx ^2 + UUy ^2 + UUz ^2)
vol = pi * rc ^ 2 * W + pi * (R ^ 2 - rc ^ 2) * Uc
Bz = pi * (rc^2 * W * gg + (R^2 - rc^2) * Uc * gg / 2)
sx = UUx / UUs: sy = UUy / UUs: sz = UUz / UUs 'new s-vector
us = (ux * sx + uy * sy + uz * sz) 'current estimate of us
unx = ux - us * sx: uny = uy - us * sy: unz = uz - us * sz
un = SQR(unx^2 + uny^2 + unz^2)
                                           'new un
nx = unx / un: ny = uny / un: nz = unz / un 'new n-vector
END SUB
```

SUB CoreWidth STATIC

```
Uas = (Uax * sx + Uay * sy + Uaz * sz)
    Uan = (Uax * nx + Uay * ny + Uaz * nz)
    ds = dx * sx + dy * sy + dz * sz
    dW = gg * dz / W
    dUas = dUax * sx + dUay * sy + dUaz * sz
    dUc = (dW + dUas) / 2
    dDs = (dW - dUas) / 2
    dms = dmx * sx + dmy * sy + dmz * sz
    deltas = (W - Uas) / 2: deltan = Uan
    Uc = (W + Uas) / 2
    dd = (betas * ABS(deltas) + betan * ABS(deltan)) / Uc * ds
    term = dms / pi / rho - 2 * dW * deltas * rc ^ 2 - 2 * W * dDs * rc ^ 2
    term = term - (1 + ks) * 2 * R * dd * Uc * deltas
    term = term - (1 + ks) * (R ^ 2 - rc ^ 2) * dUc * deltas
    term = term - (1 + ks) * (R^2 - rc^2) * Uc * dDs
    drc = term / (4 * W * deltas * rc + 2 * (1 + ks) * (R - rc) * Uc * deltas)
    dR = dd + drc
    dt = ds / UUs
END SUB
SUB IniCondition STATIC
        vol = Qo: R = SQR(vol / pi / Wo): rc = R: a = rc: d = 2 * a
        W = Wo
        x = 0: y = 0: z = .00001
        dt = 9.9999999999999900-08
        CALL AmbientEnvironment
        Bx = 0: By = 0: Bz = Fo
        UUx = Wo * COS(thetao) * COS(phi)
        UUy = Wo * COS(thetao) * SIN(phi)
        UUz = Wo * SIN(thetao)
        mx = rho * (UUx - Uax) * Qo
        my = rho * (UUy - Uay) * Qo
        mz = rho * (UUz - Uaz) * Qo
        ux = UUx - Uax
        uy = UUy - Uay
        uz = UUz - Uaz
        UUs = SQR(UUx ^ 2 + UUy ^ 2 + UUz ^ 2)
        sx = UUx / UUs: sy = UUy / UUs: sz = UUz / UUs
        us = (ux * sx + uy * sy + uz * sz)
        unx = ux - us * sx: uny = uy - us * sy: unz = uz - us * sz
        un = SQR(unx^2 + uny^2 + unz^2)
        nx = unx / un: ny = uny / un: nz = unz / un
        ds = Wo * dt
        dx = ds * sx: dy = ds * sy: dz = ds * sz
        W = Wo
        CALL CoreVelocity
END SUB
SUB PlotChassa STATIC
IF rc > 0 THEN
        xx = x / a
        zz = z / a
        xxu = (x - RR * sz) / a
```

```
zzu = (z + RR * sx) / a
        xx1 = (x + RR * sz) / a
        zz1 = (z - RR * sx) / a
        PSET (-rc / a + xx, zz)
        PSET (rc / a + xx, zz)
        PSET (xxu, zzu)
        PSET (xxl, zzl)
        PSET (xx, zz)
END IF
IF rc < 0 THEN
        xx = x / a
        zz = z / a
        xxu = (x - B * sz) / a
        zzu = (z + B * sx) / a
        xxl = (x + B * sz) / a
        zz1 = (z - B * sx) / a
IF zzu < ymax THEN PSET (xxu, zzu), 12
IF xxl < xmax THEN PSET (xxl, zzl), 12
PSET (xx, zz), 12
END IF
END SUB
SUB TermDefinition
'ks
         added mass coef. in path direction
'kn
         added mass coef. in normal to the path direction
'kx
         added mass coef. in x direction
'ky
         added mass coef. in y direction
         added mass coef. in z direction
'ky
'betas
         spreading coef. in 's' direction
         spreading coef. in 'n' direction
'betan
'xmax
         maximum value in x direction
         maximum value in y direction
'ymax
         maximum value in z direction
'zmax
'rho
         density of the 'water' in g-cm units
'rhoa
         density of the 'ambient fluid' in g-cm units
'drhoa
         variation of density of 'ambient fluid' in g-cm units
'pi
         3.14159
'Mo
         initial momentum flux
, Qo
         initial volume flux
'Fo
         initial buoyancy flux
't
, x
         position of the dominant eddy in x direction
'у
         position of the dominant eddy in y direction
'z
         position of the dominant eddy in z direction
'dt
         time increment
'dx
         x increment
         y increment
'dy
'dz
         z increment
'Bx
         buoyancy in x direction
'By
         buoyancy in y direction
```

```
'Bz
         buoyancy in z direction
'dBx
         variation of buoyancy in x direction
 'dBy
         variation of buoyancy in y direction
'dBz
         variation of buoyancy in z direction
'nЪ
         width of buoyant jet in top-hat profile
'db
         width increment
'vol
         volume
'mx
         relative momentum in x direction
'my
         relative momentum in y direction
'mz
         relative momentum in z direction
'ns
         relative momentum in path direction
'mn
         relative momentum normal to the path direction
, UUx
         absolute velocity of the eddy in x direction
, UU v
         absolute velocity of the eddy in y direction
'UUz
         absolute velocity of the eddy in z direction
'Ua
         ambient velocity
'Uax
         ambient velocity in x direction
'Uav
         ambient velocity in y direction
'Uaz
         ambient velocity in z direction
'dUax
         ambient velocity variation in x direction
'dUay
         ambient velocity variation in y direction
'dUaz
         ambient velocity variation in z direction
'sx
         tangential unit vector in x direction
'sy
         tangential unit vector in y direction
'sz
         tangential unit vector in z direction
         normal unit vector in x direction
'nx
'ny
         normal unit vector in y direction
         normal unit vector in z direction
'nz
'ux
         relative velocity of the eddy in x direction
'uy
         relative velocity of the eddy in y direction
'uz
         relative velocity of the eddy in z direction
'us
         relative velocity of the eddy in s direction
'un
         relative velocity of the eddy in n direction
'unx
         projected normal relative velocity in x direction
uny
         projected normal relative velocity in y direction
         projected normal relative velocity in z direction
'betas = .17 spreading coefficient in tangential direction
'betan = .34 spreading coefficient in normal direction
         initial radius of Buoyant Jets
'R
         jet radius
'd
         initial jet diameter
'rc
         core radius
END SUB
SUB ZfeIncrement STATIC
'-----increment according to spreading hypothesis------
                          un and us are positive
dx = UUx * dt: dy = UUy * dt: dz = UUz * dt
db = betas * ABS(us) * dt + betan * ABS(un) * dt
CALL AmbientEnvironment
dBx = gx * vol * drhoa
dBy = gy * vol * drhoa
dBz = gz * vol * drhoa
dmx = -rho * vol * dUax + Bx * dt
```

```
dmy = -rho * vol * dUay + By * dt
dmz = -rho * vol * dUaz + Bz * dt
END SUB
SUB ZfeRungeKutta STATIC
       subroutine to produce the incremental changes over a period
       of time, dt. Calculation for changes is carried out
       by four passes according to the Runge-Kutta method
'----- 1st pass ------
CALL ZfeIncrement
                          'evaluated at the beginning of the interval
dx1 = dx: dy1 = dy: dz1 = dz: db1 = db
dBx1 = dBx: dBy1 = dBy: dBz1 = dBz
dmx1 = dmx: dmy1 = dmy: dmz1 = dmz
x = x + dx1 / 2: y = y + dy1 / 2: z = z + dz1 / 2: B = B + db1 / 2
Bx = Bx + dBx1 / 2: By = By + dBy1 / 2: Bz = Bz + dBz1 / 2
mx = mx + dmx1 / 2: my = my + dmy1 / 2: mz = mz + dmz1 / 2
CALL ZfeVelocity
'evaluated at the mid-interval
CALL ZfeIncrement
dx2 = dx: dy2 = dy: dz2 = dz: db2 = db: dmx2 = dmx: dmy2 = dmy: dmz2 = dmz
dBx2 = dBx: dBy2 = dBy: dBz2 = dBz
x = x - dx1 / 2 + dx2 / 2: y = y - dy1 / 2 + dy2 / 2
z = z - dz1 / 2 + dz2 / 2: B = B - db1 / 2 + db2 / 2
Bx = Bx - dBx1 / 2 + dBx2 / 2: By = By - dBy1 / 2 + dBy2 / 2
Bz = Bz - dBz1 / 2 + dBz2 / 2
mx = mx - dmx1 / 2 + dmx2 / 2: my = my - dmy1 / 2 + dmy2 / 2
mz = mz - dmz1 / 2 + dmz2 / 2
CALL ZfeVelocity
'----- 3rd pass -----
CALL ZfeIncrement
                          'evaluated at the mid-interval
dx3 = dx: dy3 = dy: dz3 = dz: db3 = db: dmx3 = dmx: dmy3 = dmy: dmz3 = dmz
dBx3 = dBx: dBy3 = dBy: dBz3 = dBz
x = x - dx2 / 2 + dx3: y = y - dy2 / 2 + dy3
z = z - dz^2 / 2 + dz^3: B = B - db^2 / 2 + db^3
Bx = Bx - dBx2 / 2 + dBx3: By = By - dBy2 / 2 + dBy3
Bz = Bz - dBz2 / 2 + dBz3
mx = mx - dmx2 / 2 + dmx3: my = my - dmy2 / 2 + dmy3
mz = mz - dmz2 / 2 + dmz3
CALL ZfeVelocity
'----- 4th pass -----
CALL ZfeIncrement 'evaluated at the end of the interval
dBx4 = dBx: dBy4 = dBy: dBz4 = dBz
dx4 = dx: dy4 = dy: dz4 = dz: db4 = db: dmx4 = dmx: dmy4 = dmy: dmz4 = dmz
x = x - dx3: y = y - dy3 'back to the beginning of the interval z = z - dz3: B = B - db3 'actual increment at the end of the routine
Bx = Bx - dBx3: By = By - dBy3: Bz = Bz - dBz3
mx = mx - dmx3: my = my - dmy3: mz = mz - dmz3
CALL ZfeVelocity
```

```
'----- actual weight-averaged increment ------
dx = (dx1 + 2 * dx2 + 2 * dx3 + dx4) / 6: x = x + dx
dy = (dy1 + 2 * dy2 + 2 * dy3 + dy4) / 6: y = y + dy
dz = (dz1 + 2 * dz2 + 2 * dz3 + dz4) / 6: z = z + dz
db = (db1 + 2 * db2 + 2 * db3 + db4) / 6: B = B + db
dBx = (dBx1 + 2 * dBx2 + 2 * dBx3 + dBx4) / 6: Bx = Bx + dBx
dBy = (dBy1 + 2 * dBy2 + 2 * dBy3 + dBy4) / 6: By = By + dBy
dBz = (dBz1 + 2 * dBz2 + 2 * dBz3 + dBz4) / 6: Bz = Bz + dBz
dmx = (dmx1 + 2 * dmx2 + 2 * dmx3 + dmx4) / 6: mx = mx + dmx
dmy = (dmy1 + 2 * dmy2 + 2 * dmy3 + dmy4) / 6: my = my + dmy
dmz = (dmz1 + 2 * dmz2 + 2 * dmz3 + dmz4) / 6: mz = mz + dmz
CALL ZfeVelocity
END SUB
SUB ZfeVelocity STATIC
'------subroutine to find the s- and n-vectors-------
               With m-vector and volume of the element given, the
               s- and n-vectors are determined by iteration method. The
               directions of the vectors are initially assumed to be
               the same as the previous time step. It is important
               to note that ms, mn, us, and un are magnitude of the
               vectors in s- and n-directions. The directions of the
               velocities are defined by the s- and n-vectors.
CALL AmbientEnvironment
                               'for the ambient density and velocity
Uas = (Uax * sx + Uay * sy + Uaz * sz)
Uan = (Uax * nx + Uay * ny + Uaz * nz)
ms = (mx * sx + my * sy + mz * sz): us = ms / (1 + ks) / vol / rho
mn = (mx * nx + my * ny + mz * nz): un = mn / (1 + kn) / vol / rho
ux = us * sx + un * nx: uy = us * sy + un * ny: uz = us * sz + un * nz
UUx = ux + Uax: UUy = uy + Uay: UUz = uz + Uaz
UUs = SQR(UUx ^ 2 + UUy ^ 2 + UUz ^ 2)
vol = pi * B ^ 2 * UUs
sx = UUx / UUs: sy = (UUy / UUs): sz = UUz / UUs 'new s-vector
us = (ux * sx + uy * sy + uz * sz)
                                                'current estimate of us
unx = ux - us * sx: uny = uy - us * sy: unz = uz - us * sz
un = SQR(unx^2 + uny^2 + unz^2)
                                                'new un
nx = unx / un: ny = uny / un: nz = unz / un
                                               'new n-vector
END SUB
```